WVMP SAR Reference 3-13

CRC Handbook of Chemistry and Physics, 75th ed., Chapter 5, CRC Press, Boca Raton, Florida, 1994.

STANDARD THERMODYNAMIC PROPERTIES OF CHEMICAL SUBSTANCES (continued)

Name	State	$\Delta_f H°$ kJ/mol	$\Delta_f G°$ kJ/mol	$S°$ J/mol K	C_p J/mol K
Aluminum trichloride	cry	–704.2	–628.8	110.7	91.8
	gas	–583.2			
Aluminum fluoride (AlF)	gas	–258.2	–283.7	215.0	31.9
Aluminum trifluoride	cry	–1510.4	–1431.1	66.5	75.1
	gas	–1204.6	–1188.2	277.1	62.6
Sodium tetrafluoroaluminate	gas	–1869.0	–1827.5	345.7	105.9
Aluminum hydride (AlH)	gas	259.2	231.2	187.9	29.4
Aluminum hydride (AlH_3)	cry	–46.0			
Potassium tetrahydroaluminate	cry	–183.7			
Lithium tetrahydroaluminate	cry	–116.3	–44.7	78.7	83.2
Aluminum iodide (AlI)	gas	65.5			36.0
Aluminum triiodide	cry	–313.8	–300.8	159.0	98.7
	gas	–207.5			
Aluminum nitride (AlN)	cry	–318.0	–287.0	20.2	30.1
Aluminum oxide (AlO)	gas	91.2	65.3	218.4	30.9
Aluminum phosphate ($AlPO_4$)	cry	–1733.8	–1617.9	90.8	93.2
Aluminum phosphide (AlP)	cry	–166.5			
Aluminum sulfide (AlS)	gas	200.9	150.1	230.6	33.4
Aluminum (Al_2)	gas	485.9	433.3	233.2	36.4
Aluminum hexabromide	gas	–970.7			
Aluminum hexachloride	gas	–1290.8	–1220.4	490.0	
Aluminum hexafluoride	gas	–2628.0			
Aluminum hexaiodide	gas	–516.7			
Aluminum oxide (Al_2O)	gas	–130.0	–159.0	259.4	45.7
Aluminum oxide (Al_2O_3)	cry	–1675.7	–1582.3	50.9	79.0
Aluminum sulfide (Al_2S_3)	cry	–724.0			
Americium	cry	0.0			
Argon	gas	0.0		154.8	20.8
Arsenic (gray)	cry	0.0		35.1	24.6
Arsenic (yellow)	cry	14.6			
	gas	302.5	261.0	174.2	20.8
Arsenic tribromide	cry	–197.5			
	gas	–130.0	–159.0	363.9	79.2
Arsenic trichloride	liq	–305.0	–259.4	216.3	
	gas	–261.5	–248.9	327.2	75.7
Arsenic trifluoride	liq	–821.3	–774.2	181.2	126.6
	gas	–785.8	–770.8	289.1	65.6
Gallium arsenide (GaAs)	cry	–71.0	–67.8	64.2	46.2
Arsine	gas	66.4	68.9	222.8	38.1
Arsenic acid (H_3AsO_4)	cry	–906.3			
Arsenic triiodide	cry	–58.2	–59.4	213.1	105.8
	gas			388.3	80.6
Indium arsenide (InAs)	cry	–58.6	–53.6	75.7	47.8
Arsenic oxide (AsO)	gas	70.0			
Arsenic (As_2)	gas	222.2	171.9	239.4	35.0
Arsenic pentoxide (As_2O_5)	cry	–924.9	–782.3	105.4	116.5
Arsenic trisulfide (As_2S_3)	cry	–169.0	–168.6	163.6	116.3
Astatine	cry	0.0			
Gold	cry	0.0		47.4	25.4
	gas	366.1	326.3	180.5	20.8
Gold bromide (AuBr)	cry	–14.0			
Gold bromide ($AuBr_3$)	cry	–53.3			
Gold chloride (AuCl)	cry	–34.7			
Gold chloride ($AuCl_3$)	cry	–117.6			
Gold fluoride (AuF_3)	cry	–363.6			
Gold hydride (AuH)	gas	295.0	265.7	211.2	29.2
Gold iodide (AuI)	cry	0.0			

STANDARD THERMODYNAMIC PROPERTIES OF CHEMICAL SUBSTANCES (continued)

Molecular formula	Name	State	$\Delta_f H°$ kJ/mol	$\Delta_f G°$ kJ/mol	$S°$ J/mol K	C_p J/mol K
Br_4Ti	Titanium bromide ($TiBr_4$)	cry	−616.7	−589.5	243.5	131.5
		gas	−549.4	−568.2	398.4	100.8
Br_4V	Vanadium bromide (VBr_4)	gas	−336.8			
Br_4Zr	Zirconium bromide ($ZrBr_4$)	cry	−760.7			
Br_5P	Phosphorus pentabromide	cry	−269.9			
Br_5Ta	Tantalum bromide ($TaBr_5$)	cry	−598.3			
Br_6W	Tungsten bromide (WBr_6)	cry	−348.5			
Ca	Calcium	cry	0.0		41.6	25.9
		gas	177.8	144.0	154.9	20.8
$CaCl_2$	Calcium chloride	cry	−795.4	−748.8	108.4	72.9
CaF_2	Calcium fluoride	cry	−1228.0	−1175.6	68.5	67.0
CaH_2	Calcium hydride (CaH_2)	cry	−181.5	−142.5	41.4	41.0
CaH_2O_2	Calcium hydroxide	cry	−985.2	−897.5	83.4	87.5
CaI_2	Calcium iodide	cry	−533.5	−528.9	142.0	
CaN_2O_6	Calcium nitrate	cry	−938.2	−742.8	193.2	149.4
CaO	Calcium oxide	cry	−634.9	−603.3	38.1	42.0
CaO_4S	Calcium sulfate	cry	−1434.5	−1322.0	106.5	99.7
CaS	Calcium sulfide	cry	−482.4	−477.4	56.5	47.4
$Ca_3O_8P_2$	Calcium phosphate	cry	−4120.8	−3884.7	236.0	227.8
Cd	Cadmium	cry	0.0		51.8	26.0
		gas	111.8		167.7	20.8
$CdCl_2$	Cadmium chloride	cry	−391.5	−343.9	115.3	74.7
CdF_2	Cadmium fluoride	cry	−700.4	−647.7	77.4	
CdH_2O_2	Cadmium hydroxide	cry	−560.7	−473.6	96.0	
CdI_2	Cadmium iodide	cry	−203.3	−201.4	161.1	80.0
CdO	Cadmium oxide	cry	−258.4	−228.7	54.8	43.4
CdO_4S	Cadmium sulfate	cry	−933.3	−822.7	123.0	99.6
CdS	Cadmium sulfide	cry	−161.9	−156.5	64.9	
CdTe	Cadmium telluride	cry	−92.5	−92.0	100.0	
Ce	Cerium	cry	0.0		72.0	26.9
		gas	423.0	385.0	191.8	23.1
$CeCl_3$	Cerium chloride ($CeCl_3$)	cry	−1053.5	−977.8	151.0	87.4
CeO_2	Cerium oxide (CeO_2)	cry	−1088.7	−1024.6	62.3	61.6
CeS	Cerium sulfide (CeS)	cry	−459.4	−451.5	78.2	50.0
Ce_2O_3	Cerium oxide (Ce_2O_3)	cry	−1796.2	−1706.2	150.6	114.6
Cf	Californium	cry	0.0			
Cl	Chlorine	gas	121.3	105.3	165.2	21.8
ClCs	Cesium chloride	cry	−443.0	−414.5	101.2	52.5
$ClCsO_4$	Cesium perchlorate	cry	−443.1	−314.3	175.1	108.3
ClCu	Copper chloride (CuCl)	cry	−137.2	−119.9	86.2	48.5
ClF	Chlorine fluoride	gas	−50.3	−51.8	217.9	32.1
$ClFO_3$	Perchloryl fluoride	gas	−23.8	48.2	279.0	64.9
ClGe	Germanium chloride (GeCl)	gas	155.2	124.2	247.0	36.9
ClF_3	Chlorine trifluoride	liq	−189.5			
		gas	−163.2	−123.0	281.6	63.9
ClF_5S	Sulfur chloride pentafluoride	liq	−1065.7			
$ClGeH_3$	Chlorogermane	gas			263.7	54.7
ClH	Hydrogen chloride	gas	−92.3	−95.3	186.9	29.1
ClHO	Hypochlorous acid (HOCl)	gas	−78.7	−66.1	236.7	37.2
$ClHO_4$	Perchloric acid	liq	−40.6			
ClH_3Si	Chlorosilane	gas			250.7	51.0
ClH_4N	Ammonium chloride	cry	−314.4	−202.9	94.6	84.1
ClH_4NO_4	Ammonium perchlorate	cry	−295.3	−88.8	186.2	
ClH_4P	Phosphonium chloride	cry	−145.2			
ClI	Iodine chloride	liq	−23.9	−13.6	135.1	
		gas	17.8	−5.5	247.6	35.6
ClIn	Indium chloride (InCl)	cry	−186.2			

Molecular formula	Name	State	$\Delta_f H°$ kJ/mol	$\Delta_f G°$ kJ/mol	$S°$ J/mol K
		gas	−374.9	−305.0	364.6
Cl_5Pa	Protactinium chloride ($PaCl_5$)	cry	−1145.0	−1034.0	238.0
Cl_5Ta	Tantalum chloride ($TaCl_5$)	cry	−859.0		
Cl_6U	Uranium chloride (UCl_6)	cry	−1092.0	−962.0	285.8
		gas	−1013.0	−928.0	431.0
Cl_6W	Tungsten chloride (WCl_6)	cry	−602.5		
		gas	−513.8		
Cm	Curium	cry	0.0		
Co	Cobalt	cry	0.0		30.0
		gas	424.7	380.3	179.5
CoF_2	Cobalt fluoride (CoF_2)	cry	−692.0	−647.2	82.0
CoH_2O_2	Cobalt hydroxide ($Co(OH)_2$)	cry	−539.7	−454.3	79.0
CoI_2	Cobalt iodide (CoI_2)	cry	−88.7		
CoN_2O_6	Cobalt nitrate ($Co(NO_3)_2$)	cry	−420.5		
CoO	Cobalt oxide (CoO)	cry	−237.9	−214.2	53.0
CoO_4S	Cobalt sulfate ($CoSO_4$)	cry	−888.3	−782.3	118.0
CoS	Cobalt sulfide (CoS)	cry	−82.8		
Co_2S_3	Cobalt sulfide (Co_2S_3)	cry	−147.3		
Co_3O_4	Cobalt oxide (Co_3O_4)	cry	−891.0	−774.0	102.5
Cr	Chromium	cry	0.0		23.8
		gas	396.6	351.8	174.5
CrF_2	Chromium fluoride (CrF_2)	cry	−778.0		
CrF_3	Chromium fluoride (CrF_3)	cry	−1159.0	−1088.0	93.9
CrI_2	Chromium iodide (CrI_2)	cry	−156.9		
CrI_3	Chromium iodide (CrI_3)	cry	−205.0		
CrO_2	Chromium oxide (CrO_2)	cry	−598.0		
CrO_4Pb	Lead chromate ($PbCrO_4$)	cry	−930.9		
Cr_2FeO_4	Chromium iron oxide ($FeCr_2O_4$)	cry	−1444.7	−1343.8	146.0
Cr_2O_3	Chromium oxide (Cr_2O_3)	cry	−1139.7	−1058.1	81.2
Cr_3O_4	Chromium oxide (Cr_3O_4)	cry	−1531.0		
Cs	Cesium	cry	0.0		85.2
		gas	76.5	49.6	175.6
CsF	Cesium fluoride	cry	−553.5	−525.5	92.8
CsF_2H	Cesium hydrogen fluoride ($CsHF_2$)	cry	−923.8	−858.9	135.2
CsH	Cesium hydride	cry	−54.2		
CsHO	Cesium hydroxide	cry	−417.2		
$CsHO_4S$	Cesium hydrogen sulfate	cry	−1158.1		
CsH_2N	Cesium amide	cry	−118.4		
CsI	Cesium iodide	cry	−346.6	−340.6	123.1
$CsNO_3$	Cesium nitrate	cry	−506.0	−406.5	155.2
CsO_2	Cesium superoxide (CsO_2)	cry	−286.2		
Cs_2O	Cesium oxide (Cs_2O)	cry	−345.8	−308.1	146.9
Cs_2O_3S	Cesium sulfite	cry	−1134.7		
Cs_2O_4S	Cesium sulfate	cry	−1443.0	−1323.6	211.9
Cs_2S	Cesium sulfide (Cs_2S)	cry	−359.8		
Cu	Copper	cry	0.0		33.2
		gas	337.4	297.7	166.4
CuF_2	Copper fluoride (CuF_2)	cry	−542.7		
CuH_2O_2	Copper hydroxide ($Cu(OH)_2$)	cry	−449.8		
CuI	Copper iodide (CuI)	cry	−67.8	−69.5	96.7
CuN_2O_6	Copper nitrate ($Cu(NO_3)_2$)	cry	−302.9		
CuO	Copper oxide (CuO)	cry	−157.3	−129.7	42.6
CuO_4S	Copper sulfate ($CuSO_4$)	cry	−771.4	−662.2	109.2
CuO_4W	Copper tungstate ($CuWO_4$)	cry	−1105.0		
CuS	Copper sulfide (CuS)	cry	−53.1	−53.6	66.5
CuSe	Copper selenide (CuSe)	cry	−39.5		
Cu_2	Copper (Cu_2)	gas	484.2	431.9	241.6

C_p J/mol K	Molecular formula
112.8	Cu_2O
	Cu_2S
	Dy
175.7	
	Dy_2O_3
	Er
	ErF_3
94.8	Er_2O_3
230	Eu
68.3	
	Eu_2O_3
	Eu_3O_4
	F
56.2	FGa
	FGe
	$FGeH_3$
	FH
123.4	
29.4	FH_3Si
20.8	FH_4N
	FI
78.7	FIn
	FK
	FLi
	FNO
	FNO_2
133.6	FNS
118.7	FNa
	FO
92.2	FRb
20.8	FSi
51.1	FTl
87.5	
	F_2
	F_2Fe
	F_2HK
	F_2HN
52.8	F_2HNa
	F_2HRb
	F_2Mg
76.0	F_2N
	F_2N_2
134.9	F_2N_2
	F_2Ni
24.4	F_2O
20.8	F_2OS
	F_2O_2
	F_2O_2S
54.3	F_2O_2U
	F_2Pb
42.3	F_2Si
	F_2Sr
	F_2Zn
47.8	F_3Ga
	F_3Gd
56.6	F_3HSi

Molecular formula	
Cu_2O	Copper (
Cu_2S	Copper s
Dy	Dyspros
Dy_2O_3	Dyspros
Er	Erbium
ErF_3	Erbium
Er_2O_3	Erbium
Eu	Europiu
Eu_2O_3	Europiu
Eu_3O_4	Europiu
F	Fluorine
FGa	Gallium
FGe	German
$FGeH_3$	Fluorog
FH	Hydrog
FH_3Si	Fluorosi
FH_4N	Ammon
FI	Iodine fl
FIn	Indium f
FK	Potassiu
FLi	Lithium
FNO	Nitrosyl
FNO_2	Nitryl fl
FNS	Thionitr
FNa	Sodium
FO	Fluorine
FRb	Rubidiu
FSi	Fluorosi
FTl	Thalliun
F_2	Fluorine
F_2Fe	Iron fluc
F_2HK	Potassiu
F_2HN	Difluora
F_2HNa	Sodium
F_2HRb	Rubidiu
F_2Mg	Magnesi
F_2N	Difluoro
F_2N_2	*cis*-Difl
F_2N_2	*trans*-D
F_2Ni	Nickel f
F_2O	Oxygen
F_2OS	Thionyl
F_2O_2	Dioxyge
F_2O_2S	Sulfuryl
F_2O_2U	Uranyl f
F_2Pb	Lead flu
F_2Si	Difluoro
F_2Sr	Strontiu
F_2Zn	Zinc fluc
F_3Ga	Gallium
F_3Gd	Gadolini
F_3HSi	Trifluor

STANDARD THERMODYNAMIC PROPERTIES OF CHEMICAL SUBSTANCES (continued)

Molecular formula	Name	State	$\Delta_f H°$ kJ/mol	$\Delta_f G°$ kJ/mol	$S°$ J/mol K	C_p J/mol K
	Iron oxide (FeO)	cry	−272.0			
FeO_4S	Iron sulfate ($FeSO_4$)	cry	−928.4	−820.8	107.5	100.6
FeO_4W	Iron tungstate ($FeWO_4$)	cry	−1155.0	−1054.0	131.8	114.6
FeS	Iron sulfide (FeS)	cry	−100.0	−100.4	60.3	50.5
FeS_2	Iron sulfide (FeS_2)	cry	−178.2	−166.9	52.9	62.2
Fe_2O_3	Iron oxide (Fe_2O_3)	cry	−824.2	−742.2	87.4	103.9
Fe_2O_4Si	Iron silicate (Fe_2SiO_4)	cry	−1479.9	−1379.0	145.2	132.9
Fe_3O_4	Iron oxide (Fe_3O_4)	cry	−1118.4	−1015.4	146.4	143.4
Fm	Fermium	cry	0.0			
Fr	Francium	cry	0.0		95.4	
Ga	Gallium	cry	0.0		40.9	25.9
		liq	5.6			
		gas	277.0	238.9	169.1	25.4
GaH_3O_3	Gallium hydroxide ($Ga(OH)_3$)	cry	−964.4	−831.3	100.0	
GaN	Gallium nitride (GaN)	cry	−110.5			
GaO	Gallium oxide (GaO)	gas	279.5	253.5	231.1	32.1
GaP	Gallium phosphide (GaP)	cry	−88.0			
GaSb	Gallium antimonide (GaSb)	cry	−41.8	−38.9	76.1	48.5
Ga_2	Gallium (Ga_2)	gas	438.5			
Ga_2O	Gallium oxide (Ga_2O)	cry	−356.0			
Ga_2O_3	Gallium oxide (Ga_2O_3)	cry	−1089.1	−998.3	85.0	92.1
Gd	Gadolinium	cry	0.0		68.1	37.0
		gas	397.5	359.8	194.3	27.5
Gd_2O_3	Gadolinium oxide (Gd_2O_3)	cry	−1819.6			106.7
Ge	Germanium	cry	0.0		31.1	23.3
		gas	372.0	331.2	167.9	30.7
GeH_3I	Iodogermane	gas			283.2	57.5
GeH_4	Germane	gas	90.8	113.4	217.1	45.0
GeI_4	Germanium tetraiodide	cry	−141.8	−144.3	271.1	
		gas	−56.9	−106.3	428.9	104.1
GeO	Germanium oxide (GeO) (brown)	cry	−261.9	−237.2	50.0	
		gas	−46.2	−73.2	224.3	30.9
GeO_2	Germanium dioxide (tetragonal)	cry	−580.0	−521.4	39.7	52.1
GeP	Germanium phosphide (GeP)	cry	−21.0	−17.0	63.0	
GeS	Germanium sulfide (GeS)	cry	−69.0	−71.5	71.0	
		gas	92.0	42.0	234.0	33.7
Ge_2	Germanium (Ge_2)	gas	473.1	416.3	252.8	35.6
Ge_2H_6	Digermane	liq	137.3			
		gas	162.3			
Ge_3H_8	Trigermane	liq	193.7			
		gas	226.8			
H	Hydrogen	gas	218.0	203.3	114.7	20.8
HI	Hydrogen iodide	gas	26.5	1.7	206.6	29.2
HIO_3	Iodic acid	cry	−230.1			
HK	Potassium hydride	cry	−57.7			
HKO	Potassium hydroxide	cry	−424.8	−379.1	78.9	64.9
HKO_4S	Potassium hydrogen sulfate	cry	−1160.6	−1031.3	138.1	
HLi	Lithium hydride	cry	−90.5	−68.3	20.0	27.9
HLiO	Lithium hydroxide	cry	−484.9	−439.0	42.8	49.7
HN	Imidogen (NH)	gas	351.5	345.6	181.2	29.2
HNO_2	Nitrous acid (HONO)	gas	−79.5	−46.0	254.1	45.6
HNO_3	Nitric acid	liq	−174.1	−80.7	155.6	109.9
		gas	−135.1	−74.7	266.4	53.4
HN_3	Hydrazoic acid	liq	264.0	327.3	140.6	
		gas	294.1	328.1	239.0	43.7
HNa	Sodium hydride	cry	−56.3	−33.5	40.0	36.4
HNaO	Sodium hydroxide	cry	−425.6	−379.5	64.5	59.5

STANDARD THERMODYNAMIC PROPERTIES OF CHEMICAL SUBSTANCES (continued)

Molecular formula	Name	State	$\Delta_f H°$ kJ/mol	$\Delta_f G°$ kJ/mol	$S°$ J/mol K	C_p J/mol K
Li_2O_4S	Lithium sulfate	cry	−1436.5	−1321.7	115.1	117.6
Li_2S	Lithium sulfide (Li_2S)	cry	−441.4			
Li_3O_4P	Lithium phosphate	cry	−2095.8			
Lr	Lawrencium	cry	0.0			
Lu	Lutetium	cry	0.0		51.0	26.9
		gas	427.6	387.8	184.8	20.9
Lu_2O_3	Lutetium oxide (Lu_2O_3)	cry	−1878.2	−1789.0	110.0	101.8
Md	Mendelevium	cry	0.0			
Mg	Magnesium	cry	0.0		32.7	24.9
		gas	147.1	112.5	148.6	20.8
MgN_2O_6	Magnesium nitrate	cry	−790.7	−589.4	164.0	141.9
MgO	Magnesium oxide	cry	−601.6	−569.3	27.0	37.2
MgO_4S	Magnesium sulfate	cry	−1284.9	−1170.6	91.6	96.5
MgO_4Se	Magnesium selenate	cry	−968.5			
MgS	Magnesium sulfide	cry	−346.0	−341.8	50.3	45.6
Mg_2	Magnesium (Mg_2)	gas	287.7			
Mg_2O_4Si	Magnesium silicate	cry	−2174.0	−2055.1	95.1	118.5
Mn	Manganese	cry	0.0		32.0	26.3
		gas	280.7	238.5	173.7	20.8
MnN_2O_6	Manganese nitrate ($Mn(NO_3)_2$)	cry	−576.3			
$MnNa_2O_4$	Sodium permanganate	cry	−1156.0			
MnO	Manganese oxide (MnO)	cry	−385.2	−362.9	59.7	45.4
MnO_2	Manganese oxide (MnO_2)	cry	−520.0	−465.1	53.1	54.1
MnO_3Si	Manganese metasilicate ($MnSiO_3$)	cry	−1320.9	−1240.5	89.1	86.4
MnS	Manganese sulfide (MnS)	cry	−214.2	−218.4	78.2	50.0
MnSe	Manganese selenide (MnSe)	cry	−106.7	−111.7	90.8	51.0
Mn_2O_3	Manganese oxide (Mn_2O_3)	cry	−959.0	−881.1	110.5	107.7
Mn_2O_4Si	Manganese silicate (Mn_2SiO_4)	cry	−1730.5	−1632.1	163.2	129.9
Mn_3O_4	Manganese oxide (Mn_3O_4)	cry	−1387.8	−1283.2	155.6	139.7
Mo	Molybdenum	cry	0.0		28.7	24.1
		gas	658.1	612.5	182.0	20.8
$MoNa_2O_4$	Sodium molybdate	cry	−1468.1	−1354.3	159.7	141.7
MoO_2	Molybdenum oxide (MoO_2)	cry	−588.9	−533.0	46.3	56.0
MoO_3	Molybdenum oxide (MoO_3)	cry	−745.1	−668.0	77.7	75.0
MoO_4Pb	Lead molybdate ($PbMO_4$)	cry	−1051.9	−951.4	166.1	119.7
MoS_2	Molybdenum sulfide (MoS_2)	cry	−235.1	−225.9	62.6	63.6
N	Nitrogen	gas	472.7	455.5	153.3	20.8
$NNaO_2$	Sodium nitrite	cry	−358.7	−284.6	103.8	
$NNaO_3$	Sodium nitrate	cry	−467.9	−367.0	116.5	92.9
NO_2	Nitrogen dioxide	gas	33.2	51.3	240.1	37.2
NO_2Rb	Rubidium nitrite	cry	−367.4	−306.2	172.0	
NO_3Rb	Rubidium nitrate	cry	−495.1	−395.8	147.3	102.1
NO_3Tl	Thallium nitrate	cry	−243.9	−152.4	160.7	99.5
NP	Phosphorus nitride (PN)	cry	−63.0			
		gas	109.9	87.7	211.2	29.7
N_2	Nitrogen (N_2)	gas	0.0		191.6	29.1
N_2O	Nitrous oxide	gas	82.1	104.2	219.9	38.5
N_2O_3	Nitrogen trioxide	liq	50.3			
		gas	83.7	139.5	312.3	65.6
N_2O_4	Nitrogen tetroxide	liq	−19.5	97.5	209.2	142.7
		gas	9.2	97.9	304.3	77.3
N_2O_4Sr	Strontium nitrite	cry	−762.3			
N_2O_5	Nitrogen pentoxide	cry	−43.1	113.9	178.2	143.1
		gas	11.3	115.1	355.7	84.5
N_2O_6Pb	Lead nitrate ($Pb(NO_3)_2$)	cry	−451.9			
N_2O_6Ra	Radium nitrate	cry	−992.0	−796.1	222.0	
N_2O_6Sr	Strontium nitrate	cry	−978.2	−780.0	194.6	149.9

Molecular formula	Name	State	$\Delta_f H°$ kJ/mol	$\Delta_f G°$ kJ/mol	$S°$ J/mol K
N_2O_6Zn	Zinc nitrate	cry	−483.7		
N_3Na	Sodium azide	cry	21.7	93.8	96.9
N_4Si_3	Silicon nitride (Si_3N_4)	cry	−743.5	−642.6	101.3
Na	Sodium	cry	0.0		51.3
		gas	107.5	77.0	153.7
NaO_2	Sodium superoxide (NaO_2)	cry	−260.2	−218.4	115.9
Na_2	Sodium (Na_2)	gas	142.1	103.9	230.2
Na_2O	Sodium oxide (Na_2O)	cry	−414.2	−375.5	75.1
Na_2O_2	Sodium peroxide (Na_2O_2)	cry	−510.9	−447.7	95.0
Na_2O_3S	Sodium sulfite	cry	−1100.8	−1012.5	145.9
Na_2O_3Si	Sodium metasilicate	cry	−1554.9	−1462.8	113.9
Na_2O_4S	Sodium sulfate	cry	−1387.1	−1270.2	149.6
Na_2S	Sodium sulfide (Na_2S)	cry	−364.8	−349.8	83.7
Nb	Niobium	cry	0.0		36.4
		gas	725.9	681.1	186.3
NbO	Niobium oxide (NbO)	cry	−405.8	−378.6	48.1
NbO_2	Niobium oxide (NbO_2)	cry	−796.2	−740.5	54.5
Nb_2O_5	Niobium oxide (Nb_2O_5)	cry	−1899.5	−1766.0	137.2
Nd	Neodymium	cry	0.0		71.5
		gas	327.6	292.4	189.4
Nd_2O_3	Neodymium oxide	cry	−1807.9	−1720.8	158.6
Ne	Neon	gas	0.0		146.3
Ni	Nickel	cry	0.0		29.9
		gas	429.7	384.5	182.2
NiO_4S	Nickel sulfate ($NiSO_4$)	cry	−872.9	−759.7	92.0
NiS	Nickel sulfide (NiS)	cry	−82.0	−79.5	53.0
Ni_2O_3	Nickel oxide (Ni_2O_3)	cry	−489.5		
No	Nobelium	cry	0.0		
O	Oxygen	gas	249.2	231.7	161.1
OP	Phosphorus oxide (PO)	gas	−28.5	−51.9	222.8
OPb	Lead oxide (PbO) (yellow)	cry	−217.3	−187.9	68.7
	Lead oxide (PbO) (red)	cry	−219.0	−188.9	66.5
OPd	Palladium oxide (PdO)	cry	−85.4		
		gas	348.9	325.9	218.0
ORa	Radium oxide	cry	−523.0		
ORb_2	Rubidium oxide (Rb_2O)	cry	−339.0		
ORh	Rhodium oxide (RhO)	gas	385.0		
OS	Sulfur oxide (SO)	gas	6.3	−19.9	222.0
OSe	Selenium oxide (SeO)	gas	53.4	26.8	234.0
OSi	Silicon oxide (SiO)	gas	−99.6	−126.4	211.6
OSn	Tin oxide (SnO) (tetragonal)	cry	−280.7	−251.9	57.2
		gas	15.1	−8.4	232.1
OSr	Strontium oxide	cry	−592.0	−561.9	54.4
OTi	Titanium oxide (TiO)	cry	−519.7	−495.0	50.0
OTl_2	Thallium oxide (Tl_2O)	cry	−178.7	−147.3	126.0
OU	Uranium oxide (UO)	gas	21.0		
OV	Vanadium oxide (VO)	cry	−431.8	−404.2	38.9
OZn	Zinc oxide	cry	−350.5	−320.5	43.7
O_2	Oxygen (O_2)	gas	0.0		205.2
O_2P	Phosphorous oxide (PO_2)	gas	−279.9	−281.6	252.1
O_2Pb	Lead oxide (PbO_2)	cry	−277.4	−217.3	68.6
O_2Rb	Rubidium superoxide (RbO_2)	cry	−278.7		
O_2Rb_2	Rubidium peroxide (Rb_2O_2)	cry	−472.0		
O_2Ru	Ruthenium oxide (RuO_2)	cry	−305.0		
O_2S	Sulfur dioxide	liq	−320.5		
		gas	−296.8	−300.1	248.2
O_2Se	Selenium dioxide	cry	−225.4		

STANDARD THERMODYNAMIC PROPERTIES OF CHEMICAL SUBSTANCES (continued)

Molecular formula	Name	State	$\Delta_f H°$ kJ/mol	$\Delta_f G°$ kJ/mol	$S°$ J/mol K	C_p J/mol K
O_2Si	Silicon dioxide (α–quartz)	cry	–910.7	–856.3	41.5	44.4
		gas	–322.0			
O_2Sn	Tin oxide (SnO_2) (tetragonal)	cry	–577.6	–515.8	49.0	52.6
O_2Te	Tellurium dioxide	cry	–322.6	–270.3	79.5	
O_2Th	Thorium oxide (ThO_2)	cry	–1226.4	–1169.2	65.2	61.8
O_2Ti	Titanium oxide (TiO_2) (rutile)	cry	–944.0	–888.8	50.6	55.0
O_2U	Uranium oxide (UO_2)	cry	–1085.0	–1031.8	77.0	63.6
		gas	–465.7	–471.5	274.6	51.4
O_2W	Tungsten oxide (WO_2)	cry	–589.7	–533.9	50.5	56.1
O_2Zr	Zirconium oxide (ZrO_2)	cry	–1100.6	–1042.8	50.4	56.2
O_3	Ozone	gas	142.7	163.2	238.9	39.2
O_3PbS	Lead sulfite ($PbSO_3$)	cry	–669.9			
O_3PbSi	Lead metasilicate ($PbSiO_3$)	cry	–1145.7	–1062.1	109.6	90.0
O_3Pr_2	Praseodymium oxide (Pr_2O_3)	cry	–1809.6			117.4
O_3Rh_2	Rhodium oxide (Rh_2O_3)	cry	–343.0			103.8
O_3S	Sulfur trioxide	cry	–454.5	–374.2	70.7	
		liq	–441.0	–373.8	113.8	
		gas	–395.7	–371.1	256.8	50.7
O_3Sc_2	Scandium oxide (Sc_2O_3)	cry	–1908.8	–1819.4	77.0	94.2
O_3SiSr	Strontium metasilicate	cry	–1633.9	–1549.7	96.7	88.5
O_3Sm_2	Samarium oxide (Sm_2O_3)	cry	–1823.0	–1734.6	151.0	114.5
O_3Tb_2	Terbium oxide (Tb_2O_3)	cry	–1865.2			115.9
O_3Ti_2	Titanium oxide (Ti_2O_3)	cry	–1520.9	–1434.2	78.8	97.4
O_3Tm_2	Thullium oxide (Tm_2O_3)	cry	–1888.7	–1794.5	139.7	116.7
O_3U	Uranium oxide (UO_3)	cry	–1223.8	–1145.7	96.1	81.7
O_3V_2	Vanadium oxide (V_2O_3)	cry	–1218.8	–1139.3	98.3	103.2
O_3W	Tungsten oxide (WO_3)	cry	–842.9	–764.0	75.9	73.8
O_3Y_2	Yttrium oxide (Y_2O_3)	cry	–1905.3	–1816.6	99.1	102.5
O_3Yb_2	Ytterbium oxide (Yb_2O_3)	cry	–1814.6	–1726.7	133.1	115.4
O_4Os	Osmium oxide (OsO_4)	cry	–394.1	–304.9	143.9	
		gas	–337.2	–292.8	293.8	74.1
O_4PbS	Lead sulfate ($PbSO_4$)	cry	–920.0	–813.0	148.5	103.2
O_4PbSe	Lead selenate ($PbSeO_4$)	cry	–609.2	–504.9	167.8	
O_4Pb_2Si	Lead silicate (Pb_2SiO_4)	cry	–1363.1	–1252.6	186.6	137.2
O_4Pb_3	Lead oxide (Pb_3O_4)	cry	–718.4	–601.2	211.3	146.9
O_4RaS	Radium sulfate	cry	–1471.1	–1365.6	138.0	
O_4Rb_2S	Rubidium sulfate	cry	–1435.6	–1316.9	197.4	134.1
O_4Ru	Ruthenium oxide (RuO_4)	cry	–239.3	–152.2	146.4	
O_4SSr	Strontium sulfate	cry	–1453.1	–1340.9	117.0	
O_4STl_2	Thallium sulfate (Tl_2SO_4)	cry	–931.8	–830.4	230.5	
O_4SZn	Zinc sulfate	cry	–982.8	–871.5	110.5	99.2
O_4SiSr_2	Strontium silicate	cry	–2304.5	–2191.1	153.1	134.3
O_4SiZn_2	Zinc silicate	cry	–1636.7	–1523.2	131.4	123.3
O_4SiZr	Zirconium silicate ($ZrSiO_4$)	cry	–2033.4	–1919.1	84.1	98.7
O_5Ta_2	Tantalum oxide (Ta_2O_5)	cry	–2046.0	–1911.2	143.1	135.1
O_5Ti_3	Titanium oxide (Ti_3O_5)	cry	–2459.4	–2317.4	129.3	154.8
O_5V_2	Vanadium oxide (V_2O_5)	cry	–1550.6	–1419.5	131.0	127.7
O_5V_3	Vanadium oxide (V_3O_5)	cry	–1933.0	–1803.0	163.0	
O_7Re_2	Rhenium oxide (Re_2O_7)	cry	–1240.1	–1066.0	207.1	166.1
		gas	–1100.0	–994.0	452.0	
O_7U_3	Uranium oxide (U_3O_7)	cry	–3427.1	–3242.9	250.5	215.5
O_7S_2Zr	Zirconium sulfate	cry	–2217.1			172.0
O_8U_3	Uranium oxide (U_3O_8)	cry	–3574.8	–3369.5	282.6	238.4
O_9U_4	Uranium oxide (U_4O_9)	cry	–4510.4	–4275.1	334.1	293.3
Os	Osmium	cry	0.0		32.6	24.7
		gas	791.0	745.0	192.6	20.8
P	Phosphorus (white)	cry	0.0		41.1	23.8

WVMP SAR Reference 3-14

"Estimation of Heat Capacities of Solid Mixed Oxides,"
Leitner, J., P. Chuchvalec, D. Sedmidubský, A. Strejc, and
P. Abrman, Thermochim. Acta, 395, 27-46, 2003.

ELSEVIER

Thermochimica Acta 395 (2003) 27–46

thermochimica acta

www.elsevier.com/locate/tca

Estimation of heat capacities of solid mixed oxides

Jindřich Leitner[a,*], Pavel Chuchvalec[b], David Sedmidubský[c], Aleš Strejc[c], Petr Abrman[b]

[a]*Department of Solid State Engineering, Institute of Chemical Technology, Technická 5, 166 28 Praha 6, Czech Republic*
[b]*Department of Physical Chemistry, Institute of Chemical Technology, Technická 5, 166 28 Praha 6, Czech Republic*
[c]*Department of Inorganic Chemistry, Institute of Chemical Technology, Technická 5, 166 28 Praha 6, Czech Republic*

Received 30 October 2001; received in revised form 11 February 2002; accepted 11 March 2002

Abstract

Some empirical methods for the estimation of standard molar heat capacity (C°_{pm}) of solid mixed oxides are reviewed and the reliability of the obtained data in phase equilibria calculations is examined. Following the comparison of predicted values of C°_{pm}(298.15 K) with more than 300 experimental data the most widely used Neumann–Kopp rule (NKR) is found to be very universal but in some cases the mean deviation of 3.3% is too high, giving rise to a relatively large error in equilibrium calculation results. On the other hand, the method based on binary oxide contributions proposed by Berman and Brown [Contrib. Mineral. Petrol. 89 (1985) 168] for the estimation of temperature dependencies $C^{\circ}_{pm}(T)$ of silicates and other minerals formed by Al_2O_3, CaO, FeO, Fe_2O_3, K_2O, MgO, Na_2O, SiO_2 and TiO_2 is less general, but more accurate. In comparison with the NKR, the most pronounced drawback of this method is the necessity to know the experimental values of C°_{pm} for a set of mixed oxides, so that the individual contributions of constituent binary oxides can be evaluated.

Keywords: Mixed oxides; Heat capacity; Estimation; Neumann–Kopp rule; Group contribution methods

1. Introduction

The oxide based materials are presently used in a large number of applications. Let us mention only some of the most important ones in the following outline:

- Glasses (system SiO_2–Al_2O_3–B_2O_3–MgO–CaO–PbO–Na_2O–K_2O, special glasses for optical applications, optical fibers).
- Structural ceramics (system SiO_2–Al_2O_3–MgO, zirconia ceramics, sialon).
- Composite materials (oxides are used as a reinforcement in a metallic matrix or, alternatively, as a matrix toughened by non-oxidic fibres).
- Coatings and thin films (protective coatings for gas-turbine parts—system ZrO_2–Y_2O_3–CaO–MgO, dielectric layers in electronics—SiO_2, chemical sensor active layers—ZnO, SnO_2, Fe_2O_3, etc.).
- Materials for magnetic recording (Fe_2O_3, CrO_2, mixed ferrites $(Zn,Mn,Cu)Fe_2O_4$).
- Structural elements of oxide fuel cells ($(La,Ca)CrO_3$, $(La,Sr)MnO_3$, Y_2O_3–ZrO_2).
- High-temperature superconductors (YBaCuO, BiSrCaCuO, HgBaCaCuO, TlBaCaCuO).

Chemical thermodynamics is frequently used in systematic investigation of processes related with

* Corresponding author. Fax: +420-2-2431-0337.
E-mail address: jindrich.leitner@vscht.cz (J. Leitner).

0040-6031/02/$ – see front matter
PII: S0040-6031(02)00177-6

material synthesis and processing as the powerful tool to understand the interrelationship between chemical composition, structure and properties. The calculations of thermodynamic equilibria require knowledge of input thermodynamic data for each substance involved, namely the values of enthalpies of formation and entropies at 298.15 K, as well as the coefficients of temperature dependencies of isobaric molar heat capacities. Alternatively, the parameters of temperature dependence of molar Gibbs energy can be directly employed. For a number of solid oxides, such data are tabulated for a wide range of temperatures, see, e.g. [2–9] or available in a form of computer databases. In addition, comprehensive data files for silicates and other oxidic minerals are disposable, e.g. [1,10–16].

The molar heat capacity (C°_{pm}) is one of the fundamental thermodynamic functions of solid substances. Various calorimetric methods being presently applicable from very low temperatures (approx. 10^{-1} K) up to melting points are used for experimental determination of C°_{pm}. The calorimetric measurements have been taken for practically all binary oxides and a considerable number of mixed oxides. The obtained data are available in literature. However, in many cases the experimental data are still missing. Hence, a lot of empirical methods for estimation of C°_{pm} of inorganic compounds have been proposed in order to overcome this lack. These methods are described in some review papers [7,17,18].

The aim of this paper is to summarize the as yet proposed methods for estimation of molar heat capacities of solid mixed oxides,[1] to verify their credibility and to examine the reliability of estimated values in equilibrium calculations in oxide systems. The paper follows the previous study [19] focused to prediction of C°_{pm} for binary oxides.

2. Method description

Let us consider the formation of a ternary oxide $A_{2a}B_{3b}O_x$ from binary oxides A_aO_m and B_bO_n ($x = 2m + 3n$) according to the following equation:

$$2A_aO_m(s) + 3B_bO_n(s) \rightarrow A_{2a}B_{3b}O_x(s) \quad (R1)$$

The change of isobaric heat capacity accompanying the reaction, $\Delta C^\circ_{pm}(ox)$, can be expressed as:

$$\Delta C^\circ_{pm}(ox) = C^\circ_{pm}(A_{2a}B_{3b}O_x) - 2C^\circ_{pm}(A_aO_m) - 3C^\circ_{pm}(B_bO_n) \quad (1)$$

The values of $\Delta C^\circ_{pm}(ox)$ for more than 300 mixed oxides evaluated from the experimental (calorimetric) data of C°_{pm} using Eq. (1) are plotted in Fig. 1. The dispersion of the obtained values falls roughly in the interval of ± 30 J K^{-1} mol^{-1} and their average is close to zero. All below-mentioned methods can be classified into two essential groups according to whether the condition $\Delta C^\circ_{pm}(ox) = 0$ is fulfilled or not.

2.1. $\Delta C^\circ_{pm}(ox) = 0$

2.1.1. Neumann–Kopp rule

The Neumann–Kopp rule (NKR) represents presumably the simplest approach for estimation of $C^\circ_{pm}(298.15)$ as well as for temperature dependence $C^\circ_{pm}(T)$. Based on this method, the molar heat capacity of a mixed oxide is calculated as a weighted sum of heat capacities of the constituent binary oxides. For example, the heat capacity of the above-mentioned ternary oxide with the stoichiometry $A_{2a}B_{3b}O_x$ reads

$$C^\circ_{pm}(A_{2a}B_{3b}O_x) = 2C^\circ_{pm}(A_aO_m) + 3C^\circ_{pm}(B_bO_n) \quad (2)$$

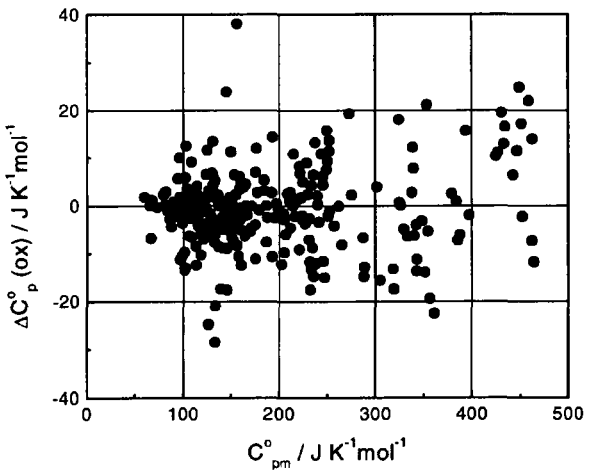

Fig. 1. Heat capacity change, $\Delta C^\circ_{pm}(ox)$, accompanying the formation of mixed oxides from constituent binary oxides at the temperature of 298.15 K.

[1] The term "mixed oxides" stands here for ternary or higher compounds of oxygen (as an anion O^{2-}) with two or more cations, as well as for compounds consisting of complex anions, which can be considered as salts of oxidic acids (chromates, wolframates) including those cases when the anions form chains, sheets of three-dimensional networks (e.g. silicates).

Such an approximation results in the case of silicates and other natural minerals in the average estimation error of approx. 5% [20]. The main advantage of the NKR lies in the availability of experimental temperature dependencies of $C^\circ_{pm}(T)$ for the respective binary oxides.

As an improvement of basic the NKR let us mention the procedure proposed by Helgeson et al. [20] for the estimation of C°_{pm} of silicates and other oxide minerals. This method is based upon the assumption of zero change of heat capacity in the course of an exchange reaction

$$A_aB_bO_x(s) + C_cO_y(s) = B_bO_z(s) + A_aC_cO_{x+y-z} \quad \text{(R2)}$$

between structurally similar substances. The unknown data for a ternary oxide $A_aC_cO_{x+y-z}$ can be thus obtained directly from the data of binary oxides B_bO_z, C_cO_y, and a mixed oxide $A_aB_bO_x$. The accuracy of estimation may be increased to about 2% in this manner.

However, the substantial drawback of this method inheres in the dependence, in many cases very important, on the choice of the given exchange reaction (R2).

A method analogous to that of Helgeson has been proposed by Ukleba et al. [21] for the estimation of $C^\circ_{pm}(298.15)$, in which the exchange reaction between two ternary oxides is considered. The mean estimation error for the set of 124 selected ternary oxides amounts to approx. 3%. In case of more possible exchange reactions, averaging of the relevant values is recommended [21].

2.2. $\Delta C^\circ_{pm}(ox) \neq 0$

2.2.1. Contribution methods—atomic and ionic contributions

For the estimation of molar heat capacities of mixed oxides, several contribution methods can be used, which have been reviewed in the previous paper [19] dealing with binary oxides. In cases when the contributions of individual cations (atoms) and the anion O^{2-} (atom O) are considered, the obtained value corresponds to $\Delta C^\circ_{pm}(ox) = 0$ (for the calculation of $\Delta C^\circ_{pm}(ox)$ according to Eq. (1), the estimated (not experimental) values of C°_{pm} of constituent binary oxides must be used).

Based on the method proposed by Kellogg [22] and later extended by Kubaschewski and Ünal [23], the particular contributions to $C^\circ_{pm}(298.15\ K)$ were evaluated for 25 different complex anions constituted from oxygen and another element (Al, B, Cr, Fe, Ge, Hf, Mo, Nb, Se, Si, Ti, U, V, W, and Zr) [18]. As the complex anion contributions differ from the sum of contributions of respective cations and the anion O^{2-}, the resulting value $\Delta C^\circ_{pm}(ox) = 0$ in such a case. The evaluated contributions are listed in Tables 1 and 2.

Kubaschewski and Ünal [23] have further proposed the method for estimation of parameters A, B, and C in a simple temperature dependence of $C^\circ_{pm}(T)$ in the form

$$C^\circ_{pm} = A + BT + \frac{C}{T^2} \quad (3)$$

The parameters A and B are estimated using the relations

$$A = \frac{10^{-3}T_m[C^\circ_{pm}(298.15\ K) + 4.7n] - 1.25n \times 10^5(T_m)^{-2} - 9.05n}{10^{-3}T_m - 0.298} \quad (4)$$

$$B = \frac{25.6n + 4.2n \times 10^5(T_m)^{-2} - C^\circ_{pm}(298.15\ K)}{10^{-3}T_m - 0.298} \quad (5)$$

where n is the number of ions (contributions) in the formula unit. The generalized value of the third parameter was set to $C = -4.2n$. The described approach can be employed only for substances whose melting temperature T_m is lower than approx. 2300 K.

The ionic contributions of complex anions consisting of oxygen and other elements (Al, B, Cr, Fe, Ge, Mn, Mo, Nb, Re, Se, Si, Ta, Tc, Ti, U, V, W, and Zr), as well as the contributions of individual cations (in this case differing for unlike valencies) were also evaluated by Kumok [24].

2.2.2. Contribution methods—structural and simple oxides contributions

A number of contribution methods has been developed directly for mixed oxides. The values of $C^\circ_{pm}(298.15\ K)$ or the parameters of $C^\circ_{pm}(T)$ dependence are additively calculated from contributions of constituent oxides or from structural contributions.

Table 1
Cationic contributions to heat capacity at 298.15 K

Cation	Contributions to $C^{\circ}_{pm}(298)$ (J K^{-1} mol^{-1})		Cation	Contributions to $C^{\circ}_{pm}(298)$ (J K^{-1} mol^{-1})		Cation	Contributions to $C^{\circ}_{pm}(298)$ (J K^{-1} mol^{-1})	
	[18,23]	[17,24]		[18,23]	[17,24]		[18,23]	[17,24]
Ag^{2+}	25.73	28.60	Ho^{2+}	23.01	26.10	Se^{6+}	21.34	
Al^{3+}	19.66	17.60	Ho^{3+}	23.01	29.60	Si^{4+}		12.10
As^{3+}	25.10	26.70	In^{+}	24.27	23.70	Sm^{2+}	25.10	35.70
As^{5+}	25.10		In^{2+}	24.27	26.50	Sm^{3+}	25.10	34.40
B^{3+}		6.10	In^{3+}	24.27	25.70	Sn^{2+}	23.43	27.80
Ba^{2+}	26.36	28.40	Ir^{3+}	23.85		Sn^{4+}	23.43	25.80
Be^{2+}	9.62	12.60	Ir^{4+}	23.85		Sr^{2+}	25.52	29.30
Bi^{3+}	26.78	29.00	K^{+}	25.94	28.00	Ta^{3+}	23.01	27.70
Ca^{2+}	24.69	27.30	La^{2+}	25.52	29.50	Ta^{4+}	23.01	
Cd^{2+}	23.01	28.00	La^{3+}	25.52	29.30	Ta^{5+}	23.01	26.30
Ce^{2+}	23.43	27.60	Li^{+}	19.66	20.70	Tb^{2+}		24.30
Ce^{3+}	23.43	31.40	Lu^{3+}		28.70	Tb^{3+}		33.00
Ce^{4+}	23.43	28.20	Mg^{2+}	19.66	22.20	Tc^{4+}		30.50
Co^{2+}	28.03	31.30	Mn^{2+}	23.43	27.90	Th^{2+}	25.52	26.10
Co^{3+}	28.03	12.40	Mn^{3+}	23.43	25.00	Th^{3+}	25.52	29.70
Cr^{2+}	23.01	21.00	Mn^{4+}	23.43	21.20	Th^{4+}	25.52	28.20
Cr^{3+}	23.01	29.10	Mo^{2+}		23.60	Ti^{2+}	21.76	21.30
Cr^{4+}	23.01	21.80	Mo^{4+}		21.40	Ti^{3+}	21.76	23.30
Cr^{6+}	23.01		Na^{+}	25.94	26.80	Ti^{4+}	21.76	25.50
Cs^{+}	26.36	31.10	Nb^{3+}	23.01	23.00	Ti^{5+}	21.76	
Cu^{+}	25.10	25.50	Nb^{4+}	23.01	23.50	Tl^{+}	27.61	30.90
Cu^{2+}	25.10	25.00	Nb^{5+}	23.01	26.70	Tl^{3+}	27.61	
Dy^{2+}		84.00	Nd^{3+}	24.27	28.30	Tm^{3+}		33.30
Dy^{3+}		31.00	Ni^{2+}	27.61	26.70	U^{2+}		30.00
Er^{3+}		29.10	P^{5+}	14.23		U^{3+}	26.78	34.10
Eu^{2+}		29.10	Pb^{2+}	26.78	29.30	U^{4+}	26.78	30.80
Eu^{3+}		33.30	Pb^{4+}	26.78	47.30	U^{5+}	26.78	33.80
Fe^{2+}	25.94	28.70	Pd^{2+}		20.60	U^{6+}	26.78	34.20
Fe^{3+}	25.94	26.20	Pm^{3+}		31.40	V^{2+}	22.18	21.60
Fr^{+}		29.50	Pr^{3+}	24.27	31.50	V^{3+}	22.18	27.10
Ga^{+}	20.92	23.90	Pr^{4+}	24.27		V^{4+}	22.18	26.90
Ga^{2+}	20.92	22.75	Pt^{4+}		24.20	V^{5+}	22.18	
Ga^{3+}	20.92	21.60	Pu^{2+}		40.70	W^{4+}		21.60
Gd^{3+}	23.43	27.80	Pu^{3+}		28.40	Y^{2+}	25.10	22.50
Ge^{2+}	20.08	25.80	Pu^{4+}		35.10	Y^{3+}	25.10	24.00
Ge^{4+}	20.08	23.00	Ra^{2+}		29.60	Yb^{2+}		29.00
Hf^{2+}	25.52		Rb^{+}	26.36	30.80	Yb^{3+}		32.60
Hf^{3+}	25.52		Sb^{3+}	23.85	30.30	Zn^{2+}	21.76	25.50
Hf^{4+}	25.52	20.20	Sc^{3+}		21.20	Zr^{2+}	23.85	24.70
Hg^{+}	25.10	26.30	Se^{4+}	21.34		Zr^{3+}	23.85	25.00
Hg^{2+}	25.10	27.70	Se^{5+}	21.34		Zr^{4+}	23.85	22.90

These methods are confined to a certain family of mixed oxides, though.

Several different methods have been brought in for the estimation of $C^{\circ}_{pm}(T)$ of silicates and other oxide materials. Robinson and Haas [25] suggested a model based on structural contributions corresponding to individual cations in particular coordination (number of the nearest neighbors O^{2-}). The parameters of the temperature function

$$C^{\circ}_{pm} = a + bT + \frac{c}{T^2} + fT^2 + \frac{g}{T^{1/2}} \quad (6)$$

Table 2
Anionic contributions to heat capacity at 298.15 K

Anion	Contributions to $C^\circ_{pm}(298)$ ($J\,K^{-1}\,mol^{-1}$)		Anion	Contributions to $C^\circ_{pm}(298)$ ($J\,K^{-1}\,mol^{-1}$)	
	[18,23]	[17,24]		[18,23]	[17,24]
$(AlO_2)^-$	49.26	47.40	$(SeO_3)^{2-}$	73.32	72.50
$(AlO_3)^{3-}$	67.73		$(SeO_4)^{2-}$		86.60
$(BO_2)^-$	41.19	40.30	$(SiO_3)^{2-}$	62.93	59.30
$(BO_3)^{3-}$	55.60	52.00	$(SiO_4)^{4-}$	78.34	73.50
$(B_4O_7)^{2-}$	134.26		$(Si_2O_5)^{2-}$	106.79	103.80
$(CrO_2)^-$	62.67	52.40	$(TaO_3)^-$		79.80
$(CrO_3)^{3-}$		84.90	$(TcO_4)^-$		95.30
$(CrO_4)^{2-}$	92.27	86.40	$(TiO_3)^{2-}$	74.45	71.90
$(Cr_2O_7)^{2-}$		166.50	$(TiO_4)^{4-}$	92.52	85.90
$(FeO_2)^-$	63.03	59.70	$(Ti_2O_5)^{2-}$	124.69	120.80
$(GeO_3)^{2-}$	72.08	68.20	$(UO_3)^-$		82.10
$(HfO_3)^{2-}$	78.47		$(UO_4)^{2-}$	107.11	97.90
$(MnO_4)^-$		91.10	$(U_2O_7)^{2-}$		171.40
$(MnO_4)^{2-}$		86.80	$(VO_3)^-$	71.54	70.90
$(MnO_4)^{3-}$		97.50	$(VO_4)^{3-}$	89.20	87.74
$(MoO_4)^{2-}$	92.77	89.80	$(V_2O_7)^{4-}$	163.50	158.90
$(Mo_2O_7)^{2-}$		163.60	$(WO_4)^{2-}$	97.49	89.70
$(NbO_3)^-$	78.00	74.90	$(W_2O_7)^{2-}$		161.30
$(ReO_4)^-$		96.40	$(ZrO_3)^{2-}$	75.06	73.40

are calculated additively from such structural contributions. A set of 20 different contributions has been assessed from the available experimental data for 61 minerals. The original experimental values have been reproduced with an accuracy higher than 2%.

For the estimation of the temperature dependence $C^\circ_{pm}(T)$ of minerals formed from binary oxides Al_2O_3, CaO, FeO, Fe_2O_3, K_2O, MgO, Na_2O, SiO_2 and TiO_2 in the form

$$C^\circ_{pm} = k_0 + \frac{k_1}{T^{1/2}} + \frac{k_2}{T^2} + \frac{k_3}{T^3} \quad (7)$$

Berman and Brown [1] evaluated the contributions of the binary oxides to parameters k_0, k_1, k_2, and k_3. They employed the calorimetric data for 101 minerals for the least square fitting of contributions. The estimation error did not exceed 2% for a large majority of substances even in this case. The calculated values of contributions at 298.15 K for the above-mentioned oxides along with the respective experimental data C°_{pm}(298.15 K) and the relative differences are given in Table 3. These differences are substantial only for FeO and K_2O. Consequently, for the mixed oxides

Table 3
Contributions of binary oxides to heat capacity at 298.15 K [1]

Oxide	Contributions to $C^\circ_{pm}(298)$ ($J\,K^{-1}\,mol^{-1}$)	$C^\circ_{pm}(298)$ ($J\,K^{-1}\,mol^{-1}$) of binary oxide	Difference (%)
Al_2O_3	77.41	79.01	−2.03
CaO	43.18	42.42	1.80
Fe_2O_3	105.17	104.77	0.39
FeO	43.38	48.04	−9.69
K_2O	71.70	84.53	−15.17
MgO	37.31	37.26	0.15
Na_2O	69.18	68.56	0.91
SiO_2	43.95	44.42	−1.05
TiO_2	55.44	55.10	0.61

formed by Al_2O_3, CaO, Fe_2O_3, MgO, Na_2O, SiO_2 and TiO_2, the values predicted by the Berman–Brown method will be very close to those ones obtained from the NKR.

Another significant family of mixed oxides is represented by high-temperature superconductors and related phases. The contributions to the estimation of parameters k_0, k_1, and k_2 to the temperature dependence of $C^\circ_{pm}(T)$ according to Eq. (7) have been proposed by Voronin and Uspenskaya [26] for mixed oxides in the system Y–Ba–Cu–O. Analyzing the experimental data for five mixed oxides, they evaluated the contributions for binary oxides Y_2O_3, BaO, CuO, and Cu_2O and predicted the parameters of Eq. (7) for another seven ternary and quaternary oxides.

2.2.3. Empirical rules in homological series and groups of chemically related substances (oxides)

Goncharov and Vorobev [27] developed the method for estimation of temperature dependency $C^\circ_{pm}(T)$ for garnets of Fe, Al and Ga with rare earth (RE) elements starting from an assumption of ΔC°_{pm}(ox) being equal for the same family of substances (e.g. $RE_3Fe_5O_{12}$, $RE_3Al_5O_{12}$, $RE_3Ga_5O_{12}$) irrespective of the particular RE element. Such assumption was found to be well satisfied with the experimental data for ferrogarnets of Y, Sm, Eu, Gd, Tb, and Lu yielding the error did not exceed 2%. Accordingly, the generalized temperature dependence of ΔC°_{pm}(ox) for $RE_3Al_5O_{12}$ and $RE_3Ga_5O_{12}$ has been obtained from data for $Y_3Al_5O_{12}$ [28] and $Gd_3Ga_5O_{12}$ [29], respectively.

The prediction method of C°_{pm}(298.15 K) using ionic contributions brought in by Aldabergenov et al. [30,31]

was based on the idea that in homological series like $A_m(B_xO_y)_n$, the molar heat capacity is a linear function of coefficient n specifying the number of complex anions $(B_xO_y)^{z-}$ in the formula unit. Thus for alkaline aluminates, the series

$$AlO_2^- \overset{+AlO_2^-}{\rightarrow} Al_2O_4^{2-} \overset{+AlO_2^-}{\rightarrow} Al_3O_6^{3-} \cdots$$

is considered, in which each higher anion differs from the previous one in an increment $(AlO_2)^-$. The higher anion contributions are considered as n-multiples of the primary anion $(AlO_2)^-$, whose value is determined from the available experimental data of C°_{pm}(298.15 K) for $KAlO_2$, $LiAlO_2$ and $NaAlO_2$ as well as from the ionic contributions for the respective cations K^+, $Li^+$and Na^+ obtained from their standard molar entropies in an infinitely diluted solution.

3. Comparison of selected methods

In the following part three selected methods, namely the NKR, the Kellogg's method of ionic contributions [22] with ionic contributions taken from Spencer [18] (KK), and the binary oxide contribution method by Berman and Brown [1] (BB) are compared. The values of C°_{pm}(298.15 K) for binary oxides used in the NKR are listed in Table 4. The methods are examined both in terms of their universality, i.e. according to the number of mixed oxides whose

Table 4
Selected values of heat capacity of solid binary oxides at 298.15 K [19]

Oxide	Phase	C°_{pm}(298) ($J\,K^{-1}\,mol^{-1}$)	Oxide	Phase	C°_{pm}(298) ($J\,K^{-1}\,mol^{-1}$)
Ag_2O	Sol	66.32	MgO	Sol	37.26
Al_2O_3	Sol	79.01	Mn_2O_3	Sol	99.04
B_2O_3	Sol	62.98	MnO	Sol	44.76
BaO	Sol	47.06	MnO_2	Sol	54.42
BeO	Sol-A	24.98	MoO_2	Sol	55.99
Bi_2O_3	Sol-A	112.13	MoO_3	Sol	75.14
CaO	Sol	42.42	Na_2O	Sol-A	68.56
CdO	Sol	44.16	Nb_2O_5	Sol	132.13
Ce_2O_3	Sol	117.05	Nd_2O_3	Sol-A	111.34
CeO_2	Sol	61.53	NiO	Sol-A	44.29
CoO	Sol	55.22	PbO	Red	45.74
Cr_2O_3	Sol	114.26	Pr_2O_3	Sol	116.63
CrO_3	Sol	79.12	Rh_2O_3	Sol	89.12
Cs_2O	Sol	75.90	Sc_2O_3	Sol	93.94
Cu_2O	Sol	62.47	SiO_2	Quartz(L)	44.42
CuO	Sol	42.26	Sm_2O_3	Sol-A	115.82
Dy_2O_3	Sol-A	116.26	SrO	Sol	45.15
Er_2O_3	Sol	108.49	Ta_2O_5	Sol	131.48
Eu_2O_3	Cubic	124.68	TeO_2	Sol	63.88
Fe_2O_3	Sol-A	104.77	TeO_3	Sol	71.47
FeO	Sol	48.04	TiO_2	Rutile	55.10
Ga_2O_3	Sol	93.86	Tl_2O_3	Sol	105.46
Gd_2O_3	Cubic	105.51	Tm_2O_3	Sol-A	116.72
GeO_2	Hexagonal	51.95	UO_2	Sol	63.59
HfO_2	Sol-A	60.26	UO_3	Sol	81.19
HgO	Sol	43.89	V_2O_5	Sol	127.37
Ho_2O_3	Sol	114.96	WO_3	Sol-A	72.80
K_2O	Sol	84.53	Y_2O_3	Sol-A	102.51
La_2O_3	Sol	108.78	Yb_2O_3	Sol-A	115.36
Li_2O	Sol	54.25	ZnO	Sol	41.07
Lu_2O_3	Sol	101.76	ZrO_2	Sol-A	56.21

C°_{pm}(298.15 K) and/or $C^{\circ}_{pm}(T)$ can be obtained, and concerning credibility of the predicted values as well.

3.1. C°_{pm}(298.15 K) experimental data set

The predicted values of C°_{pm}(298.15 K) were compared with available experimental data in order to qualitatively compare the selected estimation methods. 326 mixed oxide phases formed by 71 binary oxides of 57 elements were included into the data set given in Table 5. The values of C°_{pm}(298.15 K) were taken from more than 100 literature sources—data collections, review articles and original papers. The presented data come in all cases either from direct (calorimetric) experiments or from simultaneous processing (optimization) of more experimental data. The accuracy of the calorimetric data depends on the particular method used. The most precise values were obtained by direct measurements of C°_{pm} in adiabatic calorimeters (the determination error does not exceed 0.2–0.5% at an ambient temperature). The experimental error of C°_{pm}(298.15 K) measured in DSC calorimeters (in continuous or stepwise mode) is higher, about 1–2%. Even the higher error (2–3%) must be taken into account in case of heat content measurements, $H_T - H_{Tref}$, using drop calorimeters. The direct result here is the temperature dependence of the integral function, relative enthalpy, usually measured above 450 °C. The $C^{\circ}_{pm}(T)$ dependence is then obtained by differentiating it with respect to temperature and C°_{pm}(298.15 K) by extrapolation.

In some cases, the available experimental data were not taken into account for assessment of the reliability of the estimation methods. For instance, the values of $C^{\circ}_{pm}(T)$ above 400 K and extrapolated C°_{pm}(298.15 K) reported by Gospodinov et al. for ternary oxides formed by TeO_2 and MnO [32], MgO [33], Al_2O_3, Ga_2O_3, In_2O_3 and Tl_2O_3 [34], or CuO [35] are not treated as much reliable. Indeed, their data of C°_{pm}(298.15 K) for ternary oxides $BaZrO_3$, $CaZrO_3$ and $SrZrO_3$ [36], measured on the same calorimeter and evaluated using the same procedure, are obviously quite different from values reported by other authors [37], and, moreover, some errors have been found in the evaluation of experimental results [38]. Similarly, the data for ternary oxides of Sb_2O_5, BaO, CaO and SrO [39], CoO, NiO and ZnO [40], all reported by Kasenov et al., as well as for quaternary oxides of type $RE_2AE_2Mn_4O_{11}$, (RE: Gd, AE: Ba) [41], (RE: Dy, AE: Sr) [42], (RE: Er, Gd, Ho, La, Lu, Nd, AE: Sr) [43], (RE: La, AE: Ca) [44], and (RE: Er, Gd, Nd, AE: Ca) [45] were not included in the experimental data set. In all latter studies, the conventional calorimeter ICT-400 has been employed for C°_{pm} measurements providing the results with the relatively large error of about 10%. For example, the average value of $181 \pm 17\ J\ K^{-1}\ mol^{-1}$ resulting from five measurements of $NiSb_2O_6$ is referred in [40], which exceeds severalfold the errors of other data and would therefore, depreciate the comparison of experimental and estimated values.

In addition to complex mixed oxides, the oxides of Me_3O_4 type with a cation of one element in two valence states, $Me^{2+}$and Me^{3+}(Me: Co, Cr, Fe, Mn, Pb), have been also included in the experimental data set. For the sake of completeness, even those mixed oxides are listed in the Table 5, which C°_{pm} cannot be predicted by any of the tested methods.

3.2. Neumann–Kopp rule (NKR)

The NKR is the most universal from all considered methods—within the given experimental data set the total number of 295 values of C°_{pm}(298.15 K) can be estimated using this rule. The NKR cannot be applied only in the following cases:

- The experimental values of C°_{pm}(298.15 K) for binary oxides forming a particular mixed oxide are not available. So far the experimental data for Co_2O_3, CrO_2, MnO_3, Rb_2O, RuO_3 and Tb_2O_3 are missing, and thus only their estimated values are reported in thermodynamic tables. Since the mean prediction error of contribution methods for binary oxides varies by 5% (for C°_{pm}(298.15 K)) [19], the application of the estimated data could significantly decrease the quality of NKR results.
- A given mixed oxide cannot be obtained from a chemical reaction of bare solid binary oxides. Let us mention a quaternary oxide $YBa_2Cu_3O_7$ as the example, which formation can be described as

$$\tfrac{1}{2}Y_2O_3 + 2\,BaO + 3\,CuO + \tfrac{1}{4}O_2 \rightarrow YBa_2Cu_3O_7 \quad \text{(R3)}$$

Here the gaseous oxygen occurs as one of the starting compounds. The NKR is based on a simple

Table 5
Comparison of experimental and estimated values of heat capacity at 298.15 K of solid mixed oxides

No.	Mixed oxide	Binary oxides combination	Phase	Reference	$C^{\circ}_{pm}(298)$ ($J\,K^{-1}\,mol^{-1}$)	$C^{\circ}_{pm}(298)$(NKR) ($J\,K^{-1}\,mol^{-1}$)	ΔC°_{pm} (%)	$C^{\circ}_{pm}(298)$(KK) ($J\,K^{-1}\,mol^{-1}$)	ΔC°_{pm} (%)	$C^{\circ}_{pm}(298)$(BB) ($J\,K^{-1}\,mol^{-1}$)	ΔC°_{pm} (%)
1	Ag_2WO_4	$Ag_2O{\cdot}WO_3$	Sol	[47]	150.36	139.12	−7.48	148.95	−0.94		
2	$Al_{18}B_4O_{33}$	$9Al_2O_3{\cdot}2B_2O_3$	Sol	[6]	823.19	837.05	1.68				
3	Al_2SiO_5	$Al_2O_3{\cdot}SiO_2$	Andalusite	[1]	123.40	123.47	0.06			121.36	−1.65
4	Al_2SiO_5	$Al_2O_3{\cdot}SiO_2$	Kyanite	[1]	122.19	123.47	1.05			121.36	−0.68
5	Al_2SiO_5	$Al_2O_3{\cdot}SiO_2$	Sillimanite	[1]	122.93	123.47	0.44			121.36	−1.28
6	Al_2TiO_5	$Al_2O_3{\cdot}TiO_2$	Sol	[6]	136.40	134.11	−1.68			132.85	−2.60
7	$Al_4B_2O_9$	$2Al_2O_3{\cdot}B_2O_3$	Sol	[6]	222.64	221.00	−0.74				
8	$Al_6Si_2O_{13}$	$3Al_2O_3{\cdot}2SiO_2$	Sol	[1]	325.99	325.87	−0.04			320.13	−1.80
9	$Ba_2Si_3O_8$	$2BaO{\cdot}3SiO_2$	Sol	[8]	224.60	227.38	1.24	222.44	−0.96		
10	Ba_2TiO_4	$2BaO{\cdot}TiO_2$	Sol	[6]	149.15	149.22	0.05	145.24	−2.62		
11	$Ba_3B_2O_6$	$3BaO{\cdot}B_2O_3$	Sol	[48]	215.01	204.16	−5.05	190.28	−11.50		
12	$Ba_3LaNb_3O_{12}$	$(6BaO{\cdot}La_2O_3{\cdot}3Nb_2O_5)/2$	Sol	[49]	387.61	393.77	1.59				
13	$BaAl_2O_4$	$BaO{\cdot}Al_2O_3$	Sol	[6]	113.70	126.07	10.88	112.28	−1.25		
14	$BaAl_2Si_2O_8$	$BaO{\cdot}Al_2O_3{\cdot}2SiO_2$	Sol	[50]	221.71	214.91	−3.07	222.36	0.29		
15	$BaCeO_3$	$BaO{\cdot}CeO_2$	Sol	[51]	111.91	108.59	−2.97				
16	$BaCuO_2$	$BaO{\cdot}CuO$	Sol	[52]	95.00	89.32	−5.98				
17	$BaCuO_{2.09}$		Sol	[53]	96.89						
18	$BaMoO_4$	$BaO{\cdot}MoO_3$	Sol	[54]	122.00	122.20	0.16	119.13	−2.35		
19	$BaSiO_3$	$BaO{\cdot}SiO_2$	Sol	[6]	89.02	91.48	2.77	89.29	0.31		
20	$BaSrFe_4O_8$	$BaO{\cdot}SrO{\cdot}2Fe_2O_3$	Sol	[55]	288.90	301.75	4.45	304.00	5.23		
21	$BaTiO_3$	$BaO{\cdot}TiO_2$	Sol	[6]	102.45	102.16	−0.29	100.81	−1.60		
22	$BaUO_4$	$BaO{\cdot}UO_3$	Sol	[8]	133.50	128.25	−3.93	133.47	−0.02		
23	$BaZrO_3$	$BaO{\cdot}ZrO_2$	Sol	[37]	101.71	103.27	1.53	101.42	−0.29		
24	Be_2SiO_4	$2BeO{\cdot}SiO_2$	Sol	[6]	93.48	94.38	0.96	87.96	−5.90		
25	$Be_3B_2O_6$	$3BeO{\cdot}B_2O_3$	Sol	[6]	138.44	137.92	−0.37	140.06	1.17		
26	$BeAl_2O_4$	$BeO{\cdot}Al_2O_3$	Sol	[6]	104.94	103.99	−0.91	108.14	3.05		
27	$BeAl_6O_{10}$	$BeO{\cdot}3Al_2O_3$	Sol	[6]	261.92	262.01	0.03				
28	$BeWO_4$	$BeO{\cdot}WO_3$	Sol	[8]	96.92	97.78	0.89	107.11	10.52		
29	$Bi_2Ca_2O_5$	$Bi_2O_3{\cdot}2CaO$	Sol	[56]	197.44	196.97	−0.24				
30	Bi_2CaO_4	$Bi_2O_3{\cdot}CaO$	Sol	[56]	151.32	154.55	2.13				
31	Bi_2CuO_4	$Bi_2O_3{\cdot}CuO$	Sol	[57]	151.73	154.39	1.75				
32	$Bi_2Sr_2CuO_6$	$Bi_2O_3{\cdot}2SrO{\cdot}CuO$	Sol	[58]	241.30	244.69	1.40				
33	$Bi_2Sr_2Ca_{1.2}Cu_{1.8}O_{8.5}$		Sol	[59]	346.70						
34	$Bi_2Sr_3Cu_2O_8$	$Bi_2O_3{\cdot}3SrO{\cdot}2CuO$	Sol	[58]	353.28	332.10	−6.00				
35	$Bi_6Ca_4O_{13}$	$3Bi_2O_3{\cdot}4CaO$	Sol	[56]	504.06	506.07	0.40				
36	$Ca_{12}Al_{14}O_{33}$	$12CaO{\cdot}7Al_2O_3$	Sol	[8]	1084.82	1062.11	−2.09			1060.03	−2.29
37	$Ca_2Al_2SiO_7$	$2CaO{\cdot}Al_2O_3{\cdot}SiO_2$	Sol	[1]	205.51	208.27	1.34	210.83	2.59	207.72	1.08

Table 5 (*Continued*)

No.	Mixed oxide	Binary oxides combination	Phase	Reference	$C^{\circ}_{pm}(298)$ ($J\,K^{-1}\,mol^{-1}$)	$C^{\circ}_{pm}(298)(NKR)$ ($J\,K^{-1}\,mol^{-1}$)	ΔC°_{pm} (%)	$C^{\circ}_{pm}(298)(KK)$ ($J\,K^{-1}\,mol^{-1}$)	ΔC°_{pm} (%)	$C^{\circ}_{pm}(298)(BB)$ ($J\,K^{-1}\,mol^{-1}$)	ΔC°_{pm} (%)
38	$Ca_2B_2O_5$	$2CaO{\cdot}B_2O_3$	Sol-A	[6]	147.08	147.82	0.51	146.17	−0.62		
39	$Ca_2Fe_2O_5$	$2CaO{\cdot}Fe_2O_3$	Sol	[1]	192.38	189.61	−1.44			191.53	−0.44
40	$Ca_2MgSi_2O_7$	$2CaO{\cdot}MgO{\cdot}2SiO_2$	Sol	[1]	210.97	210.94	−0.01	210.31	−0.31	211.57	0.28
41	Ca_2SiO_4	$2CaO{\cdot}SiO_2$	Sol-A	[60]	125.76	129.26	2.78	127.72	1.56	130.31	3.62
42	$Ca_3Al_2O_6$	$3CaO{\cdot}Al_2O_3$	Sol	[1]	208.79	206.27	−1.21	209.53	0.35	206.95	−0.88
43	$Ca_3Al_2Si_3O_{12}$	$3CaO{\cdot}Al_2O_3{\cdot}3SiO_2$	Sol	[1]	333.15	339.53	1.92	348.41	4.58	338.80	1.70
44	$Ca_3B_2O_6$	$3CaO{\cdot}B_2O_3$	Sol	[6]	187.86	190.24	1.27	185.27	−1.38		
45	$Ca_3Fe_2Si_3O_{12}$	$3CaO{\cdot}Fe_2O_3{\cdot}3SiO_2$	Sol	[15]	351.38	365.29	3.96	360.97	2.73	366.56	4.32
46	$Ca_3Ga_2Ge_3O_{12}$	$3CaO{\cdot}Ga_2O_3{\cdot}3GeO_2$	Sol	[61]	379.50	376.97	−0.67				
47	$Ca_3MgSi_2O_8$	$3CaO{\cdot}MgO{\cdot}2SiO_2$	Sol	[8]	252.26	253.36	0.44	250.41	−0.73	254.75	0.99
48	$Ca_3Si_2O_7$	$3CaO{\cdot}2SiO_2$	Sol	[60]	211.51	216.10	2.17	215.34	1.81	217.44	2.81
49	Ca_3SiO_5	$3CaO{\cdot}SiO_2$	Sol	[60]	171.61	171.68	0.04			173.49	1.10
50	$Ca_3Ti_2O_7$	$3CaO{\cdot}2TiO_2$	Sol	[6]	239.59	237.46	−0.89	241.04	0.61	240.42	0.35
51	$Ca_4Ti_3O_{10}$	$4CaO{\cdot}3TiO_2$	Sol	[6]	337.77	334.98	−0.83	340.18	0.71	339.04	0.38
52	$CaAl_2O_4$	$CaO{\cdot}Al_2O_3$	Sol	[6]	120.60	121.43	0.69	123.21	2.17	120.59	−0.01
53	$CaAl_2Si_2O_8$	$CaO{\cdot}Al_2O_3{\cdot}2SiO_2$	Sol	[8]	211.31	210.27	−0.49	220.69	4.44	208.49	−1.33
54	$CaAl_2SiO_6$	$CaO{\cdot}Al_2O_3{\cdot}SiO_2$	Sol	[1]	165.82	165.85	0.02			164.54	−0.77
55	$CaAl_4O_7$	$CaO{\cdot}2Al_2O_3$	Sol	[6]	199.57	200.44	0.44			198.00	−0.79
56	CaB_2O_4	$CaO{\cdot}B_2O_3$	Sol	[6]	103.99	105.40	1.36	107.07	2.97		
57	CaB_4O_7	$CaO{\cdot}2B_2O_3$	Sol	[6]	157.85	168.38	6.67	158.95	0.70		
58	$CaCrO_4$	$CaO{\cdot}CrO_3$	Sol	[62]	113.18	121.54	7.39	116.96	3.34		
59	$CaCr_2O_4$	$CaO{\cdot}Cr_2O_3$	Sol-B	[62]	139.31	156.68	12.47	150.03	7.70		
60	$CaFe_2O_4$	$CaO{\cdot}Fe_2O_3$	Sol	[6]	153.65	147.19	−4.20	150.75	−1.89	148.35	−3.45
61	$CaFeSi_2O_6$	$CaO{\cdot}FeO{\cdot}2SiO_2$	Sol	[15]	175.37	179.30	2.24	176.49	0.64	174.46	−0.52
62	$CaHfTi_2O_7$	$CaO{\cdot}HfO_2{\cdot}2TiO_2$	Sol	[63]	206.90	212.88	2.89	217.18	4.97		
63	$CaMgSi_2O_6$	$CaO{\cdot}MgO{\cdot}2SiO_2$	Sol	[1]	166.63	168.52	1.13	170.21	2.15	168.39	1.06
64	$CaMgSiO_4$	$CaO{\cdot}MgO{\cdot}SiO_2$	Sol	[6]	123.22	124.10	0.71	122.69	−0.43	124.44	0.99
65	$CaNb_2O_6$	$CaO{\cdot}Nb_2O_5$	Sol	[6]	177.34	174.55	−1.57	180.69	1.89		
66	$CaSiO_3$	$CaO{\cdot}SiO_2$	Sol-A	[60]	86.42	86.84	0.49	87.62	1.39	87.13	0.83
67	$CaTiO_3$	$CaO{\cdot}TiO_2$	Sol-A	[6]	97.70	97.52	−0.18	99.14	1.48	98.62	0.95
68	$CaTiSiO_5$	$CaO{\cdot}TiO_2{\cdot}SiO_2$	Sol	[1]	139.11	141.94	2.03	140.43	0.95	142.57	2.49
69	$CaUO_4$	$CaO{\cdot}UO_3$	Sol-A	[6]	130.45	123.61	−5.24	131.80	1.04		
70	$CaWO_4$	$CaO{\cdot}WO_3$	Sol	[6]	113.24	115.22	1.75	122.18	7.90		
71	$CaZrO_3$	$CaO{\cdot}ZrO_2$	Sol	[37]	99.91	98.63	−1.28	99.75	−0.16		
72	$CaZrTi_2O_7$	$CaO{\cdot}ZrO_2{\cdot}2TiO_2$	Sol	[64]	211.73	208.83	−1.37	215.51	1.78		
73	$CdTiO_3$	$CdO{\cdot}TiO_2$	Sol-A	[6]	98.50	99.26	0.77	97.46	−1.06		
74	$Ce_2Si_2O_7$	$Ce_2O_3{\cdot}2SiO_2$	Sol-B	[65]	204.41	205.89	0.72	188.13	−7.96		
75	$Ce_2Zr_2O_7$	$Ce_2O_3{\cdot}2ZrO_2$	Sol	[66]	233.74	229.47	−1.83				
76	Co_2SiO_4	$2CoO{\cdot}SiO_2$	Sol	[6]	133.95	154.86	15.61	134.40	0.33		
77	Co_2TiO_4	$2CoO{\cdot}TiO_2$	Sol	[6]	160.49	165.54	3.15	148.58	−7.42		

Table 5 (*Continued*)

No.	Mixed oxide	Binary oxides combination	Phase	Reference	$C^{\circ}_{pm}(298)$ ($J\,K^{-1}\,mol^{-1}$)	$C^{\circ}_{pm}(298)$(NKR) ($J\,K^{-1}\,mol^{-1}$)	ΔC°_{pm} (%)	$C^{\circ}_{pm}(298)$(KK) ($J\,K^{-1}\,mol^{-1}$)	ΔC°_{pm} (%)	$C^{\circ}_{pm}(298)$(BB) ($J\,K^{-1}\,mol^{-1}$)	ΔC°_{pm} (%)
78	Co_3O_4	$CoO{\cdot}Co_2O_3$	Sol	[6]	123.42						
79	$CoFe_2O_4$	$CoO{\cdot}Fe_2O_3$	Sol	[6]	152.58	159.99	4.86	154.09	0.99		
80	$CoTa_2O_6$	$CoO{\cdot}Ta_2O_5$	Sol	[67]	175.59	186.70	6.33				
81	$CoTiO_3$	$CoO{\cdot}TiO_2$	Sol	[6]	107.77	110.32	2.37	102.48	−4.91		
82	$CoWO_4$	$CoO{\cdot}WO_3$	Sol-A	[6]	129.94	128.02	−1.47	125.52	−3.40		
83	Cr_3O_4	$CrO{\cdot}Cr_2O_3$	Sol	[68]	135.64						
84	$CsBO_2$	$(Cs_2O{\cdot}B_2O_3)/2$	Sol	[6]	69.48	69.44	−0.05	67.55	−2.77		
85	$Cs_2Cr_2O_7$	$Cs_2O{\cdot}2CrO_3$	Sol-A	[54]	231.54	234.14	1.12				
86	Cs_2CrO_4	$Cs_2O{\cdot}CrO_3$	Sol-A	[54]	146.06	155.02	6.13	144.99	−0.73		
87	Cs_2MnO_4	$Cs_2O{\cdot}MnO_3$	Sol-A	[69]	149.24						
88	$Cs_2Mo_2O_7$	$Cs_2O{\cdot}2MoO_3$	Sol	[70]	224.14	226.18	0.91				
89	Cs_2MoO_4	$Cs_2O{\cdot}MoO_3$	Sol-A	[6]	148.67	151.04	1.59	145.49	−2.14		
90	Cs_2RuO_4	$Cs_2O{\cdot}RuO_3$	Sol-A	[69]	156.14						
91	$Cs_2Si_2O_5$	$Cs_2O{\cdot}2SiO_2$	Sol	[6]	176.73	164.74	−6.78	159.51	−9.74		
92	$Cs_2Si_4O_9$	$Cs_2O{\cdot}4SiO_2$	Sol	[6]	272.86	253.58	−7.06				
93	Cs_2SiO_3	$Cs_2O{\cdot}SiO_2$	Sol	[6]	122.23	120.32	−1.56	115.65	−5.38		
94	$Cs_2Te_2O_5$	$Cs_2O{\cdot}2TeO_2$	Sol	[54]	193.00	203.66	5.52				
95	$Cs_2Te_4O_{12}$	$Cs_2O{\cdot}TeO_2{\cdot}3TeO_3$	Sol	[54]	343.00	354.19	3.26				
96	$Cs_2Te_4O_9$	$Cs_2O{\cdot}4TeO_2$	Sol	[54]	318.20	331.42	4.16				
97	Cs_2TeO_3	$Cs_2O{\cdot}TeO_2$	Sol	[54]	133.87	139.78	4.42				
98	Cs_2TeO_4	$Cs_2O{\cdot}TeO_3$	Sol	[54]	148.35	147.37	−0.66				
99	$Cs_2U_2O_7$	$Cs_2O{\cdot}2UO_3$	Sol	[54]	231.23	238.28	3.05				
100	$Cs_2U_4O_{12}$	$Cs_2O{\cdot}UO_2{\cdot}3UO_3$	Sol-A	[54]	384.01	383.06	−0.25				
101	Cs_2UO_4	$Cs_2O{\cdot}UO_3$	Sol	[6]	152.75	157.09	2.84	159.83	4.64		
102	Cs_2ZrO_3	$Cs_2O{\cdot}ZrO_2$	Sol	[71]	129.79	132.11	1.79	127.78	−1.55		
103	Cs_3CrO_4	$(3Cs_2O{\cdot}CrO_2{\cdot}CrO_3)/2$	Sol-A	[54]	179.92						
104	$CsAlO_2$	$(Cs_2O{\cdot}Al_2O_3)/2$	Sol	[72]	79.76	77.46	−2.89	75.62	−5.19		
105	$CuFe_2O_4$	$CuO{\cdot}Fe_2O_3$	Sol-A	[6]	148.81	147.03	−1.19	151.16	1.58		
106	$CuFeO_2$	$(Cu_2O{\cdot}Fe_2O_3)/2$	Sol-A	[6]	84.18	85.12	1.12	88.13	4.69		
107	$Dy_3Fe_5O_{12}$	$(3Dy_2O_3{\cdot}5Fe_2O_3)/2$	Sol	[73]	442.72	436.32	−1.45				
108	Dy_3NbO_7	$(3Dy_2O_3{\cdot}Nb_2O_5)/2$	Sol	[74]	251.85	240.46	−4.52				
109	$DyCrO_3$	$(Dy_2O_3{\cdot}Cr_2O_3)/2$	Sol	[75]	102.33	115.26	12.64				
110	$Er_3Fe_5O_{12}$	$(3Er_2O_3{\cdot}5Fe_2O_3)/2$	Sol	[76]	449.52	424.66	−5.53				
111	Er_3NbO_7	$(3Er_2O_3{\cdot}Nb_2O_5)/2$	Sol	[74]	233.02	228.80	−1.81				
112	$ErCrO_3$	$(Er_2O_3{\cdot}Cr_2O_3)/2$	Sol	[75]	101.74	111.38	9.48				
113	$ErMnO_3$	$(Er_2O_3{\cdot}Mn_2O_3)/2$	Sol	[77]	104.81	103.77	−0.99				
114	$Eu_3Fe_5O_{12}$	$(3Eu_2O_3{\cdot}5Fe_2O_3)/2$	Sol	[76]	462.89	448.95	−3.01				
115	Eu_3NbO_7	$(3Eu_2O_3{\cdot}Nb_2O_5)/2$	Sol	[74]	251.01	253.09	0.83				
116	$Fe_2Al_4Si_5O_{18}$	$2FeO{\cdot}2Al_2O_3{\cdot}5SiO_2$	Sol	[15]	464.41	476.20	2.54	491.40	5.81	461.33	−0.66
117	Fe_2SiO_4	$2FeO{\cdot}SiO_2$	Sol	[8]	132.90	140.50	5.72	130.22	−2.02	130.71	−1.65

Table 5 (*Continued*)

No.	Mixed oxide	Binary oxides combination	Phase	Reference	$C^{\circ}_{pm}(298)$ ($J\,K^{-1}\,mol^{-1}$)	$C^{\circ}_{pm}(298)(NKR)$ ($J\,K^{-1}\,mol^{-1}$)	ΔC°_{pm} (%)	$C^{\circ}_{pm}(298)(KK)$ ($J\,K^{-1}\,mol^{-1}$)	ΔC°_{pm} (%)	$C^{\circ}_{pm}(298)(BB)$ ($J\,K^{-1}\,mol^{-1}$)	ΔC°_{pm} (%)
118	Fe_2TiO_4	$2FeO{\cdot}TiO_2$	Sol	[8]	142.30	151.18	6.24	144.40	1.48	142.20	−0.07
119	Fe_2TiO_5	$Fe_2O_3{\cdot}TiO_2$	Sol	[1]	163.85	159.87	−2.43			160.61	−1.98
120	$Fe_3Al_2Si_3O_{12}$	$3FeO{\cdot}Al_2O_3{\cdot}3SiO_2$	Sol	[15]	342.74	356.39	3.98	352.16	2.75	339.40	−0.97
121	Fe_3O_4	$FeO{\cdot}Fe_2O_3$	Sol	[6]	151.78	152.81	0.68	152.00	0.14	148.55	−2.13
122	$FeAl_2O_4$	$FeO{\cdot}Al_2O_3$	Sol	[15]	131.40	127.05	−3.31	124.46	−5.28	120.79	−8.07
123	$FeCr_2O_4$	$FeO{\cdot}Cr_2O_3$	Sol	[6]	133.81	162.30	21.29	151.28	13.06		
124	$FeSiO_3$	$FeO{\cdot}SiO_2$	Sol	[15]	88.12	92.46	4.93	88.87	0.85	87.33	−0.90
125	$FeTa_2O_6$	$FeO{\cdot}Ta_2O_5$	Sol	[67]	184.87	179.52	−2.89				
126	$FeTiO_3$	$FeO{\cdot}TiO_2$	Sol	[6]	99.50	103.14	3.66	100.39	0.89	98.82	−0.69
127	$Gd_3Fe_5O_{12}$	$(3Gd_2O_3{\cdot}5Fe_2O_3)/2$	Sol	[78]	433.06	420.19	−2.97				
128	$Gd_3Ga_5O_{12}$	$(3Gd_2O_3{\cdot}5Ga_2O_3)/2$	Sol	[61]	385.64	392.92	1.89				
129	Gd_3NbO_7	$(3Gd_2O_3{\cdot}Nb_2O_5)/2$	Sol	[74]	237.49	224.33	−5.54				
130	$GdCrO_3$	$(Gd_2O_3{\cdot}Cr_2O_3)/2$	Sol	[75]	99.52	109.89	10.42				
131	$Hg_{0.97}Ba_2CuO_{4.05}$		Sol	[79]	189.53						
132	$HgBaO_2$	$HgO{\cdot}BaO$	Sol	[80]	103.48	90.95	−12.11				
133	$HgCaO_2$	$HgO{\cdot}CaO$	Sol	[81]	96.31	86.31	−10.38				
134	$HgSrO_2$	$HgO{\cdot}SrO$	Sol	[80]	89.90	89.04	−0.96				
135	$Ho_3Fe_5O_{12}$	$(3Ho_2O_3{\cdot}5Fe_2O_3)/2$	Sol	[82]	451.52	434.37	−3.80				
136	Ho_3NbO_7	$(3Ho_2O_3{\cdot}Nb_2O_5)/2$	Sol	[74]	252.14	238.51	−5.41				
137	Ho_6WO_{12}	$3Ho_2O_3{\cdot}WO_3$	Sol	[83]	434.20	417.68	−3.80				
138	$HoCrO_3$	$(Ho_2O_3{\cdot}Cr_2O_3)/2$	Sol	[75]	101.60	114.61	12.81				
139	$K_2B_4O_7$	$K_2O{\cdot}2B_2O_3$	Sol	[6]	170.30	210.49	23.60	186.14	9.30		
140	$K_2B_6O_{10}$	$K_2O{\cdot}3B_2O_3$	Sol	[6]	265.34	273.47	3.07				
141	$K_2B_8O_{13}$	$K_2O{\cdot}4B_2O_3$	Sol	[6]	319.06	336.45	5.45				
142	K_2CrO_4	$K_2O{\cdot}CrO_3$	Sol-A	[6]	146.05	163.65	12.05	144.15	−1.30		
143	$K_2Si_2O_5$	$K_2O{\cdot}2SiO_2$	Sol-A	[6]	160.95	173.37	7.72	158.67	−1.41	159.60	−0.84
144	$K_2Si_4O_9$	$K_2O{\cdot}4SiO_2$	Sol	[84]	247.20	262.21	6.07			247.50	0.12
145	K_2SiO_3	$K_2O{\cdot}SiO_2$	Sol	[6]	118.70	128.95	8.64	114.81	−3.28	115.65	−2.57
146	$K_2W_2O_7$	$K_2O{\cdot}2WO_3$	Sol	[85]	221.00	230.13	4.13				
147	$K_2W_3O_{10}$	$K_2O{\cdot}3WO_3$	Sol	[85]	288.10	302.93	5.15				
148	$K_2W_4O_{13}$	$K_2O{\cdot}4WO_3$	Sol	[85]	356.40	375.73	5.42				
149	K_2WO_4	$K_2O{\cdot}WO_3$	Sol-A	[6]	150.81	157.33	4.32	149.37	−0.95		
150	$KAl_3Si_3O_{11}$	$(K_2O{\cdot}3Al_2O_3{\cdot}6SiO_2)/2$	Sol	[1]	287.37	294.04	2.32	304.53	5.97	283.82	−1.24
151	$KAlSi_2O_6$	$(K_2O{\cdot}Al_2O_3{\cdot}4SiO_2)/2$	Sol	[6]	164.30	170.61	3.84	171.46	4.36	162.46	−1.12
152	$KAlSi_3O_8$	$(K_2O{\cdot}Al_2O_3{\cdot}6SiO_2)/2$	Microcline	[1]	202.84	215.03	6.01	215.32	6.15	206.41	1.76
153	$KAlSi_3O_8$	$(K_2O{\cdot}Al_2O_3{\cdot}6SiO_2)/2$	Sanidine	[1]	205.28	215.03	4.75	215.32	4.89	206.41	0.55
154	$KAlSiO_4$	$(K_2O{\cdot}Al_2O_3{\cdot}2SiO_2)/2$	Sol	[6]	119.90	126.19	5.25	123.94	3.37	118.51	−1.16
155	KBO_2	$(K_2O{\cdot}B_2O_3)/2$	Sol	[6]	66.96	73.76	10.15	67.13	0.25		
156	$KDyMo_2O_8$	$(K_2O{\cdot}Dy_2O_3{\cdot}4MoO_3)/2$	Sol	[86]	235.90	250.68	6.26				

Table 5 (*Continued*)

No.	Mixed oxide	Binary oxides combination	Phase	Reference	$C^{\circ}_{pm}(298)$ ($J\,K^{-1}\,mol^{-1}$)	$C^{\circ}_{pm}(298)(NKR)$ ($J\,K^{-1}\,mol^{-1}$)	ΔC°_{pm} (%)	$C^{\circ}_{pm}(298)(KK)$ ($J\,K^{-1}\,mol^{-1}$)	ΔC°_{pm} (%)	$C^{\circ}_{pm}(298)(BB)$ ($J\,K^{-1}\,mol^{-1}$)	ΔC°_{pm} (%)
157	$KErMo_2O_8$	$(K_2O{\cdot}Er_2O_3{\cdot}4MoO_3)/2$	Sol	[87]	233.40	246.79	5.74				
158	$KGdMo_2O_8$	$(K_2O{\cdot}Gd_2O_3{\cdot}4MoO_3)/2$	Sol-A	[88]	233.20	245.30	5.19	234.91	0.73		
159	$KHoMo_2O_8$	$(K_2O{\cdot}Ho_2O_3{\cdot}4MoO_3)/2$	Sol	[89]	232.50	250.03	7.54	234.49	0.86		
160	$KLuMo_2O_8$	$(K_2O{\cdot}Lu_2O_3{\cdot}4MoO_3)/2$	Sol	[90]	234.70	243.43	3.72				
161	$KTbMo_2O_8$	$(K_2O{\cdot}Tb_2O_3{\cdot}4MoO_3)/2$	Sol	[91]	236.80						
162	$KYbMo_2O_8$	$(K_2O{\cdot}Yb_2O_3{\cdot}4MoO_3)/2$	Sol	[92]	238.10	250.23	5.09				
163	$KYMo_2O_8$	$(K_2O{\cdot}Y_2O_3{\cdot}4MoO_3)/2$	Sol	[93]	232.10	243.80	5.04	236.58	1.93		
164	La_2CuO_4	$La_2O_3{\cdot}CuO$	Sol	[94]	151.30	151.04	−0.17				
165	$La_2Mo_3O_{12}$	$La_2O_3{\cdot}3MoO_3$	Sol	[6]	329.36	334.20	1.47	329.35	0.00		
166	La_2NiO_4	$La_2O_3{\cdot}NiO$	Sol	[95]	159.14	153.07	−3.81				
167	$La_2Si_2O_7$	$La_2O_3{\cdot}2SiO_2$	Sol-B	[65]	195.18	197.62	1.25	192.31	−1.47		
168	$La_2Zr_2O_7$	$La_2O_3{\cdot}2ZrO_2$	Sol	[66]	223.05	221.20	−0.83				
169	La_3NbO_7	$(3La_2O_3{\cdot}Nb_2O_5)/2$	Sol	[74]	235.68	229.24	−2.74				
170	$LaAlO_3$	$(La_2O_3{\cdot}Al_2O_3)/2$	Sol	[6]	92.64	93.90	1.36	93.25	0.66		
171	$LaCoO_3$	$(La_2O_3{\cdot}Co_2O_3)/2$	Sol	[96]	107.51						
172	$LaCrO_3$	$(La_2O_3{\cdot}Cr_2O_3)/2$	Sol	[75]	111.20	111.52	0.29				
173	$LaFeO_3$	$(La_2O_3{\cdot}Fe_2O_3)/2$	Sol	[96]	108.65	106.78	−1.72				
174	$LaMnO_3$	$(La_2O_3{\cdot}Mn_2O_3)/2$	Sol	[97]	102.79	103.91	1.09				
175	$LaMnO_{3.15}$		Sol	[80]	110.10						
176	$Li_2B_4O_7$	$Li_2O{\cdot}2B_2O_3$	Sol	[6]	179.32	180.21	0.50	173.58	−3.20		
177	$Li_2B_8O_{13}$	$Li_2O{\cdot}4B_2O_3$	Sol	[6]	324.23	306.17	−5.57				
178	$Li_2Si_2O_5$	$Li_2O{\cdot}2SiO_2$	Sol-A	[6]	138.77	143.09	3.11	146.11	5.29		
179	Li_2SiO_3	$Li_2O{\cdot}SiO_2$	Sol	[6]	100.00	98.67	−1.33	102.25	2.25		
180	$Li_2Ti_3O_7$	$Li_2O{\cdot}3TiO_2$	Sol	[98]	228.51	219.55	−3.92				
181	Li_2TiO_3	$Li_2O{\cdot}TiO_2$	Sol-A	[6]	109.68	109.35	−0.30	113.77	3.73		
182	Li_2ZrO_3	$Li_2O{\cdot}ZrO_2$	Sol	[99]	114.60	110.46	−3.61	114.38	−0.19		
183	Li_4SiO_4	$2Li_2O{\cdot}SiO_2$	Sol	[100]	155.23	152.92	−1.49	156.98	1.13		
184	$Li_4Ti_5O_{12}$	$2Li_2O{\cdot}5TiO_2$	Sol	[98]	361.54	384.00	6.21				
185	Li_8ZrO_6	$4Li_2O{\cdot}ZrO_2$	Sol	[99]	275.46	273.21	−0.82				
186	$LiAlO_2$	$(Li_2O{\cdot}Al_2O_3)/2$	Sol	[8]	67.83	66.63	−1.77	68.92	1.61		
187	$LiAlSi_2O_6$	$(Li_2O{\cdot}Al_2O_3{\cdot}4SiO_2)/2$	Sol-A	[6]	158.92	155.47	−2.17	165.18	3.94		
188	$LiAlSiO_4$	$(Li_2O{\cdot}Al_2O_3{\cdot}2SiO_2)/2$	Sol-A	[101]	111.15	111.05	−0.09	117.66	5.86		
189	LiB_3O_5	$(Li_2O{\cdot}3B_2O_3)/2$	Sol	[6]	145.52	121.60	−16.44				
190	$LiBO_2$	$(Li_2O{\cdot}B_2O_3)/2$	Sol	[6]	60.44	58.62	−3.02	60.85	0.68		
191	$LiFeO_2$	$(Li_2O{\cdot}Fe_2O_3)/2$	Sol	[6]	82.46	79.51	−3.58	82.62	0.19		
192	$Lu_3Fe_5O_{12}$	$(3Lu_2O_3{\cdot}5Fe_2O_3)/2$	Sol	[102]	424.90	414.57	−2.43				
193	Lu_3NbO_7	$(3Lu_2O_3{\cdot}Nb_2O_5)/2$	Sol	[74]	220.14	218.71	−0.65				
194	Lu_6WO_{12}	$3Lu_2O_3{\cdot}WO_3$	Sol	[83]	393.75	378.08	−3.98				
195	$Mg_2Al_4Si_5O_{18}$	$2MgO{\cdot}2Al_2O_3{\cdot}5SiO_2$	Sol	[1]	452.38	454.64	0.50	478.84	5.85	449.19	−0.71
196	Mg_2SiO_4	$2MgO{\cdot}SiO_2$	Sol	[6]	118.43	118.94	0.43	117.66	−0.65	118.57	0.12

Table 5 (*Continued*)

No.	Mixed oxide	Binary oxides combination	Phase	Reference	$C^{\circ}_{pm}(298)$ ($J\,K^{-1}\,mol^{-1}$)	$C^{\circ}_{pm}(298)(NKR)$ ($J\,K^{-1}\,mol^{-1}$)	ΔC°_{pm} (%)	$C^{\circ}_{pm}(298)(KK)$ ($J\,K^{-1}\,mol^{-1}$)	ΔC°_{pm} (%)	$C^{\circ}_{pm}(298)(BB)$ ($J\,K^{-1}\,mol^{-1}$)	ΔC°_{pm} (%)
197	Mg_2TiO_4	$2MgO{\cdot}TiO_2$	Sol	[6]	128.17	129.62	1.13	131.84	2.87	130.06	1.48
198	$Mg_3Al_2Si_3O_{12}$	$3MgO{\cdot}Al_2O_3{\cdot}3SiO_2$	Sol	[1]	324.76	324.05	−0.22	333.32	2.64	321.19	−1.10
199	$MgAl_2O_4$	$MgO{\cdot}Al_2O_3$	Sol	[6]	115.96	116.27	0.27	118.18	1.92	114.72	−1.07
200	$MgAl_2SiO_6$	$MgO{\cdot}Al_2O_3{\cdot}SiO_2$	Sol	[15]	160.27	160.69	0.26			158.67	−1.00
201	$MgCr_2O_4$	$MgO{\cdot}Cr_2O_3$	Sol	[6]	126.80	151.52	19.50	145.00	14.36		
202	$MgFe_2O_4$	$MgO{\cdot}Fe_2O_3$	Sol	[1]	142.94	142.03	−0.64	145.72	1.94	142.48	−0.32
203	$MgRh_2O_4$	$MgO{\cdot}Rh_2O_3$	Sol	[103]	129.84	126.38	−2.66				
204	$MgSiO_3$	$MgO{\cdot}SiO_2$	Sol-A	[6]	81.90	81.68	−0.27	82.59	0.84	81.26	−0.78
205	$MgTa_2O_6$	$MgO{\cdot}Ta_2O_5$	Sol	[67]	175.73	168.74	−3.98				
206	$MgTi_2O_5$	$MgO{\cdot}2TiO_2$	Sol	[6]	146.64	147.46	0.56	144.35	−1.56	148.19	1.06
207	$MgTiO_3$	$MgO{\cdot}TiO_2$	Sol	[6]	91.19	92.36	1.28	94.11	3.20	92.75	1.71
208	$MgUO_4$	$MgO{\cdot}UO_3$	Sol	[6]	156.51	118.45	−24.32	126.77	−19.00		
209	MgV_2O_6	$MgO{\cdot}V_2O_5$	Sol	[6]	156.35	164.63	5.30	162.74	4.09		
210	$MgWO_4$	$MgO{\cdot}WO_3$	Sol	[6]	109.89	110.06	0.16	117.15	6.61		
211	$Mn_2Al_4Si_5O_{18}$	$2MnO{\cdot}2Al_2O_3{\cdot}5SiO_2$	Sol	[15]	462.33	469.64	1.58	486.38	5.20		
212	$Mn_2Mo_3O_8$	$2MnO{\cdot}3MoO_2$	Sol	[104]	245.90	257.49	4.71				
213	Mn_2SiO_4	$2MnO{\cdot}SiO_2$	Sol	[6]	129.87	133.94	3.13	125.20	−3.60		
214	Mn_2TiO_4	$2MnO{\cdot}TiO_2$	Sol	[6]	144.60	144.62	0.01	139.38	−3.61		
215	$Mn_3Al_2Si_3O_{12}$	$3MnO{\cdot}Al_2O_3{\cdot}3SiO_2$	Sol	[15]	340.30	346.55	1.84	344.63	1.27		
216	Mn_3O_4	$MnO{\cdot}Mn_2O_3$	Tetra	[6]	140.53	143.80	2.33				
217	$MnMoO_4$	$MnO{\cdot}MoO_3$	Sol	[104]	115.77	119.90	3.57	116.20	0.37		
218	$MnSiO_3$	$MnO{\cdot}SiO_2$	Sol	[6]	86.39	89.18	3.23	86.36	−0.04		
219	$MnTiO_3$	$MnO{\cdot}TiO_2$	Sol	[6]	99.83	99.86	0.03	97.88	−1.95		
220	$MnWO_4$	$MnO{\cdot}WO_3$	Sol	[6]	124.08	117.56	−5.25	120.92	−2.55		
221	$Na_2B_4O_7$	$Na_2O{\cdot}2B_2O_3$	Sol	[6]	186.92	194.52	4.07	186.14	−0.42		
222	NaB_3O_5	$(Na_2O{\cdot}3B_2O_3)/2$	Sol	[6]	121.84	128.75	5.67				
223	$Na_2B_8O_{13}$	$Na_2O{\cdot}4B_2O_3$	Sol	[6]	304.89	320.48	5.11				
224	Na_2CrO_4	$Na_2O{\cdot}CrO_3$	Sol-A	[6]	142.78	147.68	3.43	144.15	0.96		
225	$Na_2Mo_2O_7$	$Na_2O{\cdot}2MoO_3$	Sol	[6]	216.67	218.84	1.00				
226	Na_2MoO_4	$Na_2O{\cdot}MoO_3$	Sol-A	[6]	141.46	143.70	1.58	144.65	2.26		
227	$Na_2Si_2O_5$	$Na_2O{\cdot}2SiO_2$	Sol-A	[6]	156.50	157.40	0.57	158.67	1.39	157.08	0.37
228	Na_2SiO_3	$Na_2O{\cdot}SiO_2$	Sol	[6]	111.81	112.98	1.04	114.81	2.68	113.13	1.18
229	$Na_2Ti_2O_5$	$Na_2O{\cdot}2TiO_2$	Sol	[6]	193.13	178.76	−7.44	176.57	−8.57	180.06	−6.77
230	$Na_2Ti_3O_7$	$Na_2O{\cdot}3TiO_2$	Sol	[1]	249.66	233.86	−6.33			235.50	−5.67
231	$Na_2Ti_6O_{13}$	$Na_2O{\cdot}6TiO_2$	Sol	[105]	397.23	399.16	0.49			401.82	1.16
232	Na_2TiO_3	$Na_2O{\cdot}TiO_2$	Sol-A	[1]	126.77	123.66	−2.45	126.33	−0.35	124.62	−1.70
233	$Na_2U_2O_7$	$Na_2O{\cdot}2UO_3$	Sol-A	[106]	227.26	230.94	1.62				
234	Na_2UO_4	$Na_2O{\cdot}UO_3$	Sol-A	[6]	146.74	149.75	2.05	158.99	8.35		
235	Na_2WO_4	$Na_2O{\cdot}WO_3$	Sol-A	[6]	141.77	141.36	−0.29	149.37	5.36		
236	$Na_2W_2O_7$	$Na_2O{\cdot}2WO_3$	Sol	[107]	214.22	214.16	−0.03				

Table 5 (*Continued*)

No.	Mixed oxide	Binary oxides combination	Phase	Reference	$C^{\circ}_{pm}(298)$ ($J\,K^{-1}\,mol^{-1}$)	$C^{\circ}_{pm}(298)$(NKR) ($J\,K^{-1}\,mol^{-1}$)	ΔC°_{pm} (%)	$C^{\circ}_{pm}(298)$(KK) ($J\,K^{-1}\,mol^{-1}$)	ΔC°_{pm} (%)	$C^{\circ}_{pm}(298)$(BB) ($J\,K^{-1}\,mol^{-1}$)	ΔC°_{pm} (%)
237	$Na_2W_4O_{13}$	$Na_2O{\cdot}4WO_3$	Sol	[107]	354.45	359.76	1.50				
238	Na_2ZrO_3	$Na_2O{\cdot}ZrO_2$	Sol-A	[6]	131.20	124.77	−4.90	126.94	−3.25		
239	Na_4SiO_4	$2Na_2O{\cdot}SiO_2$	Sol	[6]	184.72	181.54	−1.72	182.10	−1.42	182.31	−1.30
240	$NaAlO_2$	$(Na_2O{\cdot}Al_2O_3)/2$	Sol-A	[6]	73.52	73.79	0.36	75.23	2.33	73.30	−0.30
241	$NaAlSi_2O_6$	$(Na_2O{\cdot}Al_2O_3{\cdot}4SiO_2)/2$	Sol	[6]	159.88	162.63	1.72	171.46	7.25	161.20	0.83
242	$NaAlSi_3O_8$	$(Na_2O{\cdot}Al_2O_3{\cdot}6SiO_2)/2$	Sol-A	[6]	204.85	207.05	1.07	215.32	5.11	205.15	0.15
243	$NaAlSiO_4$	$(Na_2O{\cdot}Al_2O_3{\cdot}2SiO_2)/2$	Sol	[8]	115.81	118.21	2.07	123.94	7.02	117.25	1.24
244	$NaBO_2$	$(Na_2O{\cdot}B_2O_3)/2$	Sol	[6]	65.85	65.77	−0.12	67.13	1.94		
245	$NaCrO_2$	$(Na_2O{\cdot}Cr_2O_3)/2$	Sol	[6]	89.41	91.41	2.24	88.61	−0.89		
246	$NaFeSi_2O_6$	$(Na_2O{\cdot}Fe_2O_3{\cdot}4SiO_2)/2$	Sol	[1]	170.17	175.51	3.14	177.74	4.45	175.08	2.89
247	$NaUO_3$	$(Na_2O{\cdot}UO_2{\cdot}UO_3)/2$	Sol	[108]	108.87	106.67	−2.02				
248	Nd_2NiO_4	$Nd_2O_3{\cdot}NiO$	Sol	[109]	160.22	155.63	−2.86				
249	Nd_3NbO_7	$(3Nd_2O_3{\cdot}Nb_2O_5)/2$	Sol	[74]	243.89	233.08	−4.44				
250	$NdAlO_3$	$(Nd_2O_3{\cdot}Al_2O_3)/2$	Sol	[110]	97.05	95.18	−1.93	92.00	−5.20		
251	$NdCrO_3$	$(Nd_2O_3{\cdot}Cr_2O_3)/2$	Sol	[75]	106.48	112.80	5.94				
252	$NdGaO_3$	$(Nd_2O_3{\cdot}Ga_2O_3)/2$	Sol	[111]	105.80	102.60	−3.02				
253	Ni_2SiO_4	$2NiO{\cdot}SiO_2$	Sol	[6]	127.02	133.00	4.71	133.56	5.15		
254	$NiTa_2O_6$	$NiO{\cdot}Ta_2O_5$	Sol	[67]	171.15	175.77	2.70				
255	$NiTiO_3$	$NiO{\cdot}TiO_2$	Sol	[6]	99.25	99.39	0.14	102.06	2.83		
256	Pb_2SiO_4	$2PbO{\cdot}SiO_2$	Sol-A	[6]	136.92	135.90	−0.74	131.90	−3.67		
257	Pb_3O_4	$PbO{\cdot}Pb_2O_3$	Sol	[6]	154.94						
258	Pb_4SiO_6	$4PbO{\cdot}SiO_2$	Sol	[6]	229.73	227.38	−1.02				
259	$PbSiO_3$	$PbO{\cdot}SiO_2$	Sol	[6]	89.13	90.16	1.16	89.71	0.66		
260	$PbTiO_3$	$PbO{\cdot}TiO_2$	Sol-A	[6]	104.40	100.84	−3.41	101.23	−3.04		
261	$PbWO_4$	$PbO{\cdot}WO_3$	Sol	[6]	119.64	118.54	−0.92	124.27	3.87		
262	Pr_2NiO_4	$Pr_2O_3{\cdot}NiO$	Sol	[95]	165.46	160.92	−2.74				
263	Pr_3NbO_7	$(3Pr_2O_3{\cdot}Nb_2O_5)/2$	Sol	[74]	250.21	241.01	−3.68				
264	$PrCrO_3$	$(Pr_2O_3{\cdot}Cr_2O_3)/2$	Sol	[75]	108.92	115.45	6.00				
265	$Rb_2Cr_2O_7$	$Rb_2O{\cdot}2CrO_3$	Sol	[112]	230.17	*236.94*	*2.94*				
266	$Rb_2Mo_2O_7$	$Rb_2O{\cdot}2MoO_3$	Sol	[70]	209.72	*228.98*	*9.18*				
267	$Rb_2Si_2O_5$	$Rb_2O{\cdot}2SiO_2$	Sol	[6]	170.72	*167.54*	*−1.86*	159.51	−6.56		
268	$Rb_2Si_4O_9$	$Rb_2O{\cdot}4SiO_2$	Sol	[6]	270.89	*256.38*	*−5.36*				
269	Rb_2SiO_3	$Rb_2O{\cdot}SiO_2$	Sol	[6]	117.45	*123.12*	*4.83*	115.65	−1.53		
270	$Rb_2U_2O_7$	$Rb_2O{\cdot}2UO_3$	Sol	[72]	258.24	*241.08*	*−6.65*				
271	$RbAlO_2$	$(Rb_2O{\cdot}Al_2O_3)/2$	Sol	[72]	77.31	*78.86*	*1.99*	75.62	−2.19		
272	$RbBO_2$	$(Rb_2O{\cdot}B_2O_3)/2$	Sol	[6]	73.46	*70.84*	*−3.57*	67.55	−8.05		
273	$ScMnO_3$	$(Sc_2O_3{\cdot}Cr_2O_3)/2$	Sol	[113]	102.40	96.49	−5.77				
274	$Sm_3Fe_5O_{12}$	$(3Sm_2O_3{\cdot}5Fe_2O_3)/2$	Sol	[114]	447.10	435.66	−2.56				
275	Sm_3NbO_7	$(3Sm_2O_3{\cdot}Nb_2O_5)/2$	Sol	[74]	240.06	239.80	−0.11				
276	$SmCrO_3$	$(Sm_2O_3{\cdot}Cr_2O_3)/2$	Sol	[75]	101.62	115.04	13.21				

Table 5 (*Continued*)

No.	Mixed oxide	Binary oxides combination	Phase	Reference	$C^{\circ}_{pm}(298)$ ($J\,K^{-1}\,mol^{-1}$)	$C^{\circ}_{pm}(298)(NKR)$ ($J\,K^{-1}\,mol^{-1}$)	ΔC°_{pm} (%)	$C^{\circ}_{pm}(298)(KK)$ ($J\,K^{-1}\,mol^{-1}$)	ΔC°_{pm} (%)	$C^{\circ}_{pm}(298)(BB)$ ($J\,K^{-1}\,mol^{-1}$)	ΔC°_{pm} (%)
277	$SmNiO_3$		Sol	[115]	110.58						
278	Sr_2CuO_3	$2SrO{\cdot}CuO$	Sol	[116]	134.87	132.56	−1.71				
279	Sr_2SiO_4	$2SrO{\cdot}SiO_2$	Sol	[6]	130.80	134.72	3.00	129.38	−1.08		
280	Sr_2TiO_4	$2SrO{\cdot}TiO_2$	Sol	[6]	143.68	145.40	1.19	143.56	−0.09		
281	$Sr_3MgSi_2O_8$	$3SrO{\cdot}MgO{\cdot}2SiO_2$	Sol	[117]	257.35	261.55	1.63	252.90	−1.73		
282	$Sr_3U_{11}O_{33}$	$3SrO{\cdot}3UO_2{\cdot}8UO_3$	Sol	[118]	1064.20	975.74	−8.31				
283	$Sr_3U_2O_9$	$3SrO{\cdot}2UO_3$	Sol	[118]	301.80	297.83	−1.32				
284	$Sr_4Ti_3O_{10}$	$4SrO{\cdot}3TiO_2$	Sol	[6]	341.89	345.90	1.17	343.50	0.47		
285	$Sr_{14}Cu_{24}O_{41}$		Sol	[116]	1730.76						
286	$SrAl_2O_4$	$SrO{\cdot}Al_2O_3$	Sol-A	[6]	119.03	124.16	4.31	124.04	4.21		
287	$SrAl_2Si_2O_8$	$SrO{\cdot}Al_2O_3{\cdot}2SiO_2$	Sol	[50]	221.22	213.00	−3.71	221.52	0.14		
288	$SrCeO_3$	$SrO{\cdot}CeO_2$	Sol	[119]	108.87	106.68	−2.01				
289	$SrCuO_2$	$SrO{\cdot}CuO$	Sol	[116]	86.75	87.41	0.76				
290	$SrMnO_3$	$SrO{\cdot}MnO_2$	Sol	[80]	108.73	99.57	−8.43				
291	$SrMoO_4$	$SrO{\cdot}MoO_3$	Sol	[6]	117.06	120.29	2.76	118.29	1.05		
292	$SrSiO_3$	$SrO{\cdot}SiO_2$	Sol	[120]	89.61	89.57	−0.04	88.45	−1.29		
293	$SrTiO_3$	$SrO{\cdot}TiO_2$	Sol	[6]	99.10	100.25	1.16	99.97	0.87		
294	$SrWO_4$	$SrO{\cdot}WO_3$	Sol	[6]	131.43	117.95	−10.26	123.01	−6.41		
295	$SrZrO_3$	$SrO{\cdot}ZrO_2$	Sol	[37]	103.43	101.36	−2.00	100.58	−2.76		
296	$SrZrSi_2O_7$	$SrO{\cdot}ZrO_2{\cdot}2SiO_2$	Sol	[121]	187.81	190.20	1.27	190.64	1.51		
297	$Tb_3Fe_5O_{12}$	$(3Tb_2O_3{\cdot}5Fe_2O_3)/2$	Sol	[122]	444.40	*425.28*	*−4.30*				
298	Tb_3NbO_7	$(3Tb_2O_3{\cdot}Nb_2O_5)/2$	Sol	[74]	243.48	*229.42*	*−5.78*				
299	$TbFeO_3$	$(Tb_2O_3{\cdot}Fe_2O_3)/2$	Sol	[123]	105.02	*106.84*	*1.73*				
300	$Tl_2Ba_2Ca_2Cu_3O_{10}$	$Tl_2O_3{\cdot}2BaO{\cdot}2CaO{\cdot}3CuO$	Sol	[124]	430.73	411.20	−4.53				
301	$Tl_2Ba_2CaCu_2O_8$	$Tl_2O_3{\cdot}2BaO{\cdot}CaO{\cdot}2CuO$	Sol	[124]	338.70	326.52	−3.60				
302	$Tl_{2.1}Ba_2CaCu_2O_{8.15}$	$1.05\ Tl_2O_3{\cdot}2BaO{\cdot}CaO{\cdot}2CuO$	Sol	[125]	339.56	331.79	−2.29				
303	$Tl_2Ba_2CuO_6$	$Tl_2O_3{\cdot}2BaO{\cdot}CuO$	Sol	[124]	249.37	241.84	−3.02				
304	$Tm_3Fe_5O_{12}$	$(3Tm_2O_3{\cdot}5Fe_2O_3)/2$	Sol	[82]	458.98	437.01	−4.79				
305	Tm_3NbO_7	$(3Tm_2O_3{\cdot}Nb_2O_5)/2$	Sol	[74]	245.52	241.15	−1.78				
306	$TmBa_2Cu_3O_7$		Sol	[126]	288.80						
307	$Y_2Cu_2O_5$	$Y_2O_3{\cdot}2CuO$	Sol	[127]	187.04	187.03	−0.01				
308	$Y_3Al_5O_{12}$	$(3Y_2O_3{\cdot}5Al_2O_3)/2$	Sol	[128]	348.13	351.29	0.91	358.54	2.99		
309	$Y_3Fe_5O_{12}$	$(3Y_2O_3{\cdot}5Fe_2O_3)/2$	Sol	[123]	426.77	415.69	−2.60				
310	Y_3NbO_7	$(3Y_2O_3{\cdot}Nb_2O_5)/2$	Sol	[74]	224.85	219.83	−2.23				
311	Yb_3NbO_7	$(3Yb_2O_3{\cdot}Nb_2O_5)/2$	Sol	[74]	245.21	239.11	−2.49				
312	$YBa_2Cu_3O_{6.7}$		Sol	[129]	285.80						
313	$YBa_2Cu_3O_{6.85}$		Sol	[129]	285.80						

Table 5 (*Continued*)

No.	Mixed oxide	Binary oxides combination	Phase	Reference	$C^{\circ}_{pm}(298)$ ($J\,K^{-1}\,mol^{-1}$)	$C^{\circ}_{pm}(298)$(NKR) ($J\,K^{-1}\,mol^{-1}$)	ΔC°_{pm} (%)	$C^{\circ}_{pm}(298)$(KK) ($J\,K^{-1}\,mol^{-1}$)	ΔC°_{pm} (%)	$C^{\circ}_{pm}(298)$(BB) ($J\,K^{-1}\,mol^{-1}$)	ΔC°_{pm} (%)
314	$YBa_2Cu_3O_{6.9}$		Sol	[130]	282.25						
315	$YBa_2Cu_3O_{6.96}$		Sol	[131]	281.20						
316	$YBa_2Cu_4O_8$		Sol	[130]	320.10						
317	$YbMnO_3$	$(Yb_2O_3{\cdot}Mn_2O_3)/2$	Sol	[132]	108.70	107.20	−1.38				
318	$YCrO_3$	$(Y_2O_3{\cdot}Cr_2O_3)/2$	Sol	[75]	97.21	108.39	11.50				
319	$YMnO_3$	$(Y_2O3{\cdot}Mn_2O_3)/2$	Sol	[132]	98.37	100.78	2.45				
320	Zn_2SiO_4	$2ZnO{\cdot}SiO_2$	Sol	[6]	121.83	126.56	3.88	121.86	0.02		
321	Zn_2TiO_4	$2ZnO{\cdot}TiO_2$	Sol	[6]	137.33	137.24	−0.06	136.04	−0.94		
322	$ZnFe_2O_4$	$ZnO{\cdot}Fe_2O_3$	Sol	[6]	137.33	145.84	6.19	147.82	7.64		
323	$ZnMn_2O_4$	$ZnO{\cdot}Mn_2O_3$	Sol	[133]	140.30	140.11	−0.14				
324	$ZnWO_4$	$ZnO{\cdot}WO_3$	Sol	[6]	125.50	113.87	−9.27	119.25	−4.98		
325	$ZrTiO_4$	$ZrO_2{\cdot}TiO2$	Sol	[134]	114.03	111.31	−2.39	116.37	2.05		
326	$ZrSiO_4$	$ZrO_2{\cdot}SiO_2$	Sol	[6]	98.57	100.63	2.09	102.19	3.67		

assumption that the predominant contribution to C°_{pm} of solids results from the lattice vibrational contribution and does not practically alter during the solid state reaction between the constituent compounds. On the contrary, the translational and, in case of polyatomic molecules, also rotational contributions dominate in gaseous state.

The average error of the estimated values was found 3.3%, whereas for 74 substances (25%) the error did not exceed 1%.

3.3. Kellogg's method

From the ionic contributions proposed by Spencer [18], the values of $C^{\circ}_{pm}(298.15\,\mathrm{K})$ were estimated for 169 mixed oxides with the average error of 3.1%, whereas for 47 substances (28%) the error did not exceed 1%. The accuracy of this method is comparable to that of the NKR—using the same set of substances the average error of the NKR was 3.2% and for 44 compounds did not exceed 1%. As to the universality, the NKR is better than the KK. Indeed, the KK is inapplicable almost for one half of mixed oxides included in the primary set.

3.4. Berman and Brown's method (BB)

Using the BB method the coefficients of $C^{\circ}_{pm}(T)$ dependence in Eq. (7) were estimated and the values of $C^{\circ}_{pm}(298.15\,\mathrm{K})$ for 68 mixed oxides were evaluated with the average error of 1.5%. For 31 compounds (46%), the error did not exceed 1%. The higher accuracy than for the NKR (average error 2.2% with the same set) is due to smaller universality of the BB method, which is applicable only for the one fifth of substances from the primary set.

4. Influence of C°_{pm} estimation error on the results of equilibrium calculations

Let us consider the formation reaction of the mixed oxide $RE_2Cu_2O_5$ (RE, rare earth element) in order to demonstrate the influence of molar heat capacity error on the results of equilibrium calculations. The reaction from binary oxides is described by the equation

$$2\,CuO(s) + Ln_2O_3(s) \rightarrow Ln_2Cu_2O_5(s) \qquad (R4)$$

As all involved substances are single-species phases, they can all coexist at certain equilibrium temperature, at which $\Delta G^{\circ}{}_{r}$ (further denoted $\Delta G^{\circ}(ox)$) is equal zero. Since in general

$$\Delta G^{\circ}_{r} = \Delta H^{\circ}_{r} - T\Delta S^{\circ}_{r} \qquad (8)$$

this equilibrium temperature is given by the relation

$$T_{eq} = \frac{\Delta H^{\circ}(ox)}{\Delta S^{\circ}(ox)} \qquad (9)$$

The standard enthalpy and entropy, $\Delta H^{\circ}(ox)$ and $\Delta S^{\circ}(ox)$, respectively, of reaction (R4) are temperature dependent:

$$\Delta H^{\circ}(ox) = \Delta H^{\circ}(ox)(298.15\,\mathrm{K}) + \int_{298}^{T} \Delta C^{\circ}_{pm}(ox)\,dT \qquad (10)$$

$$\Delta S^{\circ}(ox) = \Delta S^{\circ}(ox)(298.15\,\mathrm{K}) + \int_{298}^{T} \frac{\Delta C^{\circ}_{pm}(ox)}{T}\,dT \qquad (11)$$

For the numerical calculation, the experimental data for $Yb_2Cu_2O_5$ reported by Jacob et al. [46] will be employed. The standard Gibbs energy of reaction (R4) has been obtained from the EMF measurements with solid electrolyte in the form of the linear temperature dependence

$$\Delta G^{\circ}(ox) = 9920 - 13.90T(J)$$
$$(T = 970\text{–}1323\,\mathrm{K}) \qquad (12)$$

The comparison with Eq. (8) yields for $Yb_2Cu_2O_5$ the values of $\Delta H^{\circ}(ox) = 9920$ J and $\Delta S^{\circ}(ox) = 13.9$ J. mol which can be assigned to the mean temperature of 1146.5 K. Under the assumption of both $\Delta H^{\circ}(ox)$ and $\Delta S^{\circ}(ox)$ being independent of temperature, i.e. $\Delta C^{\circ}_{pm}(ox) = 0$, the equilibrium temperature of $T_{eq} = 714$ K can be calculated from Eq. (9). For more precise calculation, the temperature dependencies of both $\Delta H^{\circ}(ox)$ and $\Delta S^{\circ}(ox)$ (Eqs. (10) and (11), respectively) are to be considered. As the experimental C°_{pm} data for $Yb_2Cu_2O_5$ are not available we have no choice but to use the estimated value. If we use the NKR $C^{\circ}_{pm}(Yb_2Cu_2O_5)(298.15\,\mathrm{K}) = 199.9\,\mathrm{J\,K^{-1}\,mol^{-1}}$ with the average estimation error 3.3%. We can expect $\Delta C^{\circ}_{pm}(ox)$ to fall in the interval $\langle -6.6; 6.6\rangle\,\mathrm{J\,K^{-1}\,mol^{-1}}$. Then, if $\Delta C^{\circ}_{pm}(ox)$ is temperature independent we obtain $T_{eq} = 750$ K and $T_{eq} = 654$ K

for the ultimate values of $\Delta C^{\circ}_{pm}(\mathrm{ox}) = 6.6$ and $-6.6\ \mathrm{J\ K^{-1}\ mol^{-1}}$, respectively.

5. Conclusions

The detailed assessment of three selected empirical methods applicable for prediction of heat capacities of mixed oxides revealed that the NKR can be used for rough estimates of $C^{\circ}_{pm}(298.15\ \mathrm{K})$. This method is highly universal, but in many cases the estimation error can exceed 5% (60 from 278 tested oxides), which is not acceptable in some types of thermodynamic calculations. More accurate values can be obtained using methods based on the individual contributions of binary oxides forming a given mixed oxide. The universality of such an approach is in the first place due to the extent of the evaluated contribution set. For instance, from the file of contributions assessed by Berman and Brown, a number of heat capacities of silicates and other oxide minerals can be predicted. The mean accuracy of such estimates is nearly comparable with experimental errors of DSC or drop calorimetry measurements of heat capacity. Thus a further extension and generalization of this method to other mixed oxide families like high-temperature oxide superconductors and related mixed oxides seem to be very promising. However, the oxygen non-stoichiometry of some phases will have to be taken into account (see Eq. (R3)) by evaluating the oxygen or O^{2-} anion contribution.

Acknowledgements

This work was supported by the Grant Agency of the Czech Republic, Grant No. 106/00/0568.

References

[1] R.G. Berman, T.H. Brown, Contrib. Mineral. Petrol. 89 (1985) 168.
[2] O. Kubaschewski, High Temp.—High Press. 4 (1972) 1.
[3] V.P. Glushko, L.V. Gurvich, G.A. Bergman, I.V. Veic, V.A. Medvedev, G.A. Khachkuruzov, V.S. Yungman, Thermodynamic Properties of Individual Substances, Tom I–IV, Nauka, Moskva, 1978–1982 (in Russian).
[4] L.B. Pankratz, Thermodynamic Properties of Elements and Oxides, Bulletin 672, US Bureau of Mines, Washington, 1982.
[5] I.S. Kulikov, Thermodynamics of Oxides, Metallurgiya, Moscow, 1986 (in Russian).
[6] O. Knacke, O. Kubaschewski, K. Hesselmann, Thermochemical Properties of Inorganic Substances, 2nd Edition, Springer, Berlin, 1991.
[7] O. Kubaschewski, C.B. Alcock, P.J. Spencer, Materials Thermochemistry, 6th Edition, Pergamon Press, Oxford, 1993.
[8] I. Barin, Thermochemical Data of Pure Substances, 3rd Edition, Wiley/VCH, Weinheim, 1995.
[9] M.W. Chase, Jr. (Ed.), NIST-JANAF Thermochemical Tables, 4th Edition, J. Phys. Chem. Ref. Data, Monograph No. 9, 1998.
[10] R.G. Berman, J. Petrol. 29 (1988) 445.
[11] T.J.B. Holland, R. Powel, J. Metamorphic Geol. 8 (1990) 89.
[12] S.K. Saxena, N. Chatterjee, Y. Fei, G. Shen, Thermodynamic Data on Oxides and Silicates, Springer, Berlin, 1993.
[13] R.A. Robie, B.S. Hemingway, Thermodynamic Properties of Minerals and Related Substances at 298.15 K and 1 bar Pressure and at Higher Temperatures, US Government and Printing Office, Washington 1995.
[14] M. Gottschalk, Eur. J. Miner. 9 (1997) 175.
[15] T.J.B. Holland, R. Powell, J. Metamorph. Geol. 16 (1998) 309.
[16] N.D. Chatterjee, R. Kruger, G. Haller, W. Olbricht, Contrib. Mineral. Petrol. 133 (1998) 149.
[17] G.K. Moiseev, J. Šesták, Prog. Cryst. Growth Charact. 30 (1995) 23.
[18] P.J. Spencer, Thermochim. Acta 314 (1998) 1.
[19] J. Leitner, P. Chuchvalec, D. Sedmidubský, Chem. Listy 95 (2001) 2.
[20] H.C. Helgeson, J.M. Delany, H.W. Nesbitt, D.K. Bird, Am. J. Sci. A 278 (1978) 1.
[21] K. Ukleba, G. Gvelesiani, J. Baratashvili, D. Tsagareishvili, J. Omiadze, A. Nadiradze, Bull. Georgian Acad. Sci. 156 (1997) 66.
[22] H.H. Kellogg, in: G.R. Fitterer (Ed.), Applications of Fundamental Thermodynamics to Metallurgical Processes, Gordon and Breach, London, 1967, p. 357.
[23] O. Kubaschewski, H. Ünal, High Temp.—High Press. 9 (1977) 361.
[24] V.N. Kumok, Problem of Correlation Methods for Evaluation of Thermodynamic Characteristics, Direct and Reverse Tasks of Chemical Thermodynamics, Nauka, Novosibirsk, 1987, p. 108 (in Russian).
[25] G.R. Robinson Jr., J.L. Haas Jr., Am. Miner. 68 (1983) 541.
[26] G.F. Voronin, I.A. Uspenskaya, Zh. Fiz. Khim. 71 (1997) 1927.
[27] O.Yu. Goncharov, Yu.P. Vorobev, Zh. Fiz. Khim. 73 (1999) 23.
[28] A.S. Pashinkin, A.S. Malkova, A.A. Ivanov, Neorg. Mater. 31 (1995) 1604.
[29] A.S. Malkova, A.S. Pashinkin, Neorg. Mater. 28 (1993) 240.
[30] M.K. Aldabergenov, G.T. Balakaeva, Zh. Fiz. Khim. 67 (1993) 425.
[31] M.K. Aldabergenov, G.T. Balakaeva, G.T. Kokibasova, Zh. Fiz. Khim. 72 (1998) 808.

[32] G.G. Gospodinov, D.I. Mihov, J. Chem. Thermodyn. 25 (1993) 1249.
[33] G.G. Gospodinov, J. Chem. Thermodyn. 26 (1994) 143.
[34] G.G. Gospodinov, J. Chem. Thermodyn. 26 (1994) 713.
[35] G.G. Gospodinov, J. Chem. Thermodyn. 26 (1994) 1111.
[36] G.G. Gospodinov, V.M. Marchev, Thermochim. Acta 222 (1993) 137.
[37] M.E. Huntelaar, E.H.P. Cordfunke, R.R. van der Laan, Thermochim. Acta 274 (1996) 101.
[38] K. Gavritchev, Thermochim. Acta 343 (2000) 63.
[39] B.K. Kasenov, M.A. Mukhanova, Sh.B. Kasenova, E.S. Mustafin, Zh. Fiz. Khim. 70 (1996) 24.
[40] Sh.B. Kasenova, B.K. Kasenov, E.S. Mustafin, M.K. Aldabergenov, Zh. Fiz. Khim. 71 (1997) 751.
[41] E.S. Mustafin, A.T. Oralova, B.K. Kasenov, Neorg. Mater. 30 (1994) 863.
[42] E.S. Mustafin, A.T. Oralova, B.K. Kasenov, Inorg. Mater. 31 (1995) 914.
[43] A.T. Oralova, B.K. Kasenov, M.M. Mataev, B.Z. Nurgaliev, Zh. Fiz. Khim. 70 (1996) 944.
[44] A.T. Oralova, E.S. Mustafin, B.K. Kasenov, Inorg. Mater. 32 (1996) 111.
[45] A.T. Oralova, B.K. Kasenov, E.S. Mustafin, High Temp. 34 (1996) 645.
[46] K.T. Jacob, T. Mathews, J.P. Hajra, High Temp. Mater. Processes 12 (1993) 251.
[47] P.G. Hall, D.A. Armitage, R.G. Linford, J. Chem. Thermodyn. 17 (1985) 657.
[48] E.H.P. Cordfunke, R.J.M. Konings, R.R. van der Laan, W. Ouweltjes, J. Chem. Thermodyn. 25 (1993) 343.
[49] N.F. Menshenina, A.A. Evdokimov, A.N. Klimenko, Zh. Neorg. Khim. 30 (1985) 568.
[50] I.V. Chernyshova, Yu.V. Semenov, V.M. Agoshov, M. Gambino, P. Gaune, J.P. Bros, Thermochim. Acta 175 (1991) 119.
[51] M.J. Scholten, J. Schoonman, J.C. van Miltenburg, E.H.P. Cordfunke, Thermochim. Acta 268 (1995) 161.
[52] K.S. Gavrichev, V.E. Gorbunov, L.N. Golushina, G.E. Nikiforova, G.A. Totrova, I.S. Shaplygin, Neorg. Mater. 29 (1993) 645.
[53] Yu.F. Minekov, N.I. Matskevich, Yu.G. Stenin, P.P. Samoilov, Thermochim. Acta 278 (1996) 1.
[54] E.H.P. Cordfunke, R.J.M. Konings (Eds.), Thermochemical Data for Reactor Materials and Fission Products, Elsevier, Amsterdam, 1990.
[55] M.E. Huntelaar, E.H.P. Cordfunke, G.D. Elzinga, R.R. van der Laan, J. Chem. Thermodyn. 32 (2000) 671.
[56] P. Abrman, D. Sedmidubský, A. Strejc, P. Voňka, J. Leitner, Thermochim. Acta 381 (2002) 1.
[57] M. Castro, R. Burriel, R. Ibanez, S. Fernando, IEEE Trans. Magn. 30 (1994) 1163.
[58] J. Leitner, D. Sedmidubský, A. Strejc, P. Abrman, B. Doušová, M. Nevřiva, in: B. Taraba (Ed.), Proceedings of the Calorim. Seminar 2000, University Ostrava, Ostrava, 2000, p. 9 (in Czech).
[59] K.S. Gavrichev, V.E. Gorbunov, I.A. Konovalova, V.B. Lazarev, E.A. Tishchenko, I.S. Shaplygin, Izv. Akad. Nauk SSSR, Neorg. Mater. 26 (1990) 1102.
[60] J.R. Taylor, A.T. Dinsdale, CALPHAD 14 (1990) 71.
[61] A.S. Malkova, A.S. Pashinkin, Neorg. Mater. 28 (1993) 240.
[62] M.Y. Lee, C.L. Nassaralla, Thermochim. Acta 371 (2001) 1.
[63] R.L. Putnam, A. Navrotsky, B.F. Woodfield, J.L. Shapiro, R. Stevens, J. Boerio-Goates, Mat. Res. Soc. Symp. Proc. 556 (1999) 11.
[64] B.F. Woodfield, J. Boerio-Goates, J.L. Shapiro, R.L. Putnam, A. Navrotsky, J. Chem. Thermodyn. 31 (1999) 245.
[65] M. Bolech, E.H.P. Cordfunke, A.C.G. van Genderen, R.R. van der Laan, F.J.J.G. Janssen, J.C. van Miltenburg, Thermochim. Acta 284 (1996) 253.
[66] M. Bolech, E.H.P. Cordfunke, A.C.G. van Genderen, R.R. van der Laan, F.J.J.G. Janssen, J.C. van Miltenburg, J. Phys. Chem. Solids 58 (1997) 433.
[67] M.A. White, G. Neshvad, J. Chem. Thermodyn. 23 (1991) 455.
[68] J.R. Taylor, A.T. Dinsdale, Z. Metallkd. 81 (1990) 354.
[69] E.H.P. Cordfunke, R.R. van der Laan, E.F. Westrum Jr., J. Chem. Thermodyn. 24 (1992) 815.
[70] R. Kohli, Thermochim. Acta 237 (1994) 241.
[71] R.P.C. Schram, V.M. Smit-Groen, E.H.P. Cordfunke, J. Chem. Thermodyn. 31 (1999) 43.
[72] R. Kohli, J. Therm. Anal. 49 (1997) 1321.
[73] T.B. Mirianashvili, T.A. Pavleniashvili, V.S. Varazashvili, D.I. Khutsishvili, M.S. Tsarakhov, G.D. Chachanidze, D.Sh. Tsagareishvili, Neorg. Mater. 29 (1993) 876.
[74] A.N. Klimenko, Yu.S. Kozlov, V.S. Sergeev, E.A. Pastukhov, Thermochim. Acta 209 (1992) 331.
[75] H. Satoh, S. Koseki, M. Takagi, W.Y. Chung, N. Kamegashira, J. Alloys Compd. 259 (1997) 176.
[76] V.S. Varazashvili, M.S. Tsarakhov, G.D. Chachanidze, Izv. Akad. Nauk SSSR, Neorg. Mater. 26 (1990) 602.
[77] H. Satoh, T. Shoji, J. Iwasaki, N. Kamegashira, Thermochim. Acta 261 (1995) 47.
[78] V.S. Varazashvili, T.A. Pavleniashvili, M.S. Tsarakhov, D.I. Khutsishvili, Neorg. Mater. 28 (1992) 2029.
[79] V.A. Aleshin, M.V. Gorbacheva, A.F. Maiorova, D.A. Mikhailova, S.N. Mudretsova, Zh. Fiz. Khim. 72 (1998) 421.
[80] D. Sedmidubský, A. Strejc, Unpublished results, 2000.
[81] D. Sedmidubský, J. Leitner, K. Knížek, A. Strejc, M. Veverka, Physica C 329 (2000) 191.
[82] V.S. Varazashvili, T.B. Mirianashvili, M.S. Tsarakhov, D.S. Tsagareishvili, Soobshch. Akad. Nauk Gruz. 142 (1991) 337.
[83] V.P. Marin, A.N. Klimenko, V.A. Levitskii, Yu.V. Menshenin, Yu.Ya. Skolis, Izv. Akad. Nauk SSSR, Neorg. Mater. 20 (1984) 461.
[84] D.W. Fasshauer, B. Wunder, N. Chatterjee, G.W.H. Hohne, Contrib. Mineral. Petrol. 131 (1998) 210.
[85] Q. Chen, S. Liu, P. Zhang, J. Chem. Thermodyn. 31 (1999) 531.
[86] G.I. Frolova, P.V. Klevtsov, I.E. Paukov, Zh. Fiz. Khim. 56 (1982) 710.
[87] G.I. Frolova, S.G. Kozlova, I.E. Paukov, Zh. Fiz. Khim. 55 (1981) 512.
[88] G.I. Frolova, L.P. Kozeeva, I.E. Paukov, Zh. Fiz. Khim. 57 (1983) 2150.

[89] G.A. Berezovskii, L.P. Kozeeva, I.E. Paukov, G.I. Frolova, S.V. Khegai, Zh. Fiz. Khim. 59 (1985) 49.
[90] G.I. Frolova, L.P. Kozeeva, I.E. Paukov, Zh. Fiz. Khim. 54 (1980) 336.
[91] G.A. Berezovskii, L.P. Kozeeva, I.E. Paukov, G.I. Frolova, S.V. Khegai, Zh. Fiz. Khim. 59 (1985) 744.
[92] G.I. Frolova, L.P. Kozeeva, I.E. Paukov, Zh. Fiz. Khim. 58 (1984) 2629.
[93] G.I. Frolova, L.P. Kozeeva, I.E. Paukov, Zh. Fiz. Khim. 57 (1983) 1802.
[94] V.E. Gorbunov, K.S. Gavrichev, G.A. Sharpataya, I.S. Shaplygin, V.L. Zalukaev, Zh. Neorg. Khim. 26 (1981) 547.
[95] M. Castro, R. Burriel, Thermochim. Acta 269/270 (1995) 537.
[96] S. Stølen, F. Grønvold, H. Brinks, T. Atake, H. Mori, J. Chem. Thermodyn. 30 (1998) 365.
[97] H. Satoh, M. Takagi, K. Kinukawa, N. Kamegashira, Thermochim. Acta 299 (1997) 123.
[98] V.I. Kolotyrkin, J.A. Kessler, V.A. Shchelkotunov, I.V. Gordeyev, Yu.G. Metlin, Yu.D. Tretyakov, Thermochim. Acta 43 (1981) 27.
[99] E.H.P. Cordfunke, R.R. van der Laan, G.P. Wyers, J.C. van Miltenburg, J. Chem. Thermodyn. 24 (1992) 1251.
[100] M. Asou, T. Terai, Y. Takahashi, J. Chem. Thermodyn. 24 (1992) 273.
[101] D.W. Fasshauer, N. Chatterjee, L. Cemic, Contrib. Mineral. Petrol. 133 (1998) 186.
[102] T.B. Mirianashvili, V.S. Varazashvili, M.S. Tsarakhov, K.S. Gavrichev, L.M. Golushina, V.E. Gorbunov, D.Sh. Tsagareishvili, Zh. Fiz. Khim. 72 (1998) 16.
[103] J. Nell, H.St.C. O'Neill, Geochim. Cosmochim. Acta 61 (1997) 4159.
[104] V.G. Bessergenev, Yu.A. Kovalenskaya, I.E. Paukov, M.A. Starikov, H. Oppermann, W. Reichelt, J. Chem. Thermodyn. 24 (1992) 85.
[105] M.J. Ferrante, Rep. Invest.—US. Bur. Mines, RI 9018 (1986).
[106] E.H.P. Cordfunke, R.P. Muis, W. Ouweltjes, H.E. Flotow, P.A.G. O'Hare, J. Chem. Thermodyn. 14 (1982) 313.
[107] S. Liu, Q. Chen, P. Zhang, Thermochim. Acta 371 (2001) 7.
[108] W.G. Lyon, D.W. Osborne, H.E. Flotow, H.R. Hoekstra, J. Chem. Thermodyn. 9 (1977) 201.
[109] M. Castro, R. Burriel, Thermochim. Acta 269/270 (1995) 523.
[110] R.R. van der Laan, R.J.M. Konings, A.C.G. van Genderen, J.C. van Miltenburg, Thermochim. Acta 329 (1999) 1.
[111] K.S. Gavrichev, V.E. Gorbunov, L.N. Golushina, G.A. Totrova, E.A. Tishchenko, Yu.G. Nadtochii, Ya.B. Polyarkov, Neorg. Mater. 30 (1994) 1443.
[112] R. Kohli, Thermochim. Acta 237 (1994) 235.
[113] H.W. Xu, J. Iwasaki, T. Shimizu, H. Satoh, N. Kamegashira, J. Alloys Compd. 221 (1995) 274.
[114] T.A. Pavlenishvili, M.S. Tsarakhov, V.S. Varazashvili, D.I. Khutsishvili, G.D. Chachanidze, Izv. Akad. Nauk SSSR, Neorg. Mater. 27 (1991) 99.
[115] J. Peréz, J. Blasco, J. García, M. Castro, J. Stankiewicz, M.C. Sánchez, R.D. Sánchez, J. Magn. Magn. Mater. 196/197 (1999) 541.
[116] R. Shaviv, E.F. Westrum Jr., T.L. Yang, C.B. Alcock, B. Li, J. Chem. Thermodyn. 22 (1990) 1025.
[117] M.E. Huntelaar, A.S. Booij, E.H.P. Cordfunke, R.R. van der Laan, J. Chem. Thermodyn. 30 (1998) 497.
[118] S. Dash, Z. Singh, R. Prasad, V. Venugopal, J. Nucl. Mater. 279 (2000) 84.
[119] E.H.P. Cordfunke, A.S. Booij, M.E. Huntelaar, J. Chem. Thermodyn. 30 (1998) 437.
[120] M.E. Huntelaar, E.H.P. Cordfunke, E.F. Westrum Jr., J. Phys. Chem. Solids 53 (1992) 801.
[121] M.E. Huntelaar, E.H.P. Cordfunke, J.C. van Miltenburg, Thermochim. Acta 254 (1995) 11.
[122] M.S. Tsarakhov, K.S. Gavrichev, V.S. Varazashvili, V.E. Gorbunov, L.N. Golushina, Zh. Fiz. Khim. 64 (1990) 550.
[123] V.A. Shchelkotunov, V.N. Danilob, L.A. Reznitskii, A.V. Korobeinikova, Izv. Akad. Nauk SSSR, Neorg. Mater. 11 (1975) 1633.
[124] A. Junod, D. Eckert, G. Triscone, V.Y. Lee, J. Muller, Phusica C 159 (1989) 215.
[125] T. Atake, H. Kawaji, M. Itoh, T. Nakamura, Y. Saito, Thermochim. Acta 183 (1991) 143.
[126] T. Atake, H. Kawaji, S. Takanabe, Y. Saito, Thermochim. Acta 139 (1989) 169.
[127] K.S. Gavrichev, V.E. Gorbunov, L.N. Golushina, V.B. Lazarev, G.E. Nikiforova, N.F. Vedernikov, G.A. Totrova, I.S. Shaplygin, Zh. Neorg. Khim. 37 (1992) 1583.
[128] R.J.M. Konings, R.R. van der Laan, A.C.G. van Genderen, J.C. van Miltenburg, Thermochim. Acta 313 (1998) 201.
[129] K.S. Gavrichev, V.E. Gorbunov, I.A. Konovalova, V.B. Lazarev, E.A. Tishchenko, I.S. Shaplygin, Izv. Akad. Nauk SSSR, Neorg. Mater. 24 (1988) 343.
[130] A. Junod, D. Eckert, T. Graf, E. Kaldis, J. Karpinski, S. Rusiecki, D. Sanchez, G. Triscone, J. Muller, Phusica C 168 (1990) 47.
[131] T. Atake, A. Honda, H. Kawaji, Physica C 190 (1991) 70.
[132] H. Satoh, J. Iwasaki, K. Kawase, N. Kamegashira, J. Alloys Compd. 268 (1998) 42.
[133] K. Chhor, J.F. Bocquet, C. Pommier, B. Chardon, J. Chem. Thermodyn. 18 (1986) 89.
[134] B.K. Hom, R. Stevens, B.F. Woodfield, J. Boero-Goates, R.L. Putnam, K.B. Helean, A. Navrotsky, J. Chem. Thermodyn. 33 (2001) 165.

WVMP SAR Reference 3-15

Spent Fuel Transportation Package Response to the Baltimore Tunnel Fire Scenario, NUREG/CR-686, Revision 2 (PNNL-15313), Adkins, H.E., Jr., J.M. Cuta, B.J. Koeppel, A.D. Guzman, and C.S. Bajwa, U. S. Nuclear Regulatory Commission, Washington, D.C., February 2009.

U.S.NRC
United States Nuclear Regulatory Commission
Protecting People and the Environment

NUREG/CR-6886, Rev. 2
PNNL-15313

Spent Fuel Transportation Package Response to the Baltimore Tunnel Fire Scenario

Office of Nuclear Materials Safety and Safeguards

AVAILABILITY OF REFERENCE MATERIALS IN NRC PUBLICATIONS

NRC Reference Material

As of November 1999, you may electronically access NUREG-series publications and other NRC records at NRC's Public Electronic Reading Room at http://www.nrc.gov/reading-rm.html. Publicly released records include, to name a few, NUREG-series publications; *Federal Register* notices; applicant, licensee, and vendor documents and correspondence; NRC correspondence and internal memoranda; bulletins and information notices; inspection and investigative reports; licensee event reports; and Commission papers and their attachments.

NRC publications in the NUREG series, NRC regulations, and *Title 10, Energy*, in the Code of *Federal Regulations* may also be purchased from one of these two sources.

1. The Superintendent of Documents
   U.S. Government Printing Office
   Mail Stop SSOP
   Washington, DC 20402–0001
   Internet: bookstore.gpo.gov
   Telephone: 202-512-1800
   Fax: 202-512-2250
2. The National Technical Information Service
   Springfield, VA 22161–0002
   www.ntis.gov
   1–800–553–6847 or, locally, 703–605–6000

A single copy of each NRC draft report for comment is available free, to the extent of supply, upon written request as follows:

Address: U.S. Nuclear Regulatory Commission
Office of Administration
Mail, Distribution and Messenger Team
Washington, DC 20555-0001
E-mail: DISTRIBUTION@nrc.gov
Facsimile: 301–415–2289

Some publications in the NUREG series that are posted at NRC's Web site address http://www.nrc.gov/reading-rm/doc-collections/nuregs are updated periodically and may differ from the last printed version. Although references to material found on a Web site bear the date the material was accessed, the material available on the date cited may subsequently be removed from the site.

Non-NRC Reference Material

Documents available from public and special technical libraries include all open literature items, such as books, journal articles, and transactions, *Federal Register* notices, Federal and State legislation, and congressional reports. Such documents as theses, dissertations, foreign reports and translations, and non-NRC conference proceedings may be purchased from their sponsoring organization.

Copies of industry codes and standards used in a substantive manner in the NRC regulatory process are maintained at—

The NRC Technical Library
Two White Flint North
11545 Rockville Pike
Rockville, MD 20852–2738

These standards are available in the library for reference use by the public. Codes and standards are usually copyrighted and may be purchased from the originating organization or, if they are American National Standards, from—

American National Standards Institute
11 West 42nd Street
New York, NY 10036–8002
www.ansi.org
212–642–4900

Legally binding regulatory requirements are stated only in laws; NRC regulations; licenses, including technical specifications; or orders, not in NUREG-series publications. The views expressed in contractor-prepared publications in this series are not necessarily those of the NRC.

The NUREG series comprises (1) technical and administrative reports and books prepared by the staff (NUREG–XXXX) or agency contractors (NUREG/CR–XXXX), (2) proceedings of conferences (NUREG/CP–XXXX), (3) reports resulting from international agreements (NUREG/IA–XXXX), (4) brochures (NUREG/BR–XXXX), and (5) compilations of legal decisions and orders of the Commission and Atomic and Safety Licensing Boards and of Directors' decisions under Section 2.206 of NRC's regulations (NUREG–0750).

U.S.NRC
United States Nuclear Regulatory Commission
Protecting People and the Environment

NUREG/CR-6886, Rev. 2
PNNL-15313

Spent Fuel Transportation Package Response to the Baltimore Tunnel Fire Scenario

Manuscript Completed: October 2006
Date Published: February 2009

Prepared by
H. E. Adkins, Jr. (PNNL)
J.M. Cuta (PNNL)
B.J. Koeppel (PNNL)
A.D. Guzman (PNNL)
C.S. Bajwa (NRC)

Pacific Northwest National Laboratory
902 Battelle Boulevard
Richland, WA 99352

C.S. Bajwa, NRC Project Manager

NRC Job Code J5167

Office of Nuclear Materials Safety and Safeguards

ABSTRACT

On July 18, 2001, a freight train carrying hazardous (non-nuclear) materials derailed and caught fire while passing through the Howard Street railroad tunnel in downtown Baltimore, Maryland. The United States Nuclear Regulatory Commission (USNRC), one of the agencies responsible for ensuring the safe transportation of radioactive materials in the United States, undertook an investigation of the train derailment and fire to determine the possible regulatory implications of this particular event for the transportation of spent nuclear fuel by railroad.

The USNRC met with the National Transportation Safety Board (NTSB) to discuss the details of the accident and the ensuing fire. Following these discussions, the USNRC assembled a team of experts from the National Institute of Standards and Technology (NIST), the Center for Nuclear Waste Regulatory Analyses (CNWRA), and Pacific Northwest National Laboratory (PNNL) to determine the thermal conditions that existed in the Howard Street tunnel fire and analyze the potential effects of those conditions on various spent nuclear fuel transportation package designs.

The Fire Dynamics Simulator (FDS) code developed by NIST was used to determine the thermal environment in the Howard Street tunnel during the fire. The FDS results were used as boundary conditions for the COBRA-SFS and ANSYS® computer models developed to evaluate the thermal performance of different package designs. The staff concluded that larger transportation packages resembling the TransNuclear Model No. TN-68 and HOLTEC Model No. HI-STAR 100 would withstand a fire with thermal conditions similar to those that existed in the Baltimore tunnel fire event with only minor damage to peripheral components. This is due to their sizable thermal inertia and design specifications in compliance with currently imposed regulatory requirements.

For the TN-68 and the NAC International Model No. LWT (legal weight truck) transportation package, the maximum temperatures predicted in the regions of the lid and the vent and drain ports exceed the seals' rated service temperatures, making it possible for a small release to occur, due to CRUD that might spall off the surfaces of the fuel rods. While a release is not expected to occur for these conditions, any release that could occur would be very small due to a number of factors. These include (1) the tight clearances maintained between the lid and cask body by the closure bolts, (2) the low pressure differential between the package interior and exterior, (3) the tendency of such small clearances to plug, and (4) the tendency of CRUD particles to settle or plate out.

USNRC staff evaluated the radiological con-sequences of the package responses to the Baltimore tunnel fire. The analysis indicates that the regulatory dose rate limits specified in 10 CFR 71.51 for accident conditions would not be exceeded by releases or direct radiation from any of these packages in this fire scenario. All three packages are designed to maintain regulatory dose rate limits even with a complete loss of neutron shielding (as documented in their respective SAR analyses). While highly unlikely, the NAC LWT could experience some decrease in gamma shielding due to slump in the lead as a consequence of this fire scenario, but a conservative analysis shows that the regulatory dose rate limits would not be exceeded.

The results of this evaluation also strongly indicate that neither spent nuclear fuel (SNF) particles nor fission products would be released from a spent fuel transportation package carrying intact spent fuel involved in a severe tunnel fire such as the Baltimore tunnel fire. None of the three package designs analyzed for the Baltimore tunnel fire scenario (TN-68, HI-STAR 100, and NAC LWT) experienced internal temperatures that would result in rupture of the fuel cladding. Therefore, radioactive material (i.e., SNF particles or fission products) would be retained within the fuel rods.

There would be no release from the HI-STAR 100, because the inner welded canister remains leak tight. While a release is unlikely, the potential releases calculated for the TN-68 rail package and the NAC LWT truck package indicate that any release of CRUD from either package would be very small - less than an A_2 quantity (see Section 8.2).

CONTENTS

FIGURES

TABLES

APPENDICES

ABBREVIATIONS

APDL	ANSYS® Parametric Design Language
BTF	Baltimore Tunnel Fire
BWR	Boiling Water Reactor
CFD	Computational Fluid Dynamics
CoC	Certificate of Compliance
CNWRA	Center for Nuclear Waste Regulatory Analyses
CRUD	Chalk River Unknown Deposit (generic term for various residues deposited on fuel rod surfaces, originally coined by Atomic Energy of Canada, Ltd. (AECL) to describe deposits observed on fuel removed from the test reactor at Chalk River.)
DOT	Department of Transportation
FDS	Fire Dynamics Simulator (computational fluid dynamics computer code)
FEA	Finite Element Analysis
HLW	High Level Waste
IAEA	International Atomic Energy Agency
ISO	International Organization for Standardization (The International Organization for Standardization has decreed the use of the initials ISO for reference to the organization, regardless of the word order of the organization's name in any given language. This defines a uniform acronym in all languages.)
MPC	Multi-Purpose Canister
NIST	National Institute of Standards and Technology
NTSB	National Transportation Safety Board
OFA	Optimized Fuel Assembly
PB	Personnel Barrier
PNNL	Pacific Northwest National Laboratory

PWR	Pressurized Water Reactor
SFST	USNRC Division of Spent Fuel Storage and Transportation
SNF	Spent nuclear fuel
USNRC	United States Nuclear Regulatory Commission

1 INTRODUCTION

Current USNRC regulations specify that spent nuclear fuel (SNF) transportation packages must be designed to survive exposure to a fully engulfing fire accident lasting no less than 30 minutes with an average flame temperature of no less than 1475°F (802°C) [1]. The package must maintain containment, shielding, and criticality functions throughout the fire event and post-fire cool down in order to meet USNRC requirements. (The term "package" refers to both the contents, in this case spent nuclear fuel, and the protective enclosing structure in which the contents are placed.)

The intent of the regulations is to ensure that spent fuel packages survive real world accidents, including those involving severe fires. The performance of spent fuel packages in severe accidents has been examined in previous studies by the NRC, as documented in NUREG-0170 (*Final Environmental Statement on the Transportation of Radioactive Material by Air and Other Modes*[1]), NUREG/CR-4829 (*Shipping Container Response to Severe Highway and Railway Accident Conditions*[2], also known as the "Modal Study"), and NUREG/CR-6672 (*Re-examination of Spent Fuel Shipment Risk Estimates*[3]). However, these studies did not explicitly examine historical accidents involving severe rail tunnel fires.

On July 18, 2001, a CSX freight train carrying hazardous (non-nuclear) materials derailed and caught fire while passing through the Howard Street railroad tunnel in downtown Baltimore, Maryland. (The event is described in Section 1.3.) The staff of the USNRC Division of Spent Fuel Storage and Transportation (SFST), formerly the Spent Fuel Project Office, undertook an investigation of the derailment and fire in order to determine what impact this event might have on the risk associated with spent nuclear fuel transportation by rail. This evaluation included an assessment of the potential severity of a tunnel fire compared to a fully engulfing fire, a review of the frequency of rail transportation accidents involving severe fires, and an analytical evaluation of the response of representative licensed SNF transportation packages to the conditions of the Baltimore tunnel fire.

1.1 Evaluation of Tunnel Fire Characteristics

The 30-minute fully engulfing fire prescribed in the current USNRC regulations defines a bounding fire for essentially all credible fire accidents involving SNF shipping packages. A fully engulfing open pool fire would generally be expected to subject a package to the hottest possible conditions for a given fuel supply. However, when considering potential accidents involving rail transport of SNF or high level waste (HLW), it is arguable that a rail tunnel fire could also present one of the more severe thermal challenges to a spent fuel transportation package. This is one of the reasons the staff chose to study the Baltimore tunnel fire event.

In examining real-world accidents that could involve a spent fuel transportation package, a number of significant differences are apparent between tunnel fires and severe fires occurring in an open (non-tunnel) environment. These factors include: 1) the possible position of a spent fuel package in relation to

[1] NUREG -0170, US Nuclear Regulatory Commission, Washington D.C., December 1977.
[2] NUREG/CR-4829, US Nuclear Regulatory Commission, Washington, D.C., February 1987.

the fire location; 2) the nature of the flammable material involved; 3) the rail bed materials; 4) the types of fires that can occur and; 5) emergency response to fire accidents.

In a fully engulfing fire, in which the fuel is generally assumed to form a pool, the most severe conditions, by definition, occur in the hottest flaming region of the fire. In a typical regulatory fire analysis (defined by the fire conditions in 10 CFR 71.73[1]), a SNF package is assumed to be located within the flaming region of the fire 3.3 ft (1 meter) above the surface of the pool. However, because many railroad tracks are elevated above grade and are constructed on porous substrate, pooling of spilled flammable liquid is less likely in an open environment when compared with a tunnel environment, where the rail bed surface is often rock, concrete, or pavement. Historically many of the fires resulting from rail accidents have involved the leakage of flammable gas (such as propane), rather than a liquid. A flammable gas cannot form a pool. If ignited, flammable gas leaking from a tank car will generally result in a localized pressure fire that is incapable of engulfing a spent fuel transportation package.

In a rail accident involving a fire, it is extremely unlikely that a spent fuel transportation package would end up directly adjacent to a tank car carrying flammable liquid. Federal regulations issued by the Department of Transportation (DOT), in 49 CFR 174.85, require very specifically defined spacing between rail cars carrying radioactive materials and hazardous materials of any kind, including flammable liquids. Typical requirements specify that a rail car carrying radioactive material must be separated from cars carrying other hazardous material by at least one buffer car. A rail car carrying a spent fuel package would not be coupled directly to a tank car carrying flammable or combustible liquid. Figure 1.1 shows an example of this arrangement in an actual radioactive material shipment by rail.

Figure 1.1. Radioactive Material Rail Shipment

[3] NUREG/CR-6672, US Nuclear Regulatory Commission, Washington D.C., March 2000.

The location of the spent fuel package relative to the fire, for a fire in an open environment (i.e., a non-tunnel fire), will determine the amount of heat absorbed by the package (assuming a direct exposure to the fire). This is because thermal radiation is the main mechanism[4] for heat transfer from the fire to the package. In an open environment, the energy imparted to the package from the fire falls off rapidly with distance from the fire. In a tunnel environment, by contrast, the fire may result in elevated temperatures on adjacent tunnel surfaces, which could result in a package being subjected to an "oven" effect due to heat radiating from hot tunnel surfaces for an extended period of time, possibly for several hours after the fire has been extinguished.

In rail accidents involving fires and hazardous materials in tank cars (including flammable gas or liquid), emergency responders follow the DOT Emergency Response Guidebook[5]. Emergency personnel are directed to provide water spray cooling to tank cars, to prevent boiling liquid expanding vapor explosions (BLEVEs) from occurring. In tunnel fires, space restrictions may make it difficult or impossible to mount an effective emergency response, either to cool tank cars or extinguish the fire. This could result in a fire burning unchecked, having a longer duration, and possibly reaching higher temperatures, compared to a fire with essentially the same fuel supply occurring in an unobstructed (non-enclosed) environment. Based on these factors, fires occurring in tunnels have the potential of being more severe than fires occurring in non-tunnel environments. The only significant limiting factor in a tunnel fire, which would not affect a fire in an open environment, is the potential for limited ventilation in a tunnel (due to tunnel length or small degree of slope), which could greatly reduce the amount of oxygen available for combustion. This would tend to reduce the burn rate, which would reduce the intensity of the fire, and thus tend to produce lower temperatures, even for a longer fire duration.

1.2 Review of Rail Transportation Accidents

As part of its investigation of the impact of the Baltimore tunnel fire on the transportation of spent nuclear fuel, NRC staff conducted a detailed survey of rail transportation accidents in the United States. The staff reviewed accident reports (particularly those of the NTSB), historical media accounts, and data from the Federal Railroad Administration (FRA) safety database, and from the Association of American Railroads (AAR). This review showed that severe rail fires, either in tunnels or open environments, are extremely infrequent events.

The staff's review revealed several facts about rail accidents in the United States in general, and those involving hazardous materials specifically. These facts, which are summarized below, aid in putting the Howard Street tunnel fire into perspective.

- In nearly 34 billion kilometers (21 billion miles) of travel on American railroads between 1975 and 2005, there have been 1700 reported incidents involving release of hazardous materials.

---

[4] For a discussion of this phenomenon see NUREG/CR-4892, *Shipping Container Response to Severe Highway and Railway Accident Conditions*, Vol. II, pages 175 to 178.

[5] 2004 Emergency Response Guidebook, U.S. Department of Transportation, Pages 115 and 128.

- Many of the 1700 incidents involved minor releases of non-flammable hazardous materials. None of the incidents reviewed involved the release of any radioactive material.

- Of the 1700 incidents, there were 8 that involved a significant quantity of flammable material and that resulted in a long duration fire. These incidents[6] were as follows:

  1) Derailment of CSXT freight train, Baltimore, Maryland, July 18, 2001 (the subject of this report)
  2) Derailment of Union Pacific Freight train, Eunice, Louisiana, May 27, 2000 [NTSB report RAR-02-03; NTIS report PB2002-916303]
  3) Derailment of Wisconsin Central freight train, Weyauwega, Wisconsin March 4, 1996[7]
  4) Derailment of BNSF freight train, Cajon Pass, California, February 1, 1996 [NTSB report RAR-96-05; NTIS report PB96-916305]
  5) Derailment of CSXT freight train, Akron, Ohio, February 26, 1989 [NTSB report HZM-90-02; NTIS report PB90-917006]
  6) Derailment of MT Rail freight train, Helena, Montana, February 2, 1989 [NTSB report RAR-89-05; NTIS report PB89-916305]
  7) Derailment of CSXT freight train, Miamisburg, OH, July 8, 1986 [NTSB report HZM-87-01; NTIS report PB-87-917004]
  8) Derailment of Illinois Gulf Central freight train, Livingston, Louisiana, September 28, 1982 [NTSB report RAR-83-05; NTIS report PB83-916305]

Of these eight accidents, only one (the Baltimore tunnel fire) occurred in a tunnel. Based on an examination of the NTSB accident reports on the seven accidents listed above that did not occur in a tunnel, the staff concluded that none of them could have provided a fully engulfing fire environment for a spent fuel package, had one been involved in the event.

This conclusion is based on three mitigating factors present in the accidents examined above: the potential proximity of a hypothetical SNF transportation package to the fire that occurred, the available fuel for the fire, and the emergency response time for each accident. These factors are expanded upon below:

(1) Proximity: Using diagrams of the rail car configurations in the seven accidents, as given in the NTSB reports, a rail car carrying a spent fuel package and its required buffer cars could not have been located close enough to any tank cars that ruptured in these accidents. An SNF package, had one been involved, would not have been positioned near enough to the burning flammable material in these accidents to be fully engulfed.

(2) Fuel for the fire: The flammable material involved in a majority of the accidents were gasses that resulted in localized pressure fires, so these accidents did not involve the pooling of

---

[6] The reports on these incidents are available on the NTSB web site, www.ntsb.gov, under the link "Accident Reports", or from the National Technical Information Service (NTIS) web site, www.ntis.gov.

[7] The NTSB did not issue a report on this accident. Information describing the accident is available in the public docket, *National Transportation Safety Board Public Docket for Railroad Accident at Weyauwega, WI, March 4, 1996*. Docket ID: 8867, Released August 18, 1997, Washington, D.C. This document is available on the website: http://www.postcrescent.com/specials/assets/APCweyauweatrain/default.htm.

flammable liquids. In those that did involve flammable liquids, pooling did not occur because of the nature of the track bed, which is elevated over porous media.

(3) Response time: The emergency response times were extremely rapid in these seven accidents (most were responded to within 1-2 hours), and response efforts included cooling the tank cars, effectively minimizing fire intensity and duration.

The Howard Street rail tunnel derailment and fire is unique in that none of the mitigating factors noted above (for non-tunnel fires) were acting to significantly limit the severity or duration of the fire. However, the staff's examination of the FRA database shows that the Howard Street tunnel derailment and fire is the only severe rail tunnel fire involving hazardous materials shipments that has occurred in the nearly 21 billion rail miles of transportation that took place in the United States between 1975 and 2005.

When this accident frequency is coupled with the expected number of shipments of radioactive material in the future, the risk of an accident of this type still remains low. In addition, several factors work to reduce the risk of this type of accident even further. These include:

(1) The intent of the Department of Energy (DOE) to ship the bulk of SNF and HLW to the Proposed Geological Repository for the Disposal of SNF and HLW at Yucca Mountain (Yucca Mountain) via dedicated rail[8];

(2) FRA consideration of enactment of regulations that would require the use of dedicated trains[9] for the shipment of SNF and HLW;

(3) AAR enacting, at the recommendation of the NRC, a "no-pass" rule[10] for single bore dual-track rail tunnels. The rule specifies that trains carrying tank cars containing hazardous materials, such as flammable or combustible liquids, and trains carrying SNF or HLW may not pass one another within the same tunnel.

This investigation has shown that accidents involving hazardous materials and long duration fires on railroads in general and in rail tunnels in particular occur with extremely low frequency. As discussed above, DOE, FRA, and AAR have taken steps to further preclude the possibility of such an accident involving SNF or HLW and other hazardous (flammable or combustible) materials in a rail tunnel. Consequently, the frequency of any rail accident involving an SNF or HLW shipment in conjunction with a long duration fire in a rail tunnel essentially approaches zero. Detailed conservative analyses of the Baltimore tunnel fire show that the potential consequences of such an accident, were it to actually occur, are minimal (as discussed in Chapter 8 of this report). The NRC staff therefore concludes that the risk to public health and safety posed by this type of transportation accident is close to nonexistent.

---

[8] Letter to Stakeholders from Paul M. Golan, Principal Deputy Director Office of Civilian Radioactive Waste Management, July 18, 2005.

[9] This consideration is mandated pursuant to Section 5105(b) of the Hazardous Materials Transportation Uniform Safety Act of 1990, As Amended.

[10] Circular No. OT-55-I (CPC-1174), American Association of Railroads, July 17, 2006.

1.3 The Baltimore Tunnel Fire Event

The Howard Street tunnel in Baltimore is a single track railroad tunnel of concrete and refractory brick. Originally constructed in 1895, later additions extended it to its current length of 1.65 mi (2.7 km). The tunnel has an average upward grade of only 0.8% from the west portal to the east portal, and at the time of the accident, the active ventilation system was not in operation. The tunnel is approximately 22 ft (6.7 m) high by 27 ft (8.2 m) wide in the vicinity of the accident; however, the dimensions vary along the length.

The freight train involved in the accident had a total of 60 cars pulled by 3 locomotives, and was carrying paper products and pulp board in boxcars as well as hydrochloric acid, liquid tripropylene[11], and other hazardous liquids in tank cars [4, 5]. As the train was passing through the tunnel, 11 of the 60 rail cars derailed. A tank car (Figure 1.2) containing approximately 28,600 gallons (108,263 liters) of liquid tripropylene had a 1.5-inch (3.81-cm) diameter hole punctured in it (Figure 1.3) by the car's brake mechanism during the derailment.

Figure 1.2. Liquid Tripropylene Tank Car

[11] Tripropylene carries an NFPA hazards rating of 3 for flammability, which is the same as that of gasoline.

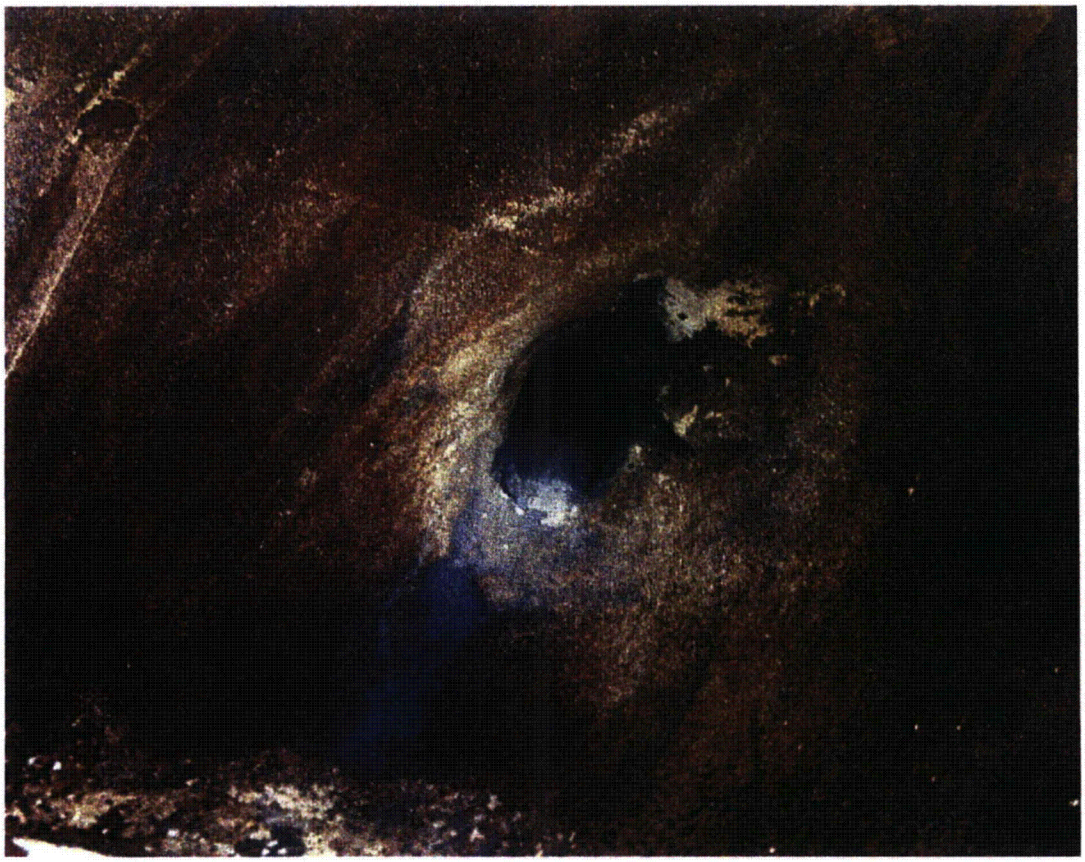

Figure 1.3. Puncture in Tank Car

Ignition of the liquid tripropylene led to the ensuing fire. The exact duration of the fire is not known with certainty. Based on NTSB interviews of emergency responders, it was determined that the most severe portion of the fire in the Howard Street tunnel lasted approximately 3 hours. Less severe fires burned in the tunnel for periods of time greater than 3 hours. Approximately 12 hours after the fire started, firefighters were able to visually confirm that the tripropylene tank car was no longer burning.

Tripropylene, which is also called Nonene, is a liquid hydrocarbon compound that is traditionally used for industrial processes. Table 1.1 lists the heat of combustion for tripropylene and a number of other hydrocarbon fuels that are commonly shipped by rail. Gasoline and jet fuel are also included in the table, but for comparison purposes only, as these fuels are rarely, if ever, transported by rail. Tripropylene has a heat of combustion comparable to that of gasoline, and has a higher heat of combustion than that of jet fuel. When compared to other common hydrocarbon liquids, tripropylene falls near the high end of the range of values for heat of combustion for hydrocarbon liquids. The range of values shown in Table 1.1 for hydrocarbon fuels is relatively narrow, however, which indicates that when burned under the same conditions, these hydrocarbon liquids will generally have similar combustion characteristics. Therefore, while tripropylene was the specific fuel for the Baltimore tunnel fire, its combustion characteristics are generally representative of the behavior of other hydrocarbon fuels.

Table 1.1. Comparison of Various Hydrocarbon Liquids

Liquid Hydrocarbons	Molecular Formula	Heat of Combustion[a] Btu/lb. (kJ/kg)
Propane	C_3H_8	19,800 (46,000)
Butane	C_4H_{10}	19,500 (45,400)
Isobutane	C_4H_{10}	19,600 (45,600)
Pentane	C_5H_{12}	19,300 (45,000)
Hexane	C_6H_{14}	19,200 (44,700)
Heptane	C_7H_{16}	19,200 (44,700)
Toluene	C_7H_8	17,400 (40,500)
Octane	C_8H_{18}	19,100 (44,400)
Nonane	C_9H_{20}	19,000 (44,300)
Nonene (tripropylene)	**C_9H_{18}**	**19, 000 (44,300)**
Decane	$C_{10}H_{22}$	19,000 (44,300)
Undecane	$C_{11}H_{24}$	19,000 (44,300)
Gasoline (mixture of heptanes, octanes, nonanes and decanes)	C_8H_{15}[b]	19,100 (44,500)[b]
Jet Fuel, grade JP-1		18,500 (43,000)
Jet Fuel, grade JP-2		18,700 (43,500)
Jet Fuel, grade JP-3		18,700 (43,500)
Jet Fuel, grade JP-4		18,500 (43,000)

[a]Values derived from Perry, Chilton, and Kirkpatrick, *Perry's Chemical Engineer's Handbook*, 4th Edition, Table 3-202, Page 3-104.
[b]Typical values. Values will vary slightly depending on formulation. Derived from Ferguson and Kirkpatrick, *Internal Combustion Engines, Applied Thermosciences*, 2nd Edition, Page 316 and Table 10.8.

1.4 Implications of the Baltimore Tunnel Fire for Transportation of Spent Nuclear Fuel

As one element of the evaluations related to the Baltimore tunnel fire accident, calculations were performed by NRC for three currently licensed spent nuclear fuel transportation packages. This analysis is a case study of a historic event, with the addition of the involvement of a spent nuclear fuel transportation package and a conservative representation of the possible fire duration. The staff's efforts were focused on providing a realistic transportation accident scenario based on the physical conditions of

the Howard Street tunnel and the actual events surrounding the derailment and ensuing fire. The analysis is not intended to determine a "worst case" tunnel fire accident involving spent nuclear fuel. However, given the extremely low frequency of this type of accident (as discussed in Section 1.2), and the intensity and duration of the fire, this accident imposes extremely severe conditions on an SNF package, and constitutes a 'beyond design-basis' scenario.

This analysis evaluated the performance of the TransNuclear Model No. TN-68 ("TN-68"), the HOLTEC International Model No. HI-STAR 100 ("HI-STAR 100"), and the NAC International Model No. LWT ("NAC LWT") transport packages when subjected to boundary conditions representing the Baltimore tunnel fire. Tunnel air, wall, floor, and ceiling temperatures obtained from fire analyses performed by the National Institute of Standards and Technology (NIST), were used to define the boundary conditions for the transient calculations. The purpose of the evaluation was to obtain an estimate of the temperature response of the various components of each of these packages during and after the fire.

This report presents general descriptions of the transportation package designs analyzed, as well as a detailed description of the analyses conducted including modeling approach, boundary conditions, and computational results. Section 2 describes the NIST tunnel fire model used to develop boundary conditions for the thermal analyses of the spent fuel transportation packages. Section 3 briefly describes the material exposure analysis used to verify the predicted temperatures obtained in the fire simulations performed by NIST. Section 4 presents a detailed description of the spent fuel transportation packages evaluated. The computational models developed for the analyses are described in Section 5. Section 6 presents a detailed description of the analysis method. Section 7 presents the results of the simulation, giving a detailed evaluation of the predicted response for each transportation package during and after the fire. Section 8 provides an analysis to determine the magnitude of any potential radiation hazard or release of radioactive material as a consequence of the effects of the fire on each of the packages.

2 NIST TUNNEL FIRE MODEL

Experts at the National Institute of Standards and Technology (NIST) developed a model [4] of the Baltimore tunnel fire using the Fire Dynamics Simulator (FDS) code [6, 7][12] to assess the thermal environment within the tunnel during the fire. The NIST study was based on information developed by the NTSB investigation of the tunnel fire, including descriptions of the tunnel structural features, the damage to the rail cars, and the sequence of events in the accident. Using this information as the starting point for the calculations, the analysis was extended to include variation of the unknown parameters to predict the range and distribution of temperatures that could have been sustained in the tunnel during and after the fire, and the duration of the fire.

FDS is a computational fluid dynamics (CFD) code that models combustion and flow of hot gas in fire environments. FDS solves the mass, momentum, and energy equations for a given computational grid, and uses a large eddy simulation technique to represent turbulence effects. The source term representing the fire is modeled by solving an additional transport equation for a conserved scalar quantity representing the mixture fraction of fuel and oxygen. Thermal radiation is modeled with the radiative transport equation for a non-scattering grey gas. The code is also able to construct a visual representation of smoke flow in a fire, taking into account the effects of the geometry of the fire environment and the material comprising surrounding structures.

The extensive validation of FDS includes comparisons to results of tunnel fire tests with conditions similar to the Baltimore tunnel fire. NIST developed fire models using FDS based on the geometry and test conditions from a series of tunnel fire experiments conducted by the Federal Highway Administration and Parsons Brinkerhoff, Inc. as part of the Memorial Tunnel Fire Ventilation Test Program [8]. NIST modeled both a 6.83×10^7 Btu/hr (20 MW) and a 1.71×10^8 Btu/hr (50 MW) unventilated fire test from the Memorial Tunnel Test Program, and achieved results using FDS that were within 100°F (56°C) of the recorded data[6,7].

The full-length, 3-dimensional representation of the Howard Street tunnel developed by NIST included the rail cars represented as solid blocks elevated 3.3 ft (1 m) above the rail bed. The rail car blocks can absorb thermal radiation, and provide obstructions to air flow in the tunnel. In the model, the blocks representing the rail cars were positioned in the center of the tunnel for the majority of the calculations. However, sensitivity studies included calculations performed with the rail cars modeled in their derailed positions in the tunnel, as documented by the NTSB. The source of the fire was specified in the simulation as a pool of burning liquid tripropylene[13] positioned below the location of the hole that was punctured in the tripropylene tank car during the derailment. The computational grid for the tunnel fire model was relatively fine in the immediate vicinity of the fire, with nodes on the order of 6 to 12 inches

[12] Formal publication of the FDS code documentation began in 2001 with Version 2. Continuing validation and development of the code led to Version 3 in 2002. Version 3 was used in the FDS analyses discussed in this report.

[13] Combustible materials in nearby box cars ignited during the fire, and continued to smolder for several days, long after the tripropylene fire self-extinguished. However, these materials contributed relatively little energy to the fire, and burned at temperatures far lower than those experienced during the flaming combustion of the liquid hydrocarbon fuel.

(0.15 to 0.30 m) in length, in order to properly capture fire and gas behavior. The mesh size was expanded at distances farther from the fire source, where less resolution was needed. The entire tunnel volume was included in the FDS calculation, in order to appropriately simulate the mixing of air and hot gasses along the full length of the tunnel.

Parametric studies of the burning rate of the fire based on the amount of available fuel, the air flow in the tunnel, the thermal conductivity of the bricks lining the tunnel, and sensitivity studies on the fuel pool area show that the Howard Street tunnel fire was oxygen-limited. In the confined space of the tunnel, the heat release rate of the fire was constrained by the supply of oxygen, rather than the supply of fuel. For a wide range of modeling assumptions, the overall heat release rate (or heat rate) for the fire was predicted to be no more than about 1.71×10^8 Btu/hr (50 MW). The highest peak temperatures predicted in these simulations were 1832-2012°F (1000-1100°C) in the flaming region of the fire. The calculational results showed that the hot gas layer above the rail cars within three to four rail car lengths of the fire was an average of 932°F (500°C). Peak temperatures on the tunnel surfaces were calculated to reach 1472°F (800°C) where flames directly impinged on the ceiling of the tunnel. The average tunnel ceiling temperature within a distance of three to four rail car lengths from the fire was calculated to be 752°F (400°C).

In these FDS simulations, the hottest temperatures occur within the first hour of the fire. After that point, the fire is oxygen-limited and temperatures are generally lower. A considerable fraction of the evaporated fuel does not burn due to lack of oxygen, and instead is predicted to have been carried out of the tunnel with the smoke and other combustion gases. However, these simulations extended only over the first 3 hours of the fire. At that point, the bursting of a water main within the tunnel introduced significant uncertainty in the boundary conditions for the fire within the tunnel. The presence of water in the tunnel would be expected to affect the fire intensity and possibly duration, but there is no means of determining how much water might have actually reached the fire location. The tripropylene fire probably burned more than 3 hours, but it could have done so only at a reduced rate due to lack of sufficient oxygen and it may also have been affected by cooling or quenching due to the presence of water in the tunnel. Within 12 hours, the fire had self-extinguished due to oxygen starvation and possibly water quenching.

Additional FDS simulations were performed using the same model of the Howard Street tunnel, to investigate possible scenarios that could produce long-duration, high-temperature fires within the tunnel environment. In these simulations, the bursting of the water main was ignored, the tunnel was assumed to be ventilated in a manner that allowed the fire to be fully oxygenated, and the fire was assumed to burn until the entire inventory of fuel in the tank car was consumed by combustion. (This assumes that no fuel was lost due to evaporation or by draining away from the fire location or by soaking into the rail bed.) The cross-sectional area of the pool of fuel was assumed to be no more than 600 ft^2 (56 m^2), corresponding to the footprint of the tank car, which is about the smallest pool that could have been sustained within the tunnel. This essentially supposes that the fuel was confined within the low "walls" formed by the rails of the track, that the tank car was fortuitously situated at a slight dip in the rail bed, and the fuel spilled from the puncture in the tank car at a rate that did not overflow this shallow pan before it could be consumed by the fire. Although somewhat unrealistic, these assumptions led to a more conservative fire duration.

This minimum size for the fuel pool was assumed in order to determine the hottest and longest-lasting potential fire conditions for this event. A larger pool size would generally mean a shorter duration for the fire (because a fire burning over a larger area consumes fuel more rapidly) and the possibility of a lower peak temperature (due to the formation of an oxygen starved "core" at the interior of the pool area). The assumed pool size is very conservative for this scenario, since it is reasonable to assume that the fuel spilled freely through the rail bed and along the floor of the Howard Street tunnel and, therefore, would have burned over a larger area and at lower temperatures than were calculated for the assumed minimal fuel pool size in the FDS calculation.

If the tunnel ventilation system had been operating at the time of the fire, air flow to the fire would have been higher, and the fire would not have been oxygen-starved to the same extent as it was with the ventilation system off. To allow sufficient ventilation within the tunnel for all of the fuel to be consumed by combustion, the FDS model was modified to include holes in the tunnel walls that connected to the ambient environment. Assuming 53.84-ft^2 (5-m^2) holes (3.3 ft (1 m) high by 16.4 ft (5 m) wide, 9.8 ft (3 m) above the tunnel floor), every 328 ft (100 m) along one side of the tunnel produced a fire lasting 6.7 hrs. The peak gas temperatures in this scenario were 2084°F (1140°C) in the flaming region of the fire and 1958°F (1070°C) at 66 ft (20 m) downstream of the fire. At the location 66 ft (20 m) downstream of the fire, peak ceiling temperatures above 1832°F (1000°C) were predicted from about 3 hours until the end of the fire at 6.7 hrs.

The heat rate for the fire in this scenario is approximately 1.71×10^9 Btu/hr (500 MW), which is an order of magnitude higher than the heat rate predicted for the actual fire. The scenario conservatively assumes a sufficient supply of oxygen for the fire (as if the tunnel had been well ventilated) and a minimum credible fuel pool area within the confines of the tunnel. These assumptions produced a fire scenario within the tunnel that is comparable in severity to an open pool fire, and is arguably the most severe fire that could possibly have occurred with the available fuel. The temperatures predicted with FDS for this scenario provided the fire boundary conditions for the ANSYS and COBRA-SFS simulations in the current study. (See Section 6.1 for a complete description of the actual boundary conditions used.)

3 CNWRA MATERIALS FIRE EXPOSURE ANALYSIS

Staff from the Center for Nuclear Waste Regulatory Analysis (CNWRA), along with staff from NRC and NIST, examined rail cars and the tank car removed from the Howard Street tunnel, to evaluate evidence of high temperatures experienced by these components. The examination of physical evidence provided the staff with further insight into the fire environment that existed in the tunnel during the accident. Staff from CNWRA also collected material samples from these boxcars and the tank car for further analysis.

By performing metallurgical analyses on the material samples collected, including sections of the boxcars exposed to the most severe portion of the fire and an air brake valve from the tripropylene tank car, CNWRA was able to estimate the fire exposure time and temperature for the samples tested. These analyses indicated that material temperatures on the roof of the boxcar located approximately 66 ft (20 m) from the tank car were in the range of 1382-1562°F (750-850°C) for approximately 4 hours. Material temperatures on other components of this boxcar were estimated to have reached values on the order of 1112°F (600°C). (Additional details associated with the analyses performed by CNWRA can be found in the report on the analysis of the rail car components [5].)

The material time and temperature exposures determined by the CNWRA analyses provide objective verification of the detailed predictions of the NIST FDS model of the Howard Street tunnel fire [4]. The FDS calculations predict peak gas temperatures of 1832-2012°F (1000-1100°C) in the flaming region of the fire, with peak surface temperatures of 1472°F (800°C) on the tunnel ceiling. Because of the insulation provided by the brick walls of the tunnel, the calculated temperatures within 3 to 4 rail car lengths (within approximately 200 ft (60 m)) of the fire were relatively uniform, as in an oven or furnace. As a result, the hot gas layer above the rail cars in this region is calculated to sustain an *average* temperature of approximately 932°F (500°C) for at least 3 hours. The local material temperatures estimated in the CNWRA analysis at 66 ft (20 m) from the fire could easily have been sustained in this predicted fire environment.

The fire scenario used to define the boundary conditions for the ANSYS and COBRA-SFS calculations in the current study, however, represents conditions that are more severe than the conditions predicted with FDS using realistic boundary conditions based on available information about the Howard Street tunnel fire. In this scenario, as described in Section 2, the fire is assumed to be fully ventilated and burns for nearly 7 hours, until all of the tripropylene fuel is consumed. The FDS simulation using these assumptions predicts peak gas temperatures above 1400°F (760°C) for more than 5 hours in the region 66 ft (20 m) from the fire center. The peak ceiling temperature at this location is above 1400°F (760°C) for more than 6 hours. This fire environment would result in far more severe conditions at the hypothetical location of an SNF package than are indicated for the actual Baltimore tunnel fire by the results of the CNWRA materials analyses.

4 TRANSPORTATION PACKAGES ANALYZED

As discussed in Section 1, NRC regulations require that spent fuel transportation packages be evaluated for a series of hypothetical accident conditions that include a 30-ft (9 m) drop test, a 40-inch (1 m) pin puncture drop test, and a fully engulfing fire with an average flame temperature of 1472°F (800°C) for a period of 30 minutes. These tests are followed by the immersion of an undamaged package under 50 ft (15 m) of water [1]. The certification process must include either an open pool fire test or an analysis of the package for a fire exposure meeting the aforementioned criteria. Packages must maintain shielding and criticality control functions throughout the hypothetical accident conditions.

This investigation evaluated how a fire similar to the Howard Street tunnel fire might affect three NRC-certified spent fuel transportation package designs. These included the TransNuclear TN-68 and HOLTEC HI-STAR 100 rail transportation packages, and the NAC LWT transportation package. The LWT was selected because it represents a typical truck (over-the-road) package that can also be transported by rail. The design of each of these packages is briefly described in the following sections.

4.1 TransNuclear TN-68 SNF Transportation Package

The TN-68 spent fuel shipping package transports BWR spent fuel assemblies. The basic design is similar to that of the HOLTEC HI-STAR 100, except that the TN-68 package does not include an inner seal-welded canister. The containment boundary is provided by the package shell and lid seals. The TN-68 package holds up to 68 BWR assemblies, with a maximum total decay heat load of 72,334 Btu/hr (21.2 kW). The fuel assemblies are contained within a basket structure consisting of 68 stainless steel tubes that have aluminum and borated aluminum (or boron carbide/aluminum composite) neutron poison plates sandwiched between the steel tubes. The general layout of the TN-68 package is illustrated in Figures 4.1 and 4.2. Detailed information on the design can be found in the appropriate sections of the TN-68 Safety Analysis Report (SAR) [9].

The basket structure is supported by aluminum alloy support rails bolted to the inner carbon steel package shell, which also serves as the inner gamma shield. This inner steel shell is shrink-fitted within an outer carbon steel shell that serves as the outer gamma shield. The gamma shielding is surrounded by the neutron shielding, which consists of a ring of aluminum boxes filled with borated polyester resin. The outer shell of the package is carbon steel.

The package bottom is carbon steel with an inner steel shield plate. The package lid is also carbon steel with a steel inner top shield plate. During transport, the ends of the package are capped with impact limiters made of redwood and balsa and covered in stainless steel plate (depicted in Figure 4.2). The TN-68 weighs approximately 260,400 lb (118,115 kg) when loaded for transport.

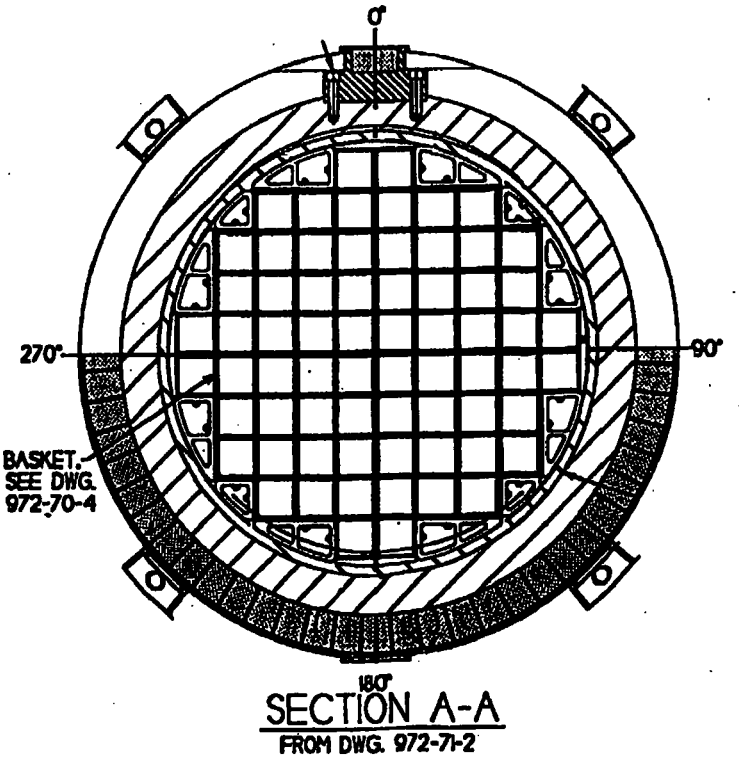

Figure 4.1. Cross-section of TN-68 Package (drawing 972-71-3 Rev. 4, "TN-68 Packaging General Arrangement: Parts List and Details")

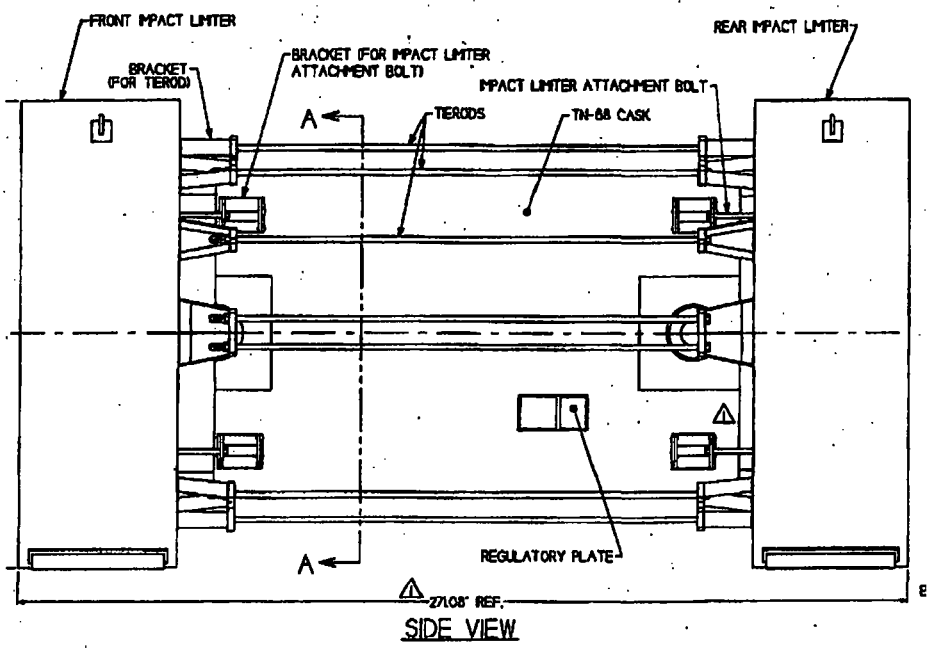

Figure 4.2. TransNuclear TN-68 Spent Fuel Transportation Package

4.2 HOLTEC HI-STAR 100 SNF Transportation Package

This design provides an additional containment boundary in the form of a welded multi-purpose canister (MPC) enclosing the spent fuel. (The outermost containment boundary is provided by the package shell and lid seals.) HOLTEC has MPC designs to accommodate three different spent fuel loading configurations: up to 24 PWR assemblies, up to 32 PWR assemblies, or up to 68 BWR assemblies. The MPC-24 was selected for this evaluation. This design has an integral fuel basket that accommodates 24 PWR spent fuel assemblies with a maximum total decay heat load of 68,240 Btu/hr (20 kW). The MPC is placed in the transportation packaging for shipment after it has been loaded with spent nuclear fuel and welded shut. A diagram of the HI-STAR 100 package system is provided in Figure 4.3. The package inner shell is stainless steel, and six layers of carbon steel plates comprise the gamma shield. The next layer is a polymeric neutron shield, strengthened by a network of carbon steel stiffening fins. The outer shell of the package is carbon steel, with a painted surface.

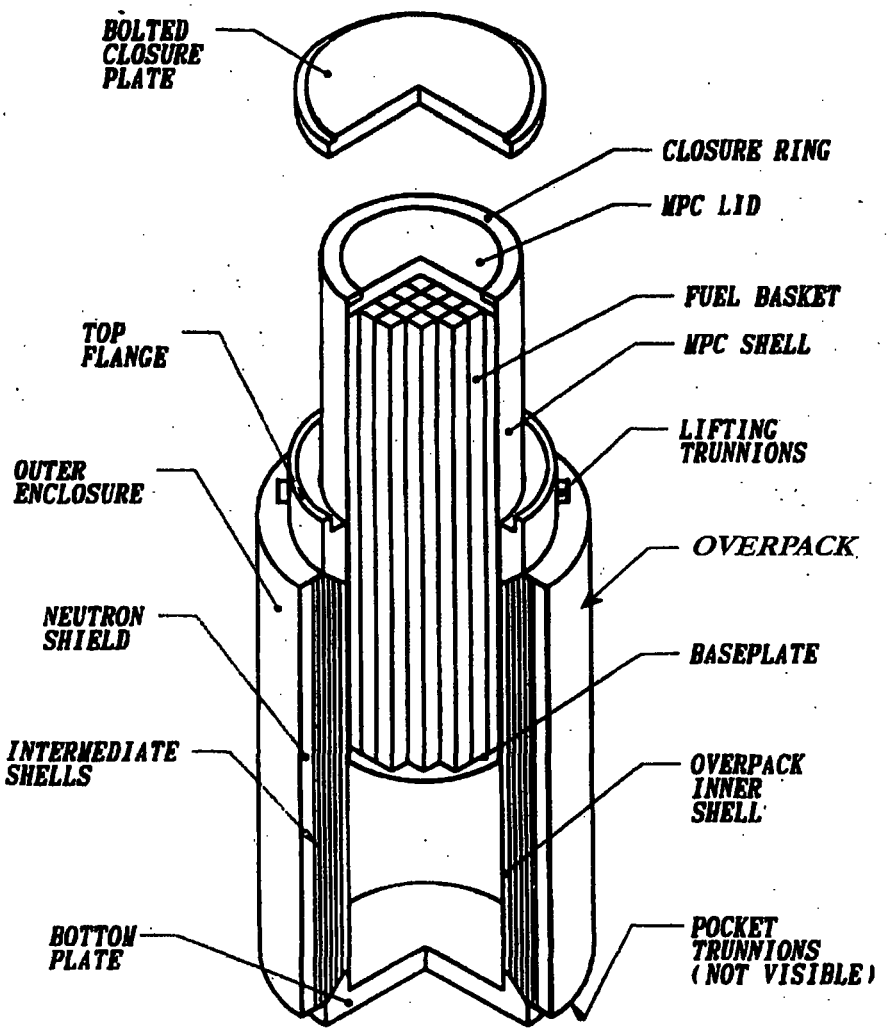

Figure 4.3. HOLTEC HI-STAR 100 Spent Fuel Package

Aluminum honeycomb impact limiters with stainless steel skin are installed on the ends of the package prior to shipping. Impact limiters protect the closure lid, MPC, fuel basket, and contents from damage in the event of a package drop accident. The impact limiters also provide thermal insulation to the lid and port cover components in the event of a fire exposure. Figure 4.4 shows an illustration of this package secured to a rail car, with impact limiters installed. This package weighs approximately 277,300 lb (125,781 kg) when loaded for transport. Additional configuration details are provided in the HI-STAR 100 Package System SAR [10].

Figure 4.4. Spent Fuel Transportation Package on Rail car[14]

4.3 NAC LWT SNF Transportation Package

The NAC LWT is a small transportation package certified for transport on a standard tractor trailer truck, which can also be transported by rail. The NAC LWT is typically enclosed within an International Organization for Standardization (ISO) shipping container when shipped by rail. The Certificate of Compliance (CoC) for this SNF package requires that it be enclosed in either a personnel barrier (PB) or ISO container. Figure 4.5 shows a picture of a NAC LWT package on a flat-bed trailer with a PB installed, but without an ISO container.

[14] Image courtesy of HOLTEC International.

PBs commonly used for truck shipments are not suitable for rail shipments, so an ISO container would generally be required. Current DOE policy requires an ISO for truck packages shipped by rail, and every rail shipment of the LWT to date has been in an ISO container. Figure 4.6 shows an exterior view of the package within an ISO container on a flat-bed trailer.

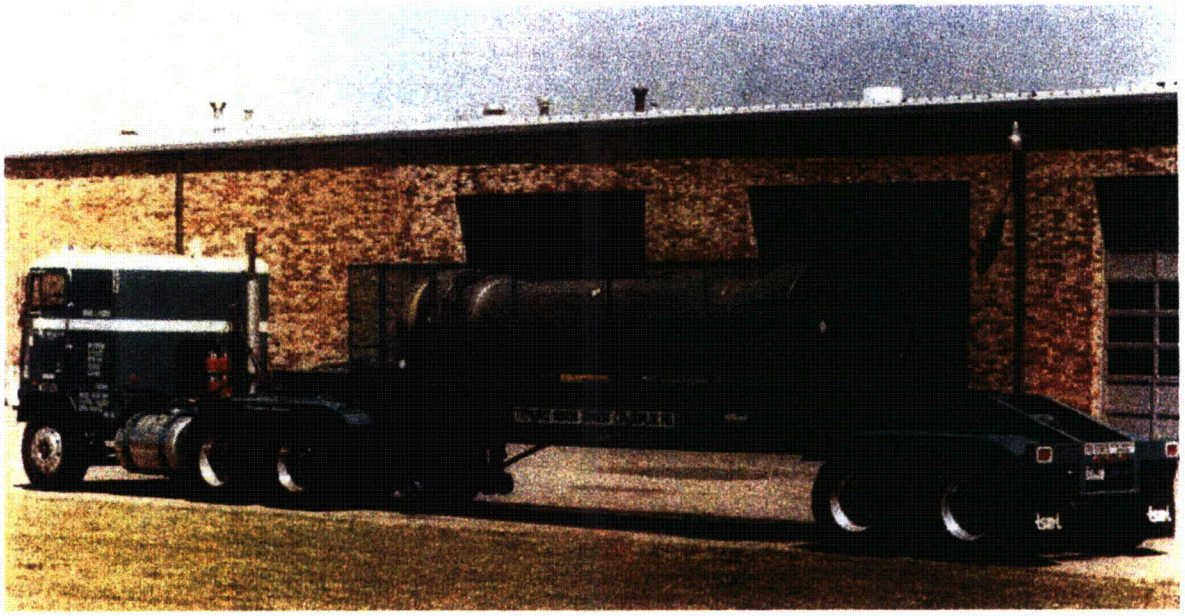

Figure 4.5. NAC LWT Transport Package (without ISO container)

Figure 4.6. NAC LWT Transport Package (within ISO container)

This package is designed to transport a variety of commercial and test reactor fuel types with widely varying maximum decay heat load specifications for the different fuels. For the purpose of this analysis, the package was assumed to contain a single PWR spent nuclear fuel assembly, with a maximum decay heat load of 8,530 Btu/hr (2.5 kW). This fuel configuration and maximum decay heat load is used for the thermal evaluation of the package presented in the SAR [11], and provides a conservative thermal load for the fire accident scenario.

The loaded package weighs approximately 52,000 lb (23,586 kg). The containment boundary provided by the stainless steel package consists of a bottom plate, outer shell, upper ring forging, and closure lid. The package has an additional outer stainless steel shell to protect the containment shell, and also to enclose the lead gamma shield. Neutron shielding is provided by a stainless steel neutron shield tank containing a water/ethylene glycol mixture. An additional annular expansion tank for the mixture is provided, external to the shield tank. This component is strengthened internally by a network of stainless steel stiffeners. Aluminum honeycomb impact limiters covered with an aluminum skin are attached to each end of the package. Additional configuration details are provided in the SAR for this transport package [11].

5 ANALYSIS APPROACH

The analytical approach chosen to evaluate the response of the selected transportation packages was to construct highly detailed analysis models capable of accounting for all the significant heat transfer paths to and from the package by means of conduction, convection, and thermal radiation. All three transportation package models were constructed in parallel to expedite the evaluation. Two different computer analysis codes were used for the large multi-assembly packages, to provide independent verification of the analytical approach. The TN-68 package was modeled using the COBRA-SFS finite-difference thermal-hydraulic analysis code [2]. The HI-STAR 100 and NAC LWT packages were modeled using the ANSYS [3] general purpose FEA code. Three-dimensional (3D) models of each of the packages were developed for these analyses. These models were subjected to boundary conditions (see Section 6) derived from a detailed simulation of the Howard Street tunnel thermal environment during and after the fire, performed with the FDS code. (See Section 2 for a discussion of the NIST analysis of the Howard Street tunnel fire and the selected fire scenario for these analyses.)

Section 5.1 presents a general description of the representation of the SNF packages within the tunnel environment. Section 5.2 contains a detailed description of the COBRA-SFS model of the TN-68 package. The ANSYS model of the HI-Star 100 is described in Section 5.3, and Section 5.4 contains a description of the ANSYS model of the NAC LWT.

5.1 Modeling SNF Packages within Tunnel

Boundary conditions for the models of the SNF packages were taken from the results of the FDS analysis at 66 ft (20 m) down stream of the fire source. This location was determined from the configuration of the rail cars within the tunnel relative to the fire, as shown in Figure 5.1. The selected location corresponds to the shortest possible distance between the tank car carrying liquid tripropylene and the nearest rail car that could have been carrying an SNF package on this particular train.

Other possible derailment configurations were examined by the staff, based on behavior commonly exhibited by rail cars that have derailed. Figure 5.2 depicts a common derailment scenario involving a single bore tunnel where the distance between the side walls is twice the width of a rail car. As can be seen from the diagram, a derailment that results in a decoupling of the rail cars and an "accordion" placement of the rail cars would actually move the cars further apart than an in-line derailment of the type that occurred in the Howard Street tunnel.

The assumed location of the SNF package in this analysis is based on Department of Transportation regulations that require rail cars carrying radioactive materials to be separated from other cars carrying hazardous materials or flammable liquids by at least one innocuous rail car (referred to as a buffer car) [12]. The dimensions of the Howard Street tunnel (depicted in Figure 5.3) would not have allowed a rail car carrying an SNF package to come any closer to the tripropylene tank car. Even if the buffer car is assumed to be a flat rail car, it would be essentially impossible, given the velocity of the train at the time of the derailment, for the buffer car to slide past either the tripropylene tank car or a rail car carrying a SNF package, and thereby decrease the distance between the SNF transportation package and the fire.

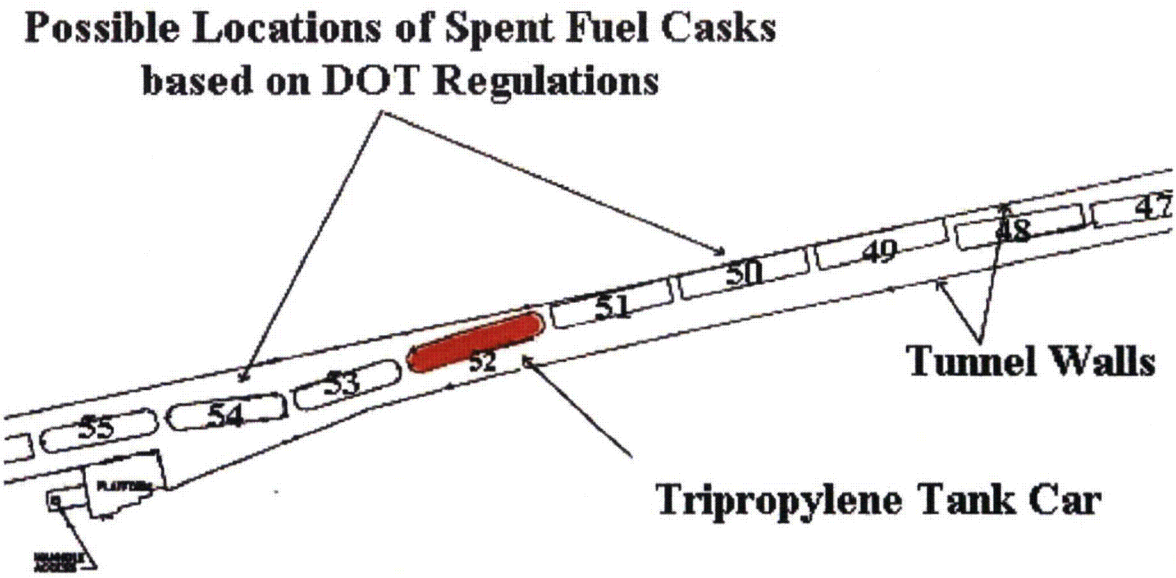

Figure 5.1. Configuration of Derailed Train in Vicinity of Fire

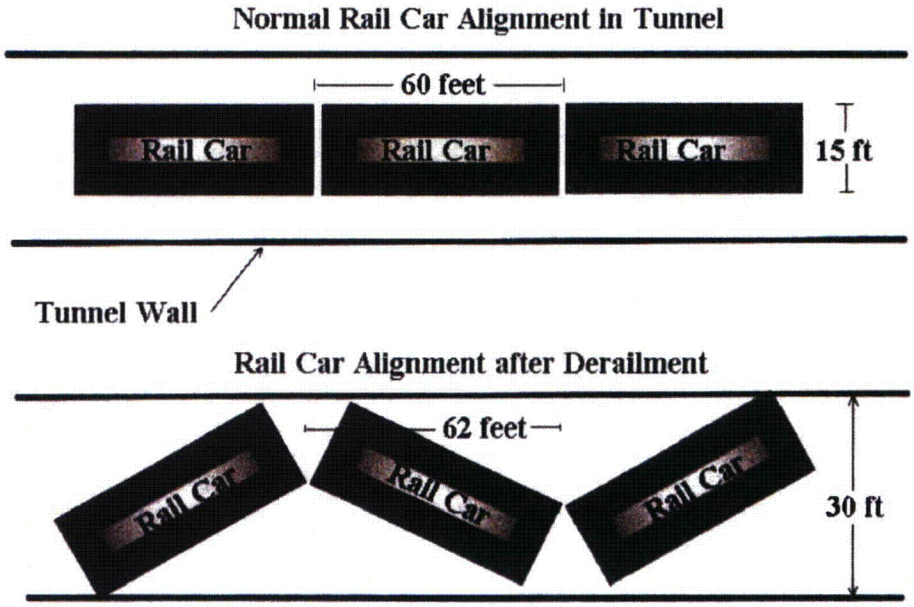

Figure 5.2. Possible Orientation of Derailed Train in Tunnel

The package was assumed to remain on the rail car in a horizontal position with one end of the package facing the fire source. This orientation results in maximum possible exposure to the fire-driven flow of hot gas along the length of the package, and is the most adverse position for free convection cooling of the package during the post-fire cool down. It also results in the maximum exposure of package surfaces to tunnel surfaces for thermal radiation exchange. This is a particularly important consideration, since radiation heat transfer to the package is the most significant mode of heat transfer during and immediately following the fire, by at least an order of magnitude.

Alternative orientations for the SNF package in this accident scenario, however plausible, would result in less severe boundary conditions during the fire transient. A vertical orientation for the package on the rail car would result in decreased exposure to the fire-driven flow of hot gas around the package and enhanced free convection cooling during the post-fire cool down phase of the transient. This orientation would also result in a decrease in thermal radiation interaction with the tunnel surfaces, due to attenuated view factors. In particular, the axial length of the package would not have the direct (essentially parallel) view of the tunnel ceiling that it has on its upper side in the horizontal orientation.

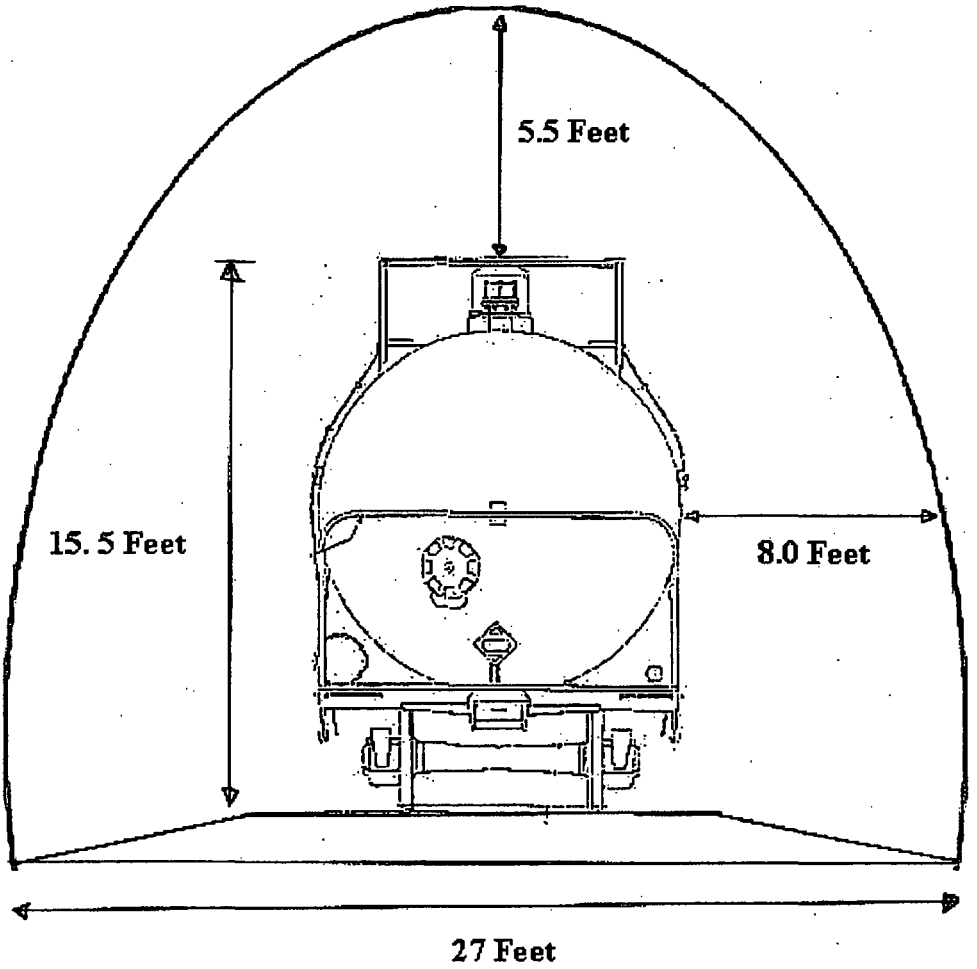

Figure 5.3. Dimensions of Howard Street Tunnel with Tank Car on Track

Postulating that the SNF package would separate from the rail car would also result in less severe boundary conditions on the package, even assuming that the package ended up closer to the fire. In such a scenario, the package would be on the floor of the tunnel, exposed to markedly lower temperatures from the surrounding air and tunnel surfaces, compared to the boundary conditions encountered at the elevation of the package on the rail car at 66 ft (20 m) down-stream of the fire. This position would also tend to attenuate thermal radiation interaction with the hottest surfaces in the tunnel (i.e., the ceiling and upper side walls).

As discussed in Section 2, the FDS simulation used to define the boundary conditions for this analysis modeled a hypothetical fire scenario with greatly enhanced ventilation, in order to fully consume the available fuel supply at a fully oxygenated burn rate, and a minimal fuel pool size, in order to achieve the highest possible fire temperatures. This extremely conservative scenario resulted in a fire lasting approximately 7 hours, with increasing temperatures at the assumed location of the SNF package in the tunnel for the entire fire duration. In the FDS analysis, the calculation was extended out to a 23-hour post-fire cool down, for a total simulation time of 30 hours. To determine the packages' complete transient temperature responses, and to explore the effects of prolonged exposure to post-fire conditions in the tunnel, the COBRA-SFS and ANSYS analyses further extended the post-fire duration to 300 hours. Tunnel wall and air temperatures predicted in the FDS analysis at 30 hours were extrapolated from 30 hours to 300 hours using a power function, to realistically model cool-down of the tunnel environment.

The FDS analysis utilized a fine-mesh noding that yielded detailed predictions of axial and radial distributions of tunnel air temperatures, gas velocities, and tunnel surface temperatures throughout the fire and post-fire cool down period. As a conservative approach to defining the thermal environment seen by the SNF packages during the fire, the peak air temperatures predicted in the FDS simulation in the top, middle, and bottom regions of the tunnel were used to define the boundary conditions around the corresponding regions on the circumference of the package during the transient. These temperatures were used to define the local ambient temperatures for convection heat transfer from the surfaces of the packages. Similarly, the peak tunnel surface temperatures on the ceiling, side walls, and floor were used to define the surface temperature boundary conditions for radiation exchange.

This conservative simplification of the detailed FDS results describing the tunnel thermal environment was implemented by dividing the tunnel cross-section into three regions, as illustrated in Figure 5.4. (This figure is a conceptual diagram, not a scale drawing; proportions have been distorted to permit labeling of boundary regions.) For the air temperature boundary conditions for convection at the package surface, the "bottom" region was defined as extending from the tunnel floor to 1 ft (0.3 m) above the floor. The "side" region was defined as extending from 1 ft (0.3 m) to 15.8 ft (4.8 m) above the tunnel floor. The "top" region was defined as extending from 15.8 ft (4.8 m) above the tunnel floor to the tunnel ceiling at 22 ft (6.7 m). Similarly, for the wall temperature boundary conditions for radiation exchange, the "bottom" region was defined as the tunnel floor; the "side" region was defined as the tunnel wall extending to 15.8 ft (4.8 m) above the tunnel floor. The "top" region included the arch of the tunnel ceiling down to 15.8 ft (4.8 m) above the tunnel floor.

The diagram in Figure 5.4 illustrates the coupling of the external thermal environment to the top, side, and bottom regions of the SNF package model, as implemented for the HI-STAR 100. For the NAC LWT,

the external boundary conditions were imposed on the ISO container, rather than the package surfaces. A similar approach was also used for the TN-68 package, except that in the COBRA-SFS analysis, the rail car and package support cradle were neglected.

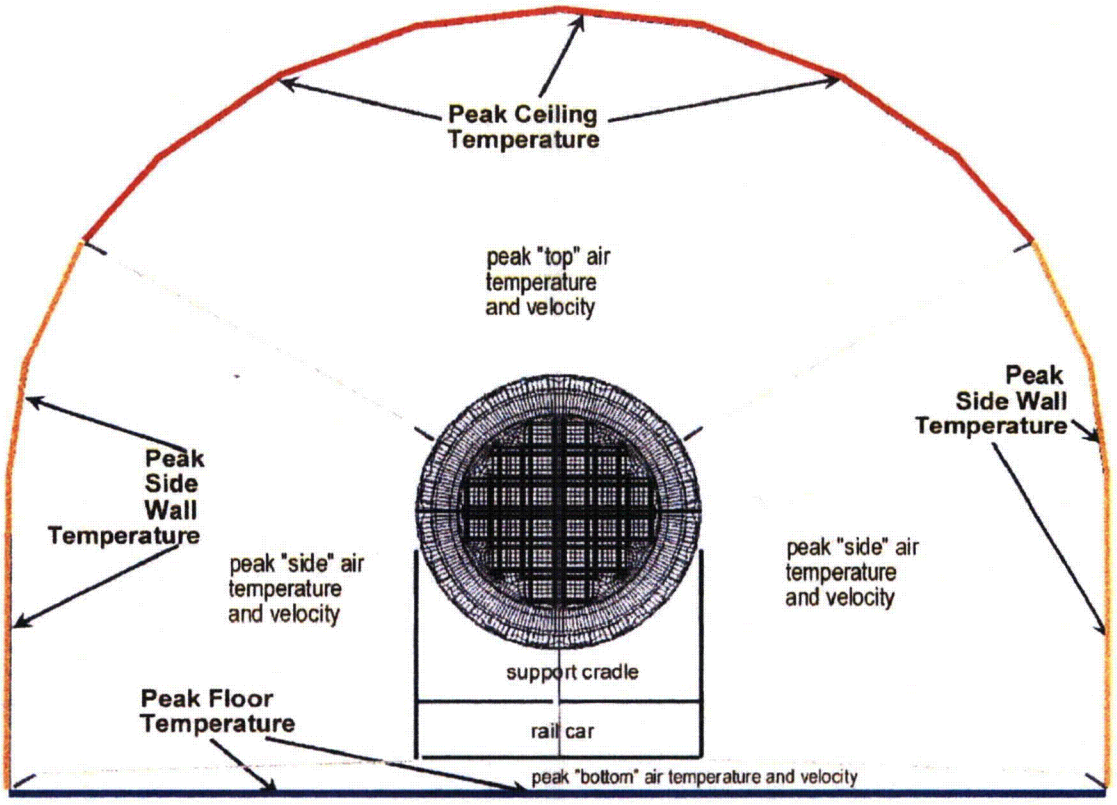

Figure 5.4. Cross-section of Tunnel (diagram not to scale) Showing "Top", "Side", and "Bottom" Regions for Fire Boundary Temperatures

5.2 Model of TN-68 Transportation Package

The TN-68 package was analyzed with COBRA-SFS, a code developed by PNNL for thermal-hydraulic analyses of multi-assembly spent fuel storage and transportation systems. The code uses a lumped-parameter finite-difference approach for predicting flow and temperature distributions in spent fuel storage systems and fuel assemblies under forced and natural circulation flow conditions. It is applicable to both steady-state and transient conditions in single-phase gas-cooled spent fuel packages with radiation, convection, and conduction heat transfer. The code has been validated in blind calculations using test data from spent fuel packages loaded with actual spent fuel assemblies as well as electrically heated single-assembly tests [13,14,15].

The TN-68 package was modeled in COBRA-SFS as a one-half section of symmetry. Figure 5.5 shows a diagram of the center cross-section of the basket and support rails as represented in the COBRA-SFS

model. The fuel assemblies within the basket are each modeled as detailed rod and subchannel arrays, and the tubes containing the fuel assemblies are represented using solid conduction nodes.

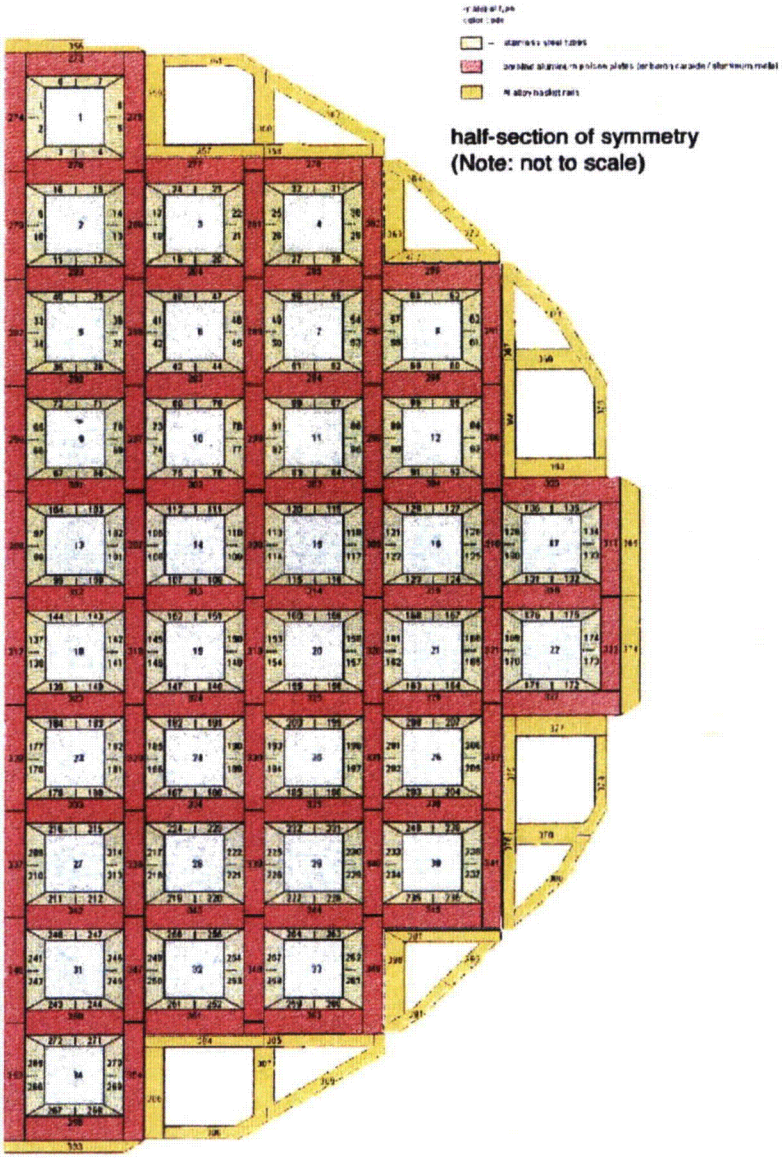

Figure 5.5. COBRA-SFS Model of TN-68 Basket and Support Rails

The aluminum and borated aluminum neutron poison plates sandwiched between the tubes are represented as an interconnected network of solid conduction nodes. The gamma shielding, neutron shielding, and outer steel shell are represented with concentric rings of interconnected solid conduction nodes with appropriate material properties. (For clarity, these nodes are not included in the diagram shown in Figure 5.5.) The half-section of the TN-68 package is represented with approximately 69,000 fluid nodes, 53,000 fuel nodes, and more than 16,000 solid conduction nodes.

The solid conduction nodes extend over 32 axial divisions comprising the axial length of the package. In cross-section, the stainless steel tubes containing the fuel assemblies are represented using two solid conduction nodes on each face of the enclosure, for a total of eight nodes per tube. The aluminum and borated aluminum neutron poison plates sandwiched between the tubes are represented as an interconnected network of solid conduction nodes that are in intimate physical contact with the stainless steel tubes and with each other. A total of 272 nodes are used to represent the 34 steel tubes in the half-section of symmetry. The borated aluminum neutron poison plates making up the rest of the basket are modeled with a total of 83 solid conduction nodes. The aluminum alloy basket rails are represented with a total of 36 solid conduction nodes, and provide appropriate thermal connections between the basket and the steel inner gamma shield.

The gamma shielding, neutron shielding, and outer steel shell are represented in the COBRA-SFS model as concentric rings of interconnected solid conduction nodes. The spent fuel arrays within the basket are assumed to be 7 x 7 BWR assemblies (the design basis fuel loading for the TN-68, as specified in the SAR [9]). Each assembly is modeled in detail, with 49 rods and 64 subchannels.

In cross-section, the gamma shielding is represented with two rings of 16 nodes each, representing the inner and outer steel shells of this component. The neutron shield in cross-section is represented with three rings of nodes (for a total of 48 nodes), with properties and connections defined to represent the material properties and thermal interactions of the ring of aluminum boxes filled with borated polyester. In cross-section, the outer steel shell of the package is represented with a ring of 16 nodes, with appropriate thermal connections to the neutron shielding on one side and ambient air on the other.

The COBRA-SFS model was verified by running the steady-state case for design basis normal hot transport conditions. The predicted peak clad temperature for these conditions was compared with the peak temperature reported in the SAR. The code predicts a peak clad temperature of 485°F (252°C); the SAR gives a value of 490°F (254°C) for these conditions (see Chapter 3, Table 3-1 in the SAR [9]).

The steady-state solution obtained for normal hot transport conditions was used to define the pre-fire condition for the package in the transient calculations simulating the Baltimore tunnel fire. This provides a reasonably conservative estimate of the initial temperatures throughout the package, since the boundary conditions for normal hot transport are specified as 100°F (38°C) ambient temperature in still air with insolation.

The external air temperatures predicted for the fire in the NIST simulation are sufficiently high to boil off the borated polyester neutron shield and completely char the wooden impact limiters. In both cases, the normal material would be replaced with material that would tend to insulate the package from the fire (i.e., air in place of the borated polyester, charred wood in place of the wooden impact limiter material).

To maximize the heat load to the package from the fire, it was assumed for the purposes of the calculation that these materials would persist intact throughout the fire (rather than gradually degrading or burning off). Then at the end of the fire (6.75 hours into the transient), these materials would be instantly transformed to a degraded condition. For the nodes modeling the neutron shield, this was simulated in the calculation by changing the material properties to those of hot air at the end of the fire. The material

properties specified for the nodes modeling the wooden impact limiters were changed from redwood to charcoal at the end of the fire.

The material properties from the package vendor's SAR were verified and then used in the analyses [9]. The material properties used in this evaluation are given in Appendix A.

5.3 Model of HI-STAR 100 Transportation Package

The ANSYS model of the HI-STAR 100 package consists of a detailed three-dimensional representation of a half-section of symmetry for the package, its cradle support[15], and the rail car decking directly below the cradle. (The remainder of the rail car was omitted from the model, as a conservatism, because it would partially shield the package from thermal radiation from the hot tunnel surfaces and block convection heat transfer to the package due to the flow of hot gas generated by the fire.) This half-section model of the package was placed within a complete cross-section of the surrounding tunnel.

The model developed for the HI-STAR 100 package utilized 120,412 SOLID70 and 1,542 SHELL57 thermal elements for conduction. It used two groups of 13,573 SURF152 surface effect elements for handling convection states in the pre-fire steady state and the fire accident transient. For radiation interaction, 288 highly structured AUX-12 generated MATRIX50 superelements were constructed using SHELL57 elements. Solar insolation (from 10CFR71 [1]) for the pre-fire condition was assigned via heat generation to the first group of 13,573 SURF152 surface effect elements. A portion of the model is shown in Figure 5.6. (In this figure most of the tunnel has been omitted for clarity.)

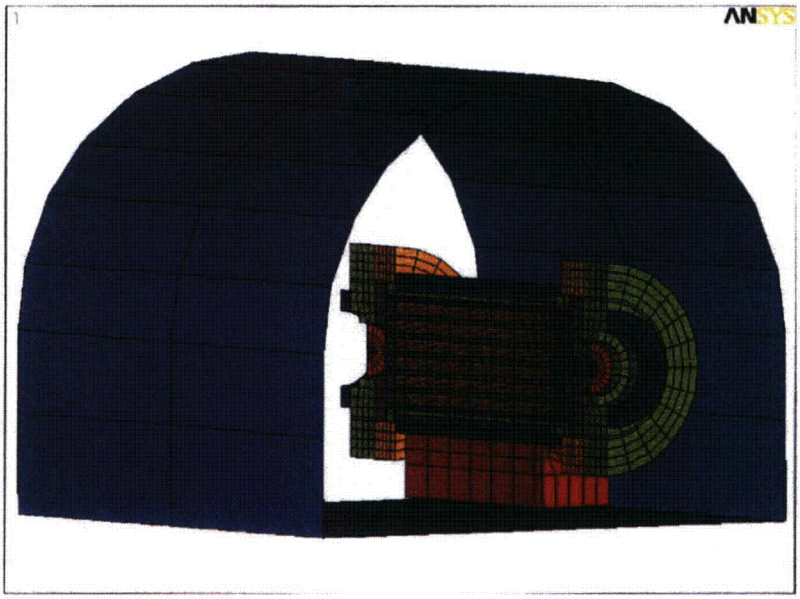

Figure 5.6. ANSYS HI-STAR 100 Package Analysis Model Element Plot

[15]Dimensions and materials for the rail car decking and the cradle were based on specifications (as of June 2005) from the package vendor. Cradle design determines the height of the package within the tunnel, the geometry of direct conduction paths to and from the package, and can affect thermal shielding of the package during the fire.

The material properties from the package vendor's SAR were verified and used in the analysis [10]. The model explicitly represents the geometry of the package, including the internal geometry of the fuel basket, all gaps associated with the basket construction, as well as the integral neutron absorber plates. Figures 5.7 through 5.11 show cross-sections of the HI-STAR model highlighting key features that were included.

Figure 5.7 shows the cross-section of the package, canister, cradle, and transport car section. In this figure, all helium conduction volumes have been removed for visualization purposes. The cradle and rail car sections were modeled as hollow enclosures. All internal thermal radiation exchange for these two enclosures were accounted for using AUX-12 generated MATRIX50 superelements (constructed with SHELL57 elements). Convection influences were accounted for using SURF152 elements with the extra node option.

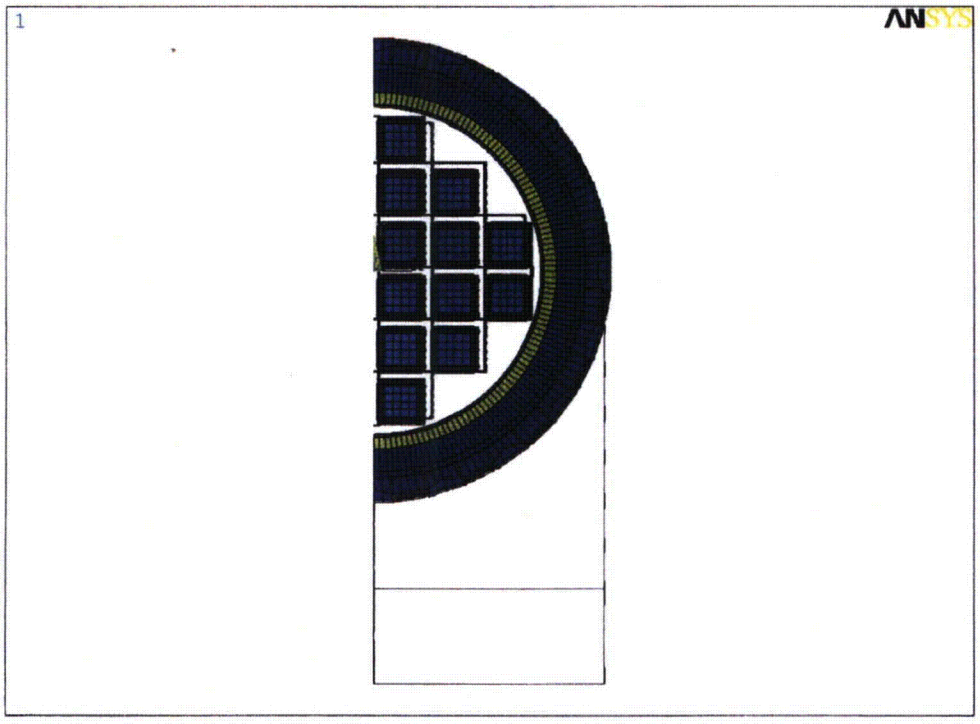

Figure 5.7. Cross-section of Package, Cradle, and Rail Car Section

Conduction within the cradle and trailer material sections was also accounted for using additional SHELL57 elements with thickness option applied. Natural convection correlations and specially constructed automated subroutines written in ANSYS Parametric Design Language (APDL) were used to continuously evaluate and update the convective coefficients of heat conductance. Fourteen separate passive computation nodes were assigned as "extra nodes" for the SURF152 surface effect elements used in specifying the convection interaction within the cradle and rail car section (seven for each – not shown in Figure 5.7). Section 6 presents a discussion of the natural convection correlations used in this analysis.

Figure 5.8 shows the cross-section of the package and canister, with the overall basket structure. As in Figure 5.7, all helium conduction volumes have been removed for visualization purposes. This figure shows the fuel compartment layout within the MPC-24 basket structure, and includes the inner shell (light green), gamma shield (dark blue), and the neutron shield (purple) components of the HI-STAR 100.

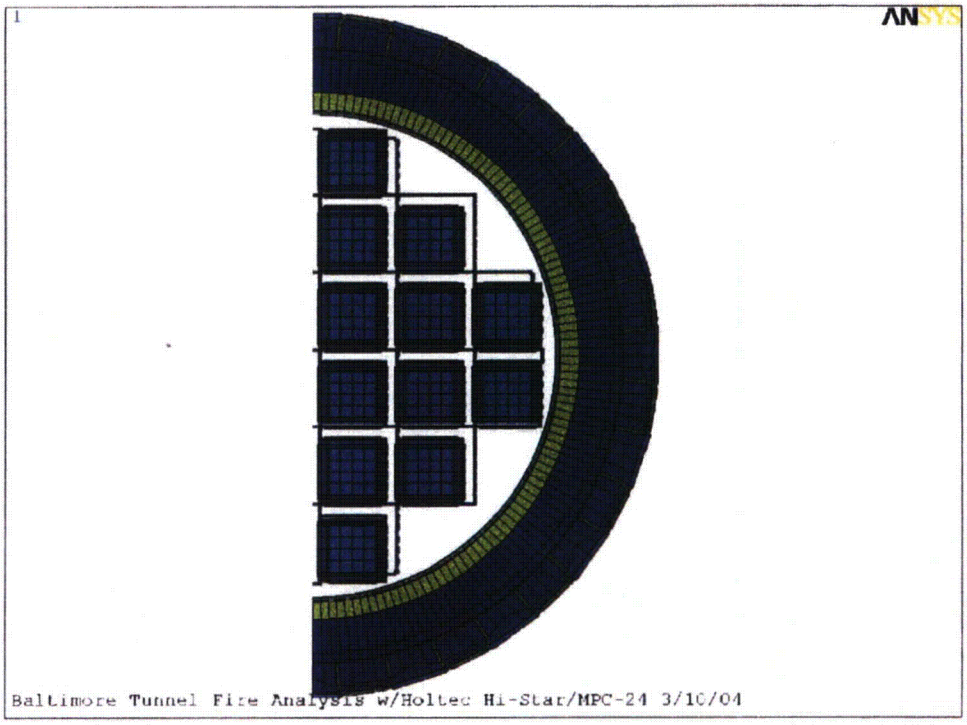

Figure 5.8. Cross-section of HI-STAR Package and MPC-24 Canister

The model cross-section in Figure 5.9 shows that the fillet welds joining the sections of the package outer skin and the expansion foam in the neutron shield area have been modeled explicitly. Special element material definitions were created for the elements providing the connection between the fins enclosing the neutron shield and the gamma shield. The material definition was specified such that the thermal conductivity could be readily degraded to represent the effect of single-sided fillet welds (i.e., not full penetration) that are used in this connection. Since the thermal conductivity through single-sided fillet welds is difficult to determine objectively, the conductivity of this material in the pre-fire steady state and post-fire transient was conservatively reduced to half of that of the solid base material. The effect of this assumption is to conservatively minimize the rejection of internal heat. During the fire, however, the thermal conductivity of these elements was assumed to be the same as the solid base material, mimicking that of a full penetration weld. This approach was used to conservatively maximize the heat input into the package during the fire.

Special material definitions were also created for the elements making up the multi-layer steel gamma shield (dark blue in Figures 5.8 and 5.9). To account for the probability of gaps between the five steel shells due to standard manufacturing practices, a gap of 0.01 inch was assumed to exist between each layer. Effective material thermal conductivities were then calculated for the gaps, accounting for

conduction through gas in the gap and radiation across the gap. These material property definitions were used in the pre-fire steady state and the post-fire transient to conservatively minimize the rejection of internal heat; However, during the fire, the conduction properties of these elements were reassigned to that of solid material (i.e., equivalent to assuming no gaps between these layers during the fire), to conservatively maximize the heat input into the package. A complete list of the material properties used in this evaluation is presented in Appendix B.

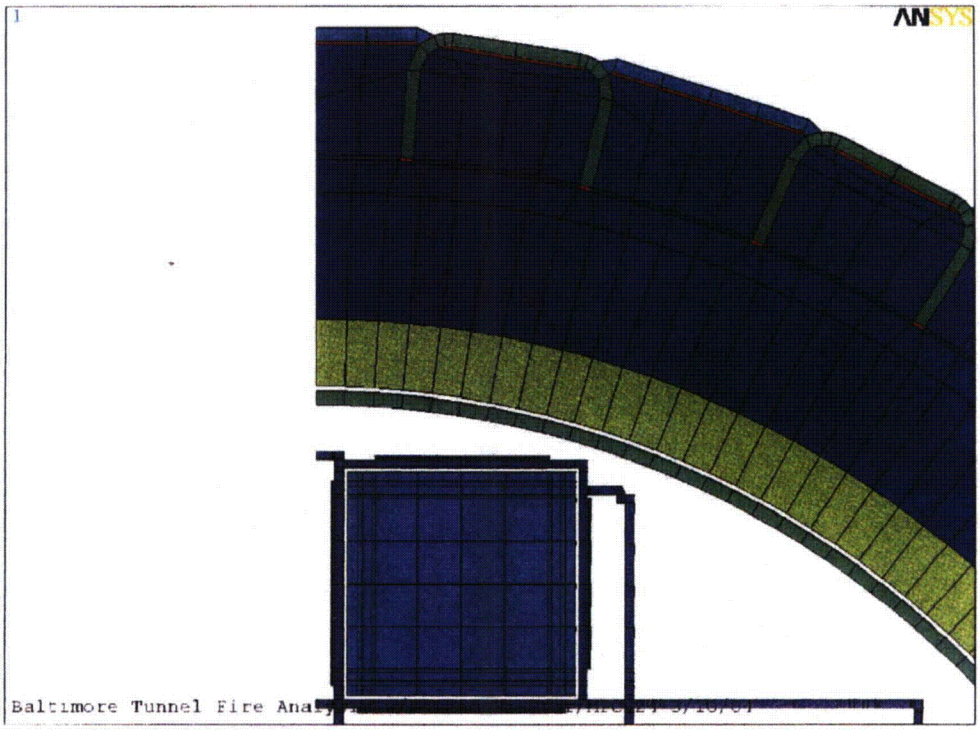

Figure 5.9. Close-up of Package Cross-section

Figure 5.10 presents a detailed view of the basket cross-section showing a typical basket fuel compartment (purple) containing a homogenized fuel assembly (light blue) surrounded by Boral sheets and their associated sheathing. Also shown in this figure are the MPC canister shell (blue-green) and the package containment/inner shell (lime). The same features are shown in Figure 5.11 with the elements for the helium regions included.

Westinghouse 17x17 OFA fuel was modeled in this evaluation. The effective fuel conductivity in the radial direction was determined using the approach documented in the HOLTEC SAR [10]. This approach uses a homogenization scheme similar to that presented by Bahney and Lotz [16], modified to include a helium gap between the homogenized fuel region and the fuel compartment, and the effect of cover gas pressurization.

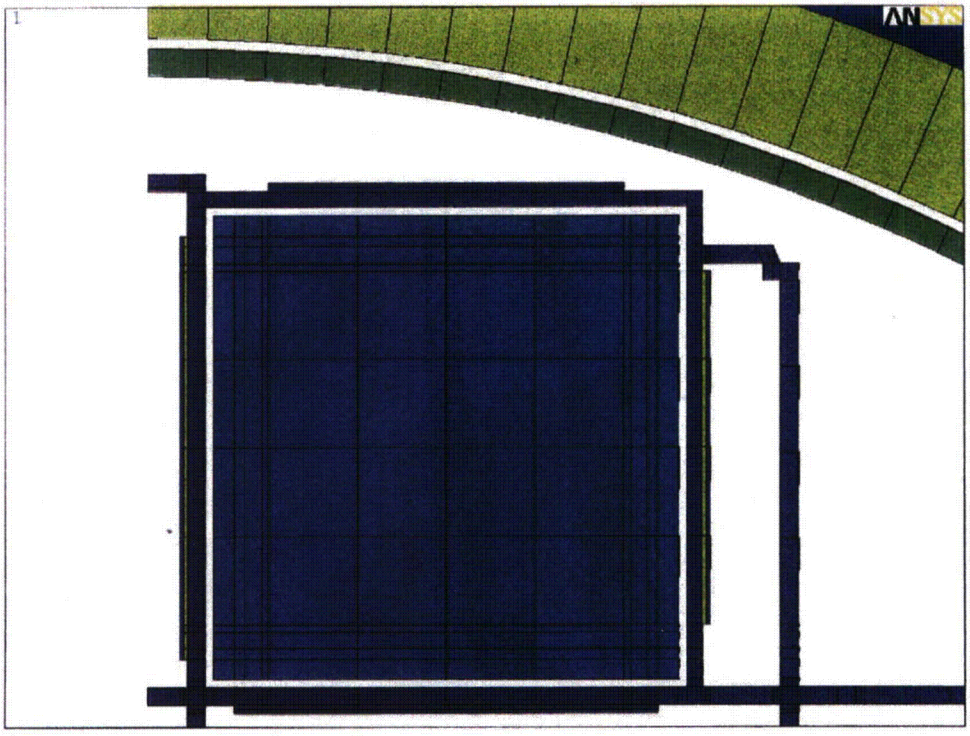

Figure 5.10. Close-up of Canister Basket and Fuel Compartment (without helium elements)

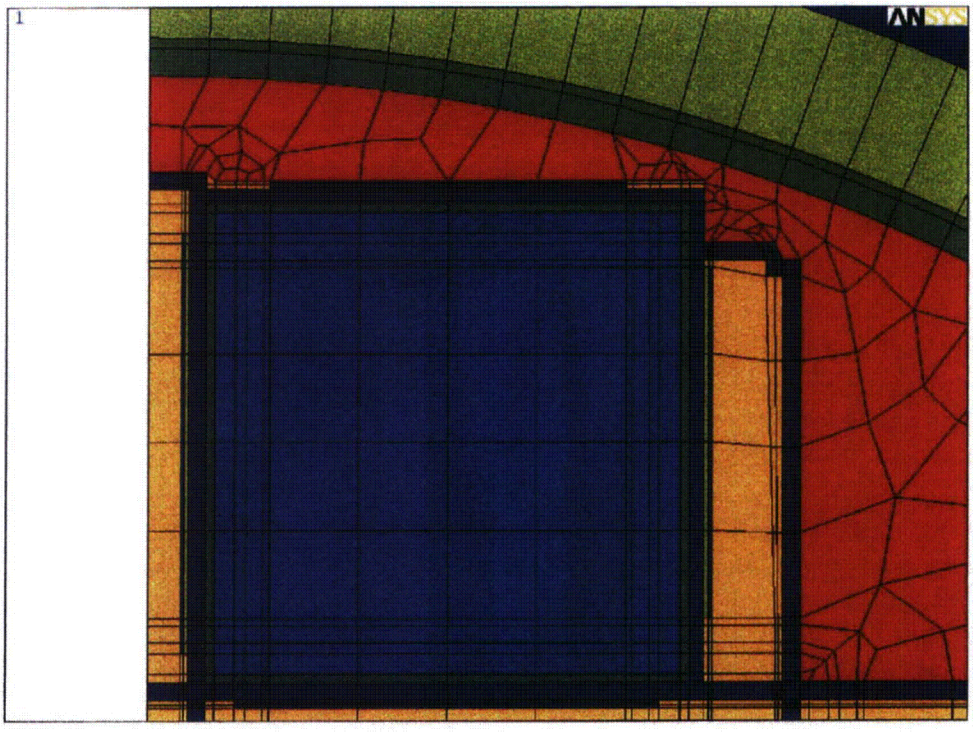

Figure 5.11. Close-up of Canister Basket and Fuel Compartment (with helium elements)

Axial conductivity for the homogenized fuel region was modeled with the cladding as the only conduction medium, using a cross-sectional area weighting scheme. The remaining portion of the homogenized region was considered to be helium. Density and heat capacity were based on volumetric averages of the cover gas, cladding, upper and lower end fittings, and uranium dioxide fuel. A normalized peaking factor of 1.1 (from the design basis axial power distribution in the SAR [10]) was used to establish the volumetric heat generation of 2,843 Btu/hr (0.833 kW) over each assembly along the active fuel length. Orthotropic effective conductivity properties were developed for the Boral to include the radiation and conduction heat transfer components through an assumed helium gap of 0.0035 inch between the Boral sheet and its stainless sheathing, and between the Boral and stainless basket structure.

Radiation interaction within the basket, canister, and package was modeled by unselecting all helium regions and coating each interacting set of surfaces forming an enclosure with SHELL57 elements with specified emissivities. The SHELL57 elements were then used to produce highly structured AUX-12 generated MATRIX50 superelements, each defined by an enclosure. A total of 269 MATRIX50 superelements were defined to capture the radiation interaction within the package and canister. Figure 5.12 shows an element plot of the top impact limiter honeycomb core and steel substructure of the HI-STAR 100 package, including the Holtite-A neutron shield material sections. (The impact limiter skin is omitted for visual clarity.) The bottom impact limiter is similar to the top impact limiter, except for the bolting configuration and the extended steel ring covering the top forging, lid, and buttress plate. Figure 5.13 shows the top impact limiter skin and support structure, without the honeycomb core and the neutron shield materials included.

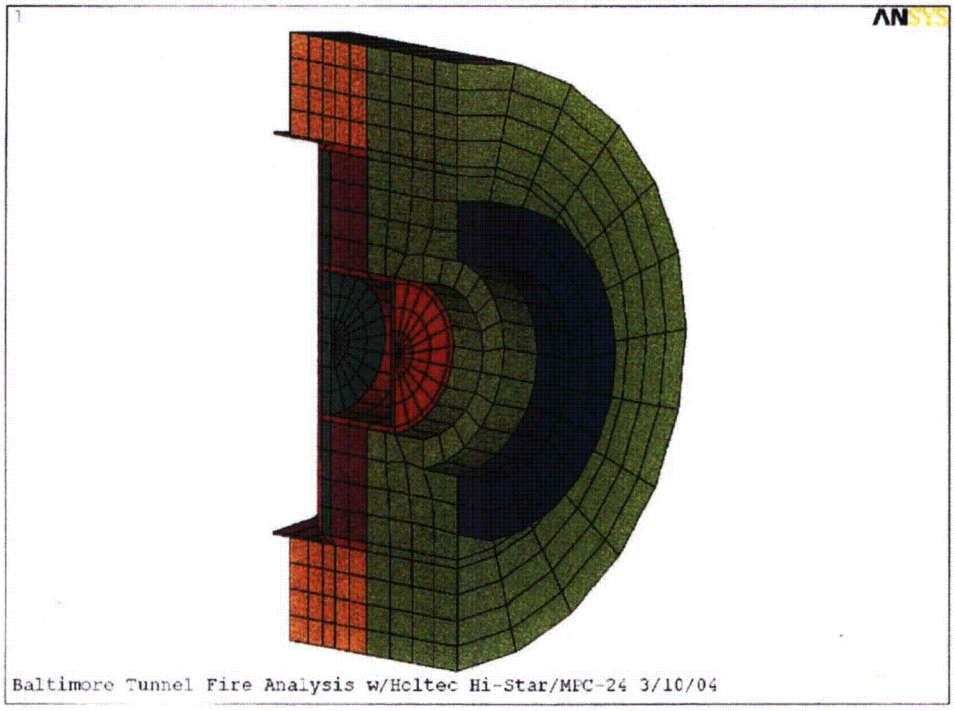

Figure 5.12. Complete Impact Limiter (Except Skin)

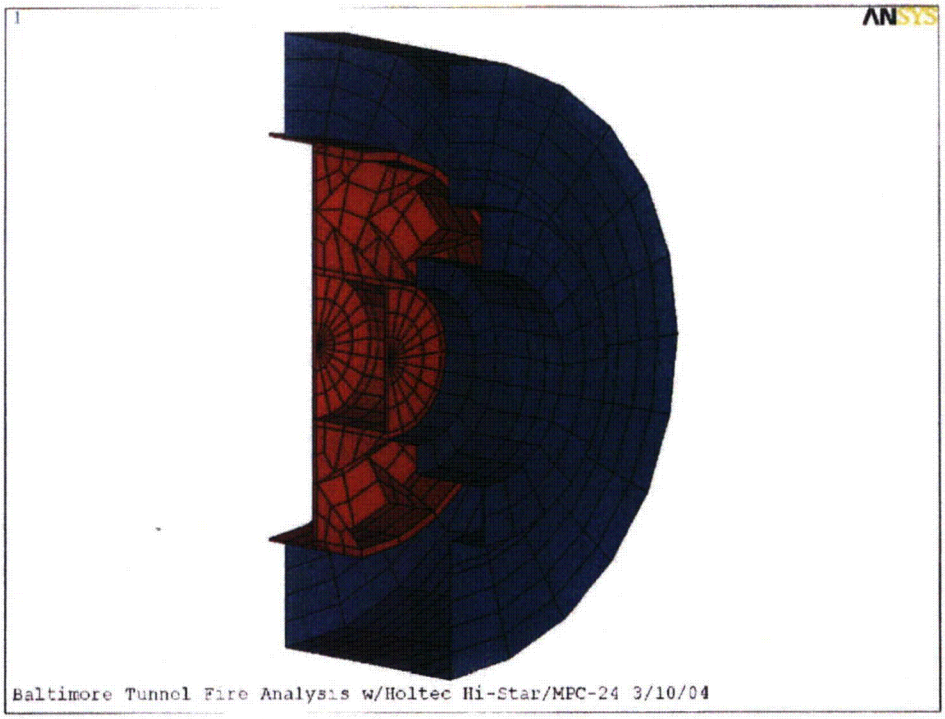

Figure 5.13. Impact Limiter Skin and Primary Support Structure

The impact limiters are assembled with five different types of honeycomb sections. Gaps between the honeycomb sections, the steel substructure, and skin were conservatively ignored to maximize heat input during the fire. Thermal properties for the honeycomb sections were based on volumetric averages of each section using properties published by the honeycomb manufacturer [17]. Radiation interaction between the package ends and impact limiters was modeled by coating each respective interacting set of surfaces with SHELL57 elements with specified emissive material properties. The SHELL57 elements were then used to produce highly structured AUX-12 generated MATRIX50 superelements. A total of 16 MATRIX50 superelements were defined to capture the radiation interaction between the package and impact limiter surfaces.

Conduction and natural convection heat transfer between the package and impact limiter surfaces was handled using SURF152 surface effect elements. Correlations and specially constructed automated subroutines written in APDL were used to continuously evaluate and update the assigned convection coefficients of heat conductance.

Sixteen separate passive computation nodes were assigned as "extra nodes" for the SURF152 surface effect elements used in specifying the convection interaction within the cradle and rail car section. (The natural convection correlations used are presented in Section 6.) Convection coefficients of heat conductance were conservatively boosted by a multiplicative factor of 100 between limiter and package during the fire to mimic enhanced heat conduction at this interface due to rapid thermal expansion. These values were returned to normal after the end of the fire.

The tunnel structure was represented by an enclosure approximately 22 ft (6.7 m) high by 27 ft (8.2 m) wide and 42 ft (12.8 m) long. The tunnel enclosure was divided into three regions; top, side, and bottom (as illustrated in Figure 5.4). The bottom region consisted of the floor of the enclosure. The top region was conservatively considered to be all surfaces in the range from 15.8 to 22 ft (4.8 to 6.7 m). All surfaces from the floor to 15.8 ft (4.8 m) were considered to be the side region. The specified boundary temperatures for each region section are the maximum calculated in that region (top, side, and bottom, corresponding to ceiling, wall, and floor in the FDS simulation from NIST; see Section 6). The enclosure was capped at both ends and assigned the same boundary condition on the end caps as on the walls and ceiling. As specified by dimensions of the rail car decking and cradle, the transport system was located such that the center axis was 8.2 ft (2.5 m) above the tunnel floor, leaving 12.2 inches (31 cm) underneath the lowest part of the rail car decking.

To determine the convection heat transfer to the package during the fire scenario, the exposed surfaces of the package were also divided into three regions. The top region was defined as all surfaces above an elevation of 9.4 ft (2.9 m). The bottom section was defined as the bottom of the rail car segment of the model. The side surfaces of the package were conservatively defined to be all remaining outer surfaces of the package. The surface elements of each of these sections are pictured in Figures 5.14, 5.15 and 5.16. Forced and natural convection correlations and specially constructed automated subroutines written in APDL were used to continuously evaluate and update the assigned convective coefficients of heat conductance for the surface of the package during pre-fire, fire, and post-fire phases based on gas velocity. The bottom surface of the rail car section was the only surface influenced by convection heat transfer in the bottom gas region. In actuality, none of the "top" surfaces would be directly exposed to the highest temperature gas region at the top of the tunnel, because the package is not positioned that high in the tunnel. This assumption therefore represents an additional conservatism in the analysis.

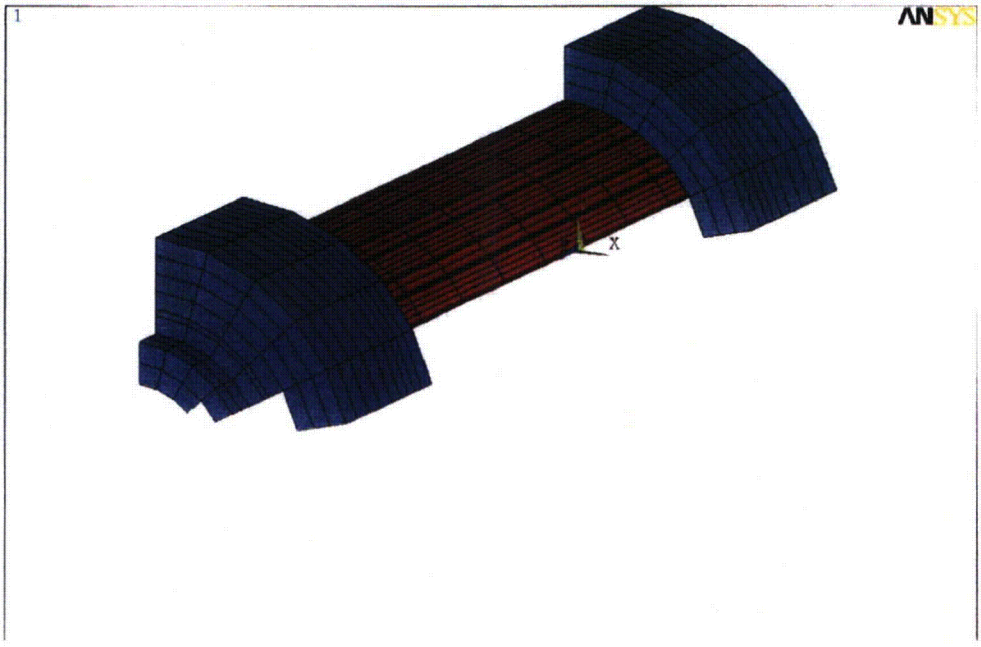

Figure 5.14. Surfaces Defined for Interaction with "Top" Gas Region

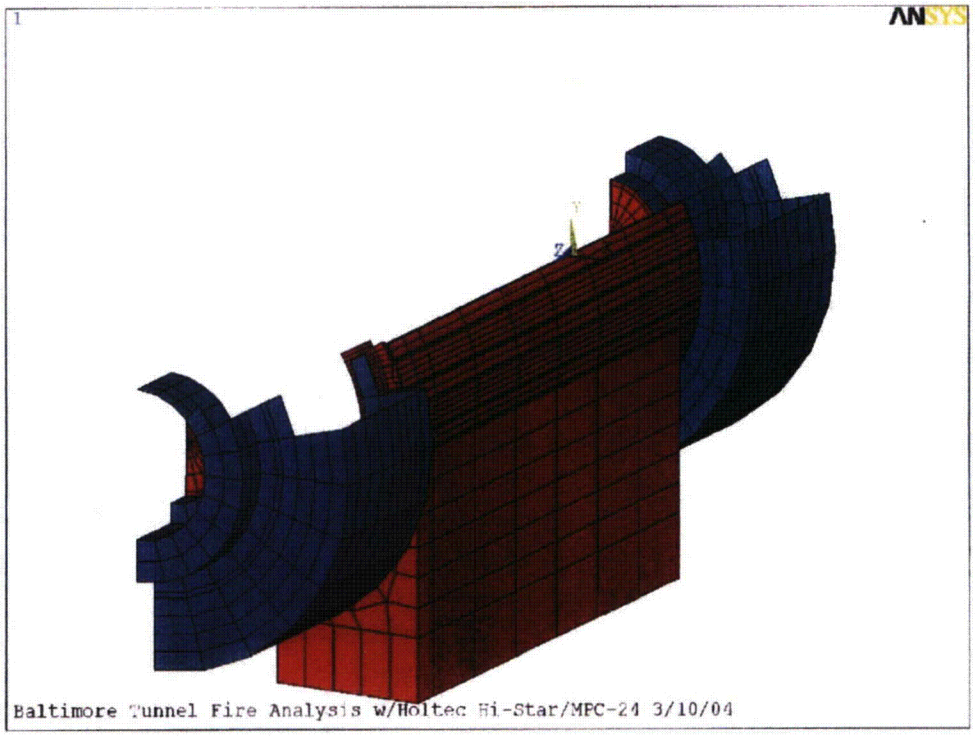

Figure 5.15. Surfaces Defined for Interaction with "Side" Gas Region

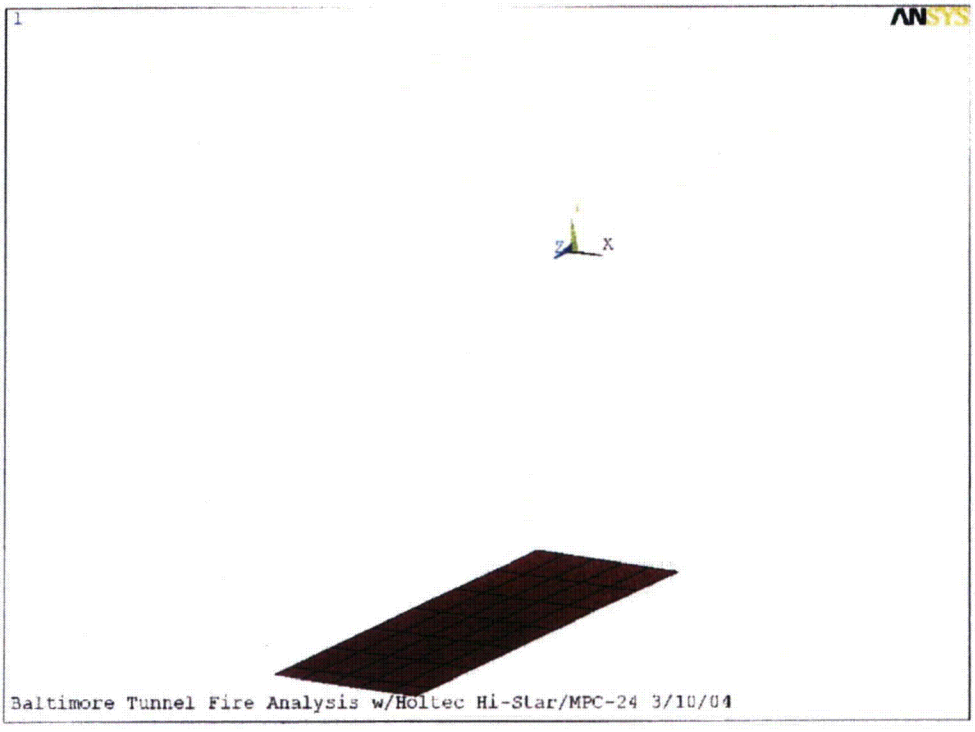

Figure 5.16. Surfaces Defined for Interaction with "Bottom" Gas Region

Radiation interaction between the transport system (with its partial conveyance) and the tunnel surfaces was established by coating all respective interacting surfaces with SHELL57 elements with specified emissive material properties. The SHELL57 elements were then used to produce a highly structured AUX-12 generated MATRIX50 superelement.

The Baltimore tunnel fire evaluation of the HI-STAR 100 was conducted in three phases. These were the pre-fire, fire, and post-fire phases. For the pre-fire phase, the hot-normal conditions of transport were evaluated assuming solar insolation and a 100°F (38°C) ambient temperature, in accordance with 10CFR71.71 [1]. This conservatively established initial component temperatures. During this phase, the fillet welds joining the fins to the gamma shield were specified with their realistically reduced conduction and conservative gas gaps were assumed between the layers of the gamma shield.

For the fire phase of the evaluation ($0 < t \leq 7$ hr), solar insolation was shut off, the tunnel surfaces were introduced, and the transport package and tunnel surfaces were assigned an emissivity of 0.9 to represent surfaces affected by sooting. Air gaps originally assumed to be present between the gamma shield plates in the initial pre-fire steady state were closed, and perfect contact for conduction was assumed to exist where the heat fins attach to the gamma shield. Convection coefficients of heat conductance were conservatively multiplied by a factor of 100 between the impact limiters and package body to mimic enhanced heat conduction due to rapid thermal expansion. In addition to these conservative measures, all aluminum honeycomb and neutron shield resin materials were assumed to remain intact during the full duration of the fire, to maximize heat input during the fire.

For the post-fire phase ($t > 7$ hr), aluminum honeycomb sections that exceeded an average temperature of 1220°F (660°C) and all neutron shield material sections were degraded to thermal properties of air. The energy that would be absorbed due to phase change in this material was not subtracted from the heat input into the package. In addition, all gamma shield gaps and reduced fin fillet weld conduction properties were reintroduced. Finally, convection coefficients of heat conductance between the impact limiters and package body were returned to normal for the remainder of the simulation.

5.4 Model of NAC LWT Transportation Package

The model for the NAC LWT package constructed in ANSYS is similar in structure to the HI-STAR 100 model described in Section 5.3, with the additional feature that the NAC LWT package is enclosed in an ISO container[16]. A detailed 3-D model of a half-section of symmetry was developed for the package and ISO container, within the same tunnel geometry as that used for the HI-STAR 100 model. A diagram of the package and shipping container model and partial tunnel is shown in Figure 5.17. The model used 40,333 SOLID70 8-node brick elements and 3,409 SHELL57 4-node quadrilateral thermal elements to represent the structural components. A total of 6,931 SURF152 elements were used to incorporate radiation and convection heat transfer to the ISO container and tunnel environment for the various surfaces, and 12 MATRIX50 elements were used to model radiation heat exchange between package

[16] The CoC for this SNF package requires that it be enclosed in either a personnel barrier (PB) or an ISO container. Current DOE policy requires an ISO for truck casks shipped by rail, and every rail shipment of the LWT to date has been in an ISO container.

surfaces. The surface effect elements were also used to generate solar insolation loads for calculation of the initial temperature distribution for the package.

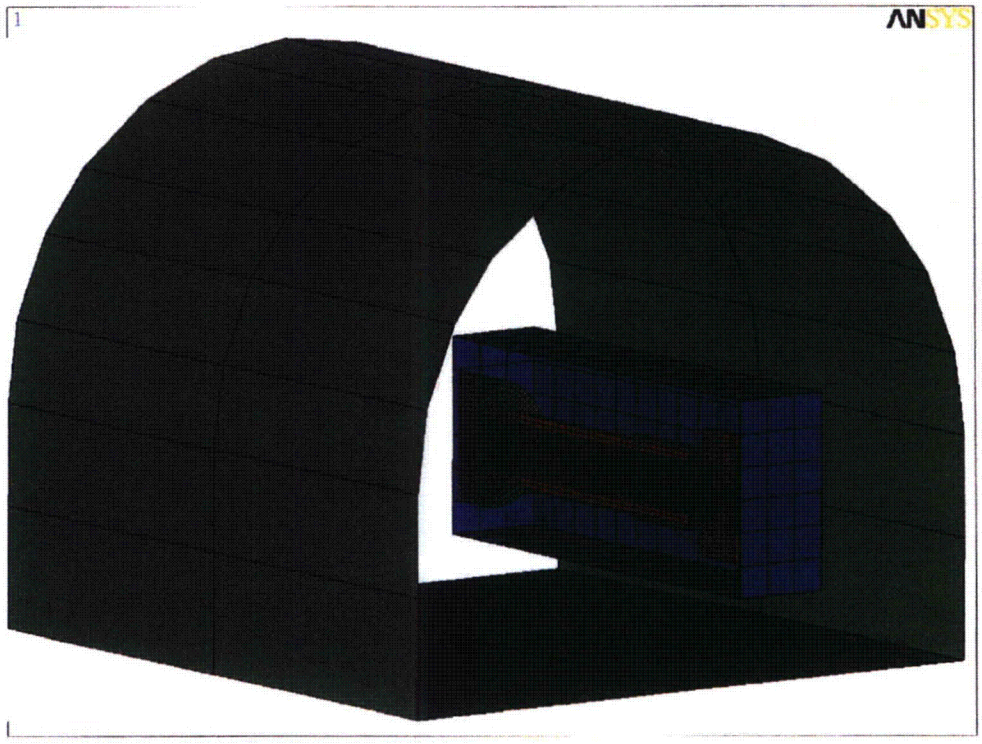

Figure 5.17. ANSYS NAC LWT Package Analysis Model Element Plot

The model geometry was developed from the vendor's engineering drawings from the package SAR [11]. The model cross-section is shown in Figure 5.18. The package contains a cylindrical solid aluminum basket that holds a single fuel assembly. The helium gaps between the fuel and the basket, and between the basket and package shell, were explicitly modeled with solid elements.

The package body is constructed of several stainless steel shells to provide structural support and gamma shielding. The innermost shell is surrounded by a layer of lead that acts as a gamma shield. The outermost stainless steel shell is surrounded by an annular tank containing a solution of ethylene glycol and water which acts as a neutron shield. The tank is contained by an outer stainless steel skin and an annular overflow tank that extends approximately one-third of the axial length of the package body. All of these components were modeled using brick elements.

The tank is constructed with eight stainless steel support ribs (in the half section) connecting the skin to the outer shell. These structures were modeled with shell elements. The package bottom is constructed with a stainless steel base, a layer of lead shielding, and a steel cover. The upper end of the package is sealed with a stainless steel lid (see Figure 5.19). Impact limiters attached to the ends of the package consist of an internal aluminum honeycomb structure covered by an aluminum skin. The expansion tank to handle overflow of the liquid neutron shield consists of an outer stainless steel skin.

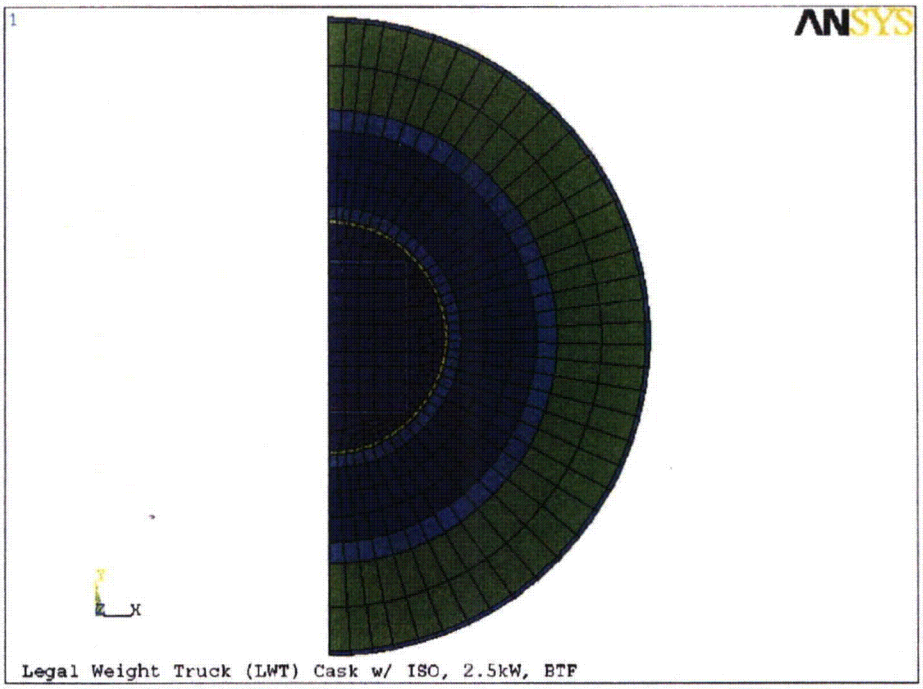

Figure 5.18. Cross-section of NAC LWT Package

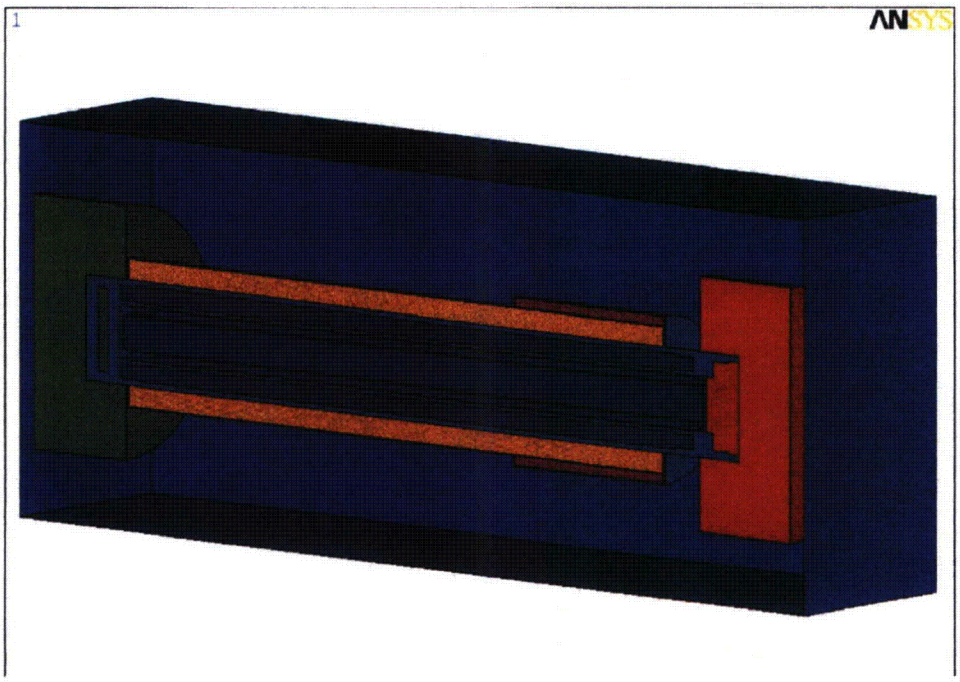

Figure 5.19. NAC LWT Package Geometry

The entire package is contained in an ISO container constructed of stainless steel plate. This is based on the assumption that an ISO container would be required if the NAC LWT were shipped by rail. (The consequences of this hypothetical accident scenario on a package shipped without an ISO container are discussed with the results of this analysis in Section 7.3.) The model of the package and container is oriented horizontally in the tunnel with the center of the ISO container 97.7 inches (248 cm) above the tunnel floor.

Heat exchange via conduction, convection, and radiation was modeled in appropriate detail between all of the components to provide a sound estimate of package temperatures during the transient fire event. Conduction is handled inherently by the elements modeling each component, but convective and radiation mechanisms must be separately implemented.

Westinghouse 17x17 OFA fuel was modeled in this evaluation. The fuel region was represented with an effective conductivity determined using a homogenization scheme similar to that presented by Bahney and Lotz [16], modified to include a helium gap between the homogenized fuel region and the fuel basket. This yields a more realistic representation of the temperature profile through the assembly, and takes into account the effect of the non-uniform wall temperature distribution around the assembly.

Axial conduction in the homogeneous fuel region was conservatively neglected in the fuel itself, and was modeled only in the cladding, using the conductivity of Zircaloy modified by a weighting scheme based on the cross-sectional area. The effective density and heat capacity for the fuel region was based on volumetric averages of the properties of the helium cover gas, fuel rod cladding, and uranium oxide fuel pellets. The design basis axial power profile from the SAR [11], which has a normalized peaking factor of 1.2, was used to establish the volumetric heat generation of 8,532 Btu/hr (2.5 kW) over the assembly along the active fuel length.

The 0.225-inch (0.57-cm) gap filled with helium cover gas between the fuel and the basket was modeled with solid elements and used standard helium thermal properties for conduction and specific heat. Convection was ignored in this small gap. Radiation exchange between the adjacent surfaces was modeled using MATRIX50 superelements. These were created by using SHELL57 elements to designate the discrete enclosure, and the AUX-12 hidden ray-tracing method was used to compute view factors for each element in the superelement. The 0.25-inch (0.64-cm) gap between the basket and the inner shell was modeled in the same manner, also assuming negligible convection.

The entire package model was enclosed within elements modeling the ISO container. For the large air volumes in the ISO container, conduction across the gaseous medium is negligible but significant convection currents will be created by the buoyant forces due to the heated surfaces. Surfaces with unobstructed views of other surfaces will also experience significant radiation exchange that is highly dependent on the surface geometry and physical condition. Therefore, heat exchange between the package exterior and the container interior was modeled with internal free convection and radiation between adjacent surfaces.

The radiation was implemented using the MATRIX50 superelement procedure described in Section 5.3 for the Holtec HI-STAR 100 model. The convection calculations were based on empirical relations for

free convection over flat plates and cylinders (see Section 6). Convection was implemented using SURF152 elements. These elements are defined on the exterior surface of a body and connect to the designated sink temperature assigned to a single node (called a "space node") to compute the heat flux. Because convection heat transfer rates are expected to vary in different regions throughout the ISO container, the single volume was divided into 17 zones. These consisted of a zone on each end of the package, three zones representing the top, side, and bottom radial surfaces for each impact limiter, and similar zones for the package for three locations along its axial length (see Figure 5.20).

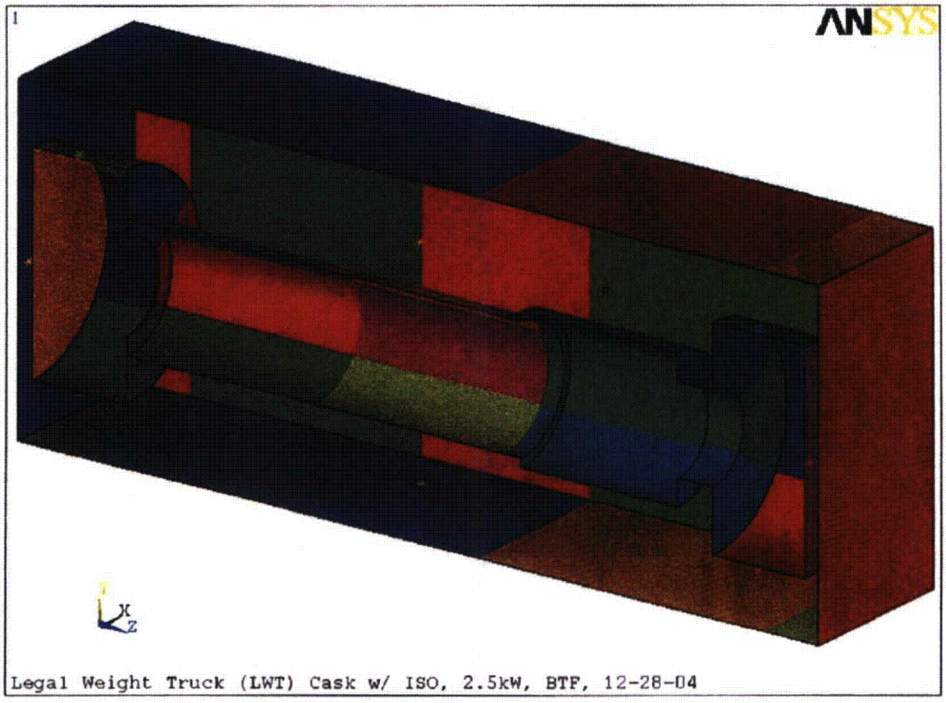

Figure 5.20. Zones for Convection Heat Transfer Within the ISO Container

A sink temperature was defined for each zone, computed as the average surface temperature of the participating package and container elements for that zone. The convective heat transfer coefficient was assigned to the package and container elements based on the temperature difference between the surface and sink temperature, and the surface geometry, as described in Section 6. The heat exchange between these surfaces and the space node was then computed by ANSYS during the solution.

Convection and radiation are also the two mechanisms required to model thermal exchange from the exterior of the ISO container. In the fire analysis, the initial temperature distribution is obtained from a steady-state solution with conditions specified by 10CFR71.71 [1], followed by a transient solution representative of the fire. For the steady-state solution, convection is handled by SURF152 elements with a constant convection coefficient of 0.891 Btu/hr-ft^2-°F (5.06 W/m^2-°K) and an ambient temperature of 100°F (38°C). Solar insolation is incorporated by using SURF152 elements with heat generation on the outer surface at the rate specified in 10CFR71 [1].

During the fire, the sink node temperature for each of the SURF152 elements is set and the external convection coefficient is computed using a forced convection relation derived using the gas temperatures and velocities from the results of the NIST fire simulation using FDS. These results were obtained for the top, side, and bottom of the tunnel, and applied to three zones defined on the top, sides, and bottom of the ISO container, as illustrated in Figure 5.21. By the end of the transient simulation using FDS (i.e., 30 hours), the predicted gas velocities have dropped to the point that free convection is the only significant mode of convection heat transfer. From this point in the transient, the convection coefficient is computed in the same manner as described for the steady-state initial conditions.

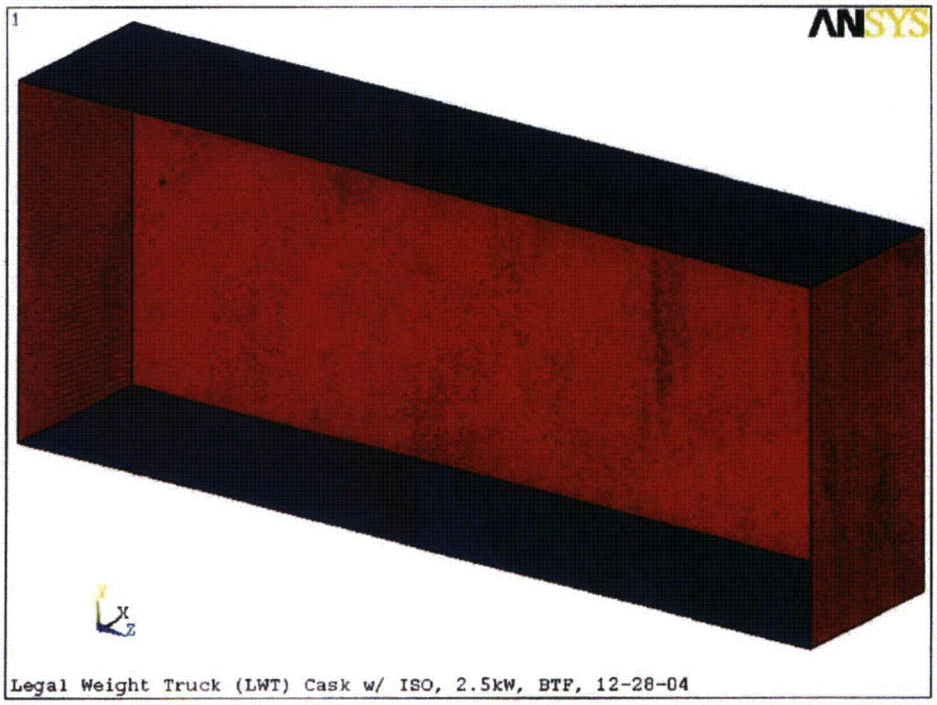

Figure 5.21. Zones for External Radiation Between ISO Container and Tunnel Surfaces

Thermal radiation between the container and the tunnel during and after the fire is incorporated by the MATRIX50 elements, as described previously, where the top, side, and bottom temperatures of the tunnel from the NIST fire simulation are imposed as boundary conditions. A conservative emissivity value of 0.9 was used for the tunnel surfaces and ISO container exterior, to account for the effect of sooting.

The material properties used in the thermal model are listed in Appendix C, and were obtained primarily from the vendor's SAR [11]. Some modifications were made to the material properties to account for structural configuration and expected effects of the fire. More comprehensive material properties were needed for the lead comprising the gamma shielding, to accommodate the effects of melting and resolidification during the transient. For the impact limiters, the significant void volume of the aluminum honeycomb material reduces the heat transfer capability compared to the same thickness of solid material. The thermal conductivity assigned to elements modeling the impact limiters was scaled by the ratio of the honeycomb density to the solid aluminum density.

Modeling of the liquid neutron shield was complicated by the expectation that the 56% ethylene glycol liquid will exceed its boiling point during a fire transient, leading to tank rupture and vaporization of the contents, which significantly affects the heat transfer of the package. Prior to rupture, the liquid in the tank is expected to sustain convective currents due to temperature gradients through the liquid between the tank surfaces. After rupture, empirical relations were used to obtain separate effective conductivities for the shield tank and expansion tank.

The empirical relations were based on correlations by Raithby and Hollands [18], as described in Section 6. The effective conductivity was then determined as a function of the average tank temperature and the radial temperature difference between the tank inner and outer surfaces. The material properties were updated between each time step during the transient solution using APDL. They were computed for the 56% ethylene glycol solution up to the point where the average temperature reached its boiling point of 350°F (177°C).

When the average temperature in the tank exceeded the boiling point, it was assumed that rupture occurred and the liquid was immediately vaporized. After that point, the effective conductivity was computed using dry air as the medium. This calculation was continued during the cool down period also. This formulation conservatively neglects energy absorbed by the phase change (i.e., the heat of vaporization for the liquid), although this is mainly as a matter of convenience, since this would constitute a relatively small deduction from the total energy imparted to the package.

The general solution procedure for this model was similar to that for the HI-STAR 100 described previously. The steady-state temperature solution for normal hot conditions was computed using solar insolation and 100°F (38°C) ambient temperature per 10CFR71.71 [1], and used as the initial temperature state. The insolation was removed and the tunnel was introduced for the transient fire analysis. The transient solution was then obtained for the 30 hours of the NIST simulation, representing the 7-hour fire and 23-hour cool down. The solution was also extended for a total simulation time of 300 hours, in the same fashion as described in Sections 5.1 and 5.2 for the other two package models.

6 ANALYSIS METHOD

The National Institute of Standards and Technology (NIST) performed analyses using the FDS code, to determine the type of fire that could have been sustained during the accident in the Howard Street tunnel and the possible fire duration. A conservative simulation was used to define the boundary conditions for COBRA-SFS and ANSYS evaluations of the thermal response of the selected spent fuel transportation packages. Section 6.1 lists the assumptions underlying the analytical approach used and describes in detail the boundary conditions obtained from the selected FDS simulation. This includes temperature boundary conditions and the approach used to define convection and radiation heat transfer rates. Section 6.2 describes the initial steady-state conditions defined for each package. Section 6.3 describes the procedure used for the transient calculations.

6.1 Modeling Assumptions and Boundary Conditions

A number of conservative assumptions were made in the evaluations of the thermal response of the three spent fuel transport packages (TN-68, HI-STAR 100, and NAC LWT) to the Baltimore tunnel fire transient. The assumptions of greatest impact are listed below.

(1) Boundary conditions were taken from a conservative simulation in which the fire is predicted to burn at a rate that is approximately an order of magnitude hotter than the rate predicted for the actual environment within the tunnel. In this conservative simulation, the fire was assumed to be fully ventilated, with a relatively small pool area, and burned until the entire supply of tripropylene fuel was consumed by combustion (as described in Section 2).

(2) Boundary temperatures for the analyses in the current study were taken from predictions of peak gas temperatures in the lower, middle, and upper zones of the tunnel and peak surface temperatures on the tunnel floor, walls, and ceiling. The peak values in each region were used to define boundary temperatures over the entire region, rather than using the local or average temperatures predicted in the FDS calculation. This approach ensures a conservative estimate of the boundary temperatures, since the package does not see the peak temperatures on all surfaces, and in some regions may not see the peak temperature on any surface. (For example, the uppermost surface of the package (in the horizontal orientation) is not high enough to be exposed to the peak gas temperature at the top of the tunnel, but this value was used as the ambient temperature for convective heat transfer to the upper surface of the package.)

(3) The package cradle and the rail car section beneath the cradle were included in the ANSYS model of the HI-STAR 100, but the rail car ends and honeycomb end blocks adjacent to the impact limiters were omitted. These structures were neglected because they would partially shield the package from thermal radiation from the hot tunnel surfaces and block convection heat transfer to the package due to the flow of hot gas generated by the fire. The rail car was omitted from the COBRA-SFS model of the TN-68 package and the ANSYS model of the NAC LWT package within the ISO container. This approach eliminated any shielding of these packages from thermal radiation and convective heat transfer from the tunnel environment.

(4) During the fire ($0 < t < 7$ hr) and in the short-term post-fire cool down (7 hr $< t < 30$ hr), it was assumed that convection heat transfer at the package surface was forced convection only (due to air flow induced in the tunnel by the temperature gradients of the fire), using gas velocities predicted in the NIST analysis. This approach neglects the possible contribution of free convection around the package (due to non-uniform circumferential temperatures around the package outer shell), which would tend to remove heat from the package. The boundary condition was switched to solely free convection after 30 hours, in the extrapolated portion of the transient. This conservatively neglects any forced convection cooling of the package during the extended cool down period, when the gas velocities in the tunnel are predicted to have dropped to relatively small values.

(5) The effect of optical densification due to combustion products and material degradation, which would tend to attenuate the radiation influence between the tunnel and package surfaces, was not taken into account in the boundary conditions defining the fire. Radiation views were treated as clear and unobscured at all times. Radiation attenuation was also neglected between the ISO container inner surfaces and the NAC LWT package surfaces.

(6) The wooden impact limiters on the TN-68 were assumed to remain intact during the fire, to maximize the heat input into the package. At the end of the fire, the thermal conductivity value for the nodes representing this material was reduced to that of charcoal. As a result, these components then present an added thermal barrier to heat removal from the package after the fire.

(7) Similarly, the aluminum honeycomb impact limiters on the NAC LWT and the HI-STAR 100 were assumed to remain intact during the fire. At the end of the fire, the thermal conductivity values for the portions of the impact limiters that had exceeded the melting temperature of aluminum were reduced to that of air. The thermal energy absorbed in the melting process, however, was conservatively neglected, and was not subtracted from the heat input to the package during the fire.

(8) For the TN-68 and the HI-STAR 100, the resin materials comprising their neutron shielding were assumed to remain intact during the fire, to maximize the heat input into the package. At the end of the fire, the thermal conductivity values for these materials were reduced to that of air. As a result, the neutron shield region then presents an added thermal barrier to heat removal from the package following the fire; however, the thermal energy absorbed in the process of melting and volatizing the resin material of the neutron shielding was conservatively neglected, and was not subtracted from the heat input to the package during the fire.

(9) For the NAC LWT, the ethylene glycol and water mixture comprising the package's neutron shielding was assumed to remain in liquid form during the fire until the average temperature in the shield tank reached the boiling point of the fluid. The fluid in the expansion tank was treated in a similar manner. This conservative approach acts to maximize the heat input into the package during the fire. After the average temperature in the tank exceeded the boiling point of the fluid, heat transfer through the tank was reduced to conduction and thermal radiation through air. As a result, the neutron shield region then presents an added thermal barrier to heat removal from the package; however, the thermal energy absorbed in the process of boiling off the large mass of liquid was conservatively neglected, and was not subtracted from the heat input to the package.

(10) In all three analyses, the package was assumed to be only 66 ft (20 m) from the center of the fire, in order to obtain the highest possible boundary temperatures due to the fire. Based on Department of Transportation regulations [12] that require rail cars carrying radioactive materials to be separated by at least one rail car (a buffer car) from other cars carrying hazardous materials or flammable liquids, 66 ft (20 m) is the shortest possible distance in this fire scenario between a hypothetical rail car carrying an SNF package and the tank car carrying liquid tripropylene.

Given these assumptions, the ANSYS and COBRA-SFS analyses constitute conservative evaluations of the response of the spent fuel transportation packages. The FDS simulations for the NIST model of the Howard Street tunnel fire produced detailed predictions of gas flow rates, gas temperatures, and tunnel wall, ceiling, and floor temperatures during the 7-hour fire and 23-hour post-fire cool down.

6.1.1 Boundary Temperatures from FDS

The FDS simulations included the entire tunnel length, from the west portal (tunnel entrance) to the east portal (tunnel exit). The results obtained for the radial plane at the location 66 ft (20 m) from the center of the fire were used to define the boundary conditions for the analyses with COBRA-SFS and ANSYS. As a conservative simplification of the finely detailed noding in the FDS simulation, the tunnel radial geometry was divided into three regions; top, side, and bottom (see Figure 5.4). Within each of these regions, the predicted peak wall temperatures and peak gas temperatures as a function of time (with the associated gas velocities) were taken as representative of the transient behavior of the entire region, rather than following the local gradients obtained in the detailed NIST simulation with FDS.

The peak temperature-vs.-time and velocity-vs.-time values from the FDS simulation were smoothed to conservatively remove the rapid stochastic variations typical of dynamic fire behavior, preserving only the major peaks and troughs related to the general physical behavior of the simulated fire. (The selected FDS results for this simulation are shown graphically in Appendix D, along with the smoothed values used in the ANSYS and COBRA-SFS calculations.) Figure 6.1 shows these smoothed peak air temperatures for the top, sides, and bottom regions in the tunnel at 66 ft (20 m) from the fire center. The smoothed peak surface temperatures for the walls, floor, and ceiling of the tunnel at this location are shown in Figure 6.2. Figure 6.3 shows the smoothed velocities predicted in the NIST analyses at the locations of the peak gas temperatures shown in Figure 6.1.

The gas temperatures (Figure 6.1) and velocities (Figure 6.3) were used to define convection heat transfer on the top, side, and bottom regions of the package surfaces. The peak tunnel surface temperatures (Figure 6.2) were used to define the boundary conditions for radiation heat transfer between tunnel surfaces and the exposed surfaces of the package. For the ANSYS models of the HI-STAR 100 and LWT packages, these temperatures were applied to corresponding tunnel surface elements comprising the ceiling, walls, and floor. For the COBRA-SFS model of the TN-68 package, radiation exchange with the tunnel walls, ceiling, and floor was incorporated by calculating a radiation heat flux at the package surface using the local package surface temperature and the regional tunnel surface temperatures defined in Figure 6.2. Blackbody view factors between the package surface and the tunnel surfaces were determined using a conventional ray-tracing scheme. (These view factors are listed in Appendix E.)

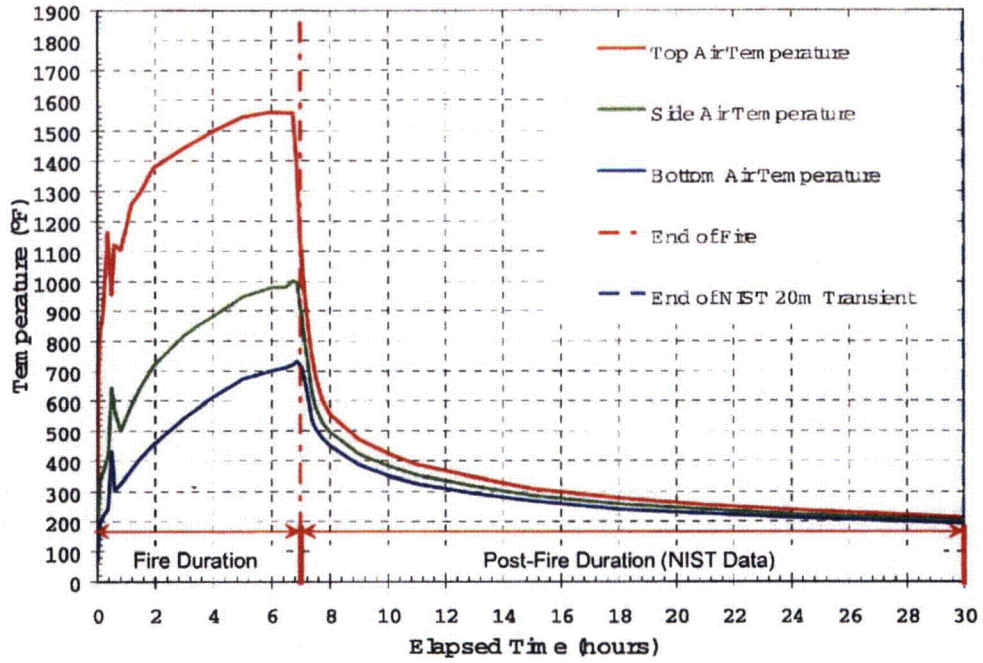

Figure 6.1. BTF Peak Transient Ambient Air Temperatures (smoothed values, NIST 20-m data)

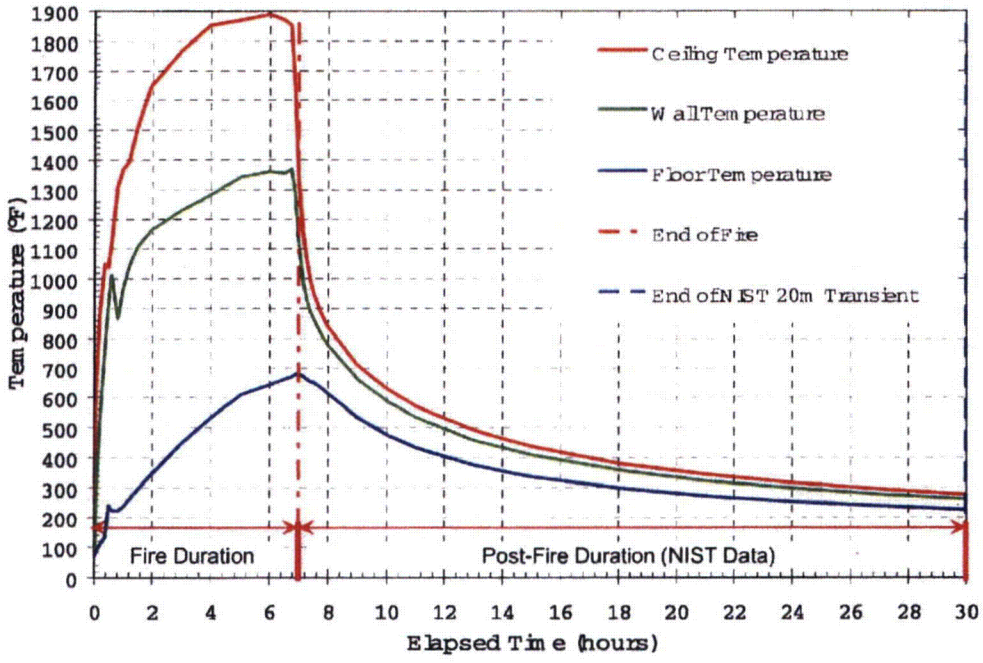

Figure 6.2. BTF Peak Transient Tunnel Surface Temperatures for Floor, Walls, and Ceiling (smoothed values, NIST 20-m data)

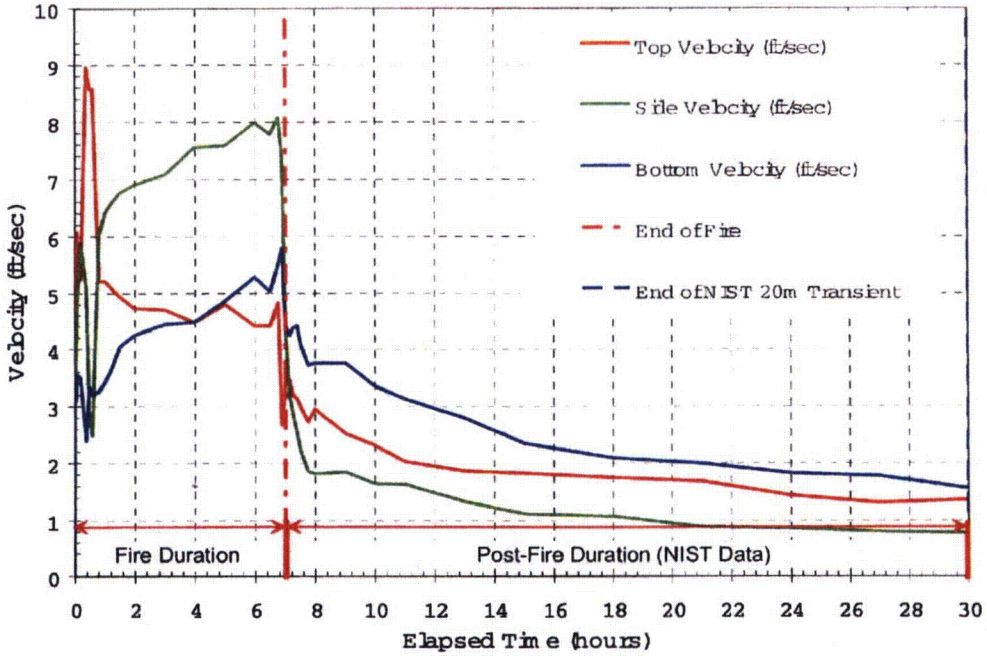

Figure 6.3. BTF Peak Transient Horizontal Velocities near Package Surface (smoothed values, NIST 20-m data)

6.1.2 Convection and Radiative Heat Transfer Boundary Conditions

The NIST analyses showed that the thermal gradients created in the tunnel due to the fire would result in significant air flow past a body located near the fire. This fire-forced convection would significantly affect heat transfer around the package and could have a strong influence on the package outer shell surface temperatures. The smoothed air temperatures in Figure 6.1 and velocities in Figure 6.3 were used to define local time-dependent Nusselt number values at the top, sides and bottom of the package. These values were used to define the local surface heat transfer coefficient for the three computational models.

To maintain consistency between the three models, the same Nusselt number correlation was used to define convection heat transfer at the package surface. The selected correlation gives the Nusselt number for gas flow over a flat or slightly curved surface at zero angle of attack [19], and has the form

for laminar flow ($Re_L < 500{,}000$), $\quad Nu_L = 0.665\, Re_L^{1/2}\, Pr^{1/3}$

for turbulent flow ($Re_L > 500{,}000$), $\quad Nu_L = 0.032\, Re_L^{0.8}\, Pr^{1/3}$

The characteristic length, L, used to define the Nusselt number and Reynolds number for this application is the package body horizontal length. For the TN-68, a value of 160 inches was used, and for the HI-STAR 100, a value of 173 inches was used. Both were based on the length of exposed package body. For the NAC LWT, a value of 240 inches was used, based on the ISO container wetted surface length.

The peak air temperatures (see Figure 6.1) from the NIST analysis define the ambient sink temperature around the package during the fire and post-fire intervals. The Nusselt number defines the rate of heat transfer from the package surface, which allows both codes (COBRA-SFS and ANSYS) to calculate the convection heat flux at the package surface. Using the above relationship, local surface temperatures, T_s, are calculated, and the convection component of the heat flux at the surface is solved for using the formula

$$q''_{conv} = Nu_L \frac{k}{L}(T_s - T_{air})$$

where k = thermal conductivity of ambient air
L = characteristic length
T_s = package surface temperature
T_{air} = ambient external air temperature.

Separate boundary types were defined for the top, sides, and bottom surfaces of the package using the external air temperatures shown in Figure 6.1. The velocities in Figure 6.3 were used to define the Reynolds number so the boundary conditions on the package could change with time as the transient proceeded. Figure 6.4 shows the resulting local convection heat transfer coefficients calculated at the top, sides and bottom of the TN-68 package with the COBRA-SFS model during the 30 hours of the NIST transient simulation.

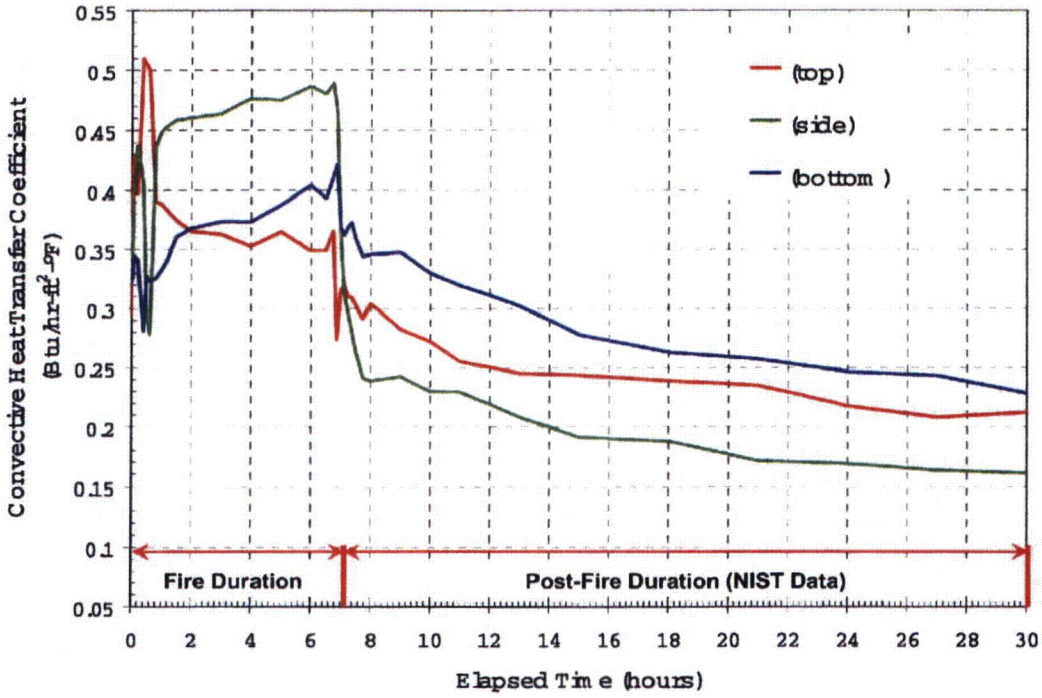

Figure 6.4. Convection Heat Transfer Coefficients at Package Surface from NIST 20 m Air Temperature and Velocity Predictions

In addition to convection heat transfer between the transport package and the surrounding air during the transient, radiation heat transfer between the package surface and the tunnel ceiling, walls, and floor was also captured. Boundary conditions to define radiation heat transfer between the package surface and the tunnel ceiling, walls, and floor were included in the COBRA-SFS model in the following fashion. The total heat flux at the surface of the package is the sum of the two components:

$$q'' = q''_{conv} + q''_{rad}$$

The tunnel surface temperature profiles shown in Figure 6.2 were used to define the radiation heat flux as an additional boundary condition at the package surface using the relationship

$$q''_{rad} = \varepsilon_i B_{ij} \sigma_{SB} \left(T^4_{package} - T^4_{surf} \right)$$

where
ε_i = emissivity of surface i
B_{ij} = blackbody viewfactor from surface i to j
σ_{SB} = Stefan-Boltzmann constant
T_{surf} = tunnel ceiling, wall or floor surface temperature
$T_{package}$ = package surface temperature.

The blackbody view factors between the package surface and the tunnel ceiling, walls, and floor were determined using a Monte Carlo ray tracing scheme based on the package diameter and a uniform axial node length along the length of the package. (See Appendix E.)

Radiation interaction between the tunnel surfaces and the package surfaces in the HI-STAR 100 model was established through the use of ANSYS superelement definitions, as described in Section 5 above. (The same approach was used to define thermal radiation between the tunnel and the ISO container surfaces in the NAC LWT system) The NIST tunnel surface temperature predictions (see Figure 6.2) were then used to establish the tunnel surface boundary condition temperatures. The emissivity of all tunnel surfaces and the package surface was assumed to be 0.9 for all evaluations during the fire and post-fire transient.

6.1.3 Extrapolated Boundary Conditions for Long-Term Cool Down

NIST's FDS analysis was carried out for a 7-hour fire and 23-hour post-fire cool-down. To determine the long-term temperature responses and explore the effects of prolonged exposure to post-fire conditions in the tunnel, the transient was extended to 300 hours (293 hours after the end of the fire). Temperatures predicted in the NIST analysis for 30 hours were extrapolated from 30 hours to 300 hours using a power function to realistically model cool-down of the tunnel environment. The extrapolated values are presented in Figures 6.5 for the air temperatures and in Figure 6.6 for the wall temperatures.

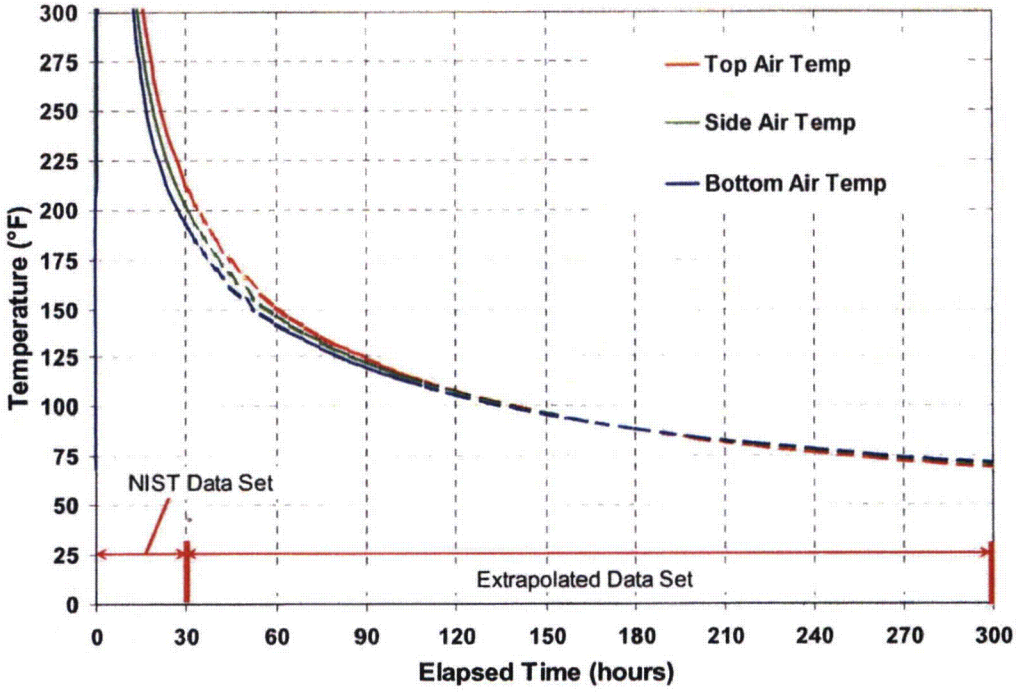

Figure 6.5. BTF Peak Transient Air Temperatures for Top, Side, and Bottom Regions (NIST Data Set and Extrapolated Values)

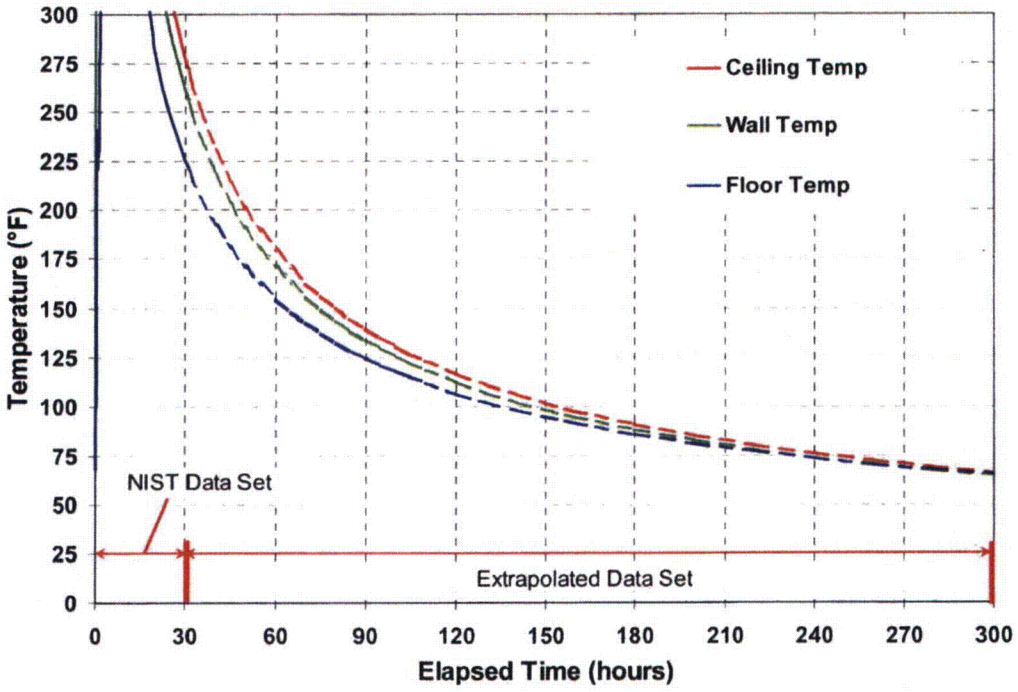

Figure 6.6. BTF Peak Transient Surface Temperatures for Floor, Walls, and Ceiling (NIST Data Set and Extrapolated Values)

About 20 hours into the transient, the velocities predicted in the NIST calculations have dropped to values of 1 to 2 ft/s (0.3 to 0.6 m/s) or less (refer to Figure 6.3). Heat transfer at the package surface for these flow conditions is a complex mixture of forced convection (due to air flow induced in the tunnel by the wall temperature gradients of the fire) and free convection (driven by the non-uniform circumferential temperatures of the package outer shell). At velocities below about 3 to 5 ft/s (1 to 1.5 m/s), heat transfer rates predicted assuming forced convection are generally lower than the heat transfer rates due to natural convection around the package body for these temperature conditions.

To avoid the modeling uncertainties associated with mixed-mode heat transfer, forced convection only was assumed until the end of the NIST simulation, at 30 hours into the transient. From 30 hours to 300 hours, the heat transfer was assumed to be natural convection only. This ensured a conservative treatment of convection heat transfer from the package surface during the entire calculation, since free convection to surface heat transfer from the package is ignored in the cool down from 7 to 30 hours, and forced convection is neglected in the period from 30 to 300 hours.

For consistency, the natural or buoyant convection coefficients were those utilized for determining the pre-fire component temperature distributions (i.e., Hot-Normal Conditions of Transport, as defined in 10 CFR 71.71(c)(1)([1]). The heat transfer coefficients were defined for the appropriate surface geometries using the following relationships [20]:

For flow along a vertical plane or cylinder :

--laminar flow ($10^4 < Gr_f \cdot Pr_f < 10^9$) $\quad h = 1.42\left(\frac{\Delta T}{L}\right)^{1/4}$

--turbulent flow ($Gr_f \cdot Pr_f > 10^9$) $\quad h = 1.31(\Delta T)^{1/3}$

where h = heat transfer coefficient, $W/(m - °C)$
$\Delta T = T_w - T_\infty$, $°C$
T_w = surface or wall temperature, $°C$
T_∞ = ambient temperature, $°C$
L = vertical or horizontal dimension, m
Gr_f = Grashoff number of the gas at film temperature,
Pr_f = Prandtl number of the gas at film temperature
where film temperature is $T_f = (T_w + T_\infty)/2$

For flow over a horizontal cylinder:

--laminar flow ($10^4 < Gr_f \cdot Pr_f < 10^9$) $\quad h = 1.32\left(\frac{\Delta T}{d}\right)^{1/4}$

where d = diameter, m

--turbulent flow ($Gr_f \cdot Pr_f > 10^9$) $\quad h = 1.24(\Delta T)^{1/3}$

For flow over a horizontal heated plate facing upward (cool side facing downward):

-- laminar flow ($10^4 < Gr_f \cdot Pr_f < 10^9$) $\quad h = 1.32\left(\frac{\Delta T}{L}\right)^{1/4}$

-- turbulent flow ($Gr_f \cdot Pr_f > 10^9$) $\quad h = 1.52(\Delta T)^{1/3}$

For laminar flow ($10^4 < Gr_f \cdot Pr_f < 10^9$) over a heated plate facing downward (cool side facing upward):

$$h = 0.59\left(\frac{\Delta T}{L}\right)^{1/4}$$

Definitions of material properties for use with these correlations were taken from Table A-3 of Kreith [21].

6.1.4 Heat Transfer through NAC LWT Liquid Neutron Shield

An empirical relationship for effective conductivity incorporating the effects of both conduction and convection was used to determine heat exchange through the liquid neutron shield. In the SAR analysis for the LWT package [11], the effective conductivity of the ethylene glycol mixture for conditions below 350°F was determined using the correlation of Bucholz [22], which defines the ratio of the effective conductivity to the actual thermal conductivity as equal to the Nusselt number, such that

$$\frac{k_{eff}}{k_c} = Nu = 0.135(Pr^2\, Gr/(1.36 + Pr))^{0.278}$$

where k_{eff} = effective thermal conductivity of material
k_c = thermal conductivity of motionless fluid
Nu = Nusselt number
Pr = Prandtl number
Gr = Grashoff number

The Baltimore tunnel fire transient is outside the range of the Bucholz correlation, and it yields unrealistically large values for k_{eff} for these conditions. An alternative correlation from Raithby and Hollands [18], based on heat transfer between two concentric cylinders, was used in this analysis instead. This correlation produces reasonable values of k_{eff}, and the transient conditions are generally within its applicable range. The form of this correlation is similar to the Bucholz correlation in that it equates the Nusselt number to the ratio of the effective conductivity over the actual conductivity, but in the Raithby and Hollands formulation, the Nusselt number is expressed as

$$\frac{k_{eff}}{k_c} = Nu = 0.386D_r(Pr/(0.861 + Pr))^{0.25}\, Ra^{0.25}$$

where Ra = Rayleigh number (Ra = Pr*Gr)
Gr = Grashoff number (based on the temperature difference across the annular gap)

The variable D_r is a dimensionless parameter based on the geometry of the annulus, and is defined:

$$D_r = \left[\frac{\ln(D_o / D_i)}{d^{3/4}(1/D_i^{3/5} + 1/D_o^{3/5})^{5/4}} \right]$$

where D_o = annulus outer diameter
D_i = annulus inner diameter
d = width of annulus.

Figure 6.7 shows a plot of the Nusselt number predicted with these two correlations for the liquid (56% ethylene glycol and water mixture) in the neutron shield annulus. Figure 6.8 shows the effective conductivity for the annulus as a function of the average temperature and temperature difference for the liquid neutron shield tank. Figure 6.9 shows the same relationship for the expansion tank. (The sharp discontinuity in the curves on both plots represents the phase change when the average temperature of the liquid reaches the boiling point of the ethylene glycol and water mixture.) For low values of the temperature difference, the results approach those for the conduction-only case.

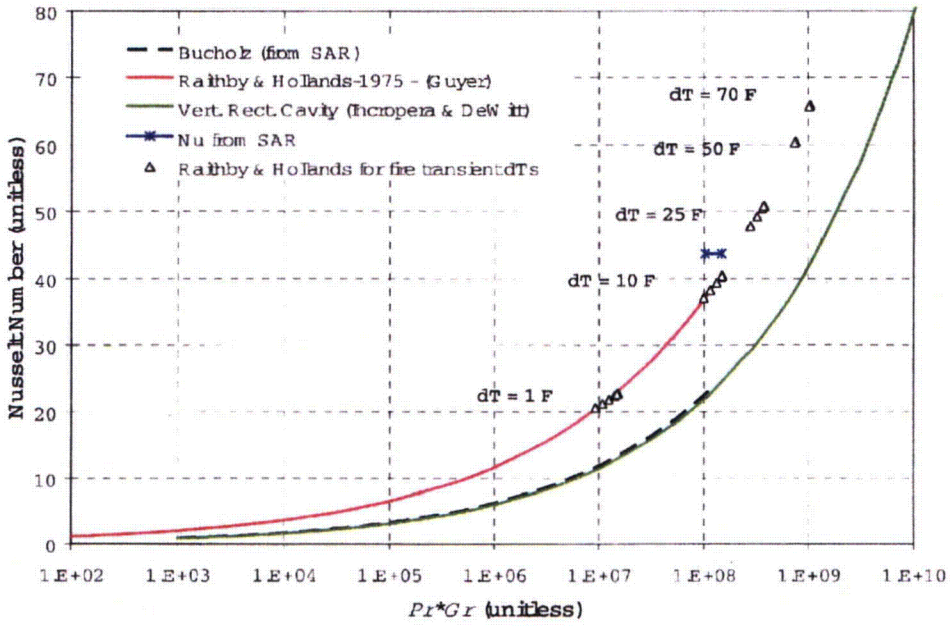

Figure 6.7. Nusselt Number for Heat Transfer in Liquid Neutron Shield

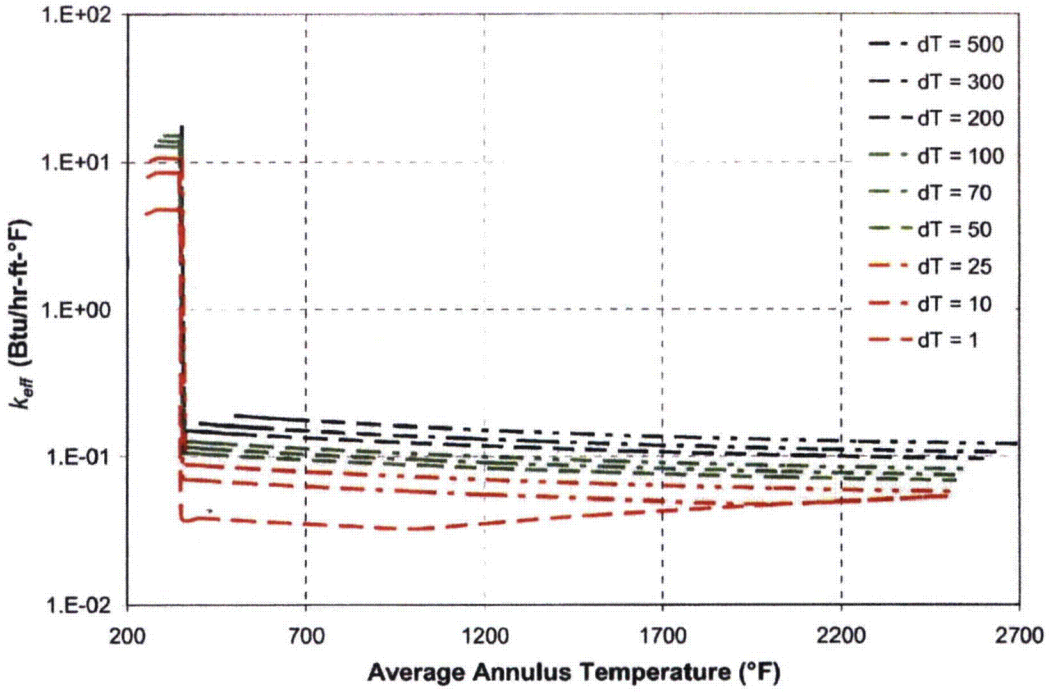

Figure 6.8. Effective Conductivity of Neutron Shield Tank Contents

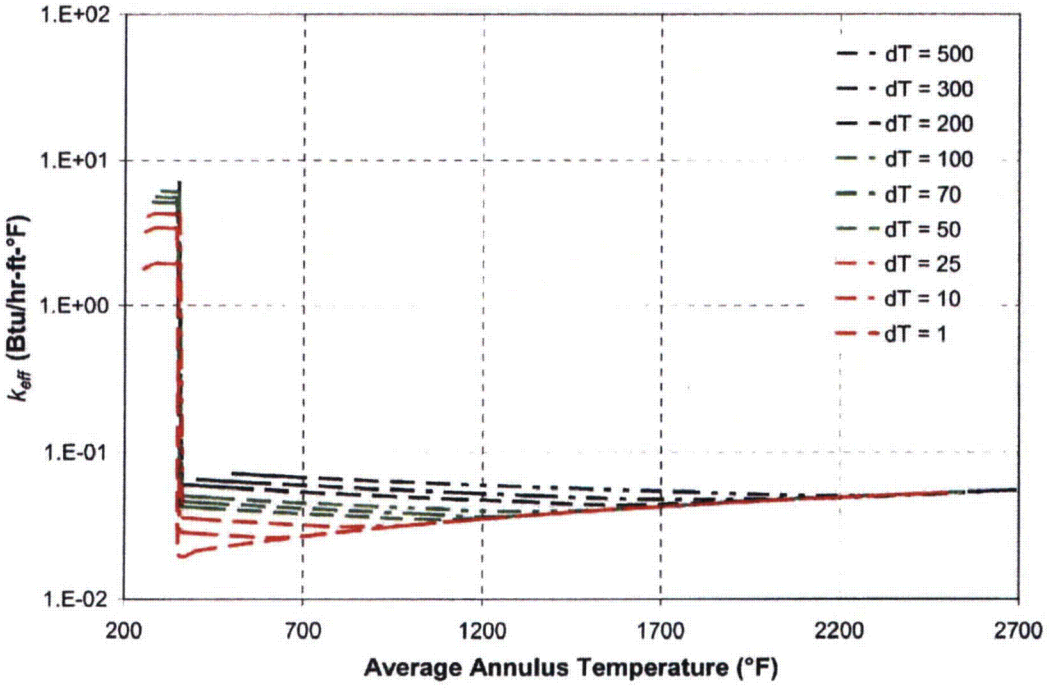

Figure 6.9. Effective Conductivity of Expansion Tank Contents

6.1.5 Heat Transfer through NAC LWT Lead Gamma Shield

Temperatures encountered in the Baltimore tunnel fire scenario are high enough to expect that the lead gamma shielding in the NAC LWT would melt in the fire transient. It would be conservative to neglect this process in the thermal analysis, since taking into account the thermal effects of lead melting would tend to slow the rate of heat input into the package. The melting of the lead absorbs energy from the fire due to the latent heat of fusion, which for lead is 10.4 Btu/lbm (24.2 kJ/kg). The lead shielding consists of about 27,134 lbm (12,308 kg) of lead, and would absorb approximately 83 kW-hr in the process of phase change. This heat would otherwise be conducted through the lead shielding to the package interior, contributing to higher basket and fuel temperatures within the package. In addition, the local temperature of the lead cannot rise above the melting temperature until the phase change is complete at that point. This will tend to slow the rate of temperature increase in the gamma shield region, and therefore slow the overall rate of temperature increase for the package internals. The thermal conductivity of molten lead is approximately 50% lower than that of solid lead. This lower conductivity would further slow the rate of heat input to the package during the hottest portion of the fire.

However, the behavior of the lead as shielding material is also an important consideration in the analysis of the response of the NAC LWT to the fire scenario. Complete evaluation of the transient requires a realistic representation of the thermal response of the package, including the effects of melting and resolidification of the material in the course of the transient. Including the effect of phase change in the lead comprising the gamma shield of the NAC LWT package involves two major considerations in the specification of the lead material properties. First, the energy absorbed in the process of melting the material must be taken into account in the process of determining the local material temperature. Second, the thermal conductivity for elements representing this material must include values for both solid and molten conditions as a function of temperature.

Figure 6.10 shows the enthalpy of lead as a function of temperature, including the 'jump' at the point of phase change. This step change corresponds to the latent heat of fusion for lead. Figure 6.11 shows the thermal conductivity for lead as a function of temperature used in the ANSYS analysis, compared to the values used for this material property from the package SAR [11]. (See Appendix C, Table C.6 for the thermal properties of lead used in this analysis.) The solid phase values from the SAR at temperatures approaching the melting point of lead conservatively ramp down to an average value of thermal conductivity for the liquid phase. The actual thermal conductivity of lead remains at a relatively high value for the solid phase all the way to the melting temperature. Upon melting, the thermal conductivity drops by more than 50%, then gradually increases with increasing temperature of the molten material.

6.2 Initial System Component Temperatures

The normal conditions of transport described in 10 CFR 71.71 [1] were used as initial conditions for each analysis. All three packages were subjected to an ambient temperature of 100°F (38°C), with solar insolation. For pre-fire conditions, the package surface was given an emissivity value representative of its surface finish (e.g., 0.3 for bare stainless steel, 0.85 for painted surfaces). In the ANSYS models for the HI-STAR 100 and NAC LWT systems, thermal radiation heat transfer to ambient was modeled using surface effect elements (SURF152).

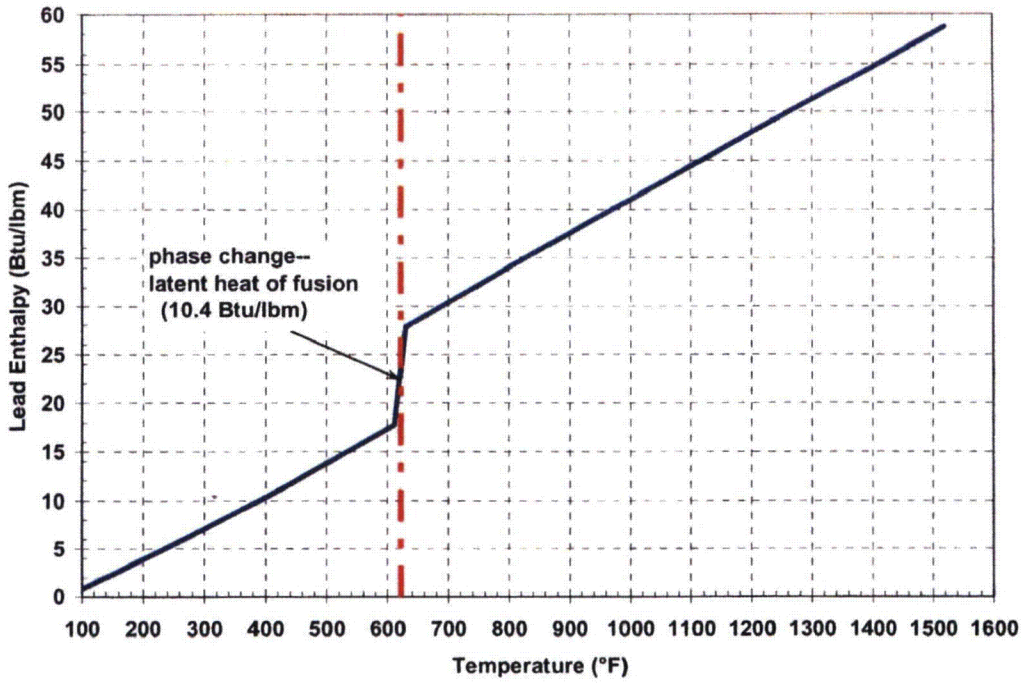

Figure 6.10. Solid and Molten Lead: Enthalpy as a Function of Temperature

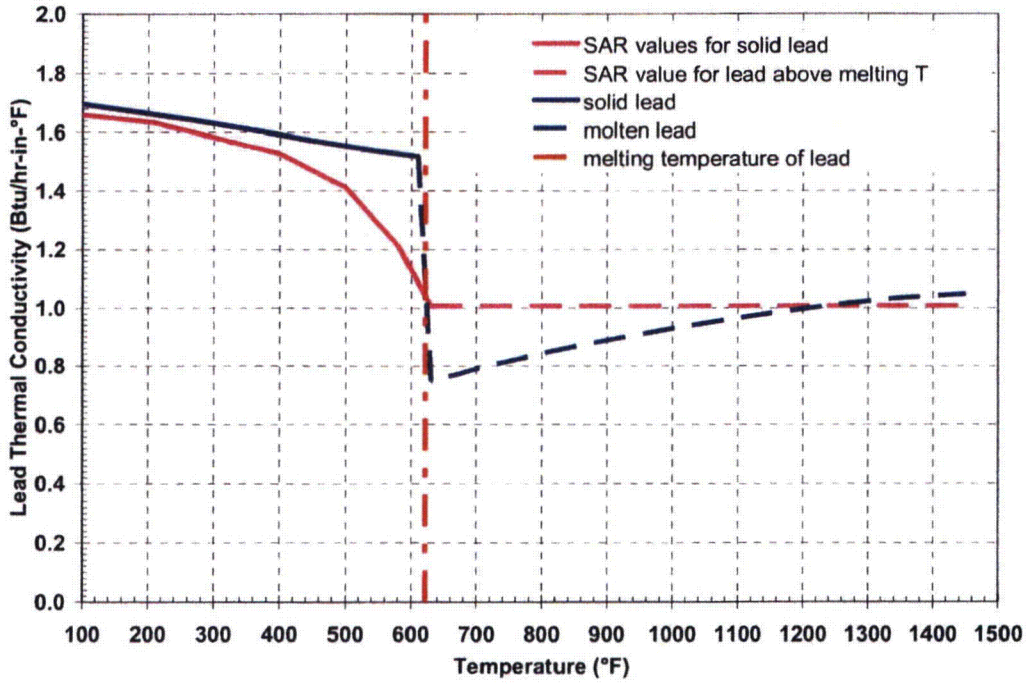

Figure 6.11. Solid and Molten Lead: Thermal Conductivity as a Function of Temperature

Convection from the surface of each package was modeled with a similar set of surface effect elements. The natural convection correlations for buoyancy driven flow discussed above were used to simulate convection heat transfer at the package surface. For the COBRA-SFS model of the TN-68 package, the surface boundary conditions also included natural convection and thermal radiation.

For the TN-68, the heat generation rate was specified as 72,334 Btu/hr (21.2 kW). For the HOLTEC HI-STAR 100, the heat generation rate was specified for a decay heat load of 68,240 Btu/hr (20 kW). For the NAC LWT, the heat generation rate was specified as 8,530 Btu/hr (2.5 kW). For all three packages, appropriate peaking factors (as reported in the respective SAR documents), were applied over the active fuel region.

A steady state normal condition temperature distribution for each package was obtained to establish pre-fire conditions. The hot-normal condition temperatures for each package were verified against the results reported in the relevant SAR. Normal condition temperatures from the ANSYS solution for the HI-STAR 100 are provided in Figure 6.12. (Appendix F contains additional plots showing the detailed steady-state temperature distributions for these conditions predicted for the HI-STAR 100.) The peak clad temperature predicted with ANSYS for the HI-STAR 100 is 738°F (392°C), compared to 701°F (372°C) reported in the SAR[10].

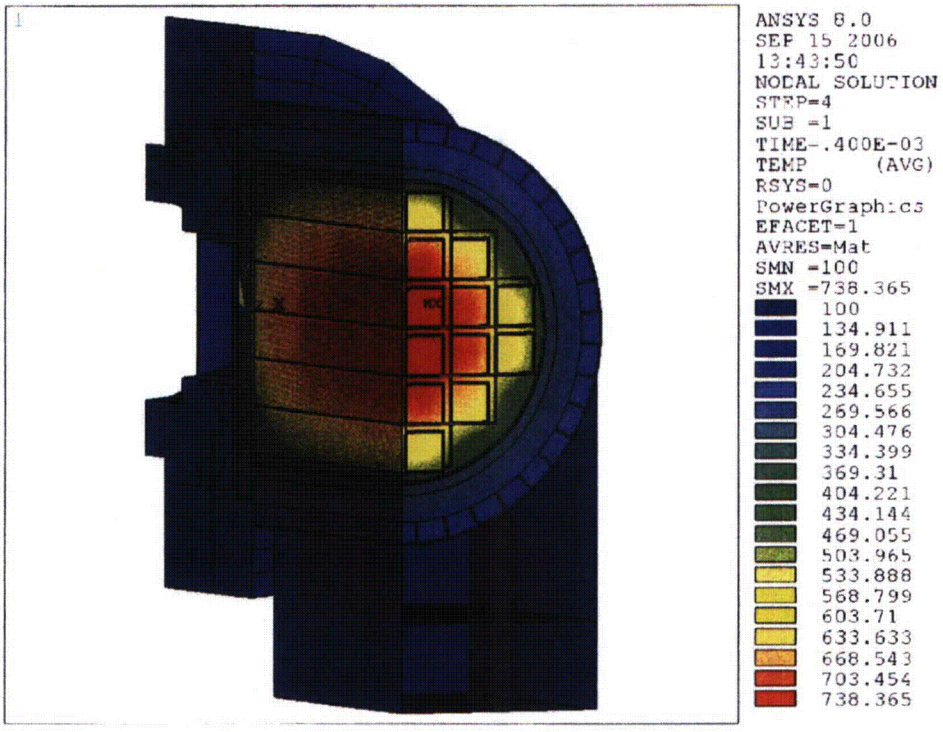

Figure 6.12. HI-STAR 100 Package Hot-Normal Condition Temperature Distribution

Since COBRA-SFS does not have a graphical post-processing module, it is not possible to produce similar color-flooded thermographs for the TN-68 evaluation. However, the analysis results are similarly

in very good agreement with the corresponding SAR values. The COBRA-SFS calculations predicted a peak clad temperature of 485°F (252°C) in the TN-68 package, compared to 490°F (254°C) reported in the TN-68 SAR [9].

Component temperature comparisons of results determined in this study and those published in the applicant's SAR documentation are presented in Table 6.1 for the TN-68 analysis with COBRA-SFS and Table 6.2 for the HI-STAR 100 analysis with ANSYS.

Table 6.1. TN-68 Hot-Normal Component Temperatures

Component	Current Study (COBRA-SFS) °F (°C)	SAR Values °F (°C) (Table 3-1 [9])
Fuel Cladding	485 (252)	490 (254)
Basket plate	467 (242)	469 (243)
Basket Rail	332 (167)	319 (159)
Inner Shell	292 (144)	262 (128)
Gamma Shell	285 (141)	260 (127)
Package Bottom	261 (127)	254 (123)
Seals	260 (127)	234 (112)
Radial Neutron Shield	256 (124)	244 (118)
Outer Shell	243 (117)	204 (96)

Table 6.2. HOLTEC HI-STAR 100 Hot-Normal Component Temperatures

Component	Current Study (ANSYS) °F (°C)	SAR Values °F (°C) (Table 3.4.10 [10])
Fuel Cladding	738 (392)	701 (372)
MPC Basket Centerline	717 (381)	667 (353)
MPC Basket Periphery	447 (231)	430 (221)
MPC Outer Shell	347 (175)	315 (157)
MPC/Overpack Helium Gap Outer Surface	299 (148)	291 (144)
Radial Neutron Shield Inner Surface	258 (126)	271 (133)
Overpack Enclosure Shell Surface	253 (123)	222 (106)
Axial Neutron Shield	228 (109)	292 (144)
Impact Limiter Exposed Surface	165 (74)	121 (49)
Overpack Closure Plate	270 (132)**	163 (73)
Overpack Bottom Plate	409 (209)**	295 (146)

** Temperatures elevated due to superimposed gap conductance between impact limiters and cask body. This gap conductance is replaced with intimate contact during the fire duration.

These tables show that the analytical results obtained for the TN-68 and HI-STAR 100 are in very good agreement with the results presented for the corresponding cases in the respective SARs. Minor differences between the SAR results and those obtained in the current study are due to differences in modeling detail and simplifying assumptions employed in the SAR models. For example, the SAR analysis of the HI-STAR 100 neglects the effect of the support cradle and possible limited gap conductance on component temperatures in the evaluation for the hot-normal conditions of transport.

For the TN-68 model and the HI-STAR 100 model, the results presented in Tables 6.1 and 6.2 are the initial conditions for the fire transient analysis. For the NAC LWT, the steady-state initial conditions for the fire transient analysis were based on similar assumptions, but direct comparison with the steady-state results presented in the SAR is not possible, due to the large number of significant differences between the approach used in the SAR analyses and the detailed modeling approach used in the current study

In the 3-D ANSYS model of the NAC LWT (shown in Figures 5.18 and 5.19), convection from the surface of the ISO container was modeled with a set of surface effect elements similar to those used in the model of the HI-STAR 100. The natural convection correlations for buoyancy-driven flow described in Section 6.1.3 were used to simulate the convective heat transfer within the ISO container and on the external surface. A heat generation rate equivalent to a decay heat load of 8,530 Btu/hr (2.5 kW) was applied, with appropriate peaking factor, over the active fuel region. This value was selected because the bounding thermal evaluation in the SAR [11] for the NAC LWT is for an intact PWR fuel assembly with a maximum decay heat load of 2.5 kW. This approach ensures a conservative decay heat load for the package in the fire transient analysis.

The steady-state initial condition temperature distribution predicted for the NAC LWT package was compared to the results reported in the SAR [11], but direct correspondence between the two sets of results is not to be expected, because the SAR [11] does not include any analytical cases similar to the detailed 3-D model used in the current study. Due to the relatively low associated decay heat load capacity of the package, the applicant chose to perform a series of highly conservative evaluations using much simpler models to qualify the system for its Certificate of Compliance (CoC).

The most complex models presented in the SAR [11] involve simple 2-D ANSYS cross-sections in which the cutting plane includes the expansion tank as well as the neutron shield tank. This approach does not allow axial heat flow out of the plane of the 2-D cross-section, and also assumes that the decay heat load axial peak occurs on that cutting plane, placing the spent nuclear fuel peak decay heat location under two concentric neutron shields. This provides conservatism for a steady-state analysis, since the expansion tank makes a longer conduction path over which to dissipate the decay heat. For the fire transient, however, the assumptions in this 2-D model would have the effect of limiting the heat input to the package from the fire, and would not constitute a conservative approach.

ANSYS 2-D cross-sectional models were also used in the SAR [11] to represent a 1.41 kW 25-rod BWR basket assembly and a 2.1 kW high burn-up PWR assembly, with detailed representation of the fuel pins, pin tubes, and can weldments with the pins resting on the pin tubes via point contact. These models included the ISO container, with boundary conditions that included solar insolation and 100°F (38°C) ambient temperature. The design basis model presented in Amendment 34 of the SAR [11] for a 2.5 kW

PWR assembly also used a 2D representation of the package. This is a HEATING5 model, and consists of a 2-D axisymmetric representation using effective diameters for the basket and fuel assembly. This model does not include an ISO container or impact limiters, convection at the assembly end cavities is neglected, and the ambient temperature boundary is specified as 130°F (54°C).

None of these cases from the SAR [11] use assumptions or boundary conditions identical to the initial conditions assumed for the fire transient in this analysis, but there are sufficient similarities to allow reasonable comparisons to be made for verification of the 3-D ANSYS model predictions. The results for these three cases are reported in Table 6.3.

Table 6.3. NAC LWT Component Temperatures at Various Decay Heat Loads

Component	2.5 kW °F (°C) (Table 3.4-2 [11])	1.41 kW °F (°C) (Table 3.4-7 [11])	2.1 kW °F (°C) (Table 3.4-10 [11])
Fuel Cladding	472 (244)	358 (181)	671 (355)
Aluminum PWR Insert	276 (136)	*	394 (201)
Inner Shell	274 (134)	249 (121)	385 (196)
Gamma Shield	273 (134)	248 (120)	375 (191)
Outer Package Surface	229 (109)	185 (85)	308 (153)
Neutron Shield	238 (114)	235 (113)	306 (152)
Lid Seal	227 (108)	*	*
Drain/Vent Ports	231 (111)	*	*
Impact Limiters	*	*	*
ISO Container	*	*	*

* value not reported by applicant

Figure 6.13 shows the predicted temperature distribution from the ANSYS solution for the 3-D model developed for the current study, obtained using 130°F (54°C) ambient temperature with a 2.5 kW decay heat load. This calculation was performed in addition to the initial conditions case at 100°F (38°C) ambient temperature, as a verification case for comparison to the results obtained for the 2.5 kW case reported in the SAR [11]. The 2-D axisymmetric model in the SAR [11], which used an ambient temperature of 130°F (54°C), is the most similar to the initial conditions in the fire transient for the purposes of this comparison, despite the exclusion of the ISO container.

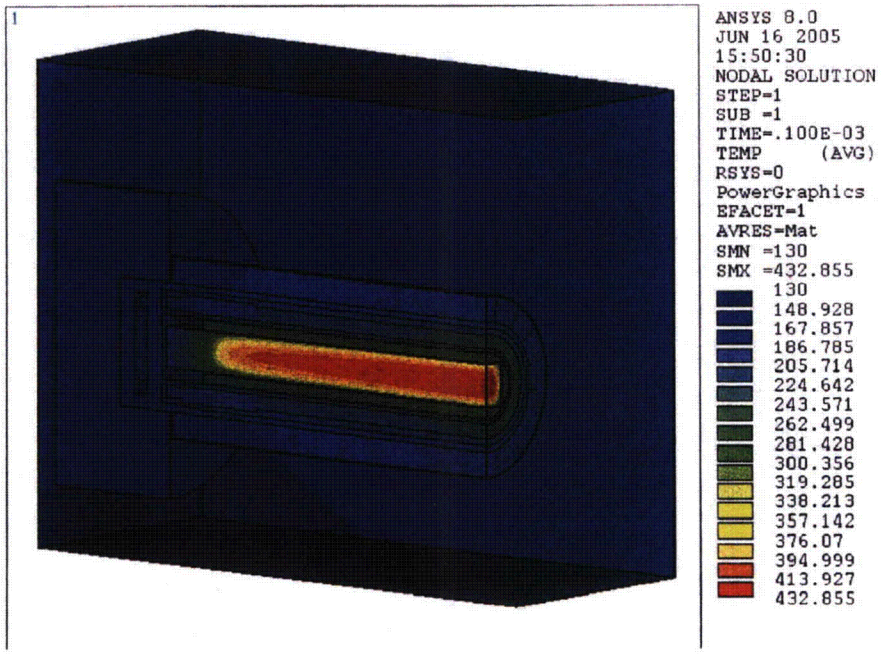

Figure 6.13. LWT Package Hot-Normal Condition Temperature Distribution (2.5 kW Decay Heat)

Table 6.4 presents detailed component temperature results obtained with the 3-D ANSYS model, compared to the values published in the SAR [11] for this decay heat load.

Table 6.4. NAC LWT Component Temperatures at 2.5 kW Decay Heat and 130°F Ambient

Component	Current Study (ANSYS) °F (°C)	SAR Values (Table 3.4-2 [11]) °F (°C)	ΔT °F (°C)
Fuel Cladding	434 (223)	472 (244)	38 (21)
Aluminum PWR Insert	265 (129)	276 (136)	11 (6)
Inner Shell	228 (109)	274 (134)	46 (26)
Gamma Shield	227 (108)	273 (134)	46 (26)
Outer Package Surface	200 (93)	229 (109)	29 (16)
Neutron Shield	204 (96)	238 (114)	34 (19)
Lid Seal	164 (73)	227 (108)	63 (35)
Drain/Vent Ports	164 (73)	231 (111)	67 (37)
Impact Limiters	167 (75)	Not Modeled	--
ISO Container	167 (75)	Not Modeled	--

At first glance, the differences between the results obtained with the two models appear to be rather sizable. The peak clad temperature predicted with the ANSYS 3-D model is 434°F (223°C), compared to

472°F (244°C) reported in the SAR [11]. The other temperatures shown in the table are also considerably lower for the ANSYS model, compared to the corresponding SAR values. However, this is an expected result, given the modeling differences between the two cases.

A more significant observation for the purposes of this comparison is to note that the differences in peak component temperatures between the two models are consistent. The radial temperature drop from the peak fuel cladding temperature to the outer package surface temperature is 234 °F (130 °C) for the 3-D ANSYS model used in the current study, compared to a temperature drop of 243 °F (135 °C) for the HEATING5 axisymmetric model used in the SAR [11]. This close agreement strongly suggests that the axisymmetric model featured in the SAR predicts essentially the same temperature distribution as the more detailed ANSYS model used in the current study. Most of the differences in the point-to-point temperatures predicted with each model are due to the differences in assumed external boundary conditions (100°F (38°C) for the current study, compared to 130°F (54°C) in the SAR analysis), and differences in modeling details.

Figure 6.14 shows the temperature distribution predicted with the ANSYS 3-D model for the initial steady-state conditions before the fire transient. The boundary conditions for this calculation are from the Normal Transport Condition case, as described in 10 CFR 71.21 [1].

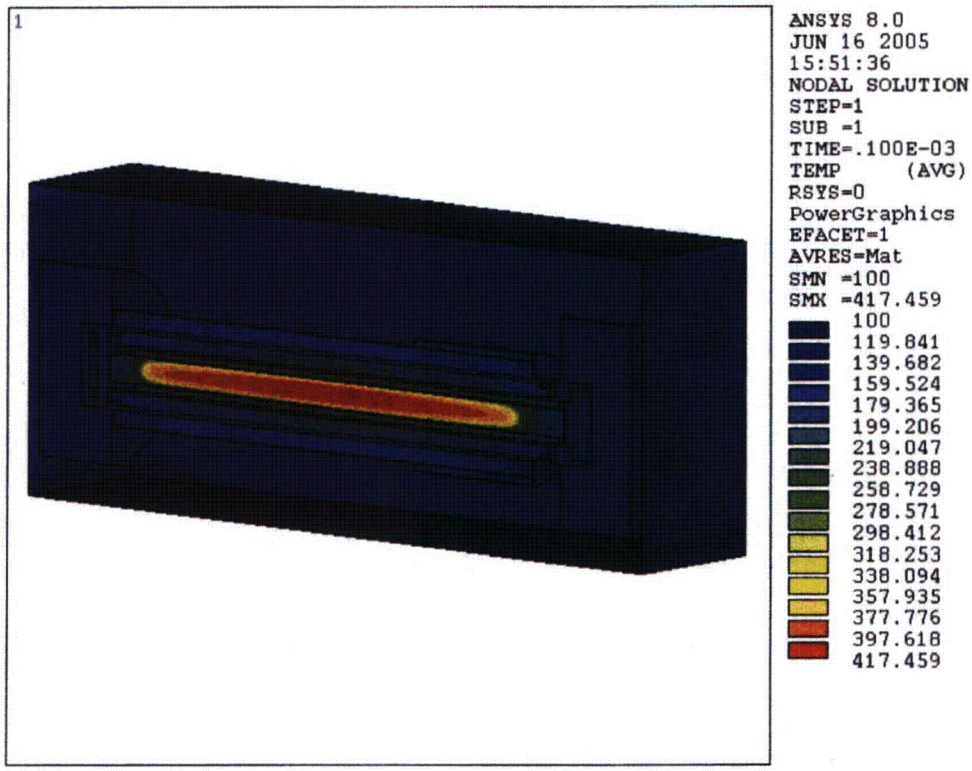

Figure 6.14. LWT Package Normal Condition Temperature Distribution (2.5 kW Decay Heat)

The hottest fuel temperature is predicted to occur near the center of the assembly, at a location that corresponds closely to the cross-section with the highest decay heat (i.e., the location of the maximum axial peaking factor). This location is some distance away from the part of the package covered by the expansion tank. This shows that the assumption placing the peak location under the expansion tank, which was used in the 2-D cross-section model in the SAR [11], is markedly conservative, and therefore can be expected to yield a higher estimate of the peak temperature.

As shown in Figure 6.14, the temperature gradients in the package are such that heat spreads and dissipates axially as well as radially. As a result, the 3D geometry yields a more realistic representation of the heat flow in the package. The conservative measures used in the simpler 2-D ANSYS cross-sectional models and the HEATING5 axisymmetric cross-sectional model (as reported in the SAR [11]) will tend to result in higher predicted temperatures for steady-state conditions. Other associated modeling assumptions and simplifications, including boundary conditions developed by the applicant, also tend to drive up component temperatures, compared to what might be obtained with a detailed 3-D representation.

The main concern in analyses for normal transport conditions is to determine a conservative rate of heat removal *from* the package. The approach employed in the SAR should yield conservative estimates of peak internal temperatures for the analysis. However, for the fire transient, the main concern is the amount of heat that the external fire can put *into* the package. In the fire transient calculations, a best estimate of component temperature distributions and heat transfer paths is more appropriate.

The conservative approach for the fire analysis in the current study is to choose assumptions that tend to enhance the heat transfer paths, making it easier for heat to move into the package from outside. For example, the treatment of internal gaps between components is conservative in the SAR, in that gaps are assumed to be as large as possible. In the ANSYS model for the fire analysis, the shrinkage gap between the lead shielding and package shell is included during the initial steady-state calculation, but is ignored during the fire transient. This approach tends to minimize heat loss from the package at the initial conditions, but then maximizes the heat input into the package internal components during the fire.

The pre-fire peak component temperature results determined in this study for the Normal Transport Condition case at 100°F (38°C), as described in 10 CFR 71.71 [1], are shown in Table 6.5.

Table 6.5. NAC LWT Pre-Fire Component Temperatures at 2.5 kW Decay Heat Load and 100°F Ambient

Component	Component Temperature °F (°C)
Fuel Cladding	418 (214)
Aluminum PWR Insert	242 (117)
Inner Shell	205 (96)
Gamma Shield	204 (96)
Outer Package Surface	176 (80)
Neutron Shield	180 (82)
Lid Seal	138 (59)
Drain/Vent Ports	138 (59)
Impact Limiters	141 (61)
ISO Container	140 (60)

6.3 Tunnel Fire Evaluations of Rail Packages

The Baltimore tunnel fire simulations for the three transport packages were conducted in three phases. These were the pre-fire steady-state (hot-normal) conditions of transport, the fire (consisting of the first 7 hours of the transient), and the post-fire phase. For the pre-fire steady state, the hot-normal conditions of transport were evaluated with solar insolation and a 100°F (38°C) ambient temperature, according to 10 CFR 71.71(c)(1) [1]. External heat transfer was assumed to be free convection in still air with thermal radiation exchange with the environment. This conservatively established component temperatures to serve as initial conditions for the transient.

For the fire phase of the evaluation ($0 \leq t \leq 7$ hours), the energy input due to solar insolation was set to zero, the tunnel surfaces were introduced, and the transport package and tunnel surfaces were assign an emissivity of 0.9 to represent surfaces affected by sooting. A forced convection regime was assumed to exist on the exterior of the package, based on the gas velocity results from the analysis performed by NIST. These results were used to determine the surface heat transfer coefficient, and with the gas temperatures from the NIST analysis defining the ambient boundary temperature, the convective heat flux at the package surface could be determined in the solution for the local surface temperature. Tunnel wall temperatures were also taken as boundary conditions from the NIST calculations, and thermal radiation exchange between the tunnel walls and the package was also accounted for in the evaluations. In addition to these measures, all aluminum honeycomb, neutron shield resin materials, or wood were assumed to remain intact during the full duration of the fire to maximize heat input during the fire.

For the post-fire phase of the evaluation ($t > 7$ hours), properties of the neutron shield resin materials, wood, and selected portions of aluminum honeycomb sections were replaced with thermal properties

identical to those of air. This change in material properties simulates the degradation of the materials due to the fire and has the effect of reducing the rate of heat release during the post-fire phase. Conservatively, the energy absorbed in the degradation of these materials was not subtracted from the heat input of the fire to the package. Other model-specific conservatisms were also incorporated, as described above in Section 5.

Analysis of the post-fire phase was carried out for a duration of 293 hours. This included the 23 hours of the post-fire portion of the transient predicted by the FDS analysis, plus an additional 270 hours in which boundary conditions at 30 hours were extrapolated to 300 hours, using a power function (as discussed in Section 5 above). Purely forced convection heat transfer correlations (based on the NIST gas velocities and temperatures) were imposed for the post-fire phase of the simulation from 7 hours to 30 hours. The forced convection boundary condition at the package surface was then transitioned to free convection correlations, to establish the buoyant convective coefficients of heat conductance for the remainder of the evaluation period.

Results obtained in the evaluations of the three packages are discussed in Section 7.

7 ANALYSIS RESULTS

Due to the temperature limits on the spent fuel cladding, closure seals, impact limiter core materials, and neutron shield core materials, these components are the most important elements to consider in evaluating the response of the transport systems to the fire scenario. The peak cladding temperature limit is important because the cladding is the primary fission product containment boundary for the spent fuel. The temperature limit for the closure seals is important because these seals constitute the outer-most containment boundary for the package. The temperature limits for the neutron shield material and impact limiters are important because these materials are the most vulnerable to damage or destruction during the fire. The results of the analyses for the three rail packages were evaluated primarily in relation to the peak predicted temperatures for these components in the fire transient.

These analyses indicate that the spent fuel cladding reaches a peak temperature of 845°F (452°C) in the TN-68 package, 930°F (499°C) in the HI-STAR 100 package, and 884°F (473°C) in the NAC LWT system. Peak cladding temperatures for the TN-68, HI-STAR 100, and NAC LWT packages are below the currently accepted short term temperature limit[17] of 1058°F (570°C) for Zircaloy clad spent nuclear fuel under accident conditions [23].

The transient results for each of the three systems are discussed in detail below. Section 7.1 discusses the response of the TN-68 package during the fire. Section 7.2 presents results for the HI-STAR 100 package. Section 7.3 discusses the response of the NAC LWT package.

7.1 TN-68 Fire Transient Results

The COBRA-SFS model of the TN-68 package consists of a total of 530,228 computational nodes that are solved for each time step. This yields an overwhelming volume of output that must be sorted, sifted, and processed to produce a coherent picture of the response of the package to this fire scenario. The following three subsections present the peak temperatures versus time for selected components, as determined with COBRA-SFS for the TN-68 package subjected to the fire transient conditions described in detail in Section 6. The results are presented separately for the three main phases of the transient. Section 7.1.1 discusses the predicted response of the TN-68 package during the fire. Section 7.1.2 presents results for the post-fire transient over the duration of the NIST simulation (to 30 hours). Section 7.1.3 discusses the response to the postulated long-term post-fire conditions, out to 300 hours.

7.1.1 TN-68 During the Fire

Figure 7.1 shows the initial temperature response of the TN-68 package predicted with COBRA-SFS during the fire portion of the transient. The fire burns for the first 6.75 to 7 hours of the transient (see Figures 6.1 and 6.2 for boundary temperatures representing the fire with the package 66 ft (20 m) from

[17] The short-term temperature limit of 1058°F (570°C) is based on creep experiments performed on two fuel cladding test samples which remained undamaged (i.e., no significant observable damage) when held at 1058°F (570°C) for up to 30 and 71 days [24]. This temperature limit is a relatively conservative limit, since the temperature at which Zircaloy fuel rods actually fail by burst rupture is approximately 1382°F (750°C)[25].

the fire center). During this time, the outer surface temperature of the package shell increases quite rapidly. The maximum temperature of the package surface increases at a rate of up to 10.5°F/min. (5.8°C/min.), reaching a peak temperature of 1789°F (976°C) at about 6.3 hours into the fire. The maximum temperature of the neutron shield material also shows a relatively rapid increase, reaching a peak of 1355°F (735°C) at approximately 6.9 hours into the fire.

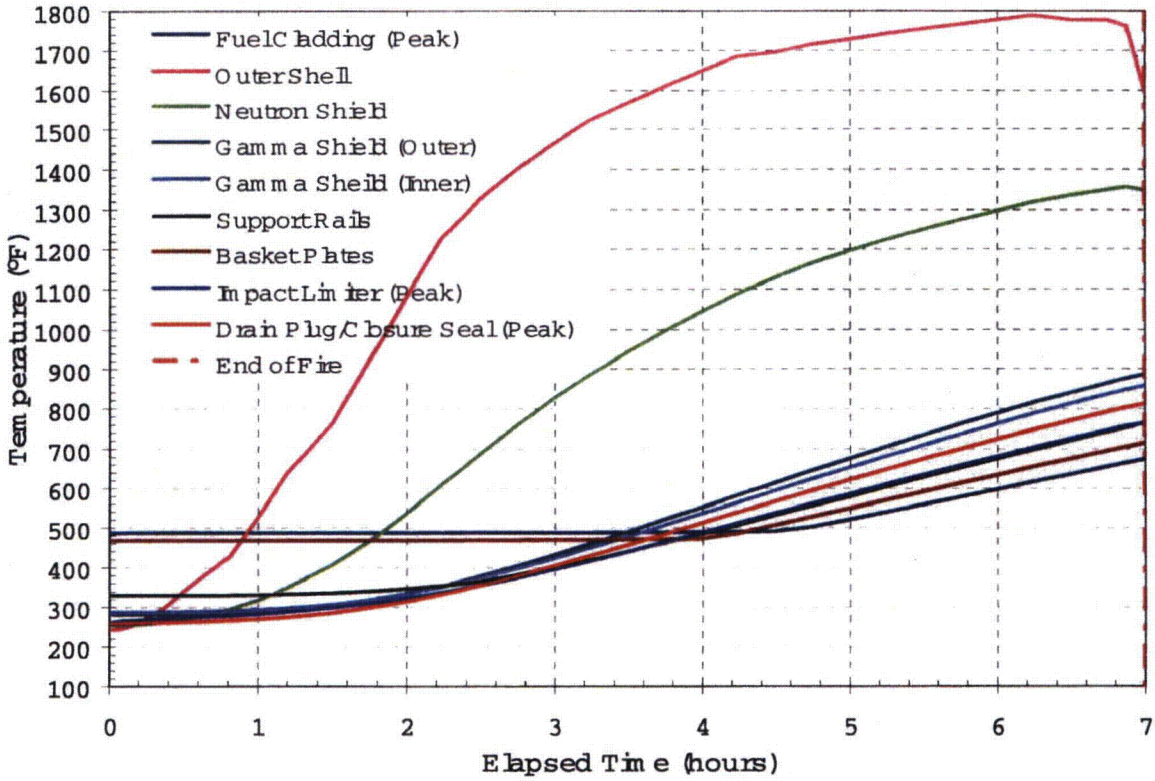

Figure 7.1. Maximum Temperature Histories for TN-68 Components During Fire Transient

The internal components of the package show a very slow thermal response during the fire. The support rails and gamma shields take more than an hour to show any noticeable increase in temperature. Approximately 3.5 hours elapse before the peak fuel cladding temperature rises as much as 1°F above the initial steady-state peak temperature of 485°F (252°C). The peak temperatures of the basket tubes and poison plates rise only about 4°F (2.2°C) in the first four hours of the fire. During this time period, the peak temperature on the outer shell of the package is predicted to go up to 1647°F (897°C), the predicted peak temperature of the neutron shield rises to 1042°F (561°C), and the peak temperature on the gamma shields increases to 549°F (287°C).

By the end of the fire, marking the point at which all volatile flammables are consumed, the peak clad temperature has risen to only 673°F (356°C), and the peak temperature of the basket tubes and poison plates is at about 714°F (379°C). The outer shell of the package is predicted to have a peak temperature of 1599°F (871°C) at the end of the fire, with the neutron shield at 1347°F (731°C) and the outer gamma shield at 886°F (474°C).

Figure 7.2 shows midline temperature profiles from top to bottom vertically through the package cross-section, including the package shell, support rails, and basket structure during the fire at approximately hourly intervals. The large difference in the predicted rate of increase in temperature for the internal and external components of the package is illustrated by these profiles. The temperatures of the nodes modeling the basket tubes and poison plates change very little during the fire. The support rails and gamma shield nodes heat up relatively slowly, while the outer shell and neutron shield region increase rapidly in temperature in response to the fire.

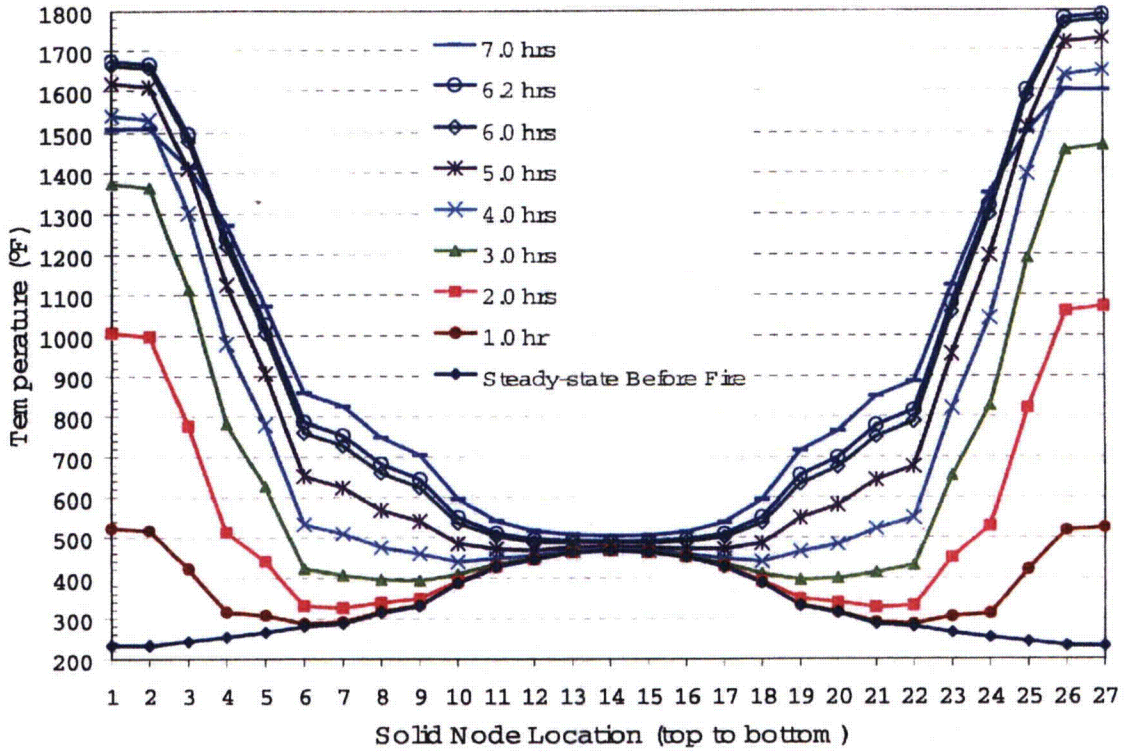

Figure 7.2. Temperature Profiles Top-To-Bottom Through TN-68 Package During Fire Transient

The neutron shield and gamma shields insulate the basket and fuel assemblies from the fire, but the slow response is also due in large part to the huge thermal inertia of the package components. The 68 assemblies within the package weight on the order of 20 to 25 metric tons (mainly uranium dioxide and Zircaloy), with roughly 8 metric tons of material in the basket (mainly steel and borated aluminum). The inner and outer gamma shields consist of approximately 40 metric tons of carbon steel, while the outer shell of the package is approximately 5 metric tons of steel. Even under the severe heat load imposed by the sustained high temperatures of a fire lasting almost 7 hours, it takes time to raise the temperature of such a large mass of material, even with its internal heat generation due to the spent fuel assemblies.

A significant detail discovered during the evaluation of the TN-68 is that during the first quarter of the fire transient, the total heat flux associated with radiation heat transfer from the tunnel to the package is nearly an order of magnitude greater than the total heat flux associated with convection heat transfer from

the tunnel environment to the package. As a consequence, the most severe conditions for this transient are those that result in the package receiving the greatest exposure to radiation heat transfer. This means that a horizontal orientation will result in the greatest possible heat input for a given fire scenario. Any package orientation other than the horizontal orientation during the fire (e.g., the package up-ended into a vertical orientation as a result of an accident) would yield less severe heat input to the package.

7.1.2 TN-68 Short-Term Post-Fire Response

Figure 7.3 shows the temperature response of the package during the first 30 hours of the COBRA-SFS simulation. (This time period represents the total duration of the NIST analysis that is the source of the boundary conditions for this calculation.) During the fire, the material in the neutron shield reaches temperatures that would heavily degrade the borated polyester. This does not mean, however, that the package would fail to meet the requirement of maintaining appropriate shielding in this scenario. This spent fuel transportation package is expected to lose its neutron shield material in the fire accident specified in current regulations, and therefore the design does not rely on the neutron shield material remaining intact in order to maintain shielding. This package is designed to attenuate neutron radiation to acceptable levels (see 10 CFR 71.51 [1]) following an accident without the assistance of the neutron shield material. However, the loss of the shield material means that the neutron shield's heat transfer capability would be expected to deteriorate rapidly during the fire.

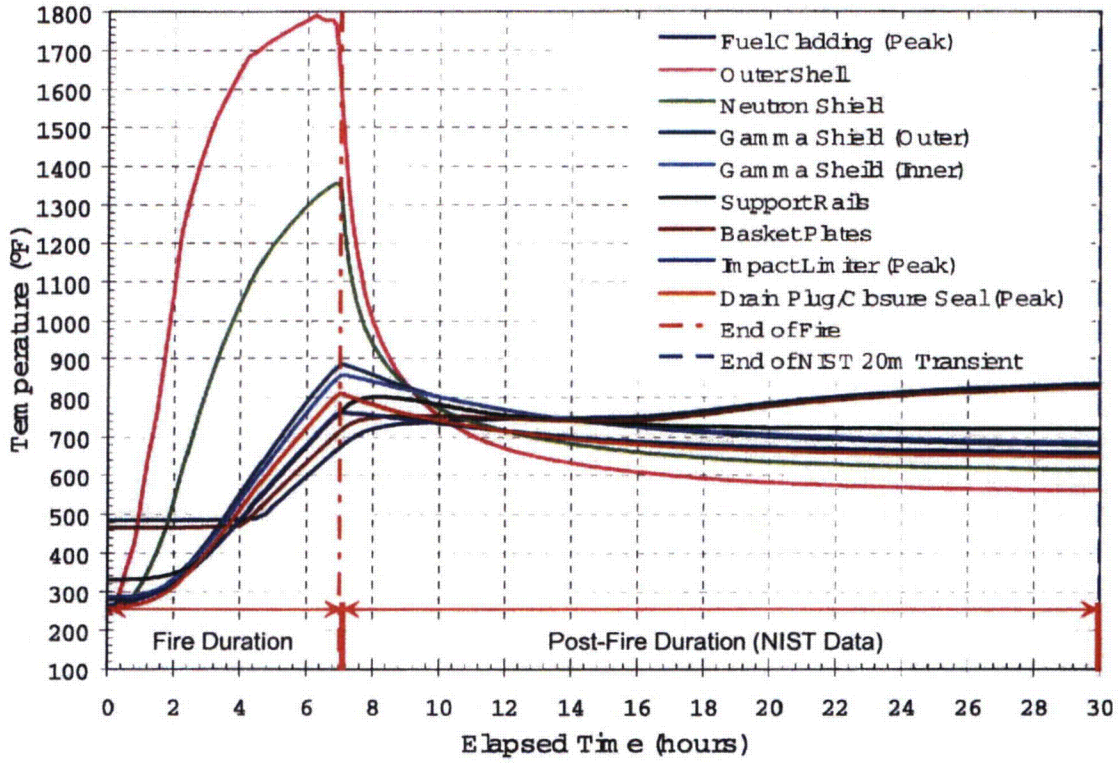

Figure 7.3. Maximum Temperature Histories for TN-68 Package Components During First 30 hr of Transient

In the COBRA-SFS evaluation, it was assumed that the borated polyester remains in place and is unaffected during the fire, but instantly degrades at the end of the fire and is replaced by hot air. This maximizes the heat input into the package during the fire, then imposes an additional barrier to heat transfer from the package after the fire. From the standpoint of the thermal response of the system, this is a conservative representation of the effect of the fire on the neutron shield. The thermal conductivity of the borated polyester is about 140 times that of air, so extending the residence time of the polyester to the end of the fire results in a calculation that overestimates the rate of heat flow into the package during the fire. This will tend to result in higher calculated temperatures on the package internals than would be obtained if it were assumed that the polyester was replaced with air earlier in the transient. In reality, the change would be more gradual and would occur earlier in the transient as the neutron shield burned away. The heat absorbed in the process of consuming the polyester material is not subtracted from the heat of the fire, as an associated conservatism.

The temperatures in Figure 7.3 show that once the fire is over, the peak temperatures on the package shell and neutron shield are predicted to begin to drop precipitately. This is primarily a response to the rapid decrease of the boundary temperatures, as can be seen in Figure 7.4. This plot shows the outer shell surface temperature predicted with COBRA-SFS compared to the tunnel ceiling temperature and the temperature of the air above the package, which are derived from the NIST calculations and used as boundary conditions.

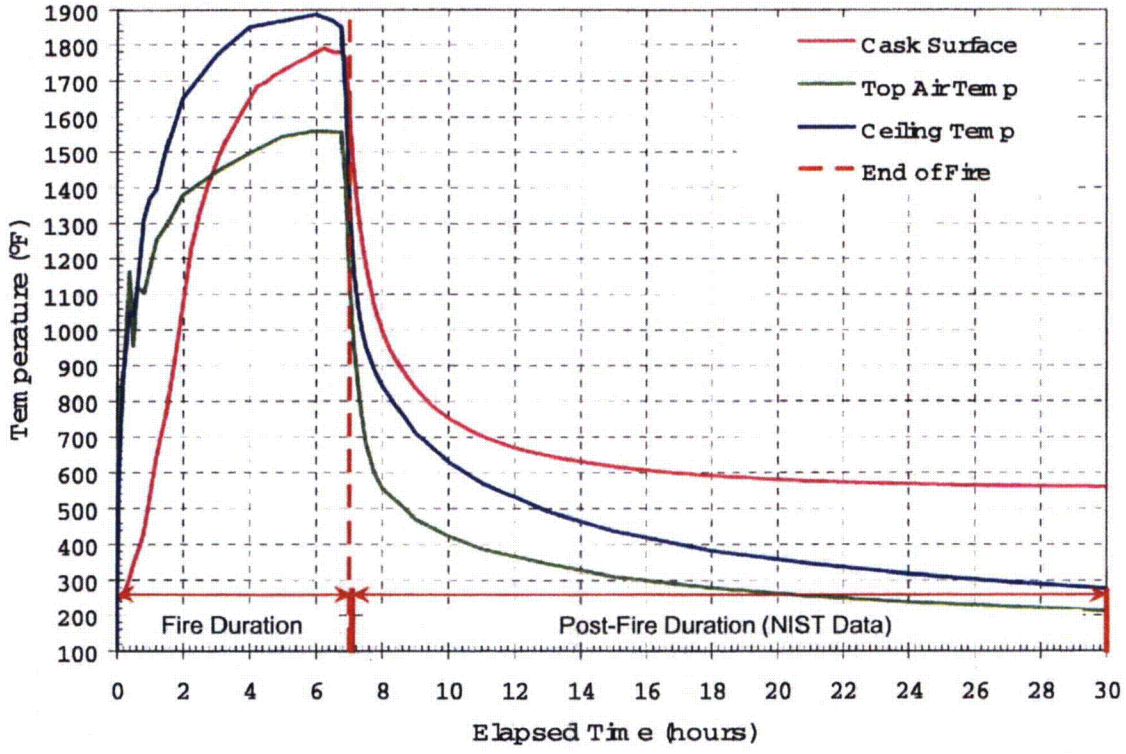

Figure 7.4. Maximum TN-68 Package Surface Temperatures Compared to NIST Boundary Condition Temperatures

Figure 7.3 also shows that the peak temperatures on the gamma shields and support rails of the package decrease after the fire ends. However, the temperature decrease for these components is much slower than for the neutron shield region and outer shell because the internal components must also absorb the thermal load from the fuel. For the same reason, the peak temperature of the basket shows a continuous increase even after the end of the fire, as does the peak clad temperature.

The plot of the predicted peak clad temperature in Figure 7.3 shows that the thermal output of the fire itself does not have much of an effect on the fuel. The observed rise in peak clad temperature is mainly a response to the effect of the external boundary conditions on the rate of heat transfer from the package. The heat of the fire does not result in much of an increase in the package internal temperatures, but the increase in the external air temperature severely compromises the rate of heat rejection from the package and continues to do so long after the fire is out. This is illustrated very clearly by the plot of the global peak clad temperature alone, shown in Figure 7.5 for 50 hours of the transient (i.e., the 30 hours of the NIST transient, plus an additional 20 hours of the extended cool down beyond the NIST calculation).

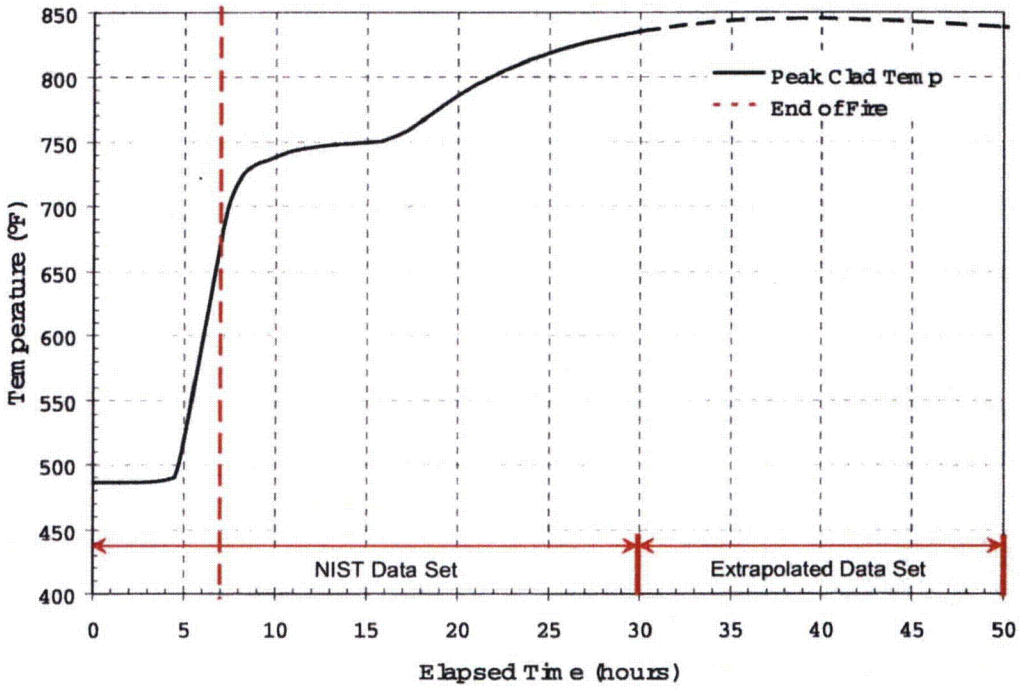

Figure 7.5. Peak Fuel Cladding Temperature History in TN-68 During First 50 hr of Transient

As shown by the plot in Figure 7.5, at about 4.5 hours into the fire the peak clad temperature begins an almost adiabatic heat up (approximately 77°F/hr (43°C/hr)) because the fire is preventing normal heat removal from the package (which occurs by thermal radiation to the external environment and natural convection at the surface). This adiabatic heat-up continues for about an hour after the end of the fire, until the package shell temperature drops low enough to permit some heat removal from the package by radiation to the tunnel surfaces.

The fuel cladding temperature increase observed shortly before the end of the fire (at ~4.5 hours) occurs in fuel in the outer periphery of the basket, because the fire is heating the outer cylinder of the package. This causes the peak fuel cladding temperature to shift first to the bottom assembly in the horizontal basket cross-section, then to the top assembly. The rate of increase in the predicted peak cladding temperature slows briefly to 1-2°F/hr (0.5-1°C/hr) before increasing again as the peak temperature location shifts back to the center assembly in the core of the basket. (The peak fuel clad temperature location is automatically tracked in these results during the transient.)

The peak clad temperature continues to increase after the fire, because thermal radiation from the tunnel ceiling, walls and floor is continuing to add heat to the package and the external ambient air temperature slows the rate of heat removal by convection. However, the rate of increase drops to only about 2°F/hr (~1°C/hr). At about 15 hours into the transient, the rate of increase of the peak clad temperature begins to climb again, to a rate of about 10°F/hr (6°C/hr), then again drops to only 3°F/hr (~2°C/hr) after about 20 hours. This behavior is due to the decrease in the rate of heat removal via thermal radiation as the tunnel surfaces cool down, and the more gradual decrease in the rate at which heat is being removed from the package by forced convection, due to the decrease in velocity and temperature of the hot air flowing past the package.

By the end of the NIST transient at 30 hours, the rate of increase of the peak clad temperature has dropped to less than 3°F/hr (<2°C/hr). The global peak cladding temperature of 845°F (452°C) is finally reached at ~40 hours into the transient. (The dashed portion of the curve in Figure 7.5 denotes results for boundary conditions extrapolated beyond the results obtained in the 30-hour NIST calculation.)

The maximum temperature history of the seals in the package closure and vacuum port is shown in Figure 7.6. The curve in this figure represents the global peak of all seal material used in the TN-68. As shown in this figure, the Helicoflex® seal material is predicted to reach a maximum temperature of 811°F (433°C) right at the end of the fire, then gradually decreases as the transient proceeds into the post-fire cool down. This peak temperature exceeds the seal manufacturer's recommended maximum long-term service temperature of 536°F (280°C) for this material, as specified in the SAR [11]. (For a discussion of the consequences of seal failure, see Section 8.2.1.)

Bolts and other subcomponents were not explicitly represented at the package ends in the COBRA-SFS model of the TN-68. However, the depicted temperature history (see Figure 7.6) conservatively represents the peak temperature history of the closure bolts due to the manner in which heat must migrate around the top impact limiter into the package upper forging, through the closure seal location, and then into the closure. This is due to the limited conduction offered by the steel-encapsulated wooden impact-damping material comprising the impact limiter.

The thermal response of the package after the end of the fire is further illustrated in Figure 7.7, with plots showing radial temperature profiles through the package at selected time intervals through the transient. These profiles show that the outer shell and former neutron shield cool rapidly once the fire is over, while the temperatures of the internal nodes representing the basket tubes and poison plates continue to rise in response to the heat load from the spent nuclear fuel.

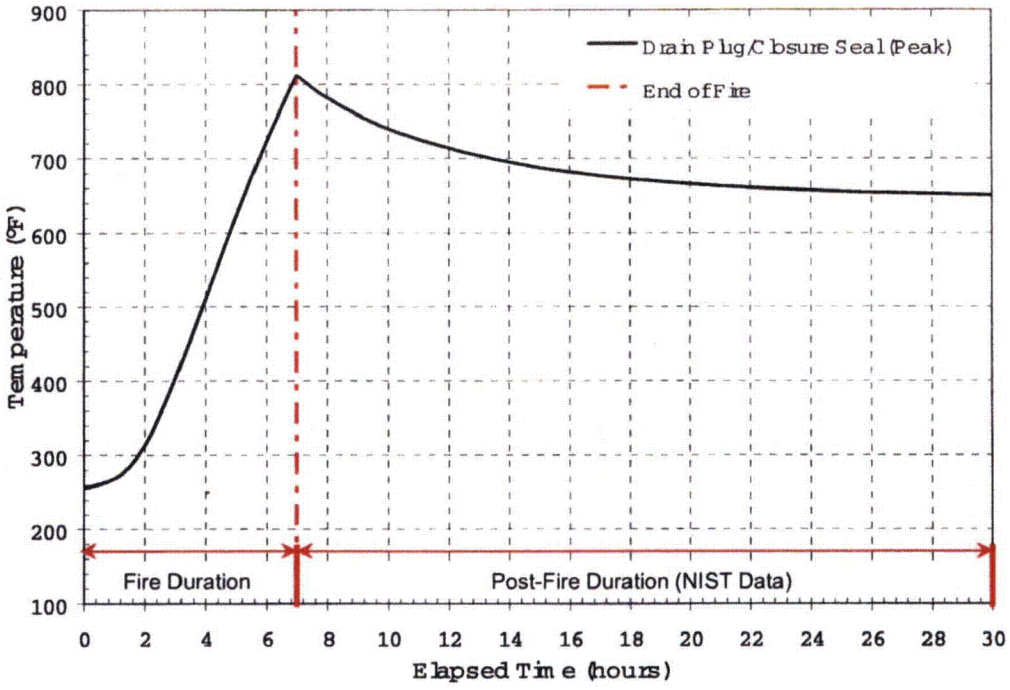

Figure 7.6. Maximum Global TN-68 Closure/Port Seal Temperature History for 30-hr Transient

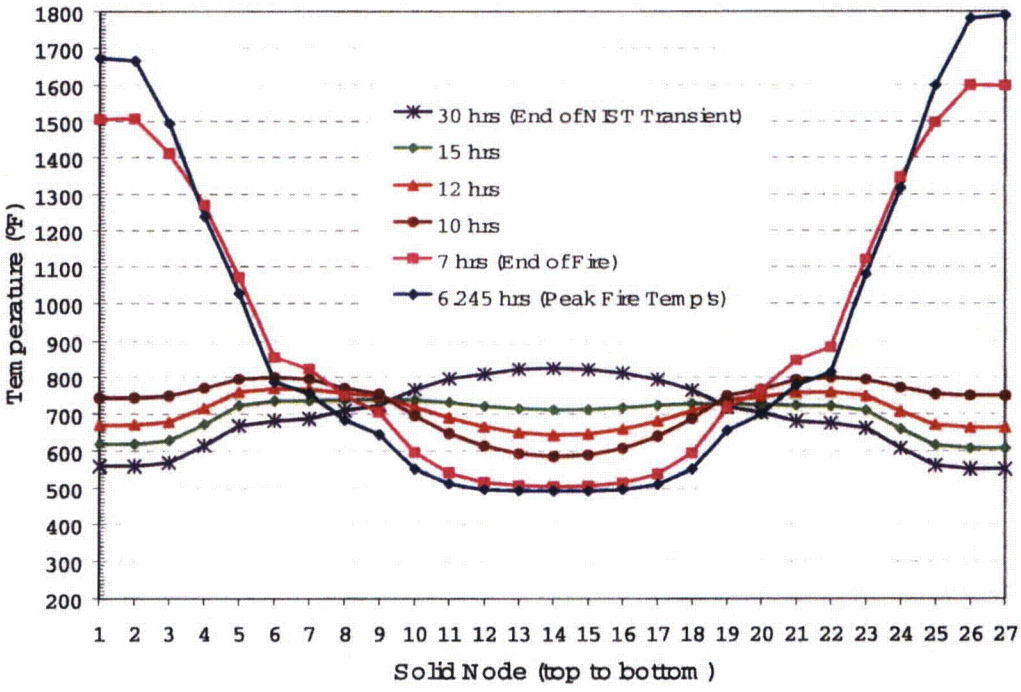

Figure 7.7. Temperature Profiles Top-To-Bottom Through TN-68 Package Axis to 30 hrs

7.1.3 TN-68 Long-Term Post-Fire Response

The NIST calculation used to define the boundary conditions for the COBRA-SFS analysis simulated the fire transient and its aftermath out to 30 hours. However, the trends exhibited by the temperatures of the various components of the package at the end of the transient indicate that the system is not yet at a new steady state by then. Temperatures predicted by NIST for the first 30 hours were extrapolated from 30 hours out to 300 hours using a power function to realistically model cool down of the tunnel environment. (The extrapolated values are presented in Figures 6.5 and 6.6 for the air and wall temperatures, respectively.)

To explore the effects of prolonged exposure to post-fire conditions in the tunnel, the calculations were carried out for the full 300 hours (293 hours after fire cessation). This is equivalent to assuming that the package will be left in the tunnel for an extended period (days or weeks rather than merely hours) without any emergency responder intervention. This assumption is not realistic but is highly conservative, defining a severe long-term ambient environment around the package.

During the first 30 hours of the transient, the heat transfer at the package surface was assumed to be forced convection at the velocities predicted in the tunnel by the NIST calculation. The basis for this approach is discussed in Section 6.0. This is a relatively conservative assumption, particularly for conditions after about 20 hours into the transient, when the velocities predicted in the NIST calculation have dropped to values of 1 to 2 ft/s (0.3 to 0.6 m/s) or less. For the latter portion of the transient ($t \geq 20$ hours), heat transfer at the package surface is a complex mixture of forced convection (due to air flow induced in the tunnel by the vertical temperature gradients from the fire) and free convection (driven by the non-uniform circumferential temperatures of the package outer shell). This was conservatively approximated by imposing a purely forced convection heat transfer coefficient (based on the NIST air velocities and temperatures) for the first 30 hours of the simulation, then imposing a free convection coefficient for the remainder of the calculation.

Figure 7.8 shows the temperature response of the various components of the package for the long term transient calculation to 300 hours. (As previously indicated, the dashed portion of the curve is used to distinguish the results that stem from the boundary conditions that were extrapolated from the NIST simulation.) As shown in Figure 7.8, the highest peak clad temperature, 845°F (452°C), is reached at approximately 40 hours. The peak temperature for the basket structure is also reached at about the same time. The predicted maximum in the peak clad temperature is below the regulatory limit of 1058°F (570°C) by a difference of 213 °F (110 °C). All other temperatures in the package have been decreasing steadily since the end of the fire.

By 100 hours, the peak clad temperature has dropped to 784°F (418°C), with temperatures decreasing at rates of about -1 °F/hr (-0.6 °C/hr). After 200 hours, the peak clad temperature has dropped to 719°F (382°C), and at 300 hours is predicted to be down to 690°F (366°C) for the specified boundary conditions. At this point in the transient calculation, the rate of change of local temperatures in the system is about -0.2°F/hr (-0.1°C/hr). The rate of cooling is very slow due to the huge thermal mass of the package and its fuel load. Projections of the cooling rate indicate that it would take an additional 175-200 hours to reach a new post-fire steady state.

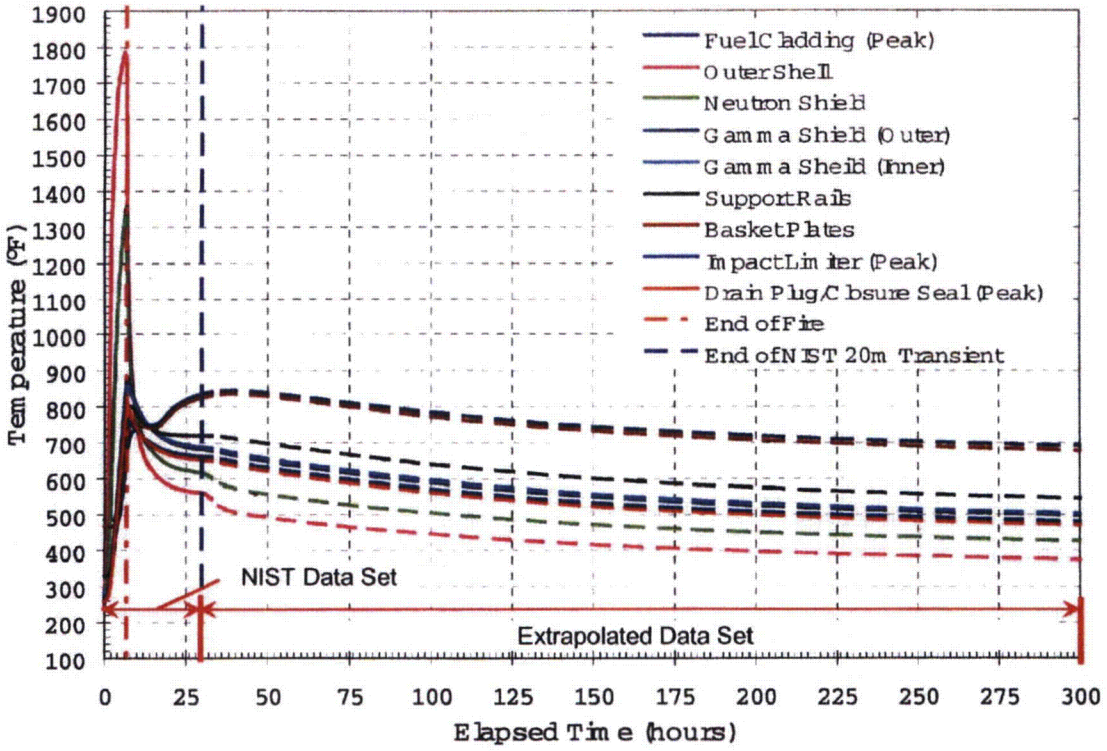

Figure 7.8. Maximum Temperature Histories for TN-68 Package Components During 300 hr of Transient

The trends in Figure 7.8 show that the overall thermal response of the package to the fire transient is essentially an accommodation to the new higher-temperature boundary conditions extrapolated from the conditions predicted at the end of 30 hours in the NIST fire analysis. The temperature of the fuel and basket is largely unaffected by the heat input to the package from the fire; the increase in peak clad temperature and peak basket temperature is due almost entirely to having no heat removal from the package during the fire and for about an hour immediately afterwards. After the ambient temperatures drop enough to allow heat removal from the package, the rate of increase of the peak clad temperature begins to level off and then finally turn around about 40 hours into the transient.

Viewed on the scale of 300 hours, the fire portion of the transient appears as a large but relatively short-lived spike in the boundary conditions that significantly affects only the outer shell, neutron shield, and impact limiters, and to a lesser extent the outer and inner gamma shielding. These components show a rapid temperature increase during the fire, but after the end of the fire immediately begin a rapid cool down. Peak component temperatures for the TN-68 package in the fire simulation are summarized in Table 7.1.

Table 7.1. TN-68 Peak Component Temperatures During Fire Transient

Component	Maximum Temperature (COBRA-SFS) °F (°C)	Time (hours)
Fuel Cladding	845 (452)	40
Basket Plate	836 (447)	40
Basket Rail	801 (427)	8.3
Inner Shell	857 (458)	7.0
Gamma Shell	886 (474)	7.0
Package Bottom	762 (406)	7.0
Seals	811 (433)	7.0
Neutron Shield	1355 (735)	6.9
Outer Shell	1789 (976)	6.3

7.2 Holtec HI-STAR 100 Fire Transient Results

The ANSYS model of the HI-STAR 100 package consists of a total of 149,100 standard computational elements and 288 superelements that are solved for each time step. Similar to the COBRA-SFS model of the TN-68, this model yields an overwhelming volume of output that must be processed to produce a coherent picture of the package response. The following three subsections present the peak temperatures versus time for selected components, as determined with ANSYS for the HI-STAR 100 subject to the hypothetical fire transient conditions described in Section 6.

7.2.1 HI-STAR 100 During the Fire

Figure 7.9 shows the initial temperature response of the HI-STAR 100 package predicted with ANSYS during the fire portion of the transient. The maximum temperature of the HI-STAR 100 package surface increases rapidly to a peak temperature of 1831°F (999°C) around 6 hours into the fire. The maximum temperature of the inner shell material, which defines the primary containment boundary, also shows a relatively rapid increase, reaching a peak of 1447°F (786°C) approximately 6.75 hours into the fire. This corresponds to the peak boundary condition temperatures defined by the fire. The fire temperatures predicted in the NIST analysis peak at 6.75 hours, and then drop off rapidly thereafter as the fire burns itself out. The peak temperature of the inner shell material is predicted to lead the gamma shield material peak temperature because the elements selected to define the primary containment boundary include the bottom and top forgings and lid. A large section of the top forging is directly exposed to the fire (un-shrouded by the gamma shield, neutron shield/fin section and upper impact limiter).

Similar to the TN-68 results with the COBRA-SFS model, the internal components of the HI-STAR 100 package also show a very slow thermal response during the fire. The gamma shield takes more than half

an hour to show any noticeable increase in temperature. Nearly three hours elapse before the internal canister shell temperature rises as much as 1 °F (0.6 °C) above the initial steady-state peak temperature of 548°F (287°C). In the first five hours of the fire, the peak temperatures of the basket structure, poison plates, and fuel rise only by about 2 °F (1 °C). This is approximately an hour later than the TN-68 response and can be attributed to the additional thermal barrier of the MPC canister. In these five hours, the peak temperature on the outer skin surrounding the neutron shield of the HI-STAR 100 is predicted to go up to 1809°F (987°C), and the peak temperature on the gamma shields increases to 1332°F (722°C).

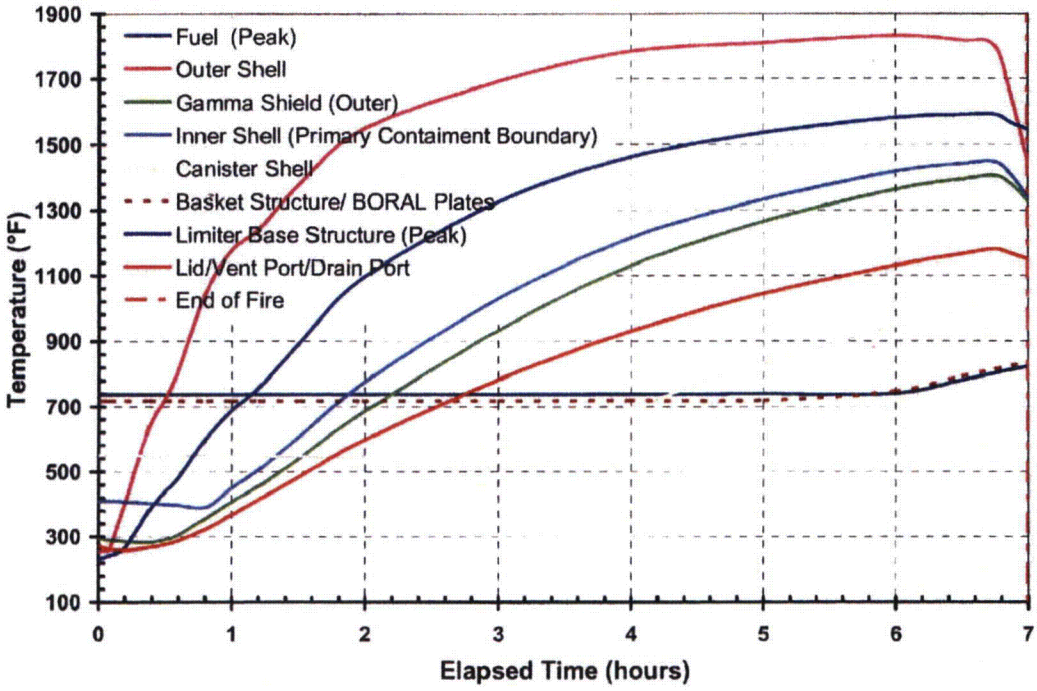

Figure 7.9. Maximum Temperature Histories for HI-STAR 100 Package Components During Fire Transient

By the end of the fire, marking the point at which all volatile flammables are consumed, the peak clad temperature has risen to only 803°F (428°C). The outer shell of the package is predicted to have a peak temperature of 1801°F (983°C) at the end of the fire, with the outer gamma shield at 1404°F (762°C). This is a bit warmer than the TN-68 at this point in time. The difference is due mainly to the larger thermal resistance to radial heat flow in the thinner skin of the HI-STAR 100, compared to the TN-68. However, both packages tend to perform similarly overall.

As with the TN-68 results, the large difference in the predicted rate of increase in temperature for the internal and external components of the HI-STAR 100 is because the neutron shield and gamma shield insulate the basket and fuel assemblies from the fire. The slow response is due mainly to the huge thermal inertia of the package components themselves. Even under the severe heat load imposed by the sustained high temperatures of a fire lasting nearly 7 hours, it takes time to raise the temperature of such a large mass of material, despite its internal heat generation component.

7.2.2 HI-STAR 100 Short-Term Post-Fire Response

Figure 7.10 shows the temperature response of selected components of the package during the first 30 hours of the ANSYS transient simulation. During the fire, the material in the neutron shield is predicted to achieve temperatures that will heavily degrade it. As noted in Section 7.1.1 for the predicted loss of the TN-68 package's neutron shield, the HI-STAR 100 is also designed to attenuate neutron radiation to acceptable levels (see 10 CFR 71.51 [1]) following an accident without the assistance of the neutron shield material. However, the neutron shield's heat transfer capability is expected to deteriorate rapidly during the fire. In the ANSYS evaluation, it was assumed that the neutron shield material (HOLTITE-A) remains in place and unaffected during the fire, but instantly degrades at the end of the fire, to be replaced by hot air. This maximizes the heat input into the package.

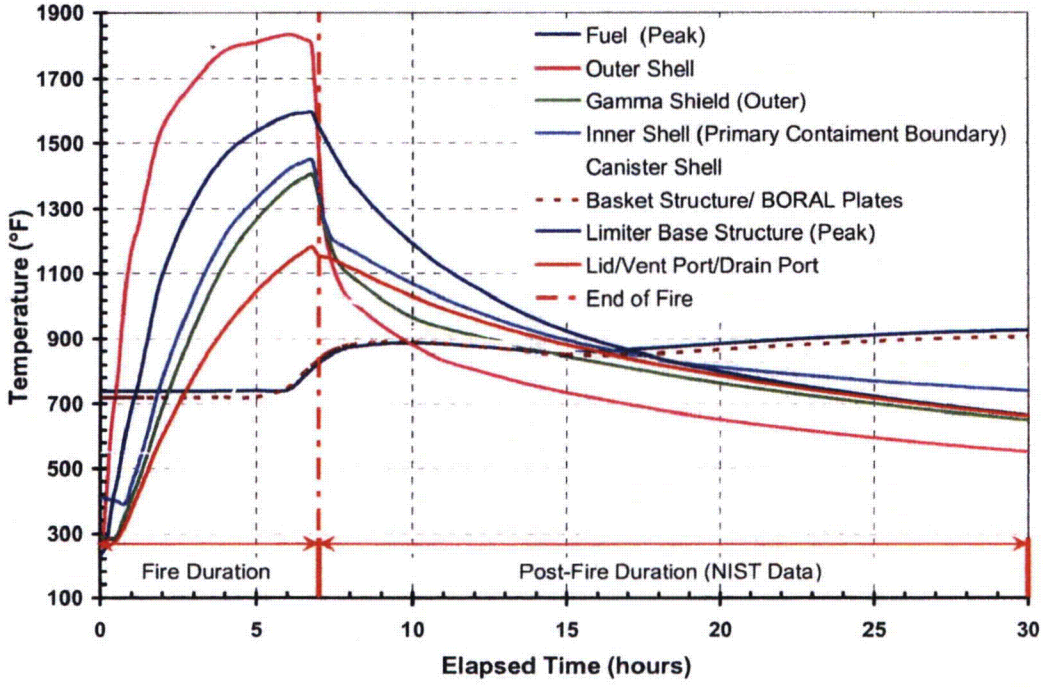

Figure 7.10. Maximum Temperature Histories for HI-STAR 100 Package Components During First 30 hr of Transient

This is a conservative representation of the effect of the fire on the neutron shield from the standpoint of the thermal response of the system. The thermal conductivity of HOLTITE-A is approximately 16 times that of air, so extending the residence time to the end of the fire results in the calculation somewhat overestimating the rate of heat flow into the package during the fire. This will result in higher calculated temperatures on the package internals than would occur if degradation were accounted for at a more realistic rate during the fire. As an additional conservatism, the latent heat absorbed in the degradation of the material, which would tend to decrease the external heat flux due to the fire, is also neglected.

The results shown in Figure 7.10 demonstrate that once the fire is over, the predicted peak temperatures on outboard components begin to drop rapidly (i.e., outer shell, gamma shield, etc.). This is primarily a response to the rapid decrease of the boundary temperatures, as can be seen in Figure 7.11, which shows the outer shell surface temperature predicted with ANSYS compared to the tunnel ceiling temperature and the temperature of the air above the package derived from the NIST calculations and used as boundary conditions.

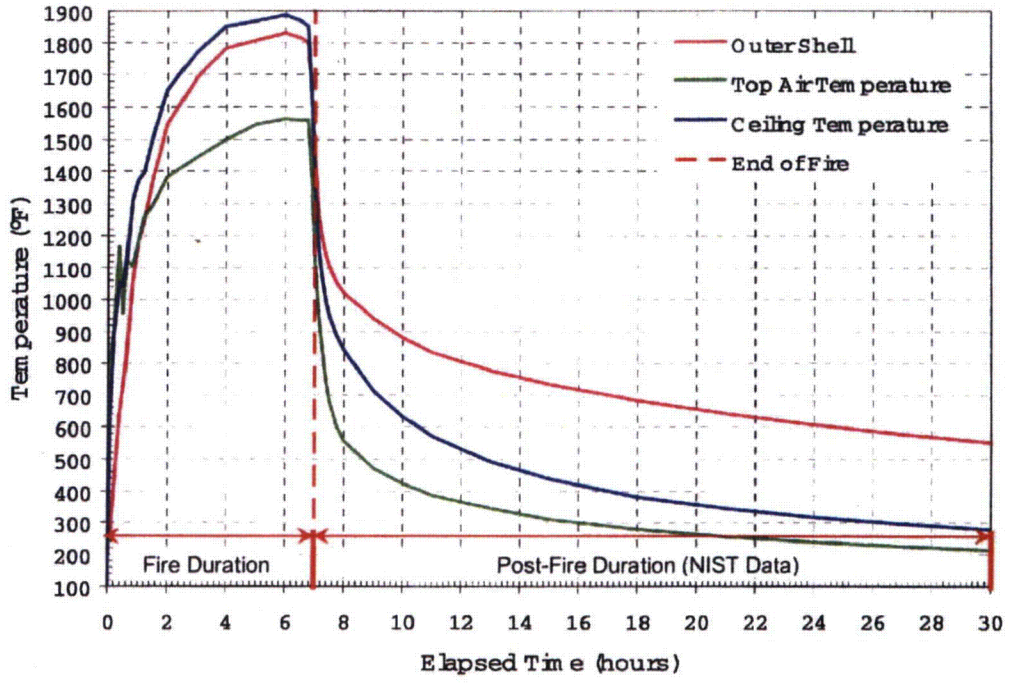

Figure 7.11. Maximum HI-STAR 100 Package Surface Temperature Compared to NIST Boundary Condition Temperatures

Figure 7.10 shows that the peak temperatures on the gamma shields and inner shell of the package decrease after the end of the fire. However, the temperature decrease for these components is much slower than for the outer shell because the internal components must absorb the thermal load from the fuel. Similarly, the peak temperature of the basket shows a continuous increase for nearly three hours after the end of the fire, as does the peak clad temperature.

The plot of the predicted peak clad temperature in Figure 7.10 shows that the thermal output of the fire itself has little effect on the fuel or its accommodating basket. As discussed for the TN-68 in Section 7.1.3, the observed rise in peak clad temperature is mainly a response to the effects of the external boundary conditions on the rate of heat transfer from the package. The heat of the fire does not result in much of an increase in the package internal temperatures, but the increase in the external air temperature severely compromises the rate of heat rejection from the package, and continues to do so long after the fire is out. This is illustrated very clearly by the plot of the peak clad temperature alone shown in Figure

7.12 for the first 50 hours of the NIST transient. The fire is very nearly over before the peak clad temperatures show a discernable increase.

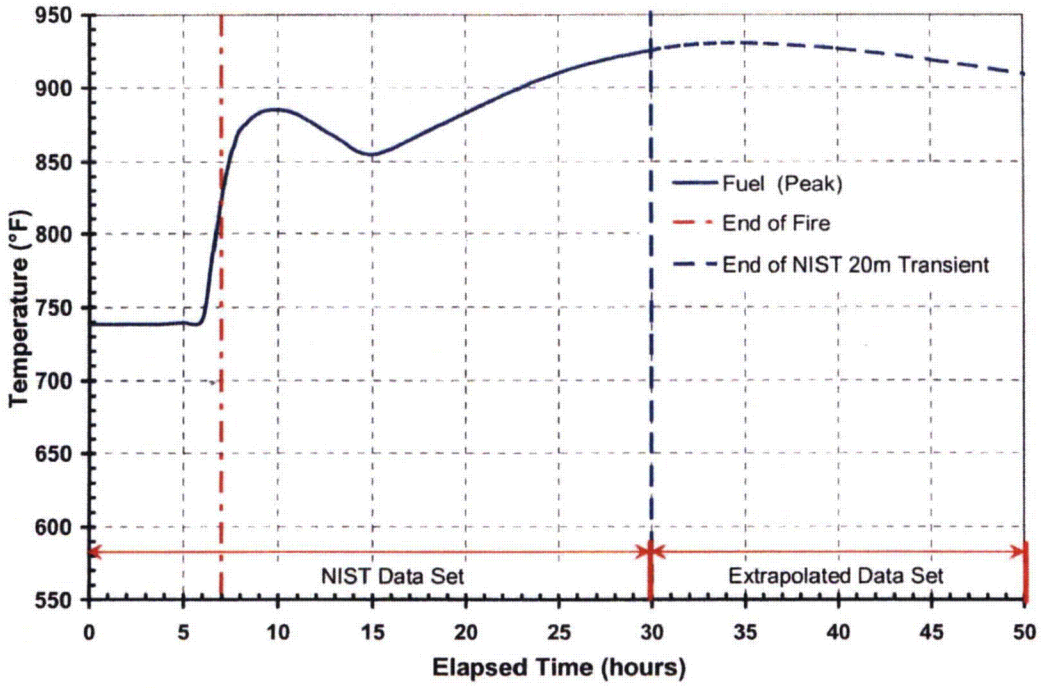

Figure 7.12. Peak Fuel Clad Temperature History in HI-STAR 100 During First 50 hr of Transient

Figure 7.12 shows that a little after 5 hours into the fire, the global peak clad temperature begins an almost adiabatic heat up (approximately 69°F/hr (38°C/hr)) because the fire prevents normal heat removal from the package by natural convection at the surface. This adiabatic heat-up continues for about an hour after the end of the fire, until the package shell temperature drops low enough to permit some heat removal from the package by radiation to the tunnel surfaces.

The initial fuel cladding temperature rise shown to initiate shortly before the end of the fire (at approximately 6 hours) occurs on rods in the outer periphery of the basket in the portion of the package facing the top of the tunnel. The fuel in this region is initially rising in temperature faster than that residing in the center of the basket. This continues until about 8 hours into the transient. However, by this time the fire has been over for more than an hour, and internal component temperatures are redistributing radially throughout the package, causing the peak fuel cladding temperature to shift from one assembly to another. The peak cladding temperature drops for a brief period, due to this internal spreading of heat, but by about 15 hours begins to rise again as fuel in the center of the basket heats up enough to exceed the temperature of the fuel on the outer periphery. (Just as with the TN-68 results, the peak fuel clad temperature is captured in the global summary as it moves from assembly to assembly within the fuel basket during the transient.)

The peak clad temperature continues to increase, because the hot air flow and hot tunnel surfaces resulting from the fire are continuing to compromise heat rejection from the package surface. The package is designed to reject heat to ambient at 100°F (38°C), but the air within the tunnel environment is still above 200°F (93°C) at 30 hours, decreasing from a peak of 1557°F (847°C) at the end of the fire. However, by the end of 30 hours, the rate of increase in the peak clad temperature has dropped to only about 2 °F/hour (1 °C/hour), in response to the decreasing boundary temperatures. The global peak cladding temperature reaches a maximum of 930°F (499°C) at approximately 35 hours into the transient.

The maximum temperature history of the seals in the package lid closure, ports, and port covers is shown in Figure 7.13. The curve in this figure represents the global peak of all seal material utilized in the HI-STAR 100. These temperatures are gathered by querying nodes at the seals' locations, even though the seals were not explicitly represented in the model. As shown in this figure, the maximum temperature in these regions is 1181°F (638°C), reached at the end of the fire. The maximum temperature then gradually begins to decrease as the transient proceeds into the post-fire cool down. Despite an abrupt rise in temperature during the fire, the peak temperature in the seal region remains below the lowest reported maximum continuous-use temperature limit of 1200°F (649°C) for the metallic mechanical seal material. (See Table 4.1.1 of the SAR [10] for the HI-STAR 100.)

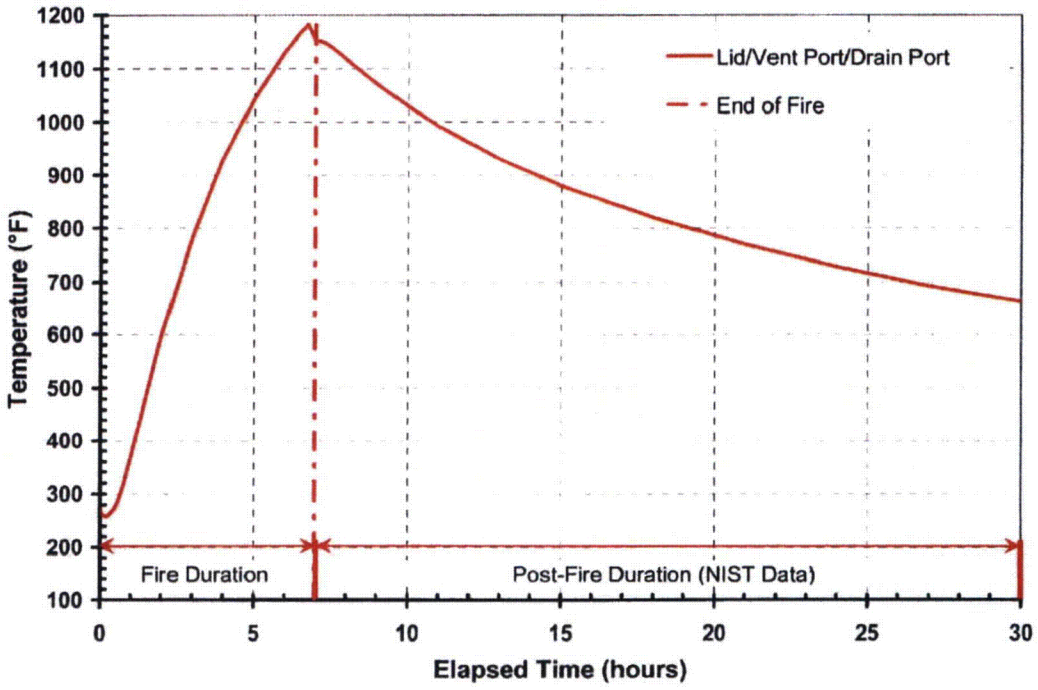

Figure 7.13. Maximum Global HI-STAR 100 Closure/Port Seal Temperature History During First 30 hr of Transient

Bolts were not explicitly represented at the package lid and buttress interface in the ANSYS model of the HI-STAR 100. However, the depicted seal temperature history conservatively represents the peak temperature history of the closure bolts due to the manner in which heat has to migrate around the top

impact limiter, into the package upper forging (between the top limiter and neutron shield/fin section), through the closure seal location, and then into the closure. This is due to the limited conduction offered by the stainless steel-encapsulated cellular honeycomb material.

7.2.3 HI-STAR 100 Long-Term Post-Fire Response

The trends exhibited by the temperatures of the various components of the HI-STAR 100 package at the end of the 30-hour transient indicate that the system is not yet at a new steady state. Boundary temperatures predicted by NIST were extrapolated from 30 hours out to 300 hours using a power function to realistically model cool down of the tunnel environment. (The extrapolated values are presented in Figures 6.5 and 6.6 for the air temperatures and wall temperatures, respectively.)

To explore the effects of prolonged exposure to post-fire conditions in the tunnel, the calculations were carried out for the full 300 hours (273 hours after fire cessation). As discussed previously, this is equivalent to assuming that the package will be left in the tunnel for up to 12.5 days without any emergency response. This assumption is not realistic, but is highly conservative, defining a relatively severe long-term ambient environment around the package.

The same conservative assumptions applied to the TN-68 evaluation for external convection during the fire and post-fire duration were applied to the HI-STAR 100 evaluation. A purely forced convection heat transfer regime and associated heat transfer coefficient was assumed for the first 30 hours of the simulation, then a purely free convection regime and associated coefficient was assumed for the remainder of the calculation ($t \geq 30$ hours). (Refer to Section 6 for detailed discussion of the heat transfer boundary conditions on the package surfaces.)

Figure 7.14 shows the temperature response of the various components of the package for the long term transient calculation to 300 hours. As previously discussed, the dashed portion of the curve is used to distinguish the results obtained with boundary conditions that were extrapolated from the NIST calculation. As noted in Section 7.2.2 (see Figure 7.12), the highest peak clad temperature is reached at approximately 35 hours, with a value of 930°F (499°C). This is 128 °F (71 °C) below the regulatory limit of 1058°F (570°C) for accident conditions. The peak temperature for the basket/poison plate structure is reached at about the same time.

All other temperatures in the package decrease steadily after the end of the fire. By 100 hours, the peak clad temperature has dropped to 817°F (436°C). Similar to the results for the TN-68, this system is not yet at a new post-fire steady-state by this time (see Section 7.1.3, Figure 7.8). The HI-STAR 100 is nearing its new post-fire steady-state at about 200 hours, with rates of temperature change on the order of approximately -0.3 °F/hr (-0.2 °C/hr). After 250 hours, the peak clad temperature has dropped to 747°F (397°C), and at 300 hours, it is predicted to be 740°F (393°C) for the specified boundary conditions. At this point in the transient calculation, the rate of decrease in local temperatures in the system is less than 0.1 °F/hr (0.06 °C/hr), and the conditions can be considered as essentially a new post-fire steady state.

The trends in Figure 7.14 show that the overall thermal response of the package to the fire transient is essentially an accommodation to the new higher temperature boundary conditions represented by the

conditions predicted at the end of 30 hours in the NIST fire analysis. Viewed on the scale of 300 hours (i.e., from pre-fire to post-fire steady state), the fire portion of the transient appears as a large but relatively short-lived spike in the boundary conditions that significantly affects only the outer shell, impact limiters, and the neutron shield, and to a lesser extent, the gamma shield, inner shell, and canister. The outer shell and neutron shield show a rapid temperature increase during the fire, but after the end of the fire immediately begin to rapidly cool down. Peak component temperatures for the HI-STAR 100 over the entire 300-hr transient fire simulation are summarized in Table 7.2.

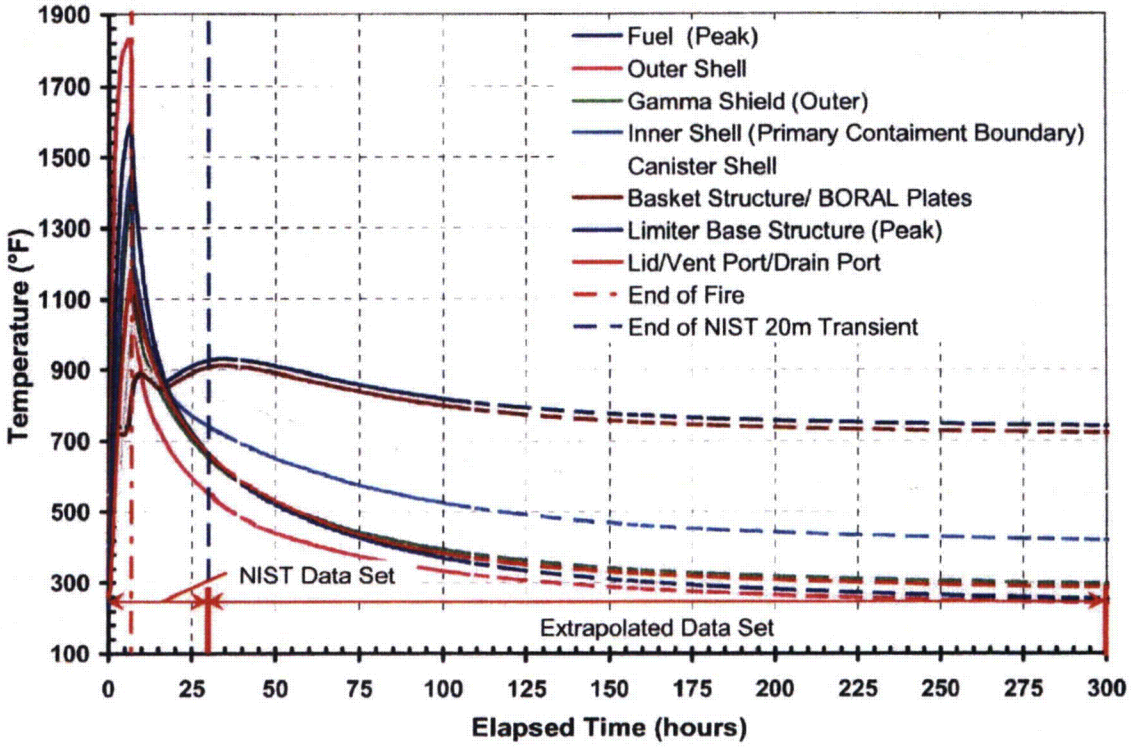

Figure 7.14. Maximum Temperature Histories for HI-STAR 100 Package Components During 300 hrs of the Transient

The temperature of the fuel and basket is largely unaffected by the heat input to the package from the fire. The increase in peak clad temperature and peak basket temperature is due almost exclusively to having essentially no heat removal from the package during the fire and for about an hour immediately afterward. After ambient temperatures drop enough to allow heat removal from the package, the rate of increase of the peak clad temperature begins to level off, and finally turns around at about 35 hours into the transient.

The TN-68 system displays a rapid peak cladding temperature increase during the interval from about 6 to 8 hours of the transient, followed by a much slower rate of increase until about 16 hours, at which point it begins to rise again toward its final peak value, reached at approximately 40 hours. The peak cladding temperature predicted for the HI-STAR 100 follows a similar pattern, but with a somewhat more dynamic

response. After reaching a peak at approximately 10 hours, the peak cladding temperature actually decreases for a time, until about 15 hours, at which point it begins to rise toward its final peak value, reached at about 35 hours.

Table 7.2. HOLTEC HI-STAR 100 Peak Component Temperatures During Fire Transient

Component	Maximum Temperature (ANSYS) °F (°C)	Time (hours)
Fuel Cladding	930 (499)	35
MPC Basket	911 (488)	35
Boral	911 (488)	35
Canister Shell	1041 (560)	7.3
Inner Shell and Forgings	1447 (786)	6.8
Gamma Shield	1404 (762)	6.8
Package Skin	1831 (999)	6
Lid/Vent/Drain Port Seals	1181 (638)	6.8
Impact Limiter Skin	1826 (997)	6
Impact Limiter Structure	1591 (866)	6.8

The difference in response of the peak clad temperature in the two packages is due to three main factors. There are significant differences in construction and thickness of the finned neutron shield regions in the two package designs. There is about a 15% difference in the thermal inertia associated with the spent fuel assemblies in each package (the HI-STAR 100 contains 24 PWR fuel assemblies, compared to 68 BWR fuel assemblies within the TN-68 package), and the two packages have very different basket designs. In addition, the high thermal conductivity of the HI-STAR 100 aluminum honeycomb impact limiters aids in ramping up component temperatures faster in the ends of the package, compared to the effect of the redwood impact limiters on the TN-68 package.

The TN-68 does not utilize an internal canister to hold spent fuel. It relies instead on the cask shell structural integrity and seals to prevent the release of radioactive materials from the fuel compartment. The maximum predicted seal temperature, which is seen by the package lid seal, is 811°F (433°C), and occurs at the end of the fire. This is below the peak seal temperature predicted for the HI-STAR 100 and is primarily due to the relatively low conductivity of the redwood material used in the TN-68 impact limiter design, compared to the aluminum honeycomb in the HI-STAR 100 impact limiter design.

When comparing the heating trends associated with the HI-STAR 100 and the TN-68 (comparing results shown in Figure 7.14 and in Figure 7.8), it appears that the HI-STAR 100 generally heats up faster during the fire than the TN-68. However, this is mainly an artifact of the differences between the initial steady-state conditions in the two packages, different exterior packaging, and differences in their respective fuel loading. The HI-STAR 100 inner components enter the fire transient hotter by 100 °F to 200 °F (56 °C to

111 °C) than the corresponding components of the TN-68. These temperature differences are due to the redundant encapsulation provided by the MPC canister in the HI-STAR system, the number of fuel assemblies that the decay heat is distributed over (24 for the HI-STAR 100 versus 68 for the TN-68), and the level of shrouding of the package surface by the support device. The HI-STAR 100 is heavily shrouded by its support cradle; the TN-68 outer surface is essentially bare to ambient conditions.

In addition to these essentially incidental differences, there are some small differences in design that affect the rate of heat-up of the outer shells of the two packages. The TN-68 has a 50% thicker solid outer skin which distributes the heat from the fire transient circumferentially to cooler regions of the package more effectively than the thinner outer skin of the HI-STAR 100 package. The outer skin of the HI-STAR 100 package consists of relatively narrow welded metal strips, rather than a single steel sheet. The 0.19-inch (0.48 cm) fillet welds joining the metal strips (which were explicitly accounted for in the ANSYS model) present an additional barrier to circumferential heat flow in the HI-STAR 100 package outer shell. However, because both packages present a very large thermal mass to the fire and have very similar overall designs, they respond in essentially the same manner to the fire transient. The differences shown in these two sets of results consist mainly of minor time-shifts in the response to the imposed boundary conditions, and in general the behavior of the two sets of curves makes them almost indistinguishable.

7.3 NAC LWT Fire Transient Results

The ANSYS model of the NAC LWT package consists of a total of 50,673 standard computational elements and 12 superelements that are solved for each time step. Similar to the TN-68 and HI-STAR 100 models, this model yields a large amount of output that has been processed to characterize the package response. The following three subsections discuss the hypothetical package response to the fire transient conditions described in Section 6 in terms of the peak temperatures versus time for selected components.

7.3.1 NAC LWT During the Fire

Figure 7.15 shows the initial temperature response for the NAC LWT package and ISO container, as predicted with ANSYS, during the fire portion of the transient. The maximum temperature on the exterior surface of the ISO container surrounding the NAC LWT package increases rapidly to a peak temperature of 1592°F (867°C) at around 6 hours into the fire. This is 307 °F (170 °C) below the HI-STAR 100 external surface peak temperature, and 265 °F (147 °C) below that of the TN-68. This difference is due to the substantial view that the hottest portion of the ISO container has of cooler nearby surfaces. The top of the ISO container can exchange energy by thermal radiation with the package body and the interior surfaces of the sides and bottom of the ISO container. In contrast, the bare external surfaces of the HI-STAR 100 and the TN-68 see only the fire and the hot walls and ceiling of the tunnel.

The maximum temperature of the exterior surface of the NAC LWT package is 1525°F (829°C), only slightly lower than the peak temperature on the ISO container surface. The maximum temperature of the package inner shell material, which defines the primary containment boundary along with the bolted lid,

shows a more gradual increase than the outer shell temperature, reaching a peak of 1261°F (683°C) at about 7 hours into the fire.

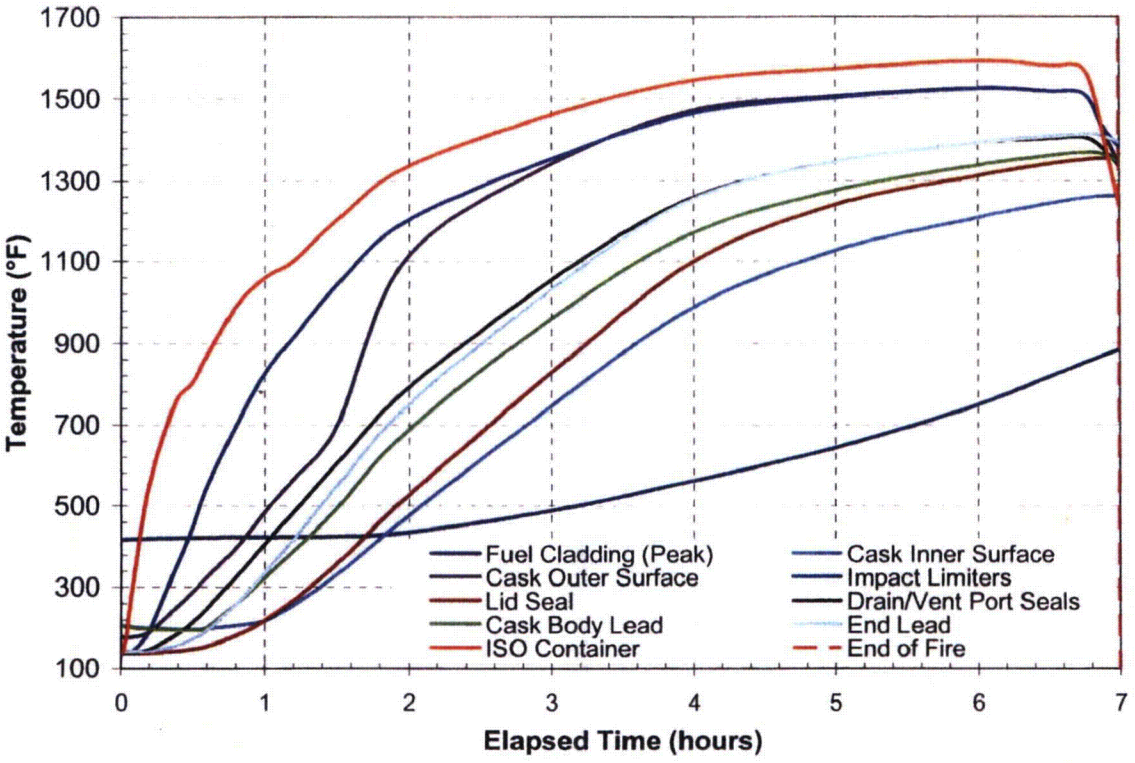

Figure 7.15. NAC LWT Component Maximum Temperature Histories During Fire Transient

Unlike the TN-68 and the HI-STAR 100, the internal components of the LWT package, particularly the fuel assembly, exhibit a noticeable thermal response during the fire. The peak fuel cladding temperature begins to rise at about two hours elapsed time, and the package structural components show a fairly rapid rise in temperature in the first hour of the fire. This occurs primarily because this package has considerably less thermal inertia than the two larger multi-assembly packages. The additional heat transfer paths available into the LWT package are also contributing factors, resulting from the fuel assembly being exposed within a cavity at each end of the package. As the inner shell surrounding the assembly ends heats up, radiation exchange within the cavities generates cladding temperatures at the ends of the fuel rods that are significantly higher than the temperatures at the center, as illustrated in Figure 7.16.

By the end of the fire (at approximately 7 hours), the predicted peak fuel cladding temperature, which occurs in the end region of the fuel, has reached 884°F (473°C) and is still rising. This value continues to increase for another three hours, but does not exceed the currently accepted short term temperature limit of 1058°F (570°C) for Zircaloy-clad spent nuclear fuel under accident conditions [23].

Other components of the package, in contrast to the peak cladding temperature, reach their peak temperature values at or very close to the end of the fire. This behavior closely follows the sudden decrease in the external thermal load on the package as the fire burns itself out. This can readily be seen in the peak temperatures reached on the gamma shield and the neutron shielding structures.

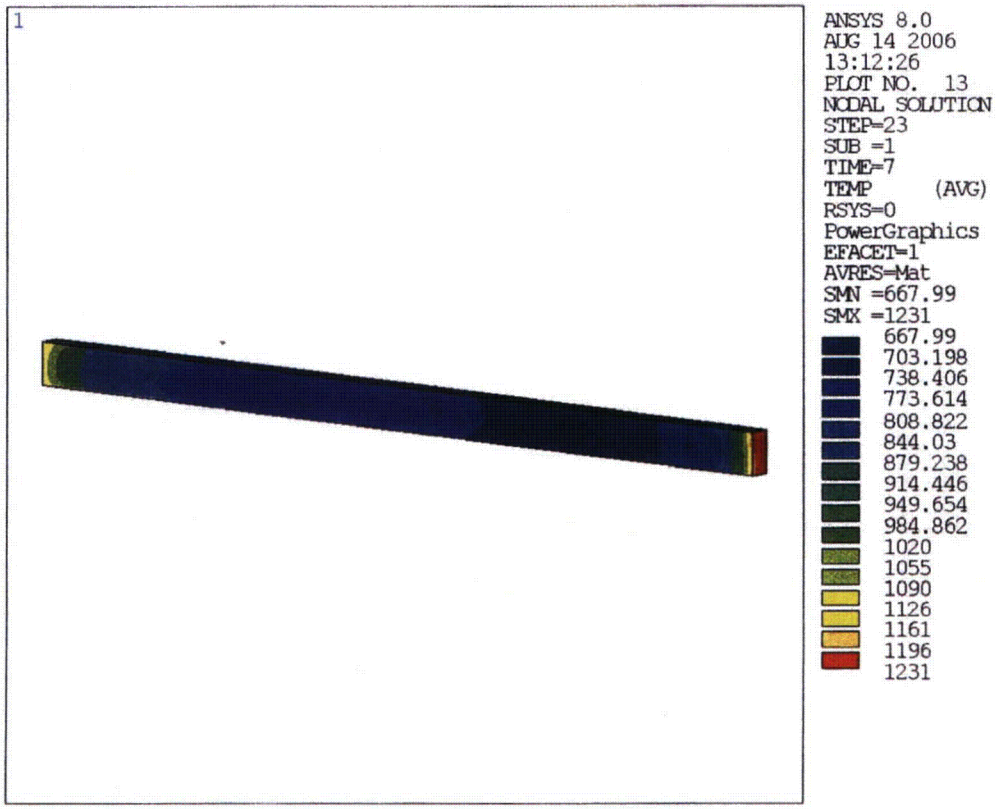

Figure 7.16. Lumped Fuel Assembly Temperature Distribution 7 hr into Transient

The gamma shielding is provided by a lead layer between the inner and outer shells as well as a lead billet in the welded base (i.e., the end opposite the package lid). The temperature of the lead in the package body reaches a maximum of 1369°F (743°C) at 6.75 hours elapsed time, and the temperature of the end billet peaks at the same time, at 1413°F (767°C). These temperatures are considerably greater than the established safe operating limit of 600°F (316°C) [11] for this material, and are significantly above the melting temperature of 622°F (328°C) for lead. High temperatures are sustained in these components long enough for the lead layer to entirely melt during the transient.

Figure 7.17 illustrates the thermal response of the lead shielding layer in the package body, showing the peak temperature in this component over time, and temperature histories of selected nodes within the lead region. Table 7.3 summarizes the process of melting and resolidification of the lead material in response to the fire transient. Melting of the lead begins at about 1.7 hrs, when the peak temperature in the end billet reaches the melting temperature of lead. The peak temperature in the package body shield is not far behind, reaching melting temperature about 9 minutes later.

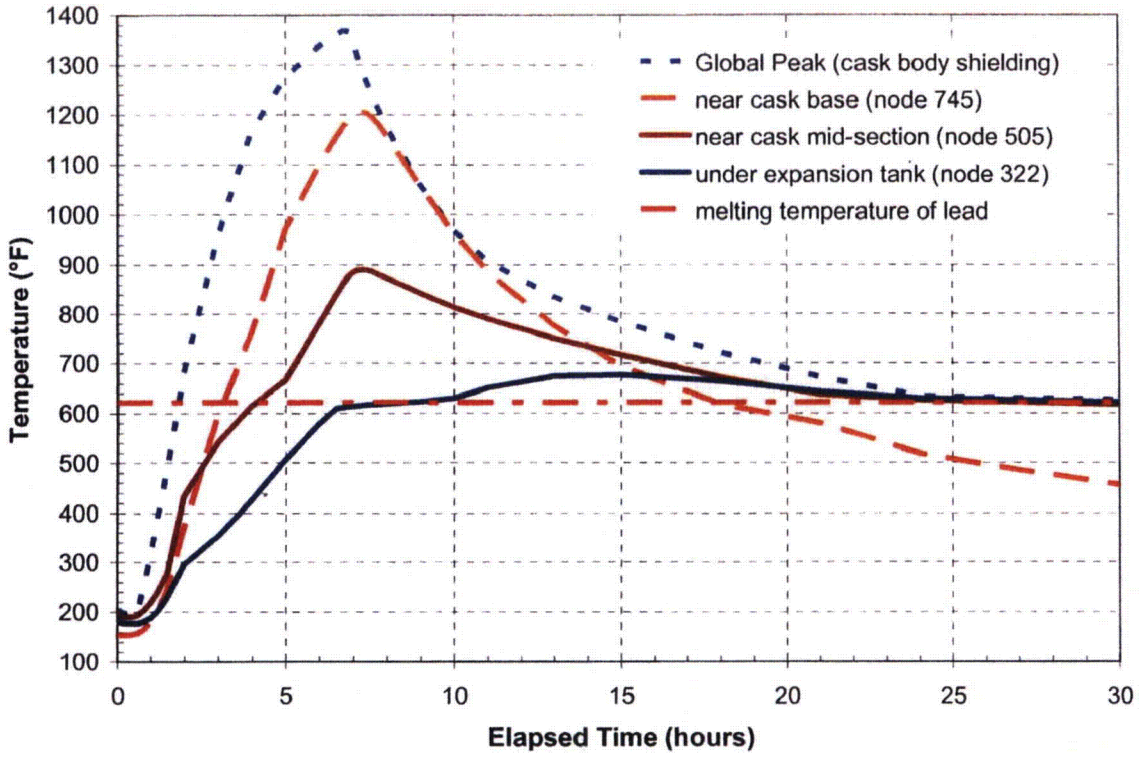

Figure 7.17. Temperature History of Selected Elements in Cask Body Lead in NAC LWT Package

Table 7.3. NAC LWT Lead Shielding Response to Fire Transient

Lead Shielding Thermal Response	Time (hours)
End billet lead begins to melt	1.69
package body shielding lead begins to melt	1.83
Melting within package body shielding near base	3.16
Melting within package body shielding near end of basket region	4.02
Melting within package body shielding near midsection	4.07-4.13
Melting within package body shielding under expansion tank	6.5
All lead shielding in molten state	9
End billet lead resolidified	16.05
Package body shielding lead begins to solidify	27
All lead shielding material resolidified	33.76

These initial melting peak temperatures occur on the very outer edge of these components, and considerably more time is required for interior temperatures in the lead region to reach melting temperature. As shown by the individual node temperature histories in Figure 7.17, at least another hour

elapses before an interior node near the base of the package body shield reaches melting temperature, at about 3.16 hours into the transient. Most of another hour elapses before the middle section of the package body shielding reaches melting temperature, at about 4 hours into the transient.

The temperature history of an interior node near the package mid-section shows the effect of the phase change process in the change in slope as the temperature approaches the melting point. The energy absorbed in the phase change process (due to the latent heat of fusion, at 10.4 Btu/lbm (24.2 kJ/kg)) tends to slow the rate of temperature increase in the interior nodes of the region. A similar effect is seen in the temperature history of the selected node in the region under the expansion tank, although the temperature response of this node is also showing the thermal shielding effect of the expansion tank. The temperature rise is much slower at this location, and this element does not reach melting temperature until very close to the end of the fire, at about 6.5 hours elapsed time. An additional 2.5 hours is required for this portion of the cask body shielding to entirely melt.

The peak temperatures for the lead components show that the lead in the end billet begins to solidify at about 16 hours into the transient. It takes an additional 11 hours (about 27 hours elapsed time) before elements in the package body shield cool back down to the melting temperature, beginning a rather slow process of solidification. It takes another 6.8 hours (to about 33.76 hours elapsed time) before the peak lead temperature in the package body shielding drops below 622°F (328°C).

To maximize heat input to the package during the transient, the lead material was treated analytically in a manner that allowed the greatest possible heat transfer into the package from the fire. It was assumed that thermal expansion and expansion of the lead due to phase change would result in the lead entirely filling the cavity between the inner and outer steel shells of the package. As a result, there would be no gap resistance to heat flowing inward from the outer shell of the package. For the thermal analysis, possible slumping of the lead as a consequence of melting was conservatively ignored. (However, the potential for reduced gamma shielding as a result of the lead slumping is considered in Section 8.1.2.)

The response of the neutron shielding material was also treated in a manner to maximize heat input to the package. As described in Section 5.3, the temperatures of the nodes representing the main tank and overflow tank, both of which contain a 56% ethylene glycol and water mixture, were monitored for temperatures indicating rupture and evaporation throughout the transient solution. Similar to assumptions in the standard fire analysis included in the SAR [11], the liquid in the tank is expected to lose its shielding capability when the temperature exceeds its 350°F (177°C) boiling point. The NAC LWT is designed to attenuate neutron radiation to acceptable levels (see 10 CFR 71.51 [1]) following an accident without the assistance of the neutron shield material (as are the TN-68 and HI-STAR 100; see Section 7.1 and 7.2 above). However, the loss of the neutron shield affects the rate of heat transfer into and out of the package during and after the fire transient.

As a measure of conservatism, tank rupture was considered to occur only after the average ethylene glycol temperature for each tank exceeded 350°F (177°C). This assumption effectively delays rupture to a slightly later point in the transient than might be expected, retaining the higher heat transfer rate through the liquid for a longer period before replacing it with lower conductivity air, and thereby maximizing heat input into the package. The model predicted that the inner neutron shield tank and the outer expansion

tank would rupture at ~1.5 hours. Following rupture, the effective conductivity of the tank was significantly decreased, due to the ethylene glycol volume being expelled and replaced with air. As a further conservatism, the energy absorbed in the phase change, due to the latent heat of vaporization for the ethylene glycol and water mixture, was not subtracted from the heat input to the package.

7.3.2 NAC LWT Short-Term Post-Fire Response

Figure 7.18 shows the peak temperatures predicted for various components of the package during the first 30 hours of the ANSYS transient simulation based on the NIST fire simulation results. The cladding peak and average temperatures continue to rise after the fire, just as in the analyses for the TN-68 and HI-STAR 100 packages, and for much the same reason. The ambient conditions in the tunnel, immediately following the fire, severely retard the rate at which the fuel decay heat can be removed from the package.

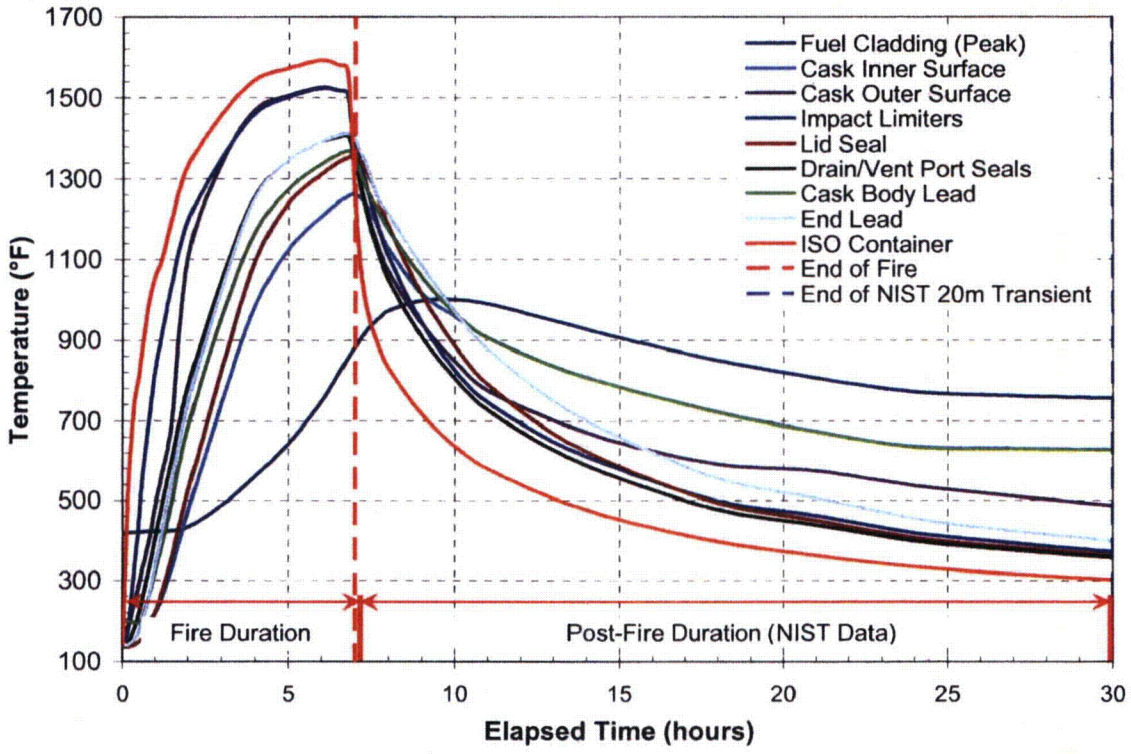

Figure 7.18. NAC LWT Package Component Maximum Temperature Histories for First 30 hours of Fire Transient

Figure 7.18 shows that the peak temperatures for all package components begin to decrease shortly after the end of the fire. The peak cladding temperature reaches its maximum value of 1001°F (589°C) at 10 hours. This is 57 °F (32 °C) below the short term limit of 1058°F (570°C), and 381 °F (212 °C) below the temperature at which Zircaloy fuel rods actually fail by burst rupture, which is approximately 1382°F

(750°C) [25]. (The maximum temperature for the basket reaches its peak of 958°F (512°C) at about 8 hours into the transient, but this temperature curve is omitted from Figure 7.18 for clarity.)

Once the fire is over, however, the predicted peak temperatures on outboard components (i.e., the ISO container and package outer surface) begin to drop rapidly in response to the rapid decrease in the boundary temperatures, as illustrated in Figure 7.19. This figure shows the outer shell surface temperature predicted with ANSYS, compared to the tunnel ceiling temperature and the temperature of the air above the ISO container, derived from the NIST calculations used as boundary conditions.

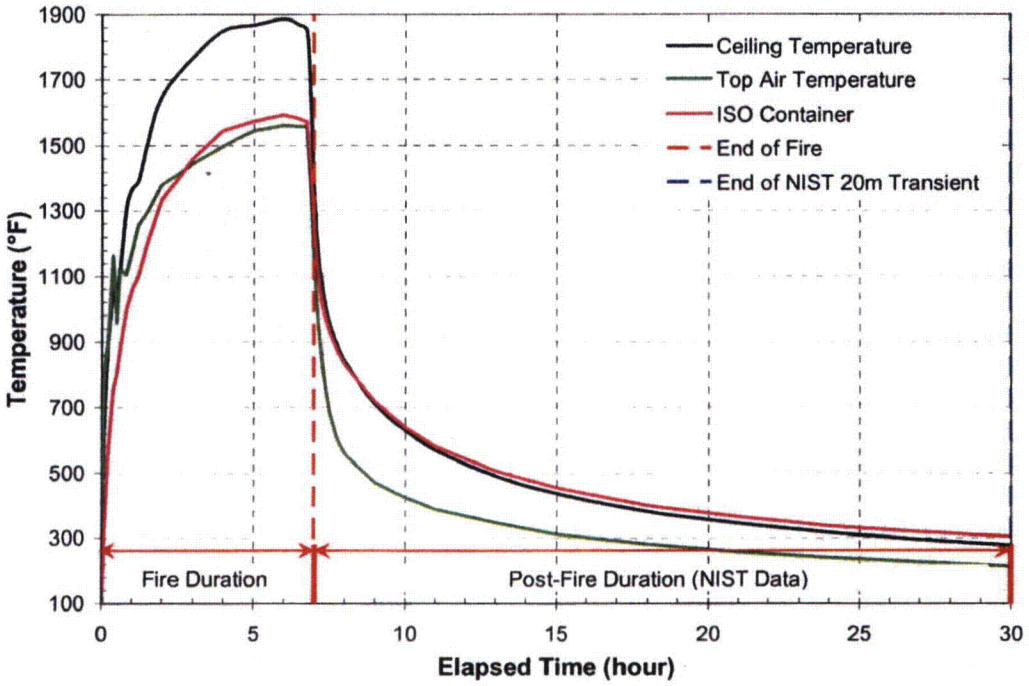

Figure 7.19. Maximum ISO Container Surface Temperature History Compared with NIST Boundary Condition Temperatures

As a result of the low thermal inertia of this package, peak temperatures in the various internal components occur within 2-3 hours of the fire being extinguished, rather than 35 or 40 hours later, as in the TN-68 and HI-STAR 100, respectively. Because of the heating of the ends of the fuel rods due to thermal radiation as a result of the fire, the *average* fuel temperature gradually increases to a maximum of 977°F (470°C). This peak is reached at 9 hours elapsed time, as shown in Figure 7.20.

The maximum temperature histories of the seals in the drain/vent ports and the lid are shown for the first 30 hours in Figure 7.21. (The calculated values were gathered by querying nodes at the seals' locations, since the seals were not explicitly represented in the model.) The drain and vent ports are sealed with Teflon O-rings. The bolted lid is sealed by both metallic and Teflon O-ring seals. The drain and vent port seals reach a maximum temperature of 1407°F (764°C), and the lid seal reaches 1356°F (735°C) at the end of the fire.

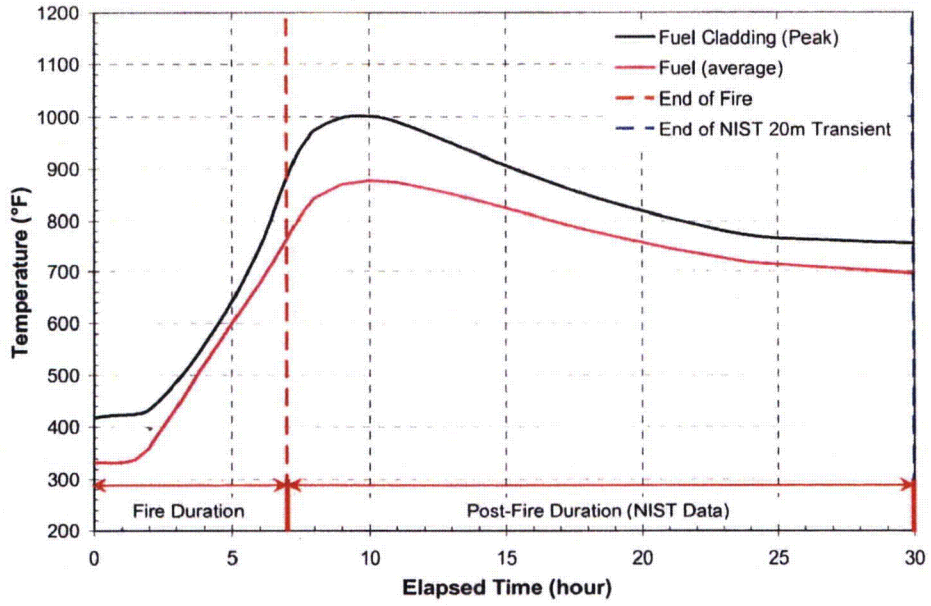

Figure 7.20. Peak and Average Fuel Cladding Temperature Histories for NAC LWT Package During First 30 hr of Fire Transient

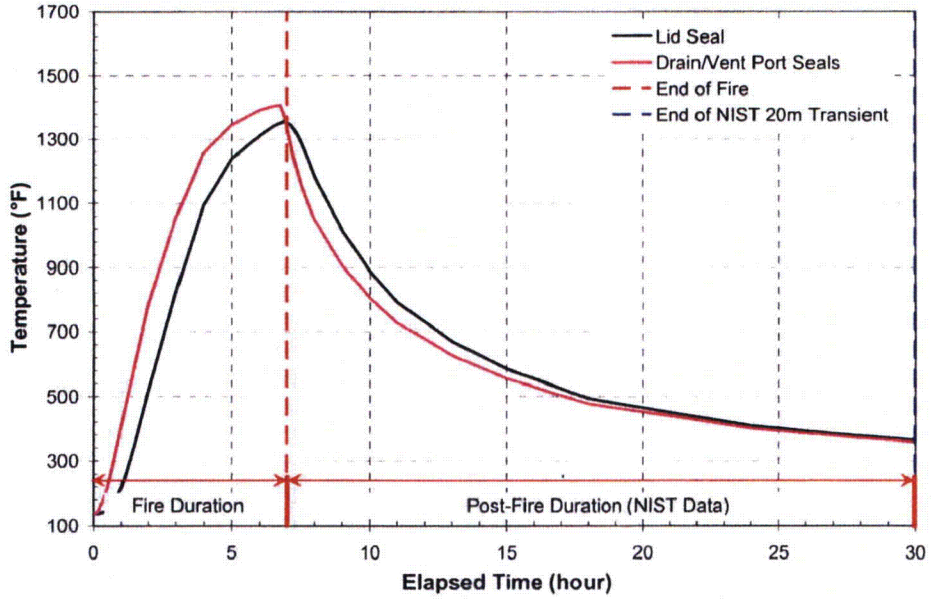

Figure 7.21. Maximum Seal Temperature Histories for Drain/Vent Ports and Package Lid During First 30 hr of Fire Transient

These materials then gradually cool as the transient proceeds into the post-fire cool down. The extreme rise in temperature is due to the low thermal inertia associated with the LWT package and the close proximity of the seals to exterior surfaces subject to thermal radiation from the thin ISO container, which is in turn subject to thermal radiation and convection heat input from the tunnel environment. The predicted seal temperatures are far greater than the maximum continuous-use seal temperature limits of 735°F (391°C) for the Teflon seals and 800°F (427°C) for the metallic seals.

7.3.3 NAC LWT Long-Term Post-Fire Response

As with the TN-68 and HI-STAR 100 analyses, the temperatures predicted in the NIST analysis were extrapolated from 30 hours to 300 hours using a power function in order to realistically model cool down of the tunnel environment. As discussed previously, this conservative approach is equivalent to assuming that the package will be left in the tunnel for nearly two weeks, without any emergency responder intervention. The same conservative assumptions used in the analysis of the TN-68 and HI-STAR 100 were used to define the convection heat transfer boundary on the NAC LWT package. A purely forced convection heat transfer regime was assumed for the first 30 hours of the simulation, then a purely free convection regime was assumed for the remainder of the calculation ($t \geq 30$ hours). (The extrapolated boundary conditions are shown in Figures 6.5 and 6.6 for the tunnel air and surface temperatures, respectively.) Peak component temperatures for the NAC LWT over the entire transient fire simulation are reported in Table 7.4.

Table 7.4. NAC LWT Peak Component Temperatures During Fire Transient

Component	Maximum Temperature (ANSYS) °F (°C)	Time (hours)
Fuel Cladding	1001 (539)	10
Aluminum PWR Insert	958 (515)	8
Inner Shell	1261 (683)	6.9
Lead Gamma Shield:		
Package body	1369 (743)	6.75
End billet	1413 (767)	6.75
Outer Shell	1525 (829)	6
Neutron Shield:		
Shield tank	1483 (806)	6
Expansion tank	1524 (829)	6
Lid Seal	1356 (732)	6.9
Drain/Vent Ports	1410 (766)	6.75
Impact Limiters	1521 (827)	6
ISO Container	1592 (867)	6

Figure 7.22 shows the temperature response of the various components of the package for the long term transient calculation to 300 hours. The maximum temperatures were reached within a short time after the end of the fire, and the LWT at 100 hours is very close to its new steady-state condition. This behavior is consistent with its lower thermal inertia, in comparison to the larger multi-assembly packages.

Temperature distributions within the package for the final steady state will be slightly different than the original, due to the dissipation of the liquid neutron shield, changes in the surface emissivities because of the fire, and tunnel ambient conditions that differ from the hot-normal conditions assumed for the pre-fire steady state (i.e., lower ambient temperature and the absence of solar insolation).

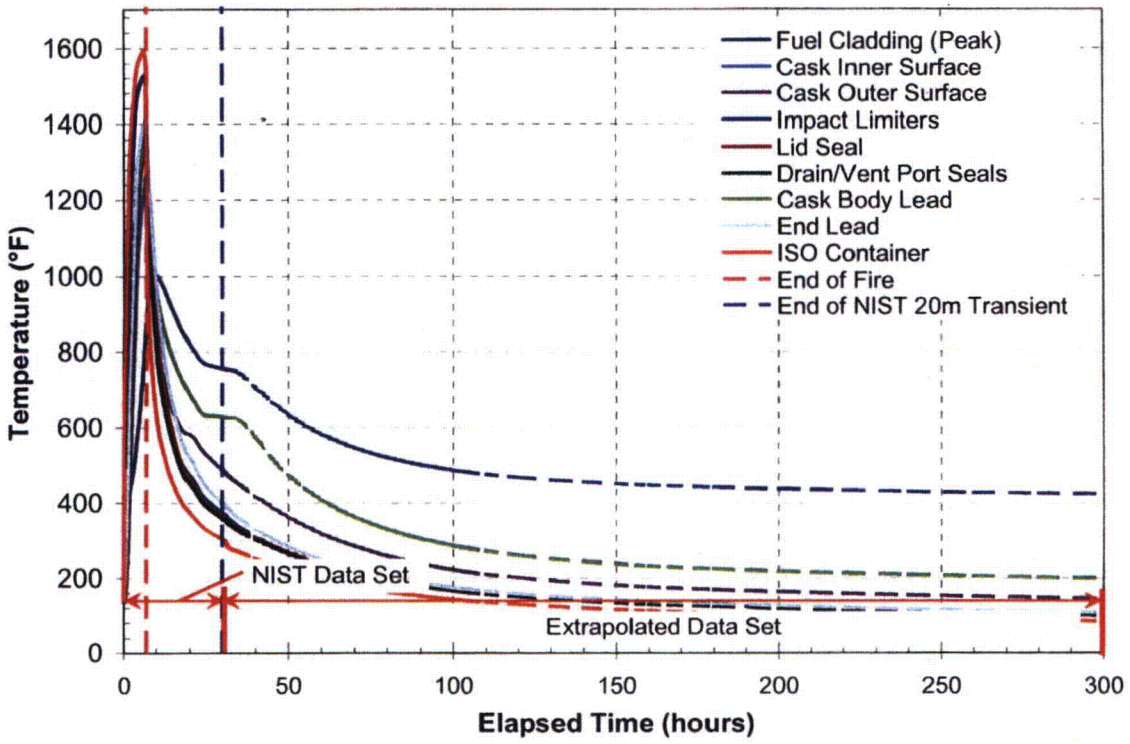

Figure 7.22. NAC LWT Package Component Maximum Temperature Histories During 300 hr Transient

8 POTENTIAL CONSEQUENCES

The potential consequences of a severe accident involving an SNF transportation package fall into two general categories: 1) the possibility of a direct radioactive dose to a member of the public due to a loss of either the neutron or gamma radiation shielding of the package, and 2) the potential release of radioactive material from the package due to a compromise of the containment boundary. Section 8.1 discusses potential loss of shielding events. Section 8.2 evaluates potential releases from each of the evaluated package designs. Section 8.3 provides a summary of the potential consequences of involving an SNF package in the Baltimore tunnel fire scenario.

8.1 Potential Consequences of Loss of Shielding

USNRC Staff evaluated the potential for increased neutron and gamma radiation dose rates from each of the three transportation packages (TN-68, HI-STAR 100, and NAC LWT) as a result of exposure to the Baltimore tunnel fire scenario. The analysis indicates that the regulatory dose rate limits for accident conditions, specified in 10 CFR 71.51, would not be exceeded by any of these packages in this fire scenario, even though all three packages would be expected to lose neutron shielding and the NAC LWT could possibly experience some loss of gamma shielding, as well. Section 8.1.1 describes the consequences of loss of the neutron shielding. Section 8.1.2 discusses the potential effects of loss of gamma shielding, with particular emphasis on the potential consequences of slump of lead shielding material in the NAC LWT.

8.1.1 Neutron Shielding

Neutron shielding in SNF transportation packages is typically provided by materials that have relatively low melting temperatures (such as hydrocarbon resins or polymers), or are liquid at ambient conditions (such as water or mixtures of water and glycol). These materials are not expected to survive the design-basis accidents specified in 10 CFR 71, and the analyses included in the SAR for an SNF transportation package typically assume loss of the neutron shield in all accident scenarios.

The packages are designed to meet the regulatory radiation dose limits for all conditions of transport, including hypothetical accident conditions. (Refer to the respective SARs [9, 10, 11] of these three packages for details on the analyses supporting this design constraint). The severe conditions of the Baltimore tunnel fire scenario could do no more damage to the neutron shields of these SNF packages than is assumed in the required regulatory fire analyses. All three of the packages considered in this evaluation can meet the regulatory limits, even when their neutron shielding has been destroyed by fire.

8.1.2 Gamma Shielding

The effectiveness of gamma shielding materials can be reduced or lost in one of two ways:.1) the gamma shield material could be dislocated due to thermal effects, or 2) the gamma shield material could be lost from a package if the package's outer wall was breached and the shield material subsequently melted. Reduction in the effectiveness of gamma shielding due to thermal effects such as thermal expansion or

contraction, or slumping, could result in shielding material that may not be in the proper position to provide the degree of shielding required,. For loss of shielding material due to a breach, molten material might escape through the breach, reducing the amount of material available to provide the required gamma shielding.

The TN-68 and the HI-STAR 100 packages would not experience a reduction in or loss of gamma shielding material effectiveness due to either of the two previously described mechanisms in this fire scenario. The gamma shielding in these packages is composed of multiple layers of carbon steel and stainless steel. Both types of steel have extremely high melting temperatures, in the range 2500-2800°F (1371-1538°C), which is far above the peak temperature attained on any package component in this fire scenario.

The possibility of a decrease in the effectiveness of the gamma shielding for the NAC LWT package, however, cannot be ruled out. In the severe conditions of the Baltimore tunnel fire scenario, the lead comprising the gamma shield of the NAC LWT is expected to begin to melt when the local temperature of the material reaches 622°F (328°C). This process of local phase change in the material absorbs additional energy from the fire due to the latent heat of fusion, which for lead is 10.4 Btu/lbm (24.2 kJ/kg). The gamma shielding in the package body consists of approximately 24,441 lbm (11,089 kg) of lead, and will absorb about 254,000 Btu (2.7 x (10^8) J or 74.5 kW-hr) in the process of melting.

This process takes considerable time in this fire scenario, beginning at approximately 2 hours into the transient and extending beyond 9 hours elapsed time, and absorbs a significant amount of energy. In a short-duration fire, the thermal input from the fire may not be large enough to cause all of the lead to melt. In the Baltimore tunnel fire scenario, however, this analysis predicts that the peak temperature of the gamma shielding material would be above the melting point of lead for approximately 25 hours, and the entire gamma shield becomes molten within the annular cavity in the steel shell and within the package base.

Melting of the lead does not necessarily imply complete loss of gamma shielding, however. For a significant amount of shielding to be lost, a puncture must penetrate the 1.2-inch thick stainless steel package shell, to allow molten lead to flow out of the package. For the derailment in the Howard Street tunnel, the impact forces involved were not of a sufficient magnitude to result in a breach of the package wall. Therefore, there is no expectation of loss of gamma shielding due to loss of molten lead from the package in this scenario.

In the absence of a breach of the package outer shell, the lead would be completely retained within the steel annulus of the package shell and within the package base. Even when molten from the effects of the fire, the lead would continue to act as a gamma shield. Some reduction of shielding effectiveness could occur, however, due to slumping of the lead within the confines of the annulus as it shrinks upon resolidification. This could result in the formation of voids between the package wall and the lead shielding material.

The NAC LWT package is designed to accommodate some amount of void space between the steel and the lead, due to fabrication constraints. The lead shielding is poured in molten form into the steel

annulus. The steel shell is heated to 550-650°F (288-343°C) during this process, and then allowed to cool to ambient temperature as the lead solidifies. Analyses presented in the SAR [11] conservatively assume a 0.35-inch (0.1374-cm) gap between the outer diameter of the lead and the inner surface of the package outer shell, due to lead shrinkage upon solidification and differential thermal expansion and contraction between the lead and the steel package body. Lead slump analyses in the SAR show that the package maintains gamma shielding when the lead slumps to fill this gap in the hypothetical drop accidents. The SAR analyses indicate dose rates below the regulatory limit of 1000 mrem/hr (10 mSv/hr) for the slumped condition.

In the Baltimore tunnel fire scenario, the slumping of the lead could be more severe than predicted for the analyses in the SAR, because of a larger increase in the volume of the annulus containing the lead. Thermal expansion of the package outer shell, due to the high temperatures reached by the steel, and increased hoop stress on the steel due to expansion of the molten lead, could result in a significant increase in the volume of the annulus between the inner and outer steel shells of the package. A conservative analysis suggests that the increase in the size of the cavity containing the lead shielding could be as great as 5%. When the molten lead resolidifies, it will not quite fill the enlarged cavity, resulting in extra void space between the lead and the steel shell of the package.

Calculations were performed by NRC staff to determine the size of this void space, assuming that gravitational settling would result in the entire void space occupying a continuous volume within the annular cavity containing the lead shielding. For the horizontal orientation of the package assumed in this fire scenario, this results in a void volume extending the full length of the upper edge of the annulus, as illustrated in the cross-section diagrams in Figure 8.1. This figure shows a schematic representation of the configuration of the lead comprising the NAC LWT gamma shield before and after the fire, including conservative estimates of the change in dimensions of the cavity containing the lead shielding material.

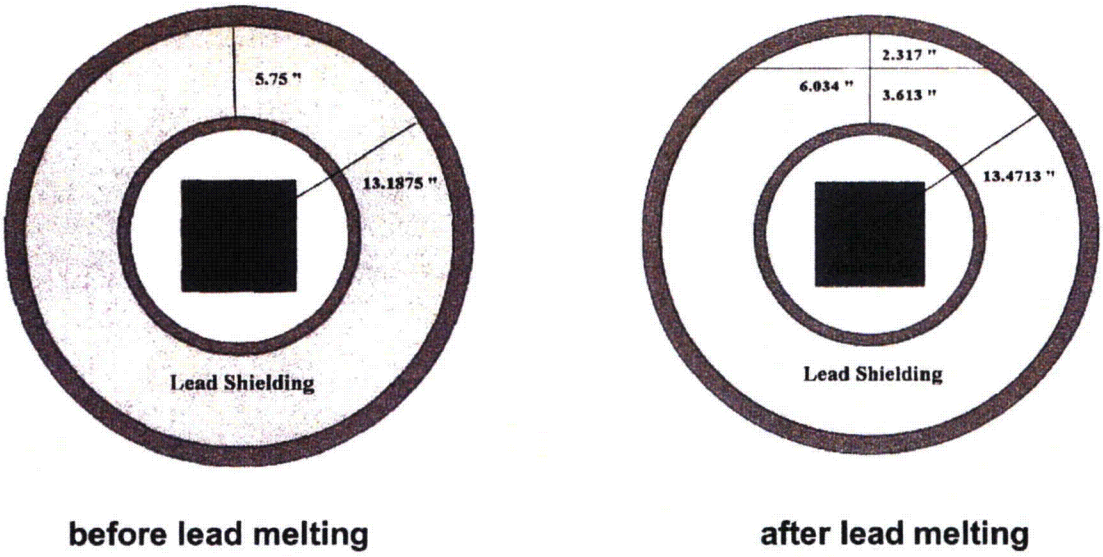

Figure 8.1. Lead Shielding Configuration in the NAC LWT Before and After Lead Melting

The analysis shows that for the horizontal orientation, the thickness of the lead in the upper region of the annulus could be reduced by up to about 2.3 inches. Because of the design of the gamma shielding, which extends at least 15.5 inches (39 cm) beyond the active fuel region and overhangs the cask inner cavity by 7.5 inches (19 cm) at either end, the horizontal orientation of the package is the most adverse orientation for lead thinning as a result of melting and relocation due to gravitational settling. If the cask were vertical, the total height of the void volume would be only 10.5 inches (27 cm), resulting in reduced shielding for only about 3 inches at the top of the cask inner cavity in a region of relatively low activity, while the shielding remained at full thickness in the active fuel region of the assembly. Geometric considerations show that if the cask were merely tilted at some angle to the vertical, rather than being fully horizontal, a large portion of the void volume would be taken up in the upper end of the annular cavity containing the lead shielding material. As a result, there would be less thinning of the shielding thickness, and the thinning would extend over a smaller area. There would therefore be a lesser potential radiation dose resulting from reduction of shielding.

An estimate of the potential radiation dose resulting from the maximum possible localized thinning of the lead shielding with the cask in a horizontal orientation is provided in Table 8.1. The total potential dose rates in Table 8.1 are due to radiation only, and include the increased neutron dose rate due to the loss of the liquid neutron shield (as documented in the SAR [11] for the NAC LWT), plus the increased ionizing radiation dose rate due to the thinning of the gamma shield. Thinning of the gamma shielding would not result in any release of radioactive material from inside the package. (See Section 8.2 for discussion of potential dose rates due to release of radioactive material.) The safety issue due to lead slumping is strictly a matter of the possible dose to first responders from a package involved in a severe fire accident scenario. However, as shown in Table 8.1, this dose rate does not exceed the accident limit of 1000 mrem/hr (10 mSv/hr) at one meter from the package surface, as specified in 10 CFR 71 and 49 CFR 173.

Table 8.1. Potential Dose Estimate from NAC LWT with Reduced Shielding

Location	Intact Package mrem/hr (mSv/hr)	After lead melt mrem/hr (mSv/hr)	Regulatory Limit * mrem/hr (mSv/hr)
Surface	**Neutron:** 7.09 (0.0709)	**Neutron:** 177.13 (1.773)	
	Gamma: 48.62 (0.4862)	**Gamma:** 1216 (12.16)	
	Total: 55.71 (0.5571)	**Total:** 1393 (13.93)	
1 m from surface	**Total:** 14.99 (0.1499)	**Neutron:** 50.93 (0.5093)	
		Gamma: 331.3 (3.313)	1000 (10)
		Total: 382.2 (3.822)	

*from 49CFR173 and 10 CFR 71.51(a)(2)

This conclusion is consistent with the results of analyses presented in the package SAR [11] for reduction of gamma shielding due to lead slumping as a consequence of the hypothetical drop accidents specified in 10 CFR 71. In the analyses presented in the SAR for these hypothetical accidents, the maximum dose rates do not exceed the design limits specified in 10 CFR 71 and 49 CFR 173, and are well below the limit of 1000 mrem/hr (10 mSv/hr) at one meter from the package surface.

8.2 Potential Release Issues

USNRC Staff evaluated the potential for a release of radioactive material from each of the three transportation packages (HI-STAR 100, TN-68 and NAC LWT) analyzed for the Baltimore tunnel fire scenario. The analysis indicates that there would be no release expected from the HI-STAR 100 package. However, the possibility of a small release cannot be entirely ruled out for either the TN-68 or NAC LWT packages, because temperatures during the fire or cool down period exceed the manufacturer's recommended service temperature limits for the package lid seals and seals on the vent and drain ports.

The thermal analyses show that the potential release would not involve a release of spent fuel or fission products, but could possibly result from CRUD detaching from the fuel rods. Any potential release from either the TN-68 or NAC LWT package would be small—less than an A_2 quantity. An A_2 quantity[18] is defined in 49CFR173.403 as the maximum activity of Class 7 (radioactive) material permitted in a Type A package. Type A packages carry such small amounts of radioactive material that an accident resistant package is not required. This is because an A_2 quantity of radioactive material would not be expected to result in a significant radiological hazard to first responders even if it were released from the package due to a transportation accident. Type B packages (which include SNF transportation packages) can carry more than an A_2 quantity of radioactive material, but must retain the integrity of containment and shielding under normal conditions of transport, as required by DOT regulations in 49 CFR part 173. Type B packages must also be designed such that if one were subjected to the hypothetical accident conditions specified in 10 CFR part 71 [1], it would release less than an A_2 quantity/week.

Staff performed an analysis to determine the magnitude of any potential release, assuming the packages contained spent fuel that was 5 years old. Because it was determined by the thermal analyses conducted for each package that the fuel cladding for the fuel assemblies remains intact, it is not expected that any radioactive material would be released from inside the fuel rods. This limits any release from the package to CRUD particles that may detach from individual fuel rods.

Rather than addressing all radionuclides that could be contained in such CRUD particles, (see Reference [26], Table I-7), the radionuclide of the greatest concern was used as the basis of the release calculation. For shipments consisting of fuel that is 5 years old or older, Co^{60} is the most important radionuclide to be considered. For fuel that is less than 5 years old, other short-lived isotopes, such as Mn^{54} and Co^{58} should be considered as well [26]. For PWR fuel cooled for 5 years, the total activity decreases to 3% of that at discharge, while after 13 years, the activity drops to 1% of that at discharge. Co^{60} accounts for 92% of the activity at 5 years and 99% at 8 years. For BWR fuel, the total activity decreases to 31% of that at fuel discharge after 5 years and 1% after 30 years. Co^{60} accounts for 98% of the activity at 5 years (see page I-50, Ref [26]).

A discussion of seal performance and leakage pathways is provided in Section 8.2.1. The results of the release analysis for the HI-STAR 100 package are provided in Section 8.2.2, and the results for the TN-68

[18] The actual amount of a particular material that constitutes an A_2 quantity depends on the radiological properties of the material. Appendix A of 10CFR71 defines the A_2 quantities for a large number of different materials in Table A-1, and specifies methods for calculating the appropriate value for any material not listed in the table.

are provided in Section 8.2.3. Results for the NAC LWT are provided in Section 8.2.4. Additional analyses are presented in Section 8.2.5, investigating the potential for releases from the HI-STAR 100 and NAC LWT when these packages are transporting failed fuel.

8.2.1 Seal Performance and Potential Leak Paths

A simple "pass/fail" criterion is used for evaluating seal performance in this study. If the manufacturer's maximum recommended service temperature was exceeded at any time during the transient on any portion of the sealing surfaces, the seal was assumed to fail. Seal failure is defined as the inability of a seal material to maintain a seal against the internal pressure of the package cavity. This constitutes a conservative criterion, because exceeding the manufacturer's service temperature limits for the seal material used in a spent fuel package lid or vent and drain port seal is not a direct indicator of seal failure, and does not necessarily mean that a release of radioactive material would occur from the package. The service temperature limits for seals are the temperature to which the manufacturer is willing to guarantee the seal's extended performance. Exceeding these temperatures does not necessarily mean that the seal will fail immediately, although it does suggest that there is a potential for seal failure to occur, due to the eventual degradation of the seal material. This could lead to the failure of the seal to hold against the internal pressure of the package cavity, thereby creating conditions that could lead to a release.

Similarly, failure of a seal does not remove all barriers to release of material from within the package. Even without the intact seals, potential releases from a package would be limited by the narrow, convoluted flow paths of the drain and vent ports, and by the tight clearances of the close metal-to-metal contact between the lid and package body. This close contact is maintained by the pre-load created by the initial torque on the lid bolts, and does not depend on the presence of the lid seals.

The exact temperature at which a particular seal will fail and the particular mechanism of that failure is not known *a priori*, because most seal manufacturers have not tested their seals to failure at higher temperatures. However, the point at which seal failure would actually occur is irrelevant to this study. Complete and total failure of the seal materials was assumed if the manufacturer's maximum recommended service temperature was exceeded at any time during the transient on any portion of the sealing surfaces. No credit is taken in the release calculation for the presence of any seals. This is considered to be a highly conservative approach.

8.2.2 Potential Release from the HI-STAR 100 Package

The thermal analysis shows that the HI-STAR 100 package design would maintain three important barriers throughout the fire and subsequent cool down period, which would prevent the release of radioactive materials. The welded inner canister remains intact and leak-tight, preventing any release from the fuel rods themselves or as a result of CRUD detaching from the fuel rods. The temperature of the fuel cladding is predicted to peak at about 930°F (499°C), well below the short-term temperature limit of 1058°F (570°C) for Zircaloy cladding, and significantly below its projected burst temperature of 1382°F (750°C). This would prevent the release of fission products from the fuel rods. The maximum temperature of 1181°F (638°C) predicted for the package's metallic O-rings is below their rated

continuous-use service temperature of 1200°F (649°C). Thus, the O-rings would not be expected to significantly degrade.

8.2.3 Potential Release from the TN-68 Package

The thermal analysis for the TN-68 package shows that during the Baltimore tunnel fire scenario, this package design would maintain the integrity of the fuel cladding, which is the single most important barrier to prevent the release of radioactive materials. At approximately 40 hours elapsed time, the temperature of the fuel cladding would peak at about 845°F (452°C), well below the short-term temperature limit of 1058°F (570°C) for Zircaloy cladding and significantly below its projected burst temperature of 1382°F (750°C). This would prevent the release of fission products from the fuel rods. However, the metallic helicoflex seals used on the TN-68 lid and the vent and drain ports reach a maximum temperature of 811°F (433°C) by the end of the fire (at 7 hours elapsed time). This exceeds the seals' rated service temperature of 536°F (280°C) by 275 °F (153 °C).

Because the predicted temperatures exceed the long-term service temperature of the seals, the seals are assumed to fail, and there is a potential for release of radioactive CRUD particles from the package. The amount of releasable CRUD in the TN-68 package was estimated using data developed by Sandia National Laboratory for analysis of CRUD contribution to shipping package containment requirements [26]. The calculation was based on package contents consisting of 68 BWR fuel assemblies, each assembly containing 49 fuel rods. An estimate of the maximum "spot" CRUD activity shows that for 90% of BWR spent fuel rods the maximum activity is 300μCi/cm^2 or less [26, Table I-17]. The ratio of the peak to average concentration on the rod surface (i.e., the maximum "spot" CRUD activity over the average value) varies by a factor of two for BWR fuel rods [26, Table I-17].

The CRUD activity estimates [26] are based on newly discharged spent nuclear fuel. The CRUD activity is expected to decay by a factor of one-half for five-year-cooled fuel, based on the decay rate for Co^{60}. This proves to be a good approximation, because 98% of the activity for five-year-cooled BWR fuel comes from Co^{60}. Based on this data, the average CRUD activity for a BWR rod with a surface area of 1600 cm^2 is about 0.12 Ci for five-year cooled fuel. The average CRUD activity for a typical 7 x 7 BWR assembly is about 5.9 Ci.

The amount of CRUD that might flake or spall from the surface of a BWR rod due to thermal stresses induced by temperature change in the fuel rods is estimated to be a maximum of 15% [26, Table I-10]. The major driving force for material release results from the increased gas pressure inside the package, due to increases in internal temperature. The temperature change in the package is bounded by the difference between the maximum gas temperature predicted during the fire transient and the fill gas temperature at the time the package is loaded. For this analysis, the loading temperature is defined as 100°F (38°C), based on the temperature reported in the SAR [9]. The maximum fill gas temperature is assumed to be the maximum inner shell temperature, predicted during the transient, of 857 °F (458 °C). This yields a conservative estimate of the temperature change.

A deposition factor of 0.90 was used to account for the settling and deposition of CRUD particles on package surfaces and fuel assemblies. The deposition factor was developed as part of NRC'ssecurity

assessments for spent nuclear fuel transport and storage packages, and is based on an analysis of the gravitational settling of small particles. The value of 0.90 is conservative because it does not consider the effects of particle conglomeration and plugging. It is also consistent with the values used in other studies [25]. The major assumptions used to estimate the potential CRUD release are given in Table 8.2.

Table 8.2. Assumptions Used for Release Estimate for TN-68 Package

Parameter	Assumed value
Number of Assemblies in TN-68 Package	68 BWR
Rods per Assembly	49
Maximum "spot" CRUD Activity on Fuel Rod	300μCi/cm^2
Peak to axial average variation	2
CRUD decay factor (5 yr; based on Co^{60})	0.5
Average surface area per rod	1600 cm^2
Average CRUD Activity on BWR Fuel Rod (5 yr cooled)	0.12 Ci
Average CRUD Activity on BWR Assembly (5 yr cooled)	5.9 Ci
Fraction of CRUD released due to heating	0.15
Deposition Factor	0.90

To estimate the potential release from the TN-68 package, a methodology similar to that developed by Sandia National Laboratory was used (see NUREG/CR-6672 [25]). This methodology was developed for evaluation of the generic risks associated with the transport of spent fuel by truck and rail from commercial power plants to potential interim storage and disposal sites.

The potential release from the TN-68 package can be estimated by adapting the equation developed in NUREG/CR-6672 ([25]) to estimate the releases from a severe fire accident. The estimated release is given by the relationship

$$R = C_I S(1-D)\left(1-\frac{T_i}{T_p}\right)$$

where
- R = release (curies)
- C_I = amount of CRUD on fuel assemblies (curies)
- S = fraction of CRUD released due to heating
- D = deposition factor
- T_p = peak internal temperature (°R)
- T_i = initial internal temperature (°R)

Table 8.3 shows the results obtained when this equation is applied using the parameter values from Table 8.2 and the temperatures predicted for the TN-68 package in this accident scenario.

Table 8.3. Potential Release Estimate for TN-68 Package

Initial temperature °F (°R)	Peak temperature °F (°R)	Potential release (curies)
100 (560)	857 (1307)	3.4

The potential CRUD release from the TN-68 package, based on five-year cooled fuel, is estimated to be approximately 3.4 curies of Co^{60}. Since the A_2 value for Co^{60} is 11 curies, the potential release is about 0.3 of an A_2 quantity (see Section 8.2).

8.2.4 Potential Release from the NAC LWT Package

The thermal analysis for the NAC LWT package shows that this package design would also maintain the integrity of the fuel cladding during the Baltimore tunnel fire scenario, and thus would maintain the single most important barrier to prevent the release of radioactive materials. The peak temperature of the fuel cladding is conservatively predicted to reach 1001°F (539°C), a temperature that is below the short-term temperature limit of 1058°F (570°C) for Zircaloy cladding, and well below its projected burst temperature of 1382°F (750°C). This peak temperature occurs at approximately 10 hours after the start of the fire (i.e., after the 7-hour fire duration, about 3 hours into the cool down period).

At about 6.9 hours elapsed time, the temperature predicted in the region of the Teflon and metallic helicoflex seals used on the NAC LWT lid reaches a maximum value of 1356°F (735°C). This value exceeds the continuous-use rated service temperature limit of 735°F (391°C) for the Teflon seal and 800°F (427°C) for the metallic helicoflex seal. Similarly, the peak temperature of 1407°F (764°C) predicted for the vent and drain port seals at approximately 6.8 hours elapsed time, exceeds the rated long-term service temperature of the Teflon seal material.

Because the predicted temperatures exceed the long-term service temperature of the seals, the seals are assumed to fail, and there is a potential for release of radioactive CRUD particles from the package. The amount of releasable CRUD in the NAC LWT package was determined based on contents consisting of one PWR fuel assembly containing 289 fuel rods. An estimate of the maximum "spot" CRUD activity shows that for 90% of PWR spent fuel rods the maximum activity is 20μCi/cm^2 or less [26, Table I-15]. The ratio of the peak (i.e., the maximum "spot" CRUD activity) to average concentration on the rod surface varies by a factor of two for PWR fuel rods [26, Table I-12].

The CRUD activity estimates [26] are based on newly discharged spent nuclear fuel. The CRUD activity is expected to decay by a factor of one-half for five-year cooled fuel, based on the decay rate for Co^{60}. This proves to be a good approximation because 92% of the activity for five-year cooled PWR fuel comes

from Co^{60}. The majority of the remaining 8% of the activity comes from Mn^{54}. By the time the fuel has aged 8 years, Co^{60} represents 99% of the activity.

Based on these data, the average CRUD activity for a PWR rod with a surface area of 1200 cm^2 is about 0.006 curies for five-year cooled fuel. The average CRUD activity for a 17 x 17 PWR assembly is about 1.73 Ci. The amount of CRUD that would flake or spall from the surface of a PWR rod due to temperatures calculated for the fuel rods in the thermal analysis is estimated to be a maximum of 15% [26, Table I-10]. Finally, a deposition factor of 0.90 was used to account for the deposition of CRUD particles on package surfaces and fuel assemblies.

The major assumptions used to estimate CRUD release are given in Table 8.4. The potential release from the NAC LWT package can be estimated from the same equation used for the TN-68 release estimate, as described in Section 8.2.1. The major driving force for material release results from the increased fill gas pressure inside the package due to increases in internal temperature. The temperature change is bounded by the difference between the maximum fill gas temperature predicted during the fire transient and the fill gas temperature inside the package at the time the package is loaded.

For this analysis, the loading temperature is defined as 100°F (38°C), based on the temperature reported in the SAR [11]. The maximum fill gas temperature is conservatively assumed to be the maximum inner shell temperature, predicted during the transient, of 1261 °F (683 °C). Table 8.5 shows the results obtained when this equation is applied using the parameter values from Table 8.4 and the temperatures predicted for the NAC LWT package in this accident scenario.

Table 8.4. Assumptions Used for Release Estimate for NAC LWT Package

Parameter	Assumed value
Number of Assemblies in Package	1 PWR
Rods per Assembly	289
Maximum "spot" CRUD Activity on Fuel Rod	20μCi/cm^2
Peak to axial average variation	2
CRUD decay factor (5 yr; based on Co^{60})	0.5
Average surface area per rod	1200 cm^2
Average CRUD Activity on PWR Fuel Rod (5 yr cooled)	0.006 Ci
Average CRUD Activity on PWR Assembly (5 yr cooled)	1.73 Ci
Fraction of CRUD released due to heating	0.15
Deposition Factor	0.90

Table 8.5. Potential Release Estimate for NAC LWT Package

Initial temperature °F (°R)	Peak temperature °F (°R)	Potential release (curies)
100 (560)	1261 (1721)	0.02

The potential CRUD release from the NAC LWT package based on five-year cooled fuel is estimated to be approximately 0.02 curies of Co^{60}. Since the A_2 value for Co^{60} is 11 curies, the potential release is about 0.002 of an A_2 quantity (see Section 8.2).

8.2.5 Potential Releases from Packages Carrying Failed Fuel

Of the three packages considered in this evaluation, only the HI-STAR 100 and the NAC LWT are approved to carry any kind of failed fuel. As discussed in Section 8.2.2, the HI-STAR 100 employs a welded inner multipurpose canister (MPC) that maintains its integrity throughout the entire fire transient. Even with failed fuel in this package, no fission products or fuel fines would be released into the cavity of the overpack for the conditions encountered in the Baltimore tunnel fire scenario. Therefore, no radioactive material from this package would be available for release into the environment. The NAC LWT, however, does present a possible path for the release of fission gasses and/or fuel fines, should a failed fuel payload be subject to conditions as severe as the tunnel fire analyzed in this study.

The staff did not analyze how a shipment of failed fuel would affect the release of spent fuel constituents from the NAC LWT. However, analyses presented in NUREG/CR-6672 [25] investigated the effect of an extraordinarily severe fully engulfing fire lasting 11 hours at 1832°F (1000°C) on a generic truck package that was based on the design of the NAC LWT. In this fire analysis for the generic truck package, it was assumed that 100% of the rods of a single PWR assembly failed due to thermal rupture. The resulting fission product release from the rods very conservatively bounds the potential release from any shipment of failed fuel rods that the NAC LWT would be allowed to carry.

The analysis in NUREG/CR-6672 [25] predicted the potential release fractions of various spent fuel constituents for a generic truck package carrying a single PWR spent fuel assembly consisting of high burn-up 3-year-cooled fuel. This assembly is far hotter than any fuel the NAC LWT is licensed to carry, and has a total activity of 7.9×10^4 Curies of Cesium 137 (Cs^{137}) (see Table 7.9 of NUREG/CR-6672 [25]). Using the release fraction 1.7×10^{-5} (see Table 7.31 of NUREG/CR-6672 [25]) for Cs^{137} calculated for the truck package, the estimated total release is approximately 1.3 Curies. This value is considerably larger than the estimated release for the fuel licensed for transport in the NAC LWT package (see Table 8.5), but is still far below the A_2 quantity of 16 Curies for Cs^{137} (see Section 8.2).

The analysis for Cs^{137}, as well as similar analyses conducted for particulates and the radionuclide Ruthenium (Ru) in NUREG/CR-6672[25], indicate that the potential release from the NAC LWT for any fuel that it is licensed to carry, whether intact or failed, would be small, even for conditions as severe as those encountered in the Baltimore tunnel fire.

8.3 Summary of Potential Releases

The results of the NTSB investigation of the Howard Street tunnel fire, the FDS tunnel fire model developed by NIST, and the rail car material fire exposure analyses completed by CNWRA, have provided a detailed picture of the potential duration and severity of the fire that occurred in the Howard Street tunnel in Baltimore on July 18, 2001. The fire transient analyses performed with ANSYS and COBRA-SFS using the FDS simulation results as boundary conditions have shown the robust nature of the larger spent fuel transportation package designs (HI-STAR 100 and TN-68). The predicted response of the smaller LWT package, if hauled by rail and exposed to the same tunnel fire environment, indicates more component degradation, but even this package survives the fire scenario without exceeding temperature limits for fuel cladding integrity or regulatory limits for radiological consequences.

For the TN-68 and the NAC LWT, the maximum temperatures predicted in the regions of the lid and the vent and drain ports exceed the seals' rated service temperatures, making it possible for a small release to occur, due to CRUD that might detach from the surfaces of the fuel rods. A release is not expected in this accident scenario, due to a number of factors, including (1) the tight clearances maintained between the lid and package body by the closure bolts, (2) the low pressure differential between the package interior and exterior, (3) the tendency of such small clearances to plug, and (4) the tendency of CRUD particles to settle or plate out. However, the above analysis shows that if a release were to occur, it would be within regulatory limits.

USNRC staff evaluated the radiological consequences of the package responses to the Baltimore tunnel fire. The results of this evaluation strongly indicate that neither spent nuclear fuel (SNF) particles nor fission products would be released from a spent fuel transportation package carrying intact spent fuel involved in a severe tunnel fire such as the Howard Street tunnel fire in Baltimore. None of the three package designs analyzed for the Baltimore Tunnel fire scenario (TN-68, HI-STAR 100, and NAC LWT) experienced internal temperatures that would result in rupture of the fuel cladding. In all three packages, the peak fuel cladding temperature is conservatively predicted to remain below the short-term limit of 1058°F (570°C).

Therefore, radioactive material (i.e., SNF particles or fission products) would be retained within the fuel rods. There would be no release from the HI-STAR 100, because the inner welded canister remains leak tight and all seals remain intact. The potential releases calculated for the TN-68 package and the NAC LWT package (as a consequence of exceeding seal temperature limits) indicate that any release of CRUD from either package would be very small - less than an A_2 quantity (see Section 8.2).

9 REFERENCES

1. 10 CFR 71. Jan. 1, 2003. *Packaging and Transportation of Radioactive Material.* Code of Federal Regulations, U.S. Nuclear Regulatory Commission, Washington D.C.

2. Michener TE, DR Rector, JM Cuta, RE Dodge, and CW Enderlin. 1995. *COBRA-SFS: A Thermal-Hydraulic Code for Spent Fuel Storage and Transportation Casks.* PNL-10782, Pacific Northwest National Laboratory, Richland, Washington.

3. ANSYS, Inc. 2003. "ANSYS Users Guide for Revision 8.0," ANSYS, Inc., Canonsburg, Pennsylvania.

4. McGrattan KB and A Hammins. February 2003. A. *Numerical Simulation of the Howard Street tunnel Fire, Baltimore, Maryland, July 2001.* NUREG/CR-6793, National Institute of Standards and Technology, Washington D.C.

5. Garabedian AS, DS Dunn, and AH Chowdhury. March 2003. Center for Nuclear Waste Regulatory Analysis, *Analysis of Rail Car Components Exposed to a Tunnel Fire Environment*, NUREG/CR-6799, Center for Nuclear Waste Regulatory Analysis, Washington, D.C.

6. McGrattan KB, HR Baum, RG Rehm, GP Forney, JE Floyd, and S Hostikka. November 2001. *Fire Dynamics Simulator (Version 2), User's Guide.* NISTIR 6784, National Institute of Standards and Technology, Gaithersburg, Maryland.

7. McGrattan KB, HR Baum, RG Rehm, GP Forney, JE Floyd, and S Hostikka. November 2001. *Fire Dynamics Simulator (Version 2), Technical Reference Guide.* NISTIR 6783, National Institute of Standards and Technology, Gaithersburg, Maryland.

8. Bechtel/Parsons Brinkerhoff, Inc. November 1995. *Memorial Tunnel Fire Ventilation Test Program, Comprehensive Test Report*, Prepared for Massachusetts Highway Department and Federal Highway Administration.

9. NRC Docket Number 71-9293. May 19, 2000. *TN-68 Transport Packaging Safety Analysis Report*, Rev. 2, TransNuclear Incorporated, New York.

10. NRC Docket Number 72-1008. March 30, 2001. *Final Safety Analysis Report for Holtec International Storage Transport and Repository Cask System* (HI-STAR 100 Cask System). HI-210610, Vol. I and II. HOLTEC, Marlton, New Jersey.

11. NRC Docket Number 71-9225. NAC LWT *Legal Weight Truck Cask System Safety Analysis Report*, June 2005, Rev. 37. Nuclear Assurance Corporation International, Norcross,, Georgia, USA.

12. 49 CFR. 171–184, Subchapter C. Oct 1, 2003. *Hazardous Materials Regulations.* Code of Federal Regulations, U.S. Department of Transportation, Washington, D.C.

13. Creer JM, TE Michener, MA McKinnon, JE Tanner, ER Gilbert, and RL Goodman. 1987. *The TN-24P PWR Spent-Fuel Storage Cask: Testing and Analysis*. EPRI-NP-5128/PNL-6054, Electric Power Research Institute, Palo Alto, California.

14. Rector DR, RA McCann, UP Jenquin, CM Heeb, JM Creer, and CL Wheeler. 1986. *CASTOR-1C Spent Fuel Storage Cask Decay Heat, Heat Transfer and Shielding Analysis*. PNL-5974. Pacific Northwest Laboratory, Richland, Washington.

15. Lombardo NJ, JM Cuta, TE Michener, DR Rector, and CL Wheeler. 1986. *COBRA-SFS: A Thermal-Hydraulic Analysis Computer Code, Volume III: Validation Assessments*, PNL-6048 Vol. III. Pacific Northwest Laboratory, Richland, Washington.

16. Bahney RH III and TL Lotz. July 1996. *Spent Nuclear Fuel Effective Thermal Conductivity Report*, BBA000000-01717-5705-00010 Rev. 00. TRW Environmental Safety Systems, Inc., Fairfax, Virginia.

17. HEXCEL. 2003. HexWeb Honeycomb Attributes and Properties. Available at http://www.hexcelcomposites.com/Markets/Products/Honeycomb/Hexweb_attrib/hwp_02.htm. Hexcel, Stamford, Connecticut.

18. Guyer EC and DL Brownell, editors. 1989. *Handbook of Applied Thermal Design*. McGraw-Hill, Inc., New York, p. 1-42.

19. Kreith F and MS Bohn. 2001. *Principles of Heat Transfer, 6th Edition*. Brooks/Cole, Pacific Grove, California.

20. Holman JP. 1986. *Heat Transfer, 6th Edition*. McGraw-Hill, Inc., New York.

21. Kreith F. 1976. *Principles of Heat Transfer, 3rd Edition*. Intext Education Publishers, New York.

22. Bucholz JA. January 1983. *Scoping Design Analyses for Optimized Shipping Casks Containing 1-, 2-, 3-, 5-, 7-, or 10-year old PWR Spent Fuel*. ORNL/CSD/TM-149. Oak Ridge National Laboratory, Oak Ridge, Tennessee.

23. U.S. Nuclear Regulatory Commission. January 1997. "Standard Review Plan for Dry Cask Storage Systems." NUREG-1536, USNRC, Washington, DC.

24. Johnson AB and ER Gilbert. September 1983. *Technical Basis for Storage of Zircaloy-Clad Spent Fuel in Inert Gases*, PNL-4835. Pacific Northwest Laboratory, Richland, Washington.

25. Sprung JL, DJ Ammerman, NL Breivik, RJ Dukart, and FL Kanipe. March 2000. *Reexamination of Spent Fuel Shipment Risk Estimates*, NUREG/CR-6672, Vol. 1 (SAND2000-0234). Sandia National Laboratories, Albuquerque, New Mexico.

26. Sandoval RP, RE Einziger, H Jordan, AP Malinauskas, and WJ Mings. January 1991. *Estimate of CRUD Contribution to Shipping Cask Containment Requirements,* SAND88-1358. Sandia National Laboratories, Albuquerque, New Mexico.

Appendix A

Material Properties for COBRA-SFS Model of TN-68 Package

Table A.1. Internal Fill Gas—Helium at Atmospheric Pressure

Temperature (°F)	Enthalpy (Btu/lbm)	Thermal Conductivity (Btu/hr-ft-°F)	Specific Heat (Btu/lbm-°F)	Specific Volume (ft^3/lbm)	Viscosity (lbm/hr-ft)
0	100	0.078	1.24	83.33	0.0410
200	348	0.097	1.24	119.76	0.0533
400	596	0.115	1.24	156.25	0.0641
600	844	0.129	1.24	192.31	0.0727
800	1092	0.138	1.24	229.36	0.0823
1000	1340	0.138	1.24	265.25	0.0907
2552	3264	0.138	1.24	549.00	0.1138

Table A.2. External Ambient Air at Atmospheric Pressure

Temperature (°F)	Enthalpy (Btu/lbm)	Thermal Conductivity (Btu/hr-ft-°F)	Specific Heat (Btu/lbm-°F)	Specific Volume (ft^3/lbm)	Viscosity (lbm/hr-ft)
60	124.5	0.0146	0.24	13.5669	0.0434
300	182.1	0.0193	0.243	19.8325	0.058
400	206.5	0.0212	0.245	22.4432	0.063
500	231.1	0.0231	0.247	25.0539	0.068
600	256	0.025	0.25	27.6645	0.072
700	281.1	0.0268	0.253	30.2752	0.077
800	306.7	0.0286	0.256	32.8859	0.081
900	332.5	0.0303	0.259	35.4966	0.085
1000	358.6	0.0319	0.262	38.1072	0.0889
2000	617.2	0.0471	0.2586	64.214	0.1242
4000	1522	0.0671	0.4524	116.428	0.1242

Table A.3. Summary of All Solid Material Properties Pre-Fire

Specific Heat (Btu/lbm-°F)	Density (lbm/ft^3)	Thermal Conductivity (Btu/hr-ft-°F)	Emissivity	Description
0.129	483.8	22.92	0.3	gamma shielding (SA-517 grade 70 carbon steel)
0.13	499.4	10.44	0.3	fuel tubes (SA-240 stainless steel)
0.214	165.9	41.72	0.3	borated aluminum poison plates
0.311	98.5	4.34	N/A	neutron shield (borated polyester)
0.228	165.9	99.84	0.3	Aluminum alloy basket rails
0.118	483.8	22.92	0.3	cask outer shell[a]
0.228	165.9	84.00	N/A	aluminum in neutron shield and thermal shield between cask and bottom impact limiter
0.420	23.1	0.064	N/A	wooden impact limiters (covered with sheet steel)
0.420	11.0	0.053	N/A	thin top layer of wood on impact limiter ends (covered with sheet steel)

[a]Based on nominal emissivity for carbon steel. SAR analyses use emissivity of 0.9 for painted cask surface, but cask specifications allow option for unpainted outer surface.

Table A.4. Summary of All Solid Material Properties Post-Fire

Specific Heat (Btu/lbm-°F)	Density (lbm/ft^3)	Thermal Conductivity (Btu/hr-ft-°F)	Emissivity	Description
0.129	483.8	22.92	0.3	gamma shielding (SA-517 grade 70 carbon steel)
0.13	499.4	10.44	0.3	fuel tubes (SA-240 stainless steel)
0.214	165.9	41.72	0.3	borated aluminum poison plates
0.26	0.027	0.03	N/A	hot air (replaces polyresin neutron shield vaporized in fire)
0.228	165.9	99.84	0.3	aluminum alloy basket rails
0.118	483.8	22.92	0.8	steel shell (SAR value post-fire is 0.95 for charred cask surface emissivity)
0.228	165.9	84.00	0.9	aluminum in neutron shield; inner and outer ring after polyresin evaporates
1020.0	134.8	0.00735	0.8	charcoal (impact limiters after the fire)
			0.9	tunnel wall

COBRA-SFS Material Properties Compared with Published SAR Values

Table A.5. BWR Spent Fuel Assemblies

SAR values determined using k-effective model for homogeneous representation of fuel rods and helium gas within fuel tube.

Temperature (°F)	Transverse Thermal Conductivity (Btu/hr-ft-°F)	Axial Thermal Conductivity (Btu/hr-ft-°F)	Specific Heat (Btu/lbm-°F)	Density (lbm/ft^3)
195.8	0.0157		0.055	257.5
200.0		0.058		
268.4	0.0178			
365.9	0.0206			
400.0		0.0646		
463.7	0.0239			
561.8	0.0277			
600.0		0.0709		
660.3	0.0319			
758.9	0.0367			
800.0		0.0769	0.055	257.5

COBRA-SFS input— BWR fuel rods; conservative values at nominal operating temperature and above.

Component	Thermal Conductivity (Btu/hr-ft-°F)	Specific Heat (Btu/lbm-°F)	Density (lbm/ft^3)
fuel pellet:	3.0	0.059	655.0
cladding:	10.0	0.1	409.0

Table A.6. Stainless Steel Type 304/304L (for fuel tubes)

SAR values			
Temperature (°F)	**Thermal Conductivity (Btu/hr-ft-°F)**	**Specific Heat (Btu/lbm-°F)**	**Density (lbm/ft^3)**
70	7.56	0.111	499.4
100	8.76		
200	9.36	0.124	
400	10.44	0.130	
600	11.28	0.134	
800	12.24	0.140	
1000	13.2		499.4
COBRA-SFS input—selected conservative representative values at nominal operating temperature and above			
all	10.44	0.13	499.4

Table A.7. Poison Plates (borated aluminum or boron carbide/aluminum matrix)

SAR values			
Temperature (°F)	**Thermal Conductivity (Btu/hr-ft-°F)**	**Specific Heat (Btu/lbm-°F)**	**Density (lbm/ft^3)**
68	69.36	0.214	169.3
212	83.76		
482	86.64		
571	86.64	0.214	169.3
COBRA-SFS input—selected conservative values based on range of allowable fabrication variations, as described for cask specifications in SAR.			
all	41.72	0.214	165.9

Table A.8. Aluminum Type 6060 (for basket support rails and shims)

SAR values			
Temperature (°F)	**Thermal Conductivity (Btu/hr-ft-°F)**	**Specific Heat (Btu/lbm-°F)**	**Density (lbm/ft^3)**
70	96.12	0.218	165.9
100	96.96	0.219	
150	98.04	0.223	
200	99	0.225	
250	99.84	0.228	
300	100.56	0.23	
350	101.28	0.233	
400	101.88	0.234	165.9
COBRA-SFS input—selected conservative representative values at nominal operating temperature and above.			
all	99.84	0.228	165.9

Table A.9. Carbon Steel SA-516 Grade 70 (for inner and outer gamma shield and lid)

SAR values			
Temperature (°F)	**Thermal Conductivity (Btu/hr-ft-°F)**	**Specific Heat (Btu/lbm-°F)**	**Density (lbm/ft^3)**
70	22.92	0.109	483.8
200	23.76	0.118	
400	23.88	0.129	
600	22.92	0.139	
800	21.6	0.152	
1000	20.16	0.169	
1200	18.24	0.206	
1400	15.48	0.184	483.8
COBRA-SFS input—selected conservative representative values at nominal operating temperature and above.			
all	22.92	0.129	483.8

Table A.10. Neutron Shield (polyester resin with aluminum boxes)

SAR values—properties are composite values for polyester resin and aluminum boxes modeled as single homogeneous material.			
Temperature (°F)	**Thermal Conductivity (Btu/hr-ft-°F)**	**Specific Heat (Btu/lbm-°F)**	**Density (lbm/ft^3)**
all	0.0996	0.311	98.5
COBRA-SFS input—selected conservative representative values at nominal operating temperature and above.			
borated polyester	4.34	0.311	98.5
aluminum	84.00	0.228	165.9

Table A.11. Carbon Steel SA-350 grade LF3 (for cask outer shell)

SAR values			
Temperature (°F)	**Thermal Conductivity (Btu/hr-ft-°F)**	**Specific Heat (Btu/lbm-°F)**	**Density (lbm/ft^3)**
70	23.64	0.106	489.0
100	23.88	0.11	
200	24.36	0.118	
400	24.24	0.128	
600	23.16	0.137	
800	21.72	0.149	
1000	20.04	0.165	
1200	18.24	0.189	
1400	15.36	0.406	489.0
COBRA-SFS input- typical values for carbon steel at nominal operating temperature and above, based on range of allowable fabrication variations described for cask specifications in SAR.			
all	22.92	0.118	483.8

Table A.12. Impact Limiters (wood covered with sheet steel)

SAR values—none provided; SAR analyses assume impact limiters act as perfect insulators on cask ends for normal, off-normal, and fire accident conditions.			
COBRA-SFS input—selected conservative representative values at nominal operating temperature and above.			
Material	**Thermal Conductivity (Btu/hr-ft-°F)**	**Specific Heat (Btu/lbm-°F)**	**Density (lbm/ft^3)**
redwood	0.064	0.311	98.5
balsa	0.053	0.228	165.9
carbon steel	22.92	0.118	483.8
charcoal	0.00735	1020.0	134.8

Table A.13. Air (replacing neutron shield polyethylene after fire)

SAR values			
Temperature (°F)	**Thermal Conductivity (Btu/hr-ft-°F)**	**Specific Heat (Btu/lbm-°F)**	**Density (lbm/ft^3)**
81	0.0156	0.231	0.0734
261	0.0192	0.237	0.0551
441	0.0228	0.239	0.0440
621	0.0264	0.246	0.0367
981	0.0336	0.264	0.0275
COBRA-SFS input—selected representative values at immediate post-fire temperature and above.			
all	0.03	0.26	0.0270

Appendix B

Material Properties for ANSYS Model of HI-STAR 100 Package

Table B.1. Homogeneous Fuel Region for Westinghouse 17x17 OFA

Temperature (°F)	Thermal Conductivity (Btu/hr-in-°F) (x)	Thermal Conductivity (Btu/hr-in-°F) (y)	Thermal Conductivity (Btu/hr-in-°F) (z)	Density (lbm/in^3)	Specific Heat (Btu/lbm-°F)	Description
0	0.04412	0.04412	0.06256	0.14353	0.05869	Fuel Region (2.25 multiplier against helium contribution to account for limited convection and pressurization enhancement)
100	0.04412	0.04412	0.06256	0.14353	0.05869	
200	0.04412	0.04412	0.06256	0.14352	0.05869	
300	0.05078	0.05078	0.06509	0.14352	0.05869	
400	0.05895	0.05895	0.06797	0.14352	0.05869	
500	0.06837	0.06837	0.07082	0.14352	0.05869	
600	0.07834	0.07834	0.07391	0.14352	0.05869	
700	0.08920	0.08920	0.07756	0.14352	0.05869	
800	0.09508	0.09508	0.08121	0.15352	0.05869	
900	0.09508	0.09508	0.08484	0.15352	0.05869	
1000	0.09508	0.09508	0.08600	0.15352	0.05869	

Table B.2. Alloy-X

Temperature (°F)	Thermal Conductivity (Btu/hr-in-°F) (x)	Thermal Conductivity (Btu/hr-in-°F) (y)	Thermal Conductivity (Btu/hr-in-°F) (z)	Density (lbm/in^3)	Specific Heat (Btu/lbm-°F)	Description
200	0.70000	*	*	0.28993	0.12000	Basket Plates, Basket Supports, Boral Plate Sheathing, MPC shell, impact limiter skin shell
450	0.81667	*	*			
700	0.91667	*	*			
1400	1.19670	*	*			

Table B.3. Helium

Temperature (°F)	Thermal Conductivity (Btu/hr-in-°F) (x)	Thermal Conductivity (Btu/hr-in-°F) (y)	Thermal Conductivity (Btu/hr-in-°F) (z)	Density (lbm/in^3)	Specific Heat (Btu/lbm-°F)	Description
0	0.00650	*	*	6.90E-06	1.24000	gas conduction between MPC and cask
200	0.00808	*	*	4.81E-06		
400	0.00958	*	*	3.69E-06		
600	0.01075	*	*	2.99E-06		
800	0.01150	*	*	2.52E-06		
1400	0.01370	*	*	1.71E-06		

Table B.4. Helium
(with 2.25 multiplier to account for limited convection and pressurization enhancement)

Temperature (°F)	Thermal Conductivity (Btu/hr-in-°F) (x)	Thermal Conductivity (Btu/hr-in-°F) (y)	Thermal Conductivity (Btu/hr-in-°F) (z)	Density (lbm/in^3)	Specific Heat (Btu/lbm-°F)	Description
0	0.01400	*	*	6.90E-06	1.24000	Conduction in: central core region, between guide tubes and basket plates, between fuel and compartments, and between basket and MPC Shell
200	0.01740	*	*	4.81E-06		
400	0.02063	*	*	3.69E-06		
600	0.02315	*	*	2.99E-06		
800	0.02476	*	*	2.52E-06		
1400	0.02950	*	*	1.71E-06		

Table B.5. Boral Plates
(includes 0.004" helium gap and gap radiation on both sides of Boral)

Temperature (°F)	Thermal Conductivity (Btu/hr-in-°F) (x)	Thermal Conductivity (Btu/hr-in-°F) (y)	Thermal Conductivity (Btu/hr-in-°F) (z)	Density (lbm/in^3)	Specific Heat (Btu/lbm-°F)	Description
0	0.30836	4.62020	4.62020	0.08390	0.24762	parallel to thickness (switch x & y to define cross-width)
100	0.34331	4.62550	4.62550	0.08390		
200	0.37738	4.64850	4.64850	0.08390		
300	0.40969	4.69040	4.69040	0.08390		
400	0.44166	4.73250	4.73250	0.08390		
500	0.46611	4.74620	4.74620	0.08390		
600	0.49024	4.75200	4.75200	0.08390		
700	0.50544	4.73700	4.73700	0.08390		
800	0.52053	4.72210	4.72210	0.08390		
900	0.53517	4.70710	4.70710	0.08390		
1000	0.54970	4.69220	4.69220	0.08390		
1100	0.56438	4.68350	4.68350	0.08390		

Table B.6. Carbon Steel (SA-516, Gr. 70)

Temperature (°F)	Thermal Conductivity (Btu/hr-in-°F) (radial)	Thermal Conductivity (Btu/hr-in-°F) (circumferential)	Thermal Conductivity (Btu/hr-in-°F) (axial)	Density (lbm/in^3)	Specific Heat (Btu/lbm-°F)	Description
200	0.17409	2.03330	2.03330	0.28299	0.10000	Gamma Shield with 0.01" air gaps between plates
450	0.22634	1.99170	1.99170			
700	0.28273	1.86670	1.86670			
1400	0.44136	1.46670	1.46670			

Table B.7. Carbon Steel (SA-515, Gr. 70)

Temperature (°F)	Thermal Conductivity (Btu/hr-in-°F) (x)	Thermal Conductivity (Btu/hr-in-°F) (y)	Thermal Conductivity (Btu/hr-in-°F) (z)	Density (lbm/in^3)	Specific Heat (Btu/lbm-°F)	Description
200	2.43330	*	*	0.28299	0.10000	For radial channels of overpack and enclosure of shells of overpack (Fins)
450	2.25830	*	*			
700	2.05000	*	*			
1400	1.46670	*	*			

Table B.8. Holtite-A

Temperature (°F)	Thermal Conductivity (Btu/hr-in-°F) (x)	Thermal Conductivity (Btu/hr-in-°F) (y)	Thermal Conductivity (Btu/hr-in-°F) (z)	Density (lbm/in^3)	Specific Heat (Btu/lbm-°F)	Description
*	0.03108	*	*	0.06076	0.39000	Neutron Shield/In impact limiter

Table B.9. HT-870

Temperature (°F)	Thermal Conductivity (Btu/hr-in-°F) (x)	Thermal Conductivity (Btu/hr-in-°F) (y)	Thermal Conductivity (Btu/hr-in-°F) (z)	Density (lbm/in^3)	Specific Heat (Btu/lbm-°F)	Description
*	0.00340	*	*	0.00868	0.39000	Foam on back side of fins

Table B.10. Air Properties Representing Degraded Materials

Temperature (°F)	Thermal Conductivity (Btu/hr-in-°F) (x)	Thermal Conductivity (Btu/hr-in-°F) (y)	Thermal Conductivity (Btu/hr-in-°F) (z)	Density (lbm/in^3)	Specific Heat (Btu/lbm-°F)	Description
200	0.00148	*	*	3.48E-05	0.24110	For degraded Holtite-A, HT-870, and Honeycomb after fire
450	0.00188	*	*	2.53E-05	0.24605	
700	0.00227	*	*	1.99E-05	0.25355	
1400	0.00336	*	*	1.31E-05	0.27445	

Table B.11. One-Quarter-Inch Fillet Weld - Carbon Steel (SA-515, Gr. 70)

Temperature (°F)	Thermal Conductivity (Btu/hr-in-°F) (x)	Thermal Conductivity (Btu/hr-in-°F) (y)	Thermal Conductivity (Btu/hr-in-°F) (z)	Density (lbm/in^3)	Specific Heat (Btu/lbm-°F)	Description
200	1.21670	2.43330	2.43330	0.28299	0.10000	Reduced radial channel conductivity (Fin Fillet Weld Root)
450	1.12920	2.25830	2.25830			
700	1.02500	2.05000	2.05000			
1400	0.73333	1.46670	1.46670			

Table B.12. Carbon Steel (SA-516, Gr. 70)

Temperature (°F)	Thermal Conductivity (Btu/hr-in-°F) (x)	Thermal Conductivity (Btu/hr-in-°F) (y)	Thermal Conductivity (Btu/hr-in-°F) (z)	Density (lbm/in^3)	Specific Heat (Btu/lbm-°F)	Description
200	2.03330	*	*	0.28299	0.10000	Gamma Shield (intimate contact) and impact limiter base structure
450	1.99170	*	*			
700	1.86670	*	*			
1400	1.46670	*	*			

Table B.13. Aluminum Honeycomb (700 psi unidirectional w/1700 psi cross-core backing)

Temperature (°F)	Thermal Conductivity (Btu/hr-in-°F) (x)	Thermal Conductivity (Btu/hr-in-°F) (y)	Thermal Conductivity (Btu/hr-in-°F) (z)	Density (lbm/in^3)	Specific Heat (Btu/lbm-°F)	Description
68	1.11710	0.47427	1.11710	0.01406	0.20800 (assumed)	Type 1: Aluminum Honeycomb
212	1.15270	0.48944	1.15270	0.01406		
752	1.42620	0.59537	1.42620	0.01406		
1400	1.75440	0.72248	1.75440	0.01406		

Table B.14. Aluminum Honeycomb (700 psi unidirectional and 2300 psi cross-core)

Temperature (°F)	Thermal Conductivity (Btu/hr-in-°F) (x)	Thermal Conductivity (Btu/hr-in-°F) (y)	Thermal Conductivity (Btu/hr-in-°F) (z)	Density (lbm/in^3)	Specific Heat (Btu/lbm-°F)	Description
68	0.82721	0.31682	0.82721	0.00579	0.20800 (assumed)	Type 2&5: Aluminum Honeycomb
212	0.85369	0.32693	0.85369	0.00579		
752	1.03810	0.39771	1.03810	0.00579		
1400	1.25940	0.48265	1.25940	0.00579		

Table B.14. Aluminum Honeycomb (2300 psi cross-core)

Temperature (°F)	Thermal Conductivity (Btu/hr-in-°F) (x)	Thermal Conductivity (Btu/hr-in-°F) (y)	Thermal Conductivity (Btu/hr-in-°F) (z)	Density (lbm/in^3)	Specific Heat (Btu/lbm-°F)	Description
68	1.40690	0.63172	1.40690	0.01684	0.20800 (assumed)	Type 3: Aluminum Honeycomb
212	1.45170	0.65194	1.45170	0.01684		
752	1.81430	0.79302	1.81430	0.01684		
1400	2.24930	0.96231	2.24930	0.01684		

Table B.16. Aluminum Honeycomb (1100 psi unidirectional and 2300 psi cross-core)

Temperature (°F)	Thermal Conductivity (Btu/hr-in-°F) (x)	Thermal Conductivity (Btu/hr-in-°F) (y)	Thermal Conductivity (Btu/hr-in-°F) (z)	Density (lbm/in^3)	Specific Heat (Btu/lbm-°F)	Description
68	1.40690	0.63172	1.40690	1.40630	0.20800 (assumed)	Type 4: Aluminum Honeycomb
212	1.45170	0.65194	1.45170	1.40630		
752	1.81430	0.79302	1.81430	1.40630		
1400	2.24930	0.96231	2.24930	1.40630		

Table B.17. Emissivity Values for Radiation Heat Transfer

Component	Material	Emissivity
Fuel	Zircaloy	0.80
Basket	Alloy-X	0.36
Support Bracket	Alloy-X	0.36
MPC Wall	Alloy-X	0.36
Borated Aluminum Plate	Boral	0.55
Bare Carbon Steel	Carbon Steel	0.65
Painted Surfaces		0.90
Cask and Impact Limiter Surfaces	Alloy-X	0.36
Tunnel Surface		0.90
Soot Surfaces		0.90

Appendix C

Material Properties for ANSYS Model of Legal Weight Truck Package

Table C.1. 304 Stainless Steel

Temperature (°F)	Thermal Conductivity (Btu/hr-in-°F)	Density (lbm/in^3)	Specific Heat (Btu/lbm-°F)	Description
70	0.7143	-	0.1141	Used for cask body, cask lid, spokes
212	0.7800	0.2888	0.1207	
392	0.8592	0.2872	0.1272	
572	0.9333	0.2855	0.1320	
752	1.0042	0.2839	0.1356	
932	1.0717	0.2822	0.1385	
1112	1.1375	0.2805	0.1412	

Table C.2. 6061-T6 Aluminum

Temperature (°F)	Thermal Conductivity (Btu/hr-in-°F)	Density (lbm/in^3)	Specific Heat (Btu/lbm-°F)	Description
32	9.7500	0.0984	0.2140	Used for basket, IL 1, 2 skin
212	9.9167			
572	11.0833			
932	12.9167			

Table C.3. 6061-T6 Aluminum Honeycomb

Temperature (°F)	Thermal Conductivity (Btu/hr-in-°F)	Density (lbm/in^3)	Specific Heat (Btu/lbm-°F)	Description
32	1.6965	0.017118056	0.214	Used for IL 1 (Honeycomb)
212	1.7255			
572	1.9285			
932	2.2475			

Table C.4. 6061-T6 Aluminum Honeycomb

Temperature (°F)	Thermal Conductivity (Btu/hr-in-°F)	Density (lbm/in^3)	Specific Heat (Btu/lbm-°F)	Description
32	1.4235	0.0144	0.214	Used for IL 2 (Honeycomb)
212	1.4478			
572	1.6182			
932	1.8858			

Table C.5. Helium

Temperature (°F)	Thermal Conductivity (Btu/hr-in-°F)	Density (lbm/in^3)	Specific Heat (Btu/lbm-°F)	Description
200	0.00808	4.83E-06	1.24	Used for cask gap and fuel gap
400	0.00942	3.70E-06		
600	0.01075	3.01E-06		
800	0.0115	2.52E-06		

Table C.6. Lead Gamma Shield

Temperature (°F)	Enthalpy[1] (Btu/lbm)	Temperature (°F)	Thermal Conductivity[2] (Btu/hr-in-°F)	Temperature (°F)	Density[3] (lbm/in^3)	Description
80.33	0.0860	80.3	1.698984	53.3	4.11060E-01	Used for lead gamma shield
260.33	5.7610	170.3	1.671552	233.3	4.07470E-01	
440.33	11.608	260.3	1.641888	413.3	4.03670E-01	
611.50	17.756	350.3	1.608588	607.7	3.99450E-01	
629.50	27.730	440.3	1.573092	622.1	3.84440E-01	
800.33	34.007	530.3	1.539792	802.1	3.80740E-01	
980.33	40.241	610.3	1.515924	982.1	3.76330E-01	
1160.33	46.432	630.3	0.746712	1162.1	3.71930E-01	
1340.33	52.580	710.3	0.796428	1342.1	3.67520E-01	
1520.33	58.641	800.3	0.84222	1522.1	3.63120E-01	
		890.3	0.884016			
		980.3	0.921852			
		1070.3	0.955764			
		1160.3	0.985716			
		1250.3	1.01171			
		1340.3	1.03378			

[1] Based on specific heat from B.J. McBride, S. Gordon and M.A. Reno, NASA Technical Paper 3287, (1993). Enthalpy as a function of temperature calculated using definition of specific heat as partial derivative of enthalpy with respect to temperature at constant pressure;

$$c_p = \left(\frac{\partial h}{\partial T}\right)_p$$

[2] C.Y. Ho, R.W. Powell and P.E. Liley, J. **Phys. Chem. Ref. Data**, v1, p279 (1972).

[3] F.C. Nix and D. MacNair, Physical Review, v60, p597 (1941) and R. Feder, A.S. Norwick, Physical Review, v109, p1959 (1958); calculated from the linear expansion.

Table C.7. 56% Ethylene Glycol Solution

Avg. Temperature (°F)	Thermal Conductivity (Btu/hr-in-°F)	Specific Heat (Btu/lbm-°F)	Density (lbm/in^3)
50	0.0188	0.7405	0.0391
70	0.0187	0.7522	0.0389
100	0.0185	0.7696	0.0385
150	0.0182	0.7979	0.0378
200	0.0179	0.8255	0.0370
250	0.0177	0.8522	0.0362
260	0.0176	0.8575	0.0360
270	0.0176	0.8627	0.0358
280	0.0175	0.8679	0.0357
290	0.0175	0.8731	0.0355
300	0.0174	0.8782	0.0353
310	0.0174	0.8833	0.0351
320	0.0173	0.8884	0.0349
330	0.0173	0.8934	0.0347
340	0.0172	0.8984	0.0345
350	0.0172	0.9034	0.0343

Table C.8. Air

Avg. Temperature (°F)	Thermal Conductivity (Btu/hr-in-°F)	Specific Heat (Btu/lbm-°F)	Density (lbm/in^3)
350	0.0017	0.2467	0.0000283
450	0.0018	0.2494	0.0000252
550	0.0020	0.2516	0.0000227
650	0.0022	0.2533	0.0000206
750	0.0023	0.2546	0.0000189
850	0.0025	0.2556	0.0000175
950	0.0026	0.2562	0.0000162
1050	0.0027	0.2566	0.0000152
1150	0.0029	0.2568	0.0000142
1250	0.0030	0.2570	0.0000134
1350	0.0031	0.2571	0.0000126
1450	0.0033	0.2571	0.0000120
1550	0.0034	0.2573	0.0000114
1650	0.0035	0.2576	0.0000108
1750	0.0036	0.2581	0.0000104
1850	0.0038	0.2589	0.0000099
1950	0.0039	0.2599	0.0000095
2050	0.0040	0.2614	0.0000091

Table C.9. Effective Conductivity for Liquid Neutron Shield with 1°F Temperature Gradient

Avg. Temperature (°F)	56% Ethylene Glycol		Air	
	Effective Conductivity Neutron Shield (Btu/hr-in-°F)	Effective Conductivity Expansion Tank (Btu/hr-in-°F)	Effective Conductivity Neutron Shield (Btu/hr-in-°F)	Effective Conductivity Expansion Tank (Btu/hr-in-°F)
250	0.364	0.149	0.003	0.002
260	0.374	0.153	0.003	0.002
270	0.384	0.157	0.003	0.002
280	0.393	0.161	0.003	0.002
290	0.398	0.163	0.003	0.002
300	0.396	0.162	0.003	0.002
310	0.395	0.162	0.003	0.002
320	0.394	0.161	0.003	0.002
330	0.393	0.161	0.003	0.002
340	0.391	0.160	0.003	0.002
350	0.390	0.160	0.003	0.002
351	*	*	0.003	0.002
400	*	*	0.003	0.002
500	*	*	0.003	0.002
600	*	*	0.003	0.002
700	*	*	0.003	0.002
800	*	*	0.003	0.002
1000	*	*	0.003	0.003
1200	*	*	0.003	0.003
1500	*	*	0.003	0.003
2000	*	*	0.004	0.004
2500	*	*	0.004	0.004

Table C.10. Effective Conductivity for Liquid Neutron Shield with 10°F Temperature Gradient

Avg. Temperature (°F)	56% Ethylene Glycol		Air	
	Effective Conductivity Neutron Shield (Btu/hr-in-°F)	Effective Conductivity Expansion Tank (Btu/hr-in-°F)	Effective Conductivity Neutron Shield (Btu/hr-in-°F)	Effective Conductivity Expansion Tank (Btu/hr-in-°F)
250	0.654	0.268	0.006	0.002
260	0.673	0.276	0.006	0.002
270	0.691	0.283	0.006	0.002
280	0.704	0.288	0.006	0.002
290	0.705	0.289	0.006	0.002
300	0.703	0.288	0.006	0.002
310	0.701	0.287	0.006	0.002
320	0.699	0.286	0.006	0.002
330	0.697	0.286	0.006	0.002
340	0.695	0.285	0.006	0.002
350	*	*	0.006	0.002
351	*	*	0.006	0.002
400	*	*	0.006	0.002
500	*	*	0.006	0.002
600	*	*	0.005	0.002
700	*	*	0.005	0.002
800	*	*	0.005	0.002
1000	*	*	0.005	0.003
1200	*	*	0.005	0.003
1500	*	*	0.004	0.003
2000	*	*	0.004	0.004
2500	*	*	0.004	0.004

Table C.11. Effective Conductivity for Liquid Neutron Shield with 25°F Temperature Gradient

Avg. Temperature (°F)	56% Ethylene Glycol		Air	
	Effective Conductivity Neutron Shield (Btu/hr-in-°F)	Effective Conductivity Expansion Tank (Btu/hr-in-°F)	Effective Conductivity Neutron Shield (Btu/hr-in-°F)	Effective Conductivity Expansion Tank (Btu/hr-in-°F)
250	0.840	0.344	0.008	0.003
260	0.863	0.353	0.008	0.003
270	0.882	0.361	0.008	0.003
280	0.888	0.364	0.008	0.003
290	0.885	0.363	0.007	0.003
300	0.883	0.361	0.007	0.003
310	0.880	0.360	0.007	0.003
320	0.877	0.359	0.007	0.003
330	0.875	0.358	0.007	0.003
340	0.872	0.357	0.007	0.003
350	*	*	0.007	0.003
351	*	*	0.007	0.003
400	*	*	0.007	0.003
500	*	*	0.007	0.003
600	*	*	0.007	0.003
700	*	*	0.007	0.003
800	*	*	0.006	0.003
1000	*	*	0.006	0.003
1200	*	*	0.006	0.003
1500	*	*	0.005	0.003
2000	*	*	0.005	0.004
2500	*	*	0.005	0.004

Table C.12. Effective Conductivity for Liquid Neutron Shield with 50°F Temperature Gradient

Avg. Temperature (°F)	56% Ethylene Glycol		Air	
	Effective Conductivity Neutron Shield (Btu/hr-in-°F)	Effective Conductivity Expansion Tank (Btu/hr-in-°F)	Effective Conductivity Neutron Shield (Btu/hr-in-°F)	Effective Conductivity Expansion Tank (Btu/hr-in-°F)
250	1.061	0.434	0.009	0.004
260	1.058	0.433	0.009	0.004
270	1.055	0.432	0.009	0.004
280	1.052	0.431	0.009	0.004
290	1.049	0.430	0.009	0.004
300	1.046	0.428	0.009	0.004
310	1.043	0.427	0.009	0.004
320	1.039	0.426	0.009	0.004
330	*	*	0.009	0.004
340	*	*	0.009	0.004
350	*	*	0.009	0.004
351	*	*	0.009	0.004
400	*	*	0.009	0.003
500	*	*	0.008	0.003
600	*	*	0.008	0.003
700	*	*	0.008	0.003
800	*	*	0.008	0.003
1000	*	*	0.007	0.003
1200	*	*	0.007	0.003
1500	*	*	0.006	0.003
2000	*	*	0.006	0.004
2500	*	*	0.006	0.004

Table C.13. Effective Conductivity for Liquid Neutron Shield with 70°F Temperature Gradient

Avg. Temperature (°F)	56% Ethylene Glycol		Air	
	Effective Conductivity Neutron Shield (Btu/hr-in-°F)	Effective Conductivity Expansion Tank (Btu/hr-in-°F)	Effective Conductivity Neutron Shield (Btu/hr-in-°F)	Effective Conductivity Expansion Tank (Btu/hr-in-°F)
250	1.151	0.471	0.010	0.004
260	1.148	0.470	0.010	0.004
270	1.144	0.469	0.010	0.004
280	1.141	0.467	0.010	0.004
290	1.138	0.466	0.010	0.004
300	1.134	0.464	0.010	0.004
310	1.131	0.463	0.010	0.004
320	*	*	0.010	0.004
330	*	*	0.010	0.004
340	*	*	0.009	0.004
350	*	*	0.009	0.004
351	*	*	0.009	0.004
400	*	*	0.009	0.004
500	*	*	0.009	0.004
600	*	*	0.009	0.004
700	*	*	0.008	0.003
800	*	*	0.008	0.003
1000	*	*	0.008	0.003
1200	*	*	0.007	0.003
1500	*	*	0.007	0.003
2000	*	*	0.006	0.004
2500	*	*	0.006	0.004

Table C.14. Effective Conductivity for Liquid Neutron Shield with 100°F Temperature Gradient

Avg. Temperature (°F)	56% Ethylene Glycol		Air	
	Effective Conductivity Neutron Shield (Btu/hr-in-°F)	Effective Conductivity Expansion Tank (Btu/hr-in-°F)	Effective Conductivity Neutron Shield (Btu/hr-in-°F)	Effective Conductivity Expansion Tank (Btu/hr-in-°F)
250	1.253	0.513	0.011	0.004
260	1.249	0.512	0.011	0.004
270	1.245	0.510	0.011	0.004
280	1.242	0.509	0.011	0.004
290	1.238	0.507	0.011	0.004
300	1.234	0.505	0.011	0.004
310	*	*	0.010	0.004
320	*	*	0.010	0.004
330	*	*	0.010	0.004
340	*	*	0.010	0.004
350	*	*	0.010	0.004
351	*	*	0.010	0.004
400	*	*	0.010	0.004
500	*	*	0.010	0.004
600	*	*	0.009	0.004
700	*	*	0.009	0.004
800	*	*	0.009	0.004
1000	*	*	0.008	0.003
1200	*	*	0.008	0.003
1500	*	*	0.008	0.003
2000	*	*	0.007	0.004
2500	*	*	0.007	0.004

Table C.15. Effective Conductivity for Liquid Neutron Shield with 200°F Temperature Gradient

Avg. Temperature (°F)	56% Ethylene Glycol		Air	
	Effective Conductivity Neutron Shield (Btu/hr-in-°F)	Effective Conductivity Expansion Tank (Btu/hr-in-°F)	Effective Conductivity Neutron Shield (Btu/hr-in-°F)	Effective Conductivity Expansion Tank (Btu/hr-in-°F)
250	1.468	0.601	0.013	0.005
260	*	*	0.013	0.005
270	*	*	0.013	0.005
280	*	*	0.013	0.005
290	*	*	0.013	0.005
300	*	*	0.012	0.005
310	*	*	0.012	0.005
320	*	*	0.012	0.005
330	*	*	0.012	0.005
340	*	*	0.012	0.005
350	*	*	0.012	0.005
351	*	*	0.012	0.005
400	*	*	0.012	0.005
500	*	*	0.012	0.005
600	*	*	0.011	0.004
700	*	*	0.011	0.004
800	*	*	0.011	0.004
1000	*	*	0.010	0.004
1200	*	*	0.010	0.004
1500	*	*	0.009	0.004
2000	*	*	0.008	0.004
2500	*	*	0.008	0.005

Table C.16. Effective Conductivity for Liquid Neutron Shield with 300°F Temperature Gradient

Avg. Temperature (°F)	56% Ethylene Glycol		Air	
	Effective Conductivity Neutron Shield (Btu/hr-in-°F)	Effective Conductivity Expansion Tank (Btu/hr-in-°F)	Effective Conductivity Neutron Shield (Btu/hr-in-°F)	Effective Conductivity Expansion Tank (Btu/hr-in-°F)
250	*	*	0.014	0.005
260	*	*	0.014	0.005
270	*	*	0.014	0.005
280	*	*	0.014	0.005
290	*	*	0.014	0.005
300	*	*	0.014	0.005
310	*	*	0.014	0.005
320	*	*	0.014	0.005
330	*	*	0.014	0.005
340	*	*	0.014	0.005
350	*	*	0.013	0.005
351	*	*	0.013	0.005
400	*	*	0.013	0.005
500	*	*	0.013	0.005
600	*	*	0.012	0.005
700	*	*	0.012	0.005
800	*	*	0.012	0.005
1000	*	*	0.011	0.004
1200	*	*	0.011	0.004
1500	*	*	0.010	0.004
2000	*	*	0.009	0.004
2500	*	*	0.009	0.005

Table C.17. Effective Conductivity for Liquid Neutron Shield with 500°F Temperature Gradient

Avg. Temperature (°F)	56% Ethylene Glycol		Air	
	Effective Conductivity Neutron Shield (Btu/hr-in-°F)	Effective Conductivity Expansion Tank (Btu/hr-in-°F)	Effective Conductivity Neutron Shield (Btu/hr-in-°F)	Effective Conductivity Expansion Tank (Btu/hr-in-°F)
250	*	*	0.016	0.006
260	*	*	0.016	0.006
270	*	*	0.016	0.006
280	*	*	0.016	0.006
290	*	*	0.016	0.006
300	*	*	0.015	0.006
310	*	*	0.015	0.006
320	*	*	0.015	0.006
330	*	*	0.015	0.006
340	*	*	0.015	0.006
350	*	*	0.015	0.006
351	*	*	0.015	0.006
400	*	*	0.015	0.006
500	*	*	0.014	0.006
600	*	*	0.014	0.005
700	*	*	0.014	0.005
800	*	*	0.013	0.005
1000	*	*	0.013	0.005
1200	*	*	0.012	0.005
1500	*	*	0.011	0.005
2000	*	*	0.011	0.004
2500	*	*	0.010	0.005

Table C.18. Emissivity Values for Radiation Heat Transfer

Component	Material	Emissivity Before Fire	Emissivity During/After Fire
Canister	stainless steel	0.36	0.36
Cask	stainless steel	0.36	0.36
Outer Neutron Shield		0.34	0.34
Inner Neutron Shield		0.34	0.34
Basket	stainless steel	0.36	0.36
Fuel Clad	zircaloy	0.8	0.8
Boral Plate	aluminum clad	0.55	0.55
Shell Interior	stainless steel	0.36	0.36
Cask Exterior	stainless steel	0.85	0.9
Tunnel/ISO	various		0.9

Appendix D

Boundary Conditions from FDS Simulation of Fully Ventilated Fire Scenario

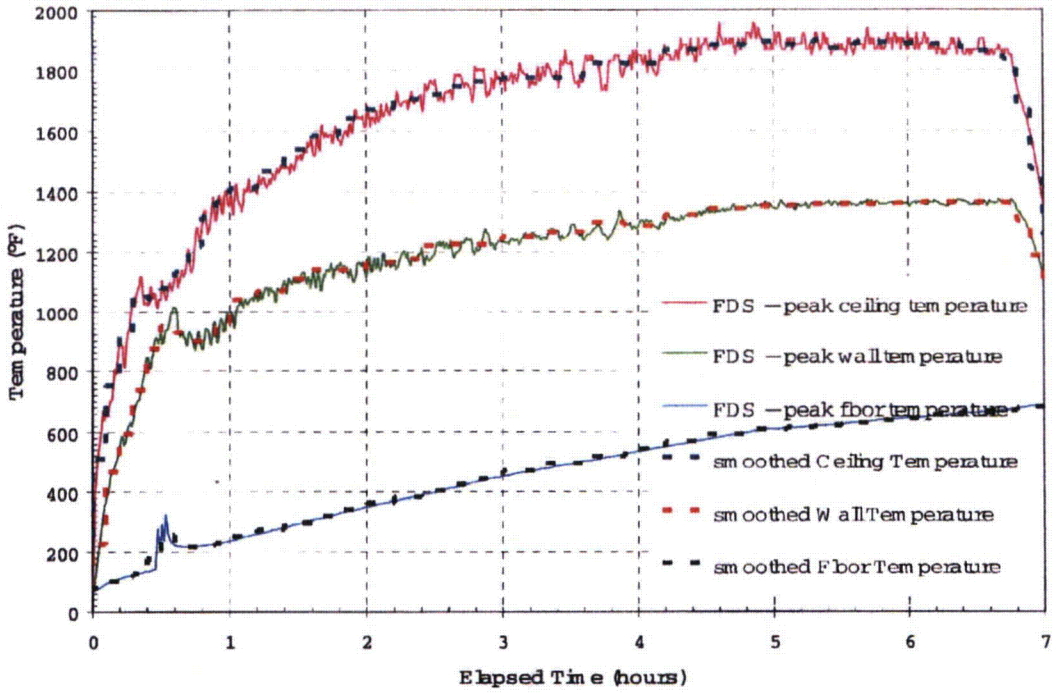

Figure D.1. Peak Surface Temperatures Calculated with FDS for Tunnel Ceiling, Wall, and Floor Regions at 20 meters from Fire Location during 7-hr Fire

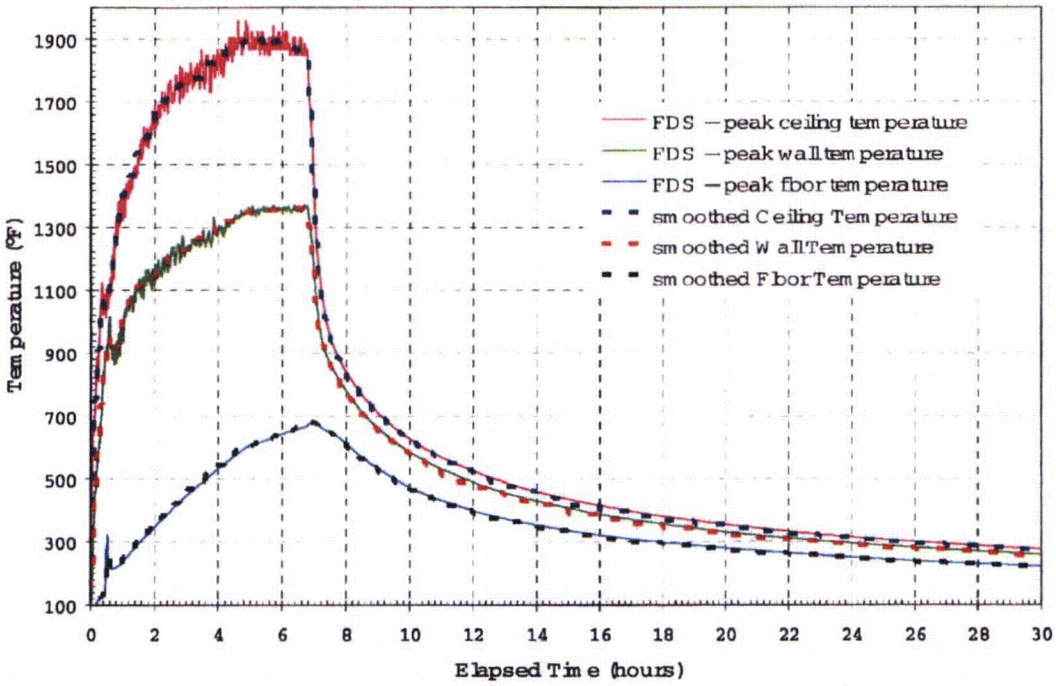

Figure D.2. Peak Surface Temperatures Calculated with FDS for Tunnel Ceiling, Wall, and Floor Regions at 20 meters from Fire Location during 7-hr Fire and 23-hr Cool Down

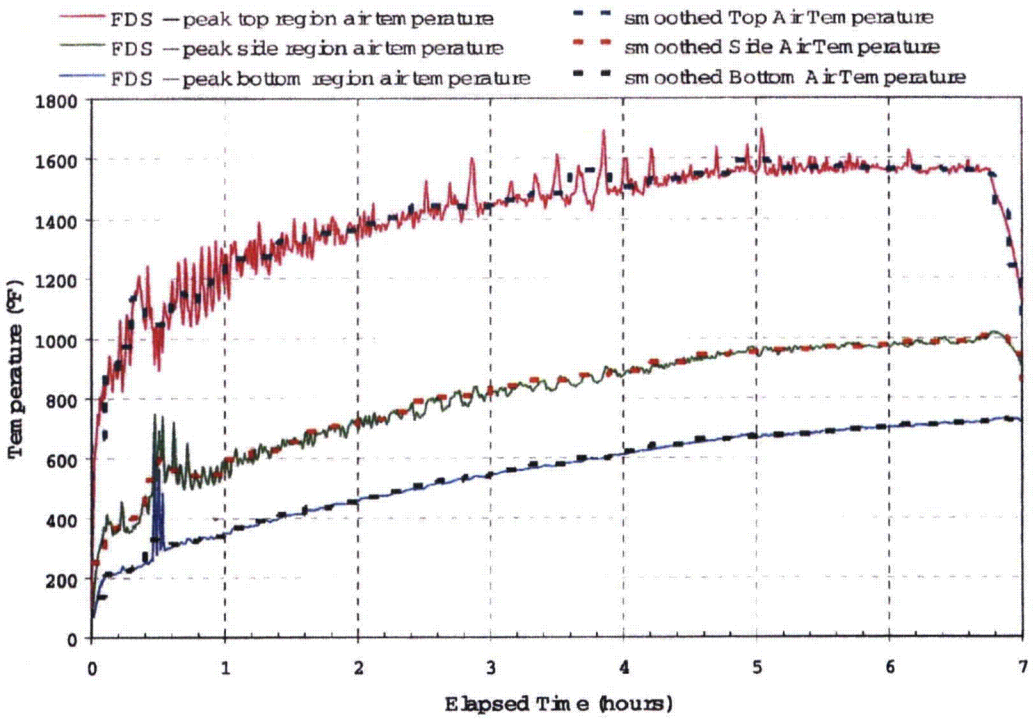

Figure D.3. Peak Air Temperatures Calculated with FDS for Top, Side, and Bottom Regions at 20 meters from Fire Location during 7-hr Fire

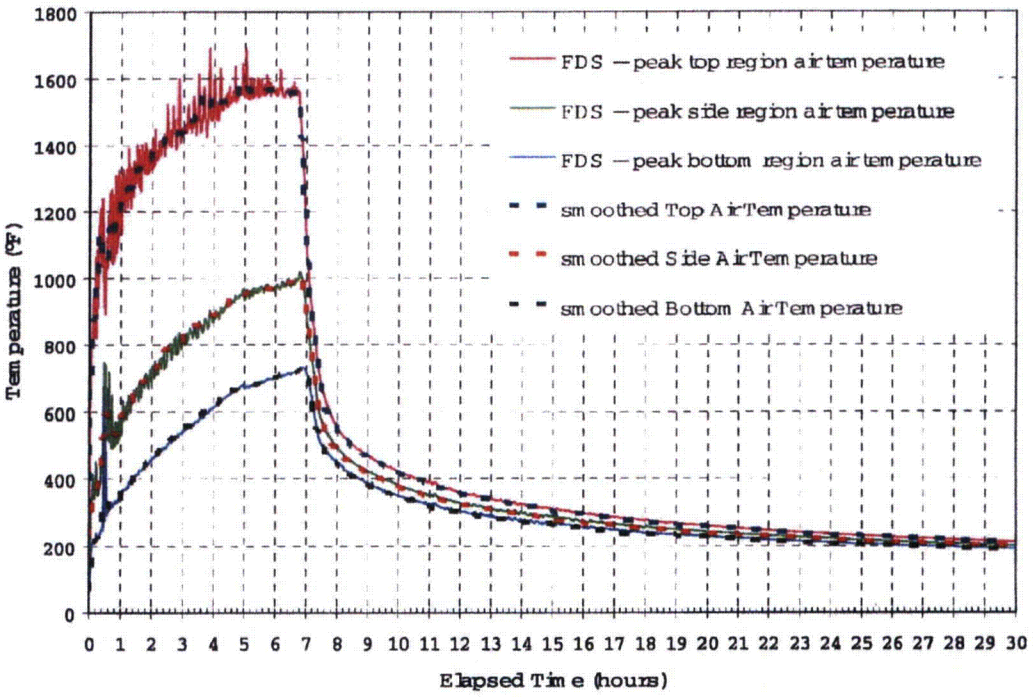

Figure D.4. Peak Air Temperatures Calculated with FDS for Top, Side, and Bottom Regions at 20 meters from Fire Location during 7-hr Fire and 23-hr Cool Down

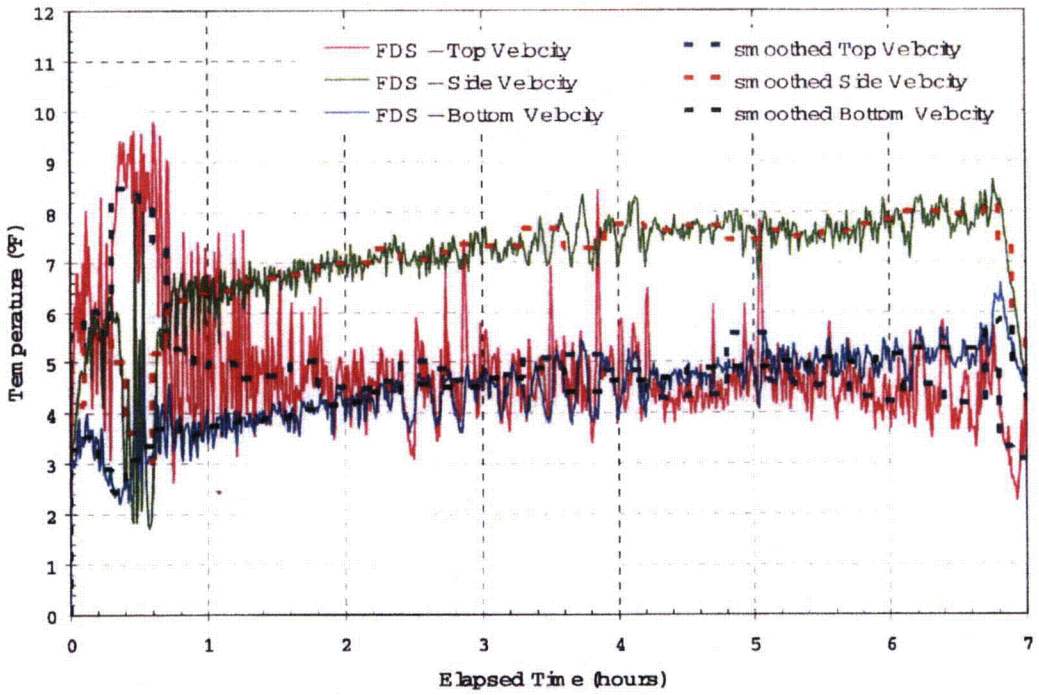

Figure D.5. Velocities at Peak Air Temperature Locations Calculated with FDS for Top, Side, and Bottom Regions at 20 meters from Fire Location during 7-hr Fire

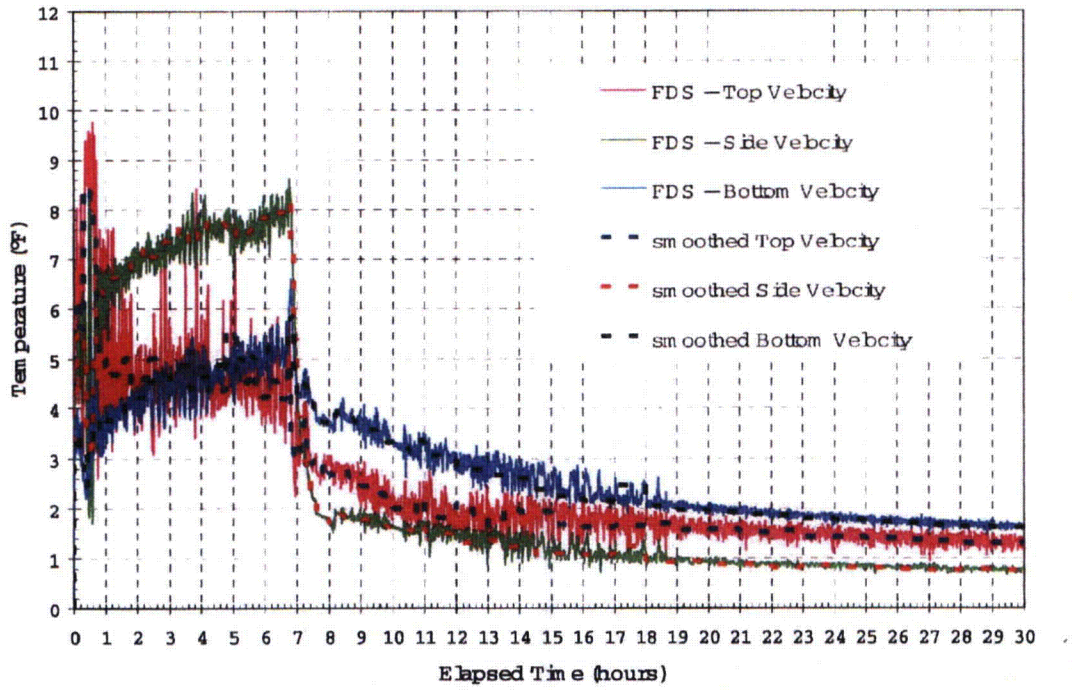

Figure D.6. Velocities at Peak Air Temperature Locations Calculated with FDS for Top, Side, and Bottom Regions at 20 meters from Fire during 7-hr Fire and 23-hr Cool Down

Appendix E

Blackbody Viewfactors for COBRA-SFS Model of TN-68 Package

```
C TUNNEL.1=TOP  TUNNEL.2=SIDE  TUNNEL.3=BOTTOM
Cnode_1      node_2      Area*e*Bij  $       Bij       Bji
 CASK.101,   TUNNEL.1,   137.54      $     0.79418,0.00045040
 CASK.101,   TUNNEL.2,   25.477      $     0.14711,7.5761e-005
 CASK.101,   TUNNEL.3,   6.3683      $    0.036772,2.1839e-005
 CASK.102,   TUNNEL.1,   67.819      $     0.39161,0.00022209
 CASK.102,   TUNNEL.2,   87.635      $     0.50603,0.00026060
 CASK.102,   TUNNEL.3,   13.723      $    0.079241,4.7061e-005
 CASK.103,   TUNNEL.1,   12.951      $    0.074781,4.2410e-005
 CASK.103,   TUNNEL.2,   90.996      $     0.52544,0.00027059
 CASK.103,   TUNNEL.3,   65.443      $     0.37789,0.00022443
 CASK.104,   TUNNEL.1,   6.2714      $    0.036213,2.0538e-005
 CASK.104,   TUNNEL.2,   31.022      $     0.17913,9.2251e-005
 CASK.104,   TUNNEL.3,   132.32      $     0.76404,0.00045376
 CASK.201,   TUNNEL.1,   138.22      $     0.79812,0.00045264
 CASK.201,   TUNNEL.2,   24.978      $     0.14423,7.4277e-005
 CASK.201,   TUNNEL.3,   6.3135      $    0.036456,2.1651e-005
 CASK.202,   TUNNEL.1,   68.135      $     0.39343,0.00022313
 CASK.202,   TUNNEL.2,   87.392      $     0.50463,0.00025988
 CASK.202,   TUNNEL.3,   13.599      $    0.078527,4.6637e-005
 CASK.203,   TUNNEL.1,   12.937      $    0.074702,4.2365e-005
 CASK.203,   TUNNEL.2,   90.689      $     0.52367,0.00026968
 CASK.203,   TUNNEL.3,   65.701      $     0.37938,0.00022531
 CASK.204,   TUNNEL.1,   6.1691      $    0.035622,2.0203e-005
 CASK.204,   TUNNEL.2,   31.104      $     0.17961,9.2494e-005
 CASK.204,   TUNNEL.3,   132.31      $     0.76399,0.00045373
 CASK.301,   TUNNEL.1,   137.98      $     0.79676,0.00045187
 CASK.301,   TUNNEL.2,   25.169      $     0.14533,7.4844e-005
 CASK.301,   TUNNEL.3,   6.3354      $    0.036583,2.1726e-005
 CASK.302,   TUNNEL.1,   68.192      $     0.39376,0.00022331
 CASK.302,   TUNNEL.2,   87.312      $     0.50417,0.00025964
 CASK.302,   TUNNEL.3,   13.687      $    0.079031,4.6936e-005
 CASK.303,   TUNNEL.1,   12.880      $    0.074375,4.2180e-005
 CASK.303,   TUNNEL.2,   91.267      $     0.52700,0.00027140
 CASK.303,   TUNNEL.3,   65.225      $     0.37663,0.00022368
 CASK.304,   TUNNEL.1,   6.1435      $    0.035475,2.0119e-005
 CASK.304,   TUNNEL.2,   31.213      $     0.18024,9.2819e-005
 CASK.304,   TUNNEL.3,   132.07      $     0.76261,0.00045291
 CASK.401,   TUNNEL.1,   138.03      $     0.79704,0.00045202
 CASK.401,   TUNNEL.2,   25.096      $     0.14491,7.4627e-005
 CASK.401,   TUNNEL.3,   6.3204      $    0.036496,2.1675e-005
 CASK.402,   TUNNEL.1,   68.295      $     0.39436,0.00022365
 CASK.402,   TUNNEL.2,   87.210      $     0.50358,0.00025934
 CASK.402,   TUNNEL.3,   13.632      $    0.078717,4.6750e-005
 CASK.403,   TUNNEL.1,   13.054      $    0.075376,4.2748e-005
 CASK.403,   TUNNEL.2,   90.720      $     0.52385,0.00026977
 CASK.403,   TUNNEL.3,   65.460      $     0.37799,0.00022448
 CASK.404,   TUNNEL.1,   6.0468      $    0.034916,1.9802e-005
 CASK.404,   TUNNEL.2,   30.945      $     0.17868,9.2020e-005
 CASK.404,   TUNNEL.3,   132.46      $     0.76484,0.00045424
 CASK.501,   TUNNEL.1,   138.12      $     0.79752,0.00045230
 CASK.501,   TUNNEL.2,   25.031      $     0.14454,7.4434e-005
 CASK.501,   TUNNEL.3,   6.3279      $    0.036539,2.1701e-005
 CASK.502,   TUNNEL.1,   68.608      $     0.39616,0.00022468
 CASK.502,   TUNNEL.2,   86.890      $     0.50173,0.00025838
 CASK.502,   TUNNEL.3,   13.693      $    0.079069,4.6959e-005
 CASK.503,   TUNNEL.1,   12.946      $    0.074757,4.2397e-005
 CASK.503,   TUNNEL.2,   91.115      $     0.52613,0.00027095
 CASK.503,   TUNNEL.3,   65.179      $     0.37636,0.00022352
 CASK.504,   TUNNEL.1,   5.9701      $    0.034474,1.9551e-005
 CASK.504,   TUNNEL.2,   30.931      $     0.17860,9.1979e-005
 CASK.504,   TUNNEL.3,   132.45      $     0.76480,0.00045422
 CASK.601,   TUNNEL.1,   138.18      $     0.79788,0.00045250
 CASK.601,   TUNNEL.2,   24.944      $     0.14403,7.4176e-005
 CASK.601,   TUNNEL.3,   6.2188      $    0.035909,2.1326e-005
 CASK.602,   TUNNEL.1,   68.688      $     0.39663,0.00022494
 CASK.602,   TUNNEL.2,   86.987      $     0.50229,0.00025867
 CASK.602,   TUNNEL.3,   13.491      $    0.077899,4.6264e-005
 CASK.603,   TUNNEL.1,   13.037      $    0.075278,4.2692e-005
 CASK.603,   TUNNEL.2,   91.088      $     0.52597,0.00027087
 CASK.603,   TUNNEL.3,   65.088      $     0.37584,0.00022321
 CASK.604,   TUNNEL.1,   5.9256      $    0.034216,1.9405e-005
 CASK.604,   TUNNEL.2,   31.061      $     0.17936,9.2367e-005
 CASK.604,   TUNNEL.3,   132.28      $     0.76385,0.00045365
 CASK.701,   TUNNEL.1,   138.29      $     0.79854,0.00045288
```

```
CASK.701,  TUNNEL.2,  24.847   $   0.14347,7.3886e-005
CASK.701,  TUNNEL.3,  6.2483   $   0.036080,2.1428e-005
CASK.702,  TUNNEL.1,  68.225   $   0.39395,0.00022342
CASK.702,  TUNNEL.2,  87.042   $   0.50261,0.00025884
CASK.702,  TUNNEL.3,  13.824   $   0.079826,4.7408e-005
CASK.703,  TUNNEL.1,  13.006   $   0.075103,4.2593e-005
CASK.703,  TUNNEL.2,  90.921   $   0.52501,0.00027037
CASK.703,  TUNNEL.3,  65.304   $   0.37709,0.00022395
CASK.704,  TUNNEL.1,  5.8582   $   0.033827,1.9184e-005
CASK.704,  TUNNEL.2,  31.026   $   0.17916,9.2263e-005
CASK.704,  TUNNEL.3,  132.40   $   0.76454,0.00045406
CASK.801,  TUNNEL.1,  138.10   $   0.79744,0.00045225
CASK.801,  TUNNEL.2,  25.102   $   0.14495,7.4647e-005
CASK.801,  TUNNEL.3,  6.2315   $   0.035983,2.1370e-005
CASK.802,  TUNNEL.1,  67.889   $   0.39201,0.00022232
CASK.802,  TUNNEL.2,  87.307   $   0.50414,0.00025963
CASK.802,  TUNNEL.3,  13.869   $   0.080083,4.7561e-005
CASK.803,  TUNNEL.1,  12.847   $   0.074182,4.2071e-005
CASK.803,  TUNNEL.2,  90.805   $   0.52434,0.00027003
CASK.803,  TUNNEL.3,  65.535   $   0.37842,0.00022474
CASK.804,  TUNNEL.1,  5.7617   $   0.033270,1.8868e-005
CASK.804,  TUNNEL.2,  31.064   $   0.17937,9.2374e-005
CASK.804,  TUNNEL.3,  132.36   $   0.76430,0.00045391
CASK.901,  TUNNEL.1,  138.13   $   0.79764,0.00045236
CASK.901,  TUNNEL.2,  25.128   $   0.14510,7.4724e-005
CASK.901,  TUNNEL.3,  6.2207   $   0.035921,2.1333e-005
CASK.902,  TUNNEL.1,  68.091   $   0.39318,0.00022298
CASK.902,  TUNNEL.2,  87.277   $   0.50396,0.00025953
CASK.902,  TUNNEL.3,  13.700   $   0.079107,4.6981e-005
CASK.903,  TUNNEL.1,  12.952   $   0.074789,4.2415e-005
CASK.903,  TUNNEL.2,  90.982   $   0.52536,0.00027055
CASK.903,  TUNNEL.3,  65.132   $   0.37609,0.00022336
CASK.904,  TUNNEL.1,  5.7522   $   0.033215,1.8837e-005
CASK.904,  TUNNEL.2,  31.124   $   0.17972,9.2553e-005
CASK.904,  TUNNEL.3,  132.31   $   0.76400,0.00045374
CASK.1001, TUNNEL.1,  137.84   $   0.79593,0.00045139
CASK.1001, TUNNEL.2,  25.412   $   0.14674,7.5569e-005
CASK.1001, TUNNEL.3,  6.2311   $   0.035981,2.1369e-005
CASK.1002, TUNNEL.1,  68.564   $   0.39591,0.00022453
CASK.1002, TUNNEL.2,  86.856   $   0.50153,0.00025828
CASK.1002, TUNNEL.3,  13.655   $   0.078849,4.6828e-005
CASK.1003, TUNNEL.1,  12.716   $   0.073426,4.1642e-005
CASK.1003, TUNNEL.2,  90.924   $   0.52502,0.00027038
CASK.1003, TUNNEL.3,  65.500   $   0.37822,0.00022462
CASK.1004, TUNNEL.1,  5.6573   $   0.032667,1.8526e-005
CASK.1004, TUNNEL.2,  31.197   $   0.18014,9.2770e-005
CASK.1004, TUNNEL.3,  132.27   $   0.76378,0.00045361
CASK.1101, TUNNEL.1,  138.17   $   0.79782,0.00045247
CASK.1101, TUNNEL.2,  25.006   $   0.14440,7.4362e-005
CASK.1101, TUNNEL.3,  6.1872   $   0.035727,2.1218e-005
CASK.1102, TUNNEL.1,  68.446   $   0.39523,0.00022415
CASK.1102, TUNNEL.2,  87.049   $   0.50265,0.00025886
CASK.1102, TUNNEL.3,  13.505   $   0.077980,4.6312e-005
CASK.1103, TUNNEL.1,  12.985   $   0.074982,4.2524e-005
CASK.1103, TUNNEL.2,  91.145   $   0.52630,0.00027104
CASK.1103, TUNNEL.3,  65.061   $   0.37568,0.00022312
CASK.1104, TUNNEL.1,  5.6898   $   0.032855,1.8633e-005
CASK.1104, TUNNEL.2,  30.943   $   0.17868,9.2016e-005
CASK.1104, TUNNEL.3,  132.40   $   0.76453,0.00045405
CASK.1201, TUNNEL.1,  137.88   $   0.79616,0.00045153
CASK.1201, TUNNEL.2,  25.412   $   0.14674,7.5567e-005
CASK.1201, TUNNEL.3,  6.1750   $   0.035657,2.1176e-005
CASK.1202, TUNNEL.1,  67.908   $   0.39212,0.00022238
CASK.1202, TUNNEL.2,  87.439   $   0.50490,0.00026002
CASK.1202, TUNNEL.3,  13.717   $   0.079208,4.7041e-005
CASK.1203, TUNNEL.1,  12.998   $   0.075055,4.2566e-005
CASK.1203, TUNNEL.2,  90.706   $   0.52377,0.00026973
CASK.1203, TUNNEL.3,  65.409   $   0.37769,0.00022431
CASK.1204, TUNNEL.1,  5.5919   $   0.032289,1.8312e-005
CASK.1204, TUNNEL.2,  31.129   $   0.17975,9.2567e-005
CASK.1204, TUNNEL.3,  132.27   $   0.76380,0.00045362
CASK.1301, TUNNEL.1,  138.25   $   0.79830,0.00045274
CASK.1301, TUNNEL.2,  24.993   $   0.14432,7.4320e-005
CASK.1301, TUNNEL.3,  6.1782   $   0.035675,2.1187e-005
CASK.1302, TUNNEL.1,  68.155   $   0.39355,0.00022319
```

```
CASK.1302,  TUNNEL.2,  87.155    $    0.50326,0.00025917
CASK.1302,  TUNNEL.3,  13.671    $   0.078943,4.6884e-005
CASK.1303,  TUNNEL.1,  12.737    $   0.073546,4.1710e-005
CASK.1303,  TUNNEL.2,  91.130    $    0.52622,0.00027099
CASK.1303,  TUNNEL.3,  65.245    $    0.37674,0.00022375
CASK.1304,  TUNNEL.1,  5.6600    $   0.032683,1.8535e-005
CASK.1304,  TUNNEL.2,  31.047    $    0.17928,9.2325e-005
CASK.1304,  TUNNEL.3,  132.30    $    0.76396,0.00045372
CASK.1401,  TUNNEL.1,  138.04    $    0.79707,0.00045204
CASK.1401,  TUNNEL.2,  25.121    $    0.14506,7.4703e-005
CASK.1401,  TUNNEL.3,  6.2019    $   0.035812,2.1269e-005
CASK.1402,  TUNNEL.1,  68.195    $    0.39378,0.00022332
CASK.1402,  TUNNEL.2,  87.073    $    0.50279,0.00025893
CASK.1402,  TUNNEL.3,  13.807    $   0.079729,4.7351e-005
CASK.1403,  TUNNEL.1,  12.669    $   0.073153,4.1487e-005
CASK.1403,  TUNNEL.2,  91.365    $    0.52757,0.00027169
CASK.1403,  TUNNEL.3,  65.069    $    0.37573,0.00022314
CASK.1404,  TUNNEL.1,  5.5888    $   0.032272,1.8302e-005
CASK.1404,  TUNNEL.2,  31.163    $    0.17994,9.2668e-005
CASK.1404,  TUNNEL.3,  132.22    $    0.76345,0.00045341
CASK.1501,  TUNNEL.1,  138.17    $    0.79785,0.00045249
CASK.1501,  TUNNEL.2,  25.075    $    0.14479,7.4565e-005
CASK.1501,  TUNNEL.3,  6.1911    $   0.035749,2.1231e-005
CASK.1502,  TUNNEL.1,  68.139    $    0.39346,0.00022314
CASK.1502,  TUNNEL.2,  87.197    $    0.50350,0.00025930
CASK.1502,  TUNNEL.3,  13.646    $   0.078797,4.6798e-005
CASK.1503,  TUNNEL.1,  12.784    $   0.073818,4.1864e-005
CASK.1503,  TUNNEL.2,  91.009    $    0.52552,0.00027063
CASK.1503,  TUNNEL.3,  65.230    $    0.37666,0.00022370
CASK.1504,  TUNNEL.1,  5.6144    $   0.032419,1.8386e-005
CASK.1504,  TUNNEL.2,  31.011    $    0.17907,9.2217e-005
CASK.1504,  TUNNEL.3,  132.37    $    0.76434,0.00045394
CASK.1601,  TUNNEL.1,  138.38    $    0.79906,0.00045317
CASK.1601,  TUNNEL.2,  24.861    $    0.14355,7.3928e-005
CASK.1601,  TUNNEL.3,  6.1468    $   0.035493,2.1079e-005
CASK.1602,  TUNNEL.1,  68.267    $    0.39420,0.00022356
CASK.1602,  TUNNEL.2,  87.153    $    0.50325,0.00025917
CASK.1602,  TUNNEL.3,  13.587    $   0.078457,4.6595e-005
CASK.1603,  TUNNEL.1,  12.646    $   0.073025,4.1414e-005
CASK.1603,  TUNNEL.2,  90.521    $    0.52270,0.00026918
CASK.1603,  TUNNEL.3,  65.886    $    0.38045,0.00022595
CASK.1604,  TUNNEL.1,  5.5843    $   0.032245,1.8287e-005
CASK.1604,  TUNNEL.2,  30.824    $    0.17799,9.1661e-005
CASK.1604,  TUNNEL.3,  132.56    $    0.76547,0.00045461
CASK.1701,  TUNNEL.1,  137.89    $    0.79623,0.00045156
CASK.1701,  TUNNEL.2,  25.339    $    0.14632,7.5351e-005
CASK.1701,  TUNNEL.3,  6.1499    $   0.035511,2.1090e-005
CASK.1702,  TUNNEL.1,  68.793    $    0.39723,0.00022528
CASK.1702,  TUNNEL.2,  86.707    $    0.50067,0.00025784
CASK.1702,  TUNNEL.3,  13.529    $   0.078123,4.6397e-005
CASK.1703,  TUNNEL.1,  12.704    $   0.073359,4.1604e-005
CASK.1703,  TUNNEL.2,  91.173    $    0.52646,0.00027112
CASK.1703,  TUNNEL.3,  65.193    $    0.37645,0.00022357
CASK.1704,  TUNNEL.1,  5.5697    $   0.032161,1.8240e-005
CASK.1704,  TUNNEL.2,  31.366    $    0.18112,9.3274e-005
CASK.1704,  TUNNEL.3,  132.07    $    0.76260,0.00045290
CASK.1801,  TUNNEL.1,  138.30    $    0.79856,0.00045289
CASK.1801,  TUNNEL.2,  24.981    $    0.14425,7.4286e-005
CASK.1801,  TUNNEL.3,  6.1334    $   0.035416,2.1034e-005
CASK.1802,  TUNNEL.1,  68.068    $    0.39304,0.00022291
CASK.1802,  TUNNEL.2,  87.271    $    0.50393,0.00025952
CASK.1802,  TUNNEL.3,  13.649    $   0.078815,4.6808e-005
CASK.1803,  TUNNEL.1,  12.694    $   0.073297,4.1569e-005
CASK.1803,  TUNNEL.2,  91.352    $    0.52750,0.00027165
CASK.1803,  TUNNEL.3,  65.097    $    0.37589,0.00022324
CASK.1804,  TUNNEL.1,  5.5500    $   0.032047,1.8175e-005
CASK.1804,  TUNNEL.2,  31.344    $    0.18099,9.3208e-005
CASK.1804,  TUNNEL.3,  132.06    $    0.76255,0.00045287
CASK.1901,  TUNNEL.1,  138.28    $    0.79848,0.00045284
CASK.1901,  TUNNEL.2,  24.841    $    0.14344,7.3870e-005
CASK.1901,  TUNNEL.3,  6.1732    $   0.035646,2.1170e-005
CASK.1902,  TUNNEL.1,  68.778    $    0.39714,0.00022523
CASK.1902,  TUNNEL.2,  86.557    $    0.49981,0.00025739
CASK.1902,  TUNNEL.3,  13.637    $   0.078746,4.6767e-005
CASK.1903,  TUNNEL.1,  12.841    $   0.074146,4.2051e-005
```

```
CASK.1903,  TUNNEL.2,  91.151   $   0.52633,0.00027105
CASK.1903,  TUNNEL.3,  65.209   $   0.37654,0.00022362
CASK.1904,  TUNNEL.1,  5.6276   $  0.032496,1.8429e-005
CASK.1904,  TUNNEL.2,  30.798   $   0.17784,9.1584e-005
CASK.1904,  TUNNEL.3,  132.57   $   0.76549,0.00045462
CASK.2001,  TUNNEL.1,  138.26   $   0.79837,0.00045278
CASK.2001,  TUNNEL.2,  24.969   $   0.14418,7.4252e-005
CASK.2001,  TUNNEL.3,  6.1633   $  0.035589,2.1136e-005
CASK.2002,  TUNNEL.1,  67.893   $   0.39204,0.00022234
CASK.2002,  TUNNEL.2,  87.430   $   0.50485,0.00025999
CASK.2002,  TUNNEL.3,  13.778   $  0.079561,4.7251e-005
CASK.2003,  TUNNEL.1,  12.702   $  0.073347,4.1597e-005
CASK.2003,  TUNNEL.2,  90.326   $   0.52157,0.00026860
CASK.2003,  TUNNEL.3,  66.063   $   0.38147,0.00022655
CASK.2004,  TUNNEL.1,  5.6088   $  0.032387,1.8368e-005
CASK.2004,  TUNNEL.2,  30.836   $   0.17806,9.1696e-005
CASK.2004,  TUNNEL.3,  132.54   $   0.76530,0.00045451
CASK.2101,  TUNNEL.1,  137.99   $   0.79682,0.00045190
CASK.2101,  TUNNEL.2,  25.223   $   0.14564,7.5005e-005
CASK.2101,  TUNNEL.3,  6.2208   $  0.035921,2.1333e-005
CASK.2102,  TUNNEL.1,  68.122   $   0.39336,0.00022308
CASK.2102,  TUNNEL.2,  87.248   $   0.50380,0.00025945
CASK.2102,  TUNNEL.3,  13.695   $  0.079082,4.6967e-005
CASK.2103,  TUNNEL.1,  12.623   $  0.072889,4.1338e-005
CASK.2103,  TUNNEL.2,  91.084   $   0.52595,0.00027086
CASK.2103,  TUNNEL.3,  65.444   $   0.37790,0.00022443
CASK.2104,  TUNNEL.1,  5.6251   $  0.032481,1.8421e-005
CASK.2104,  TUNNEL.2,  30.935   $   0.17863,9.1992e-005
CASK.2104,  TUNNEL.3,  132.48   $   0.76497,0.00045431
CASK.2201,  TUNNEL.1,  138.00   $   0.79686,0.00045192
CASK.2201,  TUNNEL.2,  25.240   $   0.14575,7.5057e-005
CASK.2201,  TUNNEL.3,  6.1738   $  0.035650,2.1172e-005
CASK.2202,  TUNNEL.1,  68.741   $   0.39693,0.00022511
CASK.2202,  TUNNEL.2,  86.917   $   0.50189,0.00025847
CASK.2202,  TUNNEL.3,  13.480   $  0.077838,4.6228e-005
CASK.2203,  TUNNEL.1,  12.900   $  0.074490,4.2246e-005
CASK.2203,  TUNNEL.2,  91.269   $   0.52702,0.00027141
CASK.2203,  TUNNEL.3,  64.953   $   0.37506,0.00022275
CASK.2204,  TUNNEL.1,  5.6790   $  0.032793,1.8598e-005
CASK.2204,  TUNNEL.2,  30.883   $   0.17833,9.1837e-005
CASK.2204,  TUNNEL.3,  132.53   $   0.76527,0.00045449
CASK.2301,  TUNNEL.1,  137.99   $   0.79683,0.00045190
CASK.2301,  TUNNEL.2,  25.190   $   0.14546,7.4909e-005
CASK.2301,  TUNNEL.3,  6.2267   $  0.035955,2.1354e-005
CASK.2302,  TUNNEL.1,  68.414   $   0.39504,0.00022404
CASK.2302,  TUNNEL.2,  86.942   $   0.50203,0.00025854
CASK.2302,  TUNNEL.3,  13.674   $  0.078957,4.6892e-005
CASK.2303,  TUNNEL.1,  12.930   $  0.074664,4.2344e-005
CASK.2303,  TUNNEL.2,  90.672   $   0.52357,0.00026963
CASK.2303,  TUNNEL.3,  65.491   $   0.37816,0.00022459
CASK.2304,  TUNNEL.1,  5.6849   $  0.032826,1.8617e-005
CASK.2304,  TUNNEL.2,  31.044   $   0.17926,9.2315e-005
CASK.2304,  TUNNEL.3,  132.32   $   0.76406,0.00045377
CASK.2401,  TUNNEL.1,  137.91   $   0.79636,0.00045164
CASK.2401,  TUNNEL.2,  25.207   $   0.14555,7.4957e-005
CASK.2401,  TUNNEL.3,  6.2003   $  0.035803,2.1263e-005
CASK.2402,  TUNNEL.1,  68.065   $   0.39303,0.00022290
CASK.2402,  TUNNEL.2,  87.281   $   0.50399,0.00025955
CASK.2402,  TUNNEL.3,  13.655   $  0.078847,4.6827e-005
CASK.2403,  TUNNEL.1,  12.813   $  0.073989,4.1961e-005
CASK.2403,  TUNNEL.2,  90.843   $   0.52456,0.00027014
CASK.2403,  TUNNEL.3,  65.521   $   0.37834,0.00022470
CASK.2404,  TUNNEL.1,  5.7547   $  0.033229,1.8845e-005
CASK.2404,  TUNNEL.2,  31.095   $   0.17955,9.2466e-005
CASK.2404,  TUNNEL.3,  132.32   $   0.76405,0.00045377
CASK.2501,  TUNNEL.1,  138.26   $   0.79836,0.00045277
CASK.2501,  TUNNEL.2,  25.000   $   0.14436,7.4342e-005
CASK.2501,  TUNNEL.3,  6.1776   $  0.035672,2.1185e-005
CASK.2502,  TUNNEL.1,  68.473   $   0.39539,0.00022424
CASK.2502,  TUNNEL.2,  87.067   $   0.50275,0.00025891
CASK.2502,  TUNNEL.3,  13.573   $  0.078375,4.6547e-005
CASK.2503,  TUNNEL.1,  12.768   $  0.073729,4.1814e-005
CASK.2503,  TUNNEL.2,  91.066   $   0.52584,0.00027080
CASK.2503,  TUNNEL.3,  65.294   $   0.37703,0.00022391
CASK.2504,  TUNNEL.1,  5.8355   $  0.033696,1.9110e-005
```

```
CASK.2504,  TUNNEL.2,  30.930    $    0.17860,9.1976e-005
CASK.2504,  TUNNEL.3,  132.43    $    0.76468,0.00045414
CASK.2601,  TUNNEL.1,  138.10    $    0.79746,0.00045226
CASK.2601,  TUNNEL.2,  25.102    $    0.14495,7.4647e-005
CASK.2601,  TUNNEL.3,  6.2378    $   0.036019,2.1392e-005
CASK.2602,  TUNNEL.1,  68.554    $    0.39585,0.00022450
CASK.2602,  TUNNEL.2,  86.943    $    0.50203,0.00025854
CASK.2602,  TUNNEL.3,  13.613    $   0.078605,4.6684e-005
CASK.2603,  TUNNEL.1,  12.843    $   0.074160,4.2058e-005
CASK.2603,  TUNNEL.2,  91.332    $    0.52738,0.00027160
CASK.2603,  TUNNEL.3,  64.991    $    0.37528,0.00022288
CASK.2604,  TUNNEL.1,  5.8796    $   0.033951,1.9254e-005
CASK.2604,  TUNNEL.2,  31.149    $    0.17987,9.2628e-005
CASK.2604,  TUNNEL.3,  132.23    $    0.76355,0.00045347
CASK.2701,  TUNNEL.1,  138.10    $    0.79741,0.00045224
CASK.2701,  TUNNEL.2,  25.040    $    0.14459,7.4462e-005
CASK.2701,  TUNNEL.3,  6.3016    $   0.036387,2.1610e-005
CASK.2702,  TUNNEL.1,  68.016    $    0.39275,0.00022274
CASK.2702,  TUNNEL.2,  87.294    $    0.50407,0.00025959
CASK.2702,  TUNNEL.3,  13.821    $   0.079805,4.7396e-005
CASK.2703,  TUNNEL.1,  12.778    $   0.073785,4.1846e-005
CASK.2703,  TUNNEL.2,  90.618    $    0.52326,0.00026947
CASK.2703,  TUNNEL.3,  65.768    $    0.37977,0.00022554
CASK.2704,  TUNNEL.1,  5.8947    $   0.034038,1.9304e-005
CASK.2704,  TUNNEL.2,  31.135    $    0.17978,9.2585e-005
CASK.2704,  TUNNEL.3,  132.22    $    0.76350,0.00045344
CASK.2801,  TUNNEL.1,  137.92    $    0.79641,0.00045167
CASK.2801,  TUNNEL.2,  25.255    $    0.14583,7.5100e-005
CASK.2801,  TUNNEL.3,  6.2785    $   0.036254,2.1531e-005
CASK.2802,  TUNNEL.1,  68.305    $    0.39442,0.00022369
CASK.2802,  TUNNEL.2,  87.253    $    0.50383,0.00025946
CASK.2802,  TUNNEL.3,  13.602    $   0.078545,4.6648e-005
CASK.2803,  TUNNEL.1,  12.785    $   0.073827,4.1869e-005
CASK.2803,  TUNNEL.2,  91.110    $    0.52610,0.00027094
CASK.2803,  TUNNEL.3,  65.358    $    0.37740,0.00022414
CASK.2804,  TUNNEL.1,  6.0104    $   0.034706,1.9683e-005
CASK.2804,  TUNNEL.2,  31.037    $    0.17922,9.2294e-005
CASK.2804,  TUNNEL.3,  132.37    $    0.76435,0.00045394
CASK.2901,  TUNNEL.1,  137.95    $    0.79655,0.00045175
CASK.2901,  TUNNEL.2,  25.208    $    0.14556,7.4961e-005
CASK.2901,  TUNNEL.3,  6.3047    $   0.036405,2.1621e-005
CASK.2902,  TUNNEL.1,  68.094    $    0.39320,0.00022299
CASK.2902,  TUNNEL.2,  87.286    $    0.50402,0.00025956
CASK.2902,  TUNNEL.3,  13.756    $   0.079430,4.7173e-005
CASK.2903,  TUNNEL.1,  12.735    $   0.073535,4.1704e-005
CASK.2903,  TUNNEL.2,  91.049    $    0.52575,0.00027075
CASK.2903,  TUNNEL.3,  65.491    $    0.37817,0.00022459
CASK.2904,  TUNNEL.1,  6.0330    $   0.034837,1.9757e-005
CASK.2904,  TUNNEL.2,  31.507    $    0.18193,9.3691e-005
CASK.2904,  TUNNEL.3,  131.85    $    0.76133,0.00045215
CASK.3001,  TUNNEL.1,  137.97    $    0.79670,0.00045183
CASK.3001,  TUNNEL.2,  25.049    $    0.14464,7.4489e-005
CASK.3001,  TUNNEL.3,  6.3339    $   0.036574,2.1721e-005
CASK.3002,  TUNNEL.1,  68.734    $    0.39689,0.00022509
CASK.3002,  TUNNEL.2,  86.655    $    0.50038,0.00025769
CASK.3002,  TUNNEL.3,  13.815    $   0.079771,4.7376e-005
CASK.3003,  TUNNEL.1,  12.791    $   0.073857,4.1886e-005
CASK.3003,  TUNNEL.2,  91.080    $    0.52592,0.00027084
CASK.3003,  TUNNEL.3,  65.432    $    0.37783,0.00022439
CASK.3004,  TUNNEL.1,  6.1398    $   0.035453,2.0106e-005
CASK.3004,  TUNNEL.2,  31.115    $    0.17967,9.2525e-005
CASK.3004,  TUNNEL.3,  132.27    $    0.76378,0.00045361
CASK.3101,  TUNNEL.1,  137.70    $    0.79510,0.00045093
CASK.3101,  TUNNEL.2,  25.393    $    0.14663,7.5511e-005
CASK.3101,  TUNNEL.3,  6.3698    $   0.036781,2.1844e-005
CASK.3102,  TUNNEL.1,  68.267    $    0.39420,0.00022356
CASK.3102,  TUNNEL.2,  87.177    $    0.50339,0.00025924
CASK.3102,  TUNNEL.3,  13.703    $   0.079126,4.6993e-005
CASK.3103,  TUNNEL.1,  12.902    $   0.074502,4.2252e-005
CASK.3103,  TUNNEL.2,  91.407    $    0.52781,0.00027182
CASK.3103,  TUNNEL.3,  65.078    $    0.37578,0.00022317
CASK.3104,  TUNNEL.1,  6.2118    $   0.035869,2.0342e-005
CASK.3104,  TUNNEL.2,  30.914    $    0.17851,9.1928e-005
CASK.3104,  TUNNEL.3,  132.43    $    0.76470,0.00045415
CASK.3201,  TUNNEL.1,  138.23    $    0.79819,0.00045268
```

```
CASK.3201,  TUNNEL.2,  24.820    $    0.14332,7.3808e-005
CASK.3201,  TUNNEL.3,  6.3863    $   0.036877,2.1901e-005
CASK.3202,  TUNNEL.1,  67.949    $    0.39236,0.00022252
CASK.3202,  TUNNEL.2,  87.413    $    0.50475,0.00025994
CASK.3202,  TUNNEL.3,  13.866    $   0.080068,4.7552e-005
CASK.3203,  TUNNEL.1,  13.070    $   0.075471,4.2802e-005
CASK.3203,  TUNNEL.2,  90.901    $    0.52489,0.00027031
CASK.3203,  TUNNEL.3,  65.388    $    0.37757,0.00022424
CASK.3204,  TUNNEL.1,  6.2751    $   0.036235,2.0550e-005
CASK.3204,  TUNNEL.2,  31.217    $    0.18026,9.2829e-005
CASK.3204,  TUNNEL.3,  132.12    $    0.76292,0.00045309
```

Appendix F

HOLTEC HI-STAR 100 Component Temperature Distributions

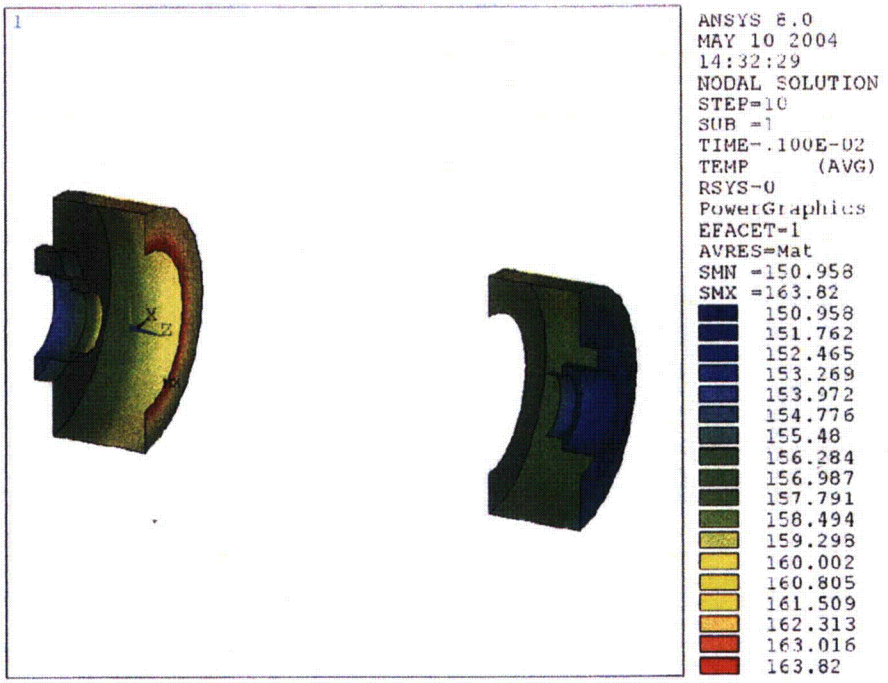

Figure F.1. Impact Limiter Skin Temperature Distribution - Normal Transport Conditions.

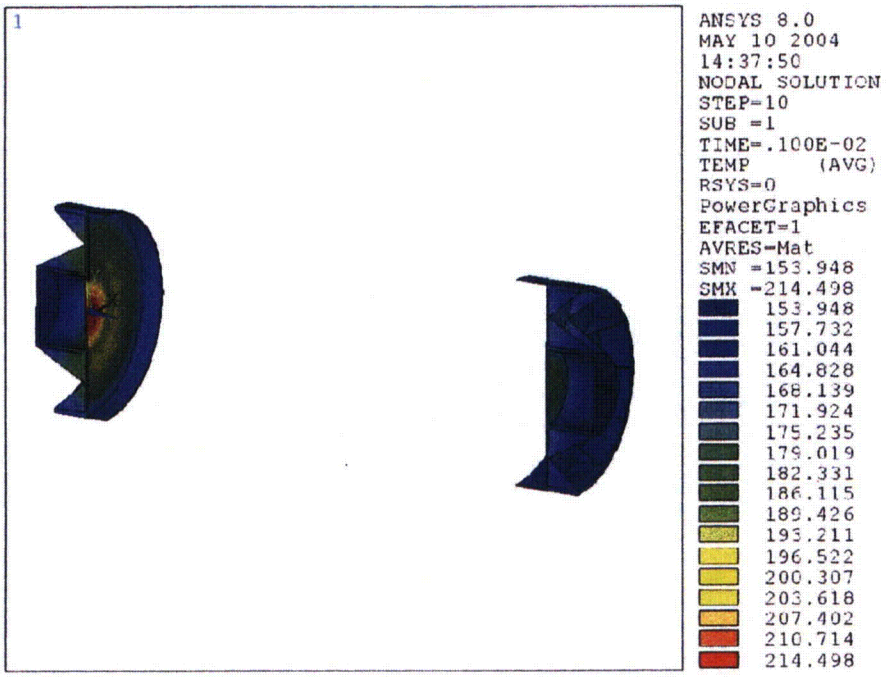

Figure F.2. Impact Limiter Structure Temperature Distribution - Normal Transport Conditions.

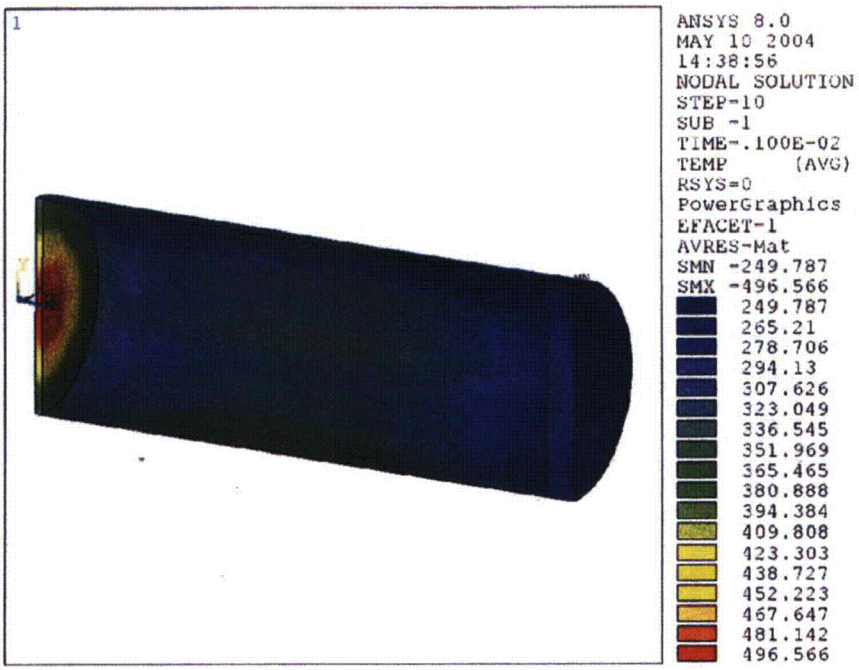

Figure F.3. Canister Shell Temperature Distribution - Normal Transport Conditions.

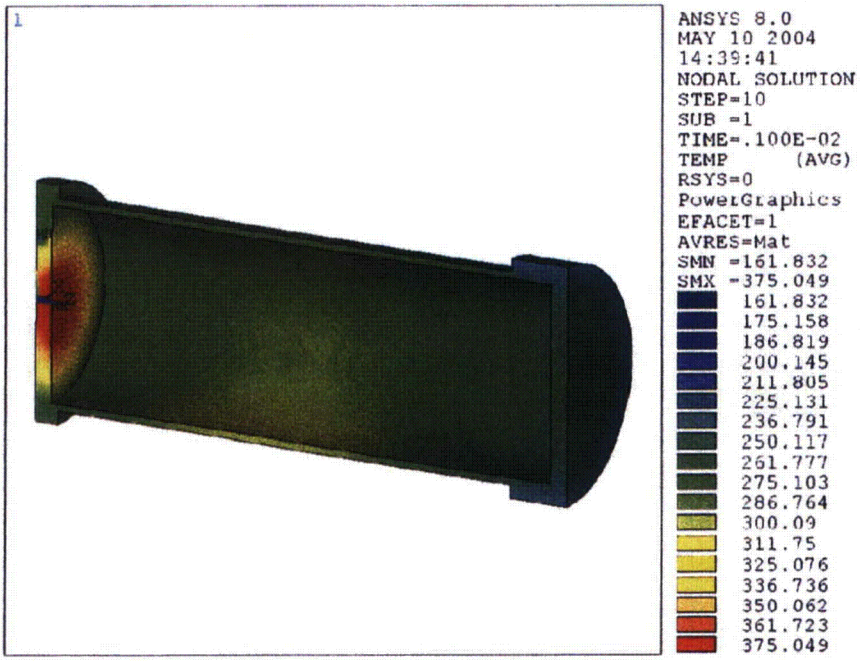

Figure F.4. Cask Inner Shell (Primary Containment Boundary) Temperature Distribution - Normal Transport Conditions.

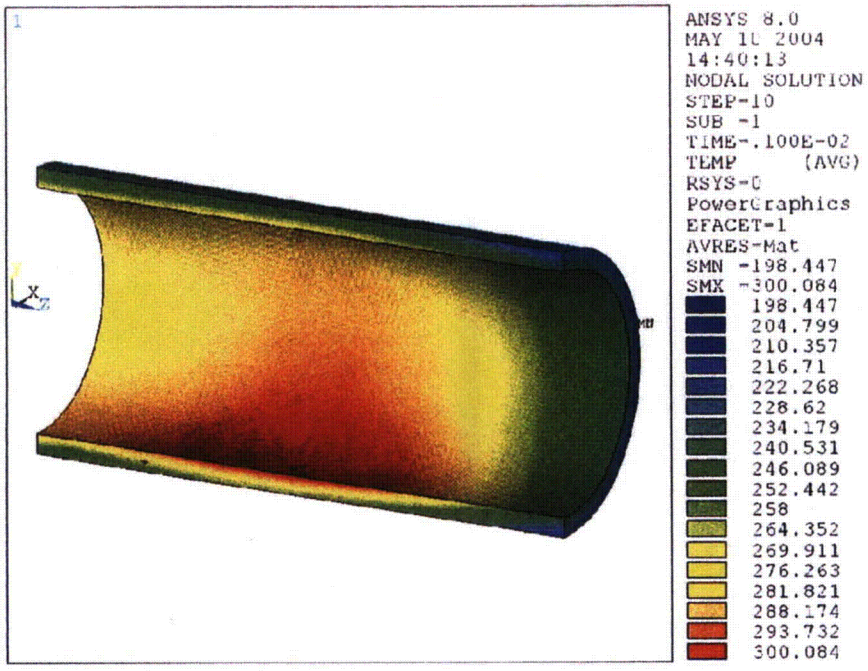

Figure F.5. Gamma Shield Temperature Distribution - Normal Transport Conditions.

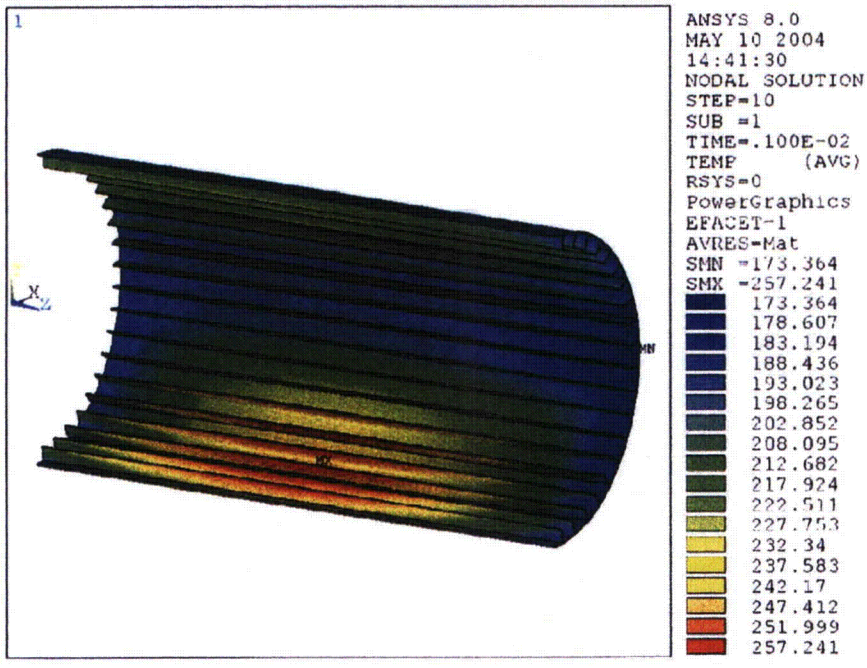

Figure F.6. Fin Structure Temperature Distribution - Normal Transport Conditions.

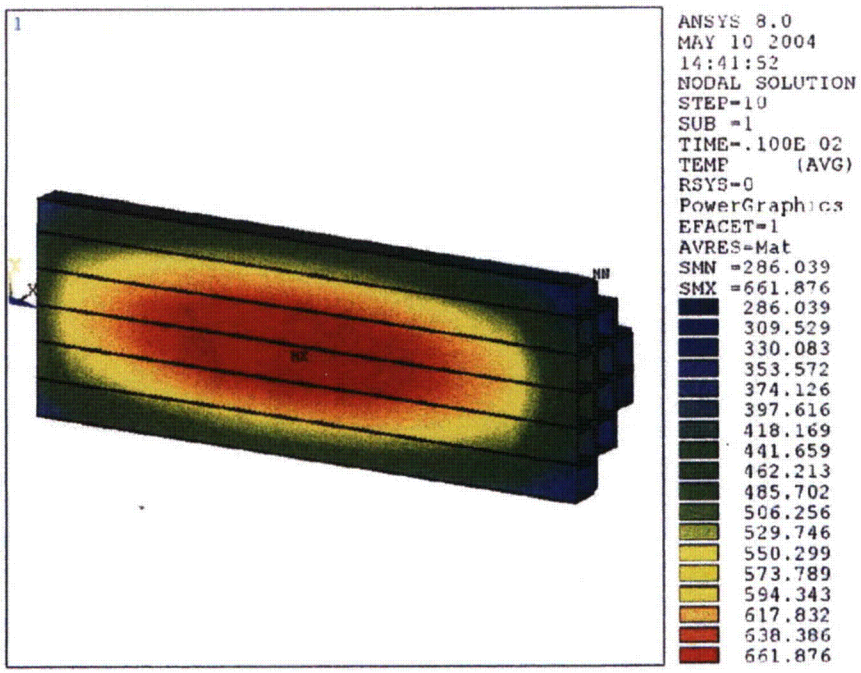

Figure F.7. Basket Axial Temperature Distribution - Normal Transport Conditions.

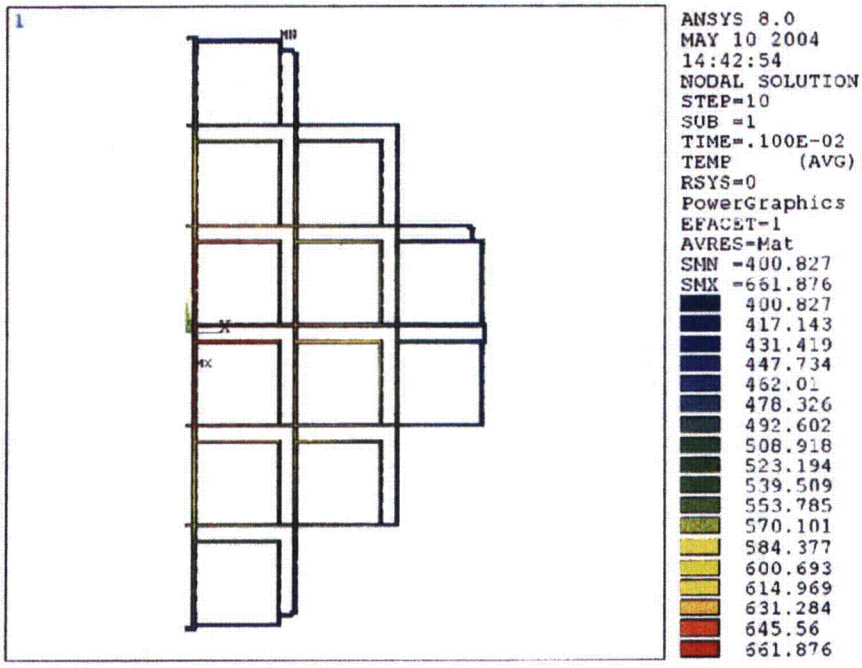

Figure F.8. Basket Radial Temperature Distribution - Normal Transport Conditions.

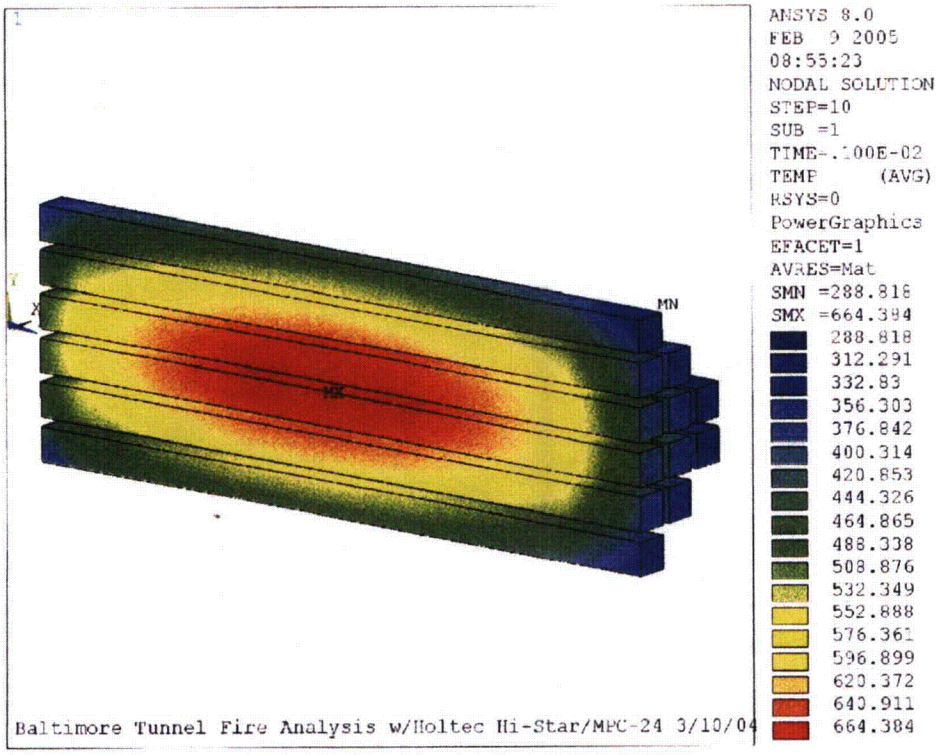

Figure F.9. Spent Fuel Axial Temperature Distribution - Normal Transport Conditions.

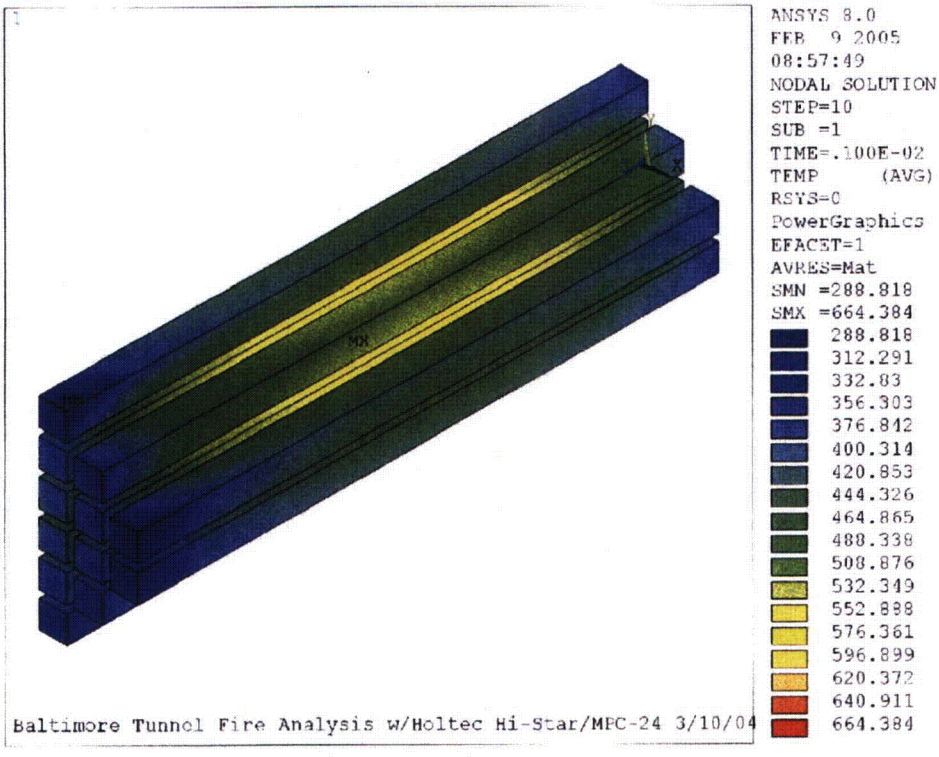

Figure F.10. Spent Fuel Axial Temperature Distribution - Normal Transport Conditions.

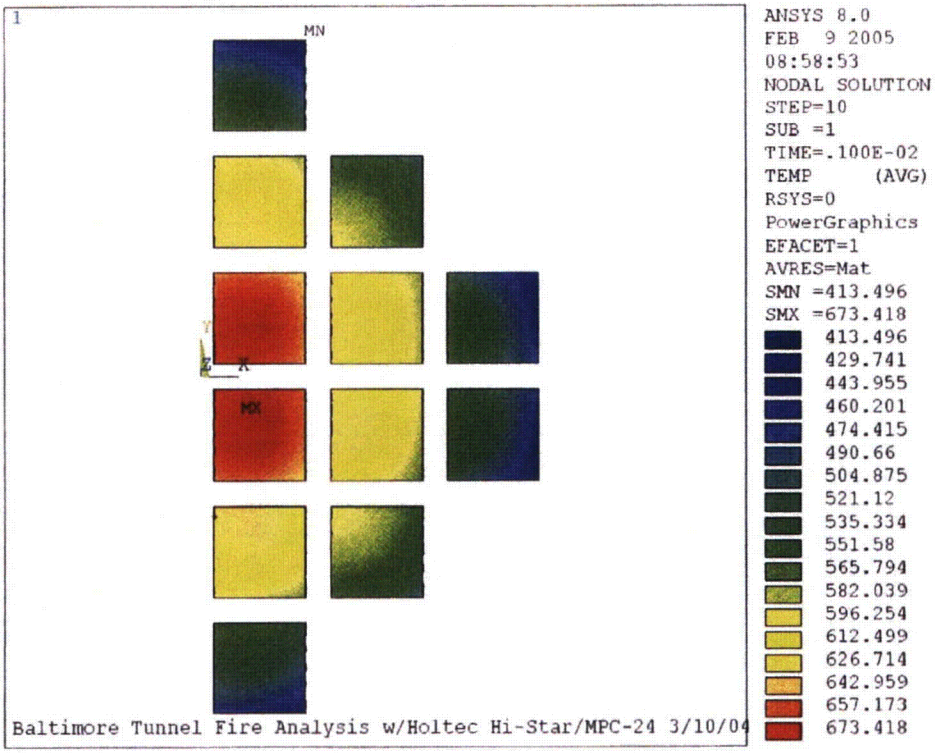

Figure F.11. Spent Fuel Radial Temperature Distribution - Normal Transport Conditions.

APPENDIX G

Comments and Responses from Public Posting in the Federal Register

Comments on NUREG/CR-6886 were solicited via a Federal Register Notice dated September 16, 2005. A second Federal Register Notice was posted on November 30, 2005, extending the comment period on this document to December 30, 2005. The NRC received comments from a diverse group of external stakeholders, consisting of

Northeast High Level Radioactive Waste Transportation Project
Brotherhood of Locomotive Engineers and Trainmen
Agency for Nuclear Projects, State of Nevada
William Rothman, M.D. (private citizen)

Comments ranged from concerns about the potential consequences of the effects of the fire transient on spent fuel transportation packages to comments that raised questions related to the basis for the staff's analysis. A revised version of this document (NUREG/CR-6886, Revision 1) has been developed, which includes additional discussion addressing the issues raised in these comments, an expanded level of detail in the explanation of the analysis methodology, and additional analysis of the potential consequences of the accident scenario. The comments[19] submitted by external stakeholders and the staff's responses to those comments are summarized in the following table.

[19] Some comments have been condensed slightly to remove redundancies or edited to correct typographical errors, without omitting any relevant point of the comment. Full text of the original comments, as submitted to the NRC point of contact for this document, can be obtained from the Agencywide Documents Access and Management System (ADAMS) under the accession number **ML062340334**.

Summary of Comments and Responses from Public Posting on the Federal Register (9/16/2005 through 12/30/2005) of NUREG/CR-6886

Spent Fuel Transportation Package Response to the Baltimore Tunnel Fire Scenario

No.	Comment	Response
1	On page 5.1 the statement is made that 66 ft. down-stream from the fire source is the shortest possible distance between the fire center and an SNF package because of the existence of a buffer car. This assumption seems problematic: even in the Baltimore Tunnel and certainly in wider tunnels with more than one track – it seems possible that the cask car and a buffer car could become uncoupled and slide past each other, that the buffer car could over-ride or be overridden by the package car or that the derailment could realign the cars in such a way that the minimum distance between the fire Center and the package could be only a few feet.	The 66-ft (20-m) location was chosen as a reasonable estimate of where the package could have been located in this particular fire, based on Federal regulations issued by the Department of Transportation (DOT). DOT regulations, in 49CFR174.85, require very specifically defined spacing between rail cars carrying hazardous materials of any kind, including flammable liquids and radioactive materials. Typical requirements specify that a rail car carrying radioactive material must be separated from cars carrying other hazardous material by at least one buffer car. Therefore, the package was placed in a realistic location for this particular accident, not a 'worst possible location' for any tunnel fire scenario. Additions to Chapter 5 address this issue in an expanded discussion of the fire scenario, the configuration of the derailed train cars, and the modeling approach. Additions to Chapter 1 evaluate the Baltimore tunnel fire in relation to the frequency and severity of rail transportation accidents involving hazardous material and severe fires.

No.	Comment	Response
2	The study assumes that the package remains horizontal with one end facing the fire source. It states that this orientation results in the maximum possible exposure and in the least post-fire free convection cooling. While I do not doubt that that is true, it would seem that there should be some discussion or study of an inclined or vertical package particularly, as I believe is pointed out later, because of the vertical temperature distributions both in the air and on the tunnel walls. (Would the seals in a vertical [c]ask where the end is near the heated ceiling of the Tunnel – or sitting just above a pool of flammable liquid – exceed rated service temperatures sooner than in the assumed position?)	The position and orientation of the package within the tunnel was selected to maximize heat input to the package from convection and radiation heat transfer. Peak gas and tunnel surface temperatures were used as boundary conditions on the package surface, as a conservative estimate of the distributed temperature gradients the package would actually see within the tunnel environment at any orientation. This is of particular importance in terms of maximizing heat input to the seals, because the package ends (and therefore the seals) are covered by the impact limiters, which shield the seal region from direct convection and thermal radiation from the tunnel environment. The heat input to the package side governs the rate of heat up of the seals, rather than heat input to the package ends, since the seals heat up primarily because of conduction from the package side. Additions to Chapters 5 and 6, which expand the discussion of the modeling approach, include a review of the conservative assumptions underlying the selection of the package orientation, location relative to the fire, and boundary conditions.
3	on page 5.7, the analysis assumed that the center axis of the package would be 8.2 ft. above the Tunnel floor. ... it is not obvious that it is a worst-case position .... (While I understand from the comment in the first numbered paragraph of section 6.1 that the peak gas temperature at the top of the Tunnel was used as the ambient temperature for active heat transfer to the upper surfaces of the packages, it is not clear to me that this is equivalent to assuming that the package itself were higher in the Tunnel.)	Using the peak gas temperatures for the boundary conditions is equivalent to assuming the package is located at that corresponding position in the tunnel. The 'worst case' for convection would be to assume that the package is positioned near the tunnel ceiling, and the peak air temperature is seen by all package surfaces; however, radiation view factors to the tunnel walls and floor would be attenuated. Since radiation heat transfer is at least an order of magnitude greater than convection, this position would not produce the worst heat transfer conditions for the package. The 'worst case' for radiation assumes the package is oriented horizontally, near the center of the tunnel, so that it has the most direct radiation view factors on all surfaces, particularly the sides of the package. This orientation is used in the analysis, and is arguably the 'most adverse orientation' for heat transfer during the fire and in the post-fire cool down. Additions to Chapters 5 and 6 expand the discussion of the modeling approach, including discussion of the conservative assumptions underlying the selection of the package orientation, location relative to the fire, and boundary conditions.

No.	Comment	Response
4	regarding the use of a seven-hour fire [based on the predictions of the NIST Fire Dynamics Simulator code calculations for the tunnel fire], ...there should be some discussion of both the confidence of the 7-hr FDS prediction and of the [potential consequences] of a fire lasting 10 or more hours.	Seven hours is an extremely conservative estimate of the possible duration of the Baltimore tunnel fire. Based on known facts about the Baltimore tunnel fire (e.g., from NTSB accounts of the accident and testimony of emergency responders at the scene), the most severe portion of the Howard Street tunnel fire lasted approximately 3 hours. Sensitivity studies conducted by NIST with the FDS model of the Howard Street tunnel evaluated variables in the fire scenario (e.g., tunnel geometry, fuel pool size, wall material properties), and determined that the heat release rate of the fire was limited to about 50 MW, due to oxygen starvation. Varying the fuel pool size can yield longer a duration fire, but peak fire temperatures are limited due to lack of sufficient oxygen in the confines of the tunnel. The 7-hr fire duration used to define the boundary conditions for the current study was obtained by assuming a fully ventilated fire that burned until all available fuel was consumed. The heat release rate for this fire scenario is approximately 500 MW, an order of magnitude higher than the heat rate predicted for a realistic representation of the fire conditions. Simulation of a longer fire requires reducing the burn rate or limiting the available oxygen for the fire, or both, which would result in lower fire temperatures. The scenario selected for the current study is a conservative representation of a potentially 'worst case' fire scenario for this accident. Additions to Chapter 2 expand the discussion of the fire scenario assumed in the FDS simulation used to determine the boundary conditions for the analyses of the SNF transportation packages.

No.	Comment	Response
5	In NRC's report on the Baltimore Tunnel fire, it appears that far too much emphasis is placed on investigating the possibility of loss of containment and not enough on the possibility of a loss of shielding scenario regarding the TN-68, Hi-Star 100, and NAC LWT SNF shipping casks. Loss of shielding is of particular concern to the Brotherhood of Locomotive Engineers and Trainmen for the following reasons:	Licensing regulations specified in 10 CFR 71 require that neutron and gamma shielding must be maintained within specified limits in all design basis accidents, including the regulatory fire transient. All three packages evaluated are expected to lose their neutron shield in the regulatory fire, and still maintain required neutron shielding. How this is accomplished is described in their respective SARs. Additions to Chapter 8 discuss the possible consequences of loss of neutron shielding and gamma shielding in terms of potential exposure. These analyses show that the potential dose would be below the limit of 1000 mrem/hr prescribed in 10CFR49 and 10CFR71 for all three packages in this fire scenario.
6	Shielding is an internal component of the cask design and any damage to the shielding would not be visually apparent to railroad employees.	All three packages evaluated can lose their neutron shield and still maintain external dose rates within regulatory limits, as documented in their respective SARs. Gamma shielding is provided by steel in the TN-68 and the HI-STAR 100 packages, and this shielding will not be reduced by any fire scenario. Some reduction of gamma shielding due to lead slumping as a consequence of melting and resolidifying is possible with the NAC LWT package. However, a significant increase in radiation dose from the NAC LWT would require physical damage to the package outer shell (such as a puncture), which could result in loss of lead shielding due to molten lead leaking from the package. Analysis of the conditions of this fire scenario show that the physical forces are not sufficient to result in damage to the package shell, and the lead shielding would remain within the cavity between the inner and outer shell during melting and resolidification. Potential dose increases due to possible slumping of the lead within the cavity are below the regulatory limit for accident conditions. Additions to Chapter 8 discuss the potential consequences of reduction in gamma shielding in the NAC LWT due to this fire scenario.
7	Train crews are not expected to be provided with dosimetry to measure off-link or on-link exposure during normal transportation, let alone emergency situations.	Additions to Chapter 8 discuss the potential consequences of loss of neutron shielding in all three packages, and potential reduction in gamma shielding in the NAC LWT due to this fire scenario. All three packages are designed to operate within regulatory limits without neutron shielding in place, and analysis shows

No.	Comment	Response
		that the NAC LWT also maintains radiation shielding within regulatory limits even when the potential reduction in gamma shielding is considered. Train crews that observe current regulations and procedures (e.g., 49 CFR part 171: §§ 171.15 and 171.16, 49 CFR part 172: subparts C G, and H, 49 CFR part 174: subparts A through D and K) governing the transportation of hazardous materials (including radioactive material) would not be at risk of exposure to hazards beyond the current regulatory limits for accident conditions from an SNF package subjected to the conditions of the Baltimore tunnel fire. It is the purpose of OCRWM and DOE to ensure that all appropriate measures are taken to protect carriers, workers, and the general public from adverse consequences associated with shipments of spent nuclear fuel and high-level radioactive waste. Regulations and procedures are currently in place that are designed to further the safety and security of SNF shipments. This includes instituting a "no pass" rule in tunnels for trains carrying radioactive material and trains carrying hazardous or flammable materials, to further reduce the extremely low probability of a tunnel fire accident involving an SNF transportation package (See discussion of AAR Circular OT-55 in Chapter 1.) This analysis of the Baltimore tunnel fire and previous evaluations (as discussed in Chapter 1) show that the risks associated with SNF shipments are extremely low. Additional measures under consideration to further mitigate the risk of this activity include - providing dosimeters for specific workers involved in the normal handling of SNF shipments - instituting 'dedicated' rail lines on specific sections of transportation routes where the consequences of an accident are deemed severe enough to warrant such precaution, despite the low probability of a severe accident

No.	Comment	Response
8	There are no plans to equip locomotives with radiation detectors to alert crews to dangerous spikes in dose rate.	See response to Comment 7 above.
9	In all three models, the loss of neutron shielding was a given, but loss of gamma shielding was scarcely touched upon. Lead has a melting point of 621 degrees[F (328°C)]. In all three models, the gamma shield exceeded that temperature. The TN-68 exceeded that temperature after 5 hours, both the Hi-Star 100 and the NAC LWT casks reached that point in just two hours. The NAC LWT uses lead rather than carbon steel as its gamma shield. The shielding would have likely failed at the two-hour mark, eventually reaching 1378 degrees[F (748°C)] after 6.75 hours in the fire.	Gamma shielding is not lost in the TN-68 or HI-STAR 100 during the Baltimore tunnel fire, since these packages use steel for gamma shielding, not lead. For the NAC LWT, the lead reaches its melting point, but in this accident scenario, the lead remains encapsulated within the steel shell of the package body and base, and continues to function as a gamma shield. Additions to Chapter 8 provide an expanded discussion of the consequences of the lead melting during the fire, and the consequent effect on gamma shielding in the NAC LWT. The analyses presented show that this package maintains shielding such that the dose rate at 1 meter from the package surface is below 1000 mrem/hr, as required in all accident conditions. (See response to Comments 5, 6, and 7.)
10	The final version of NUREG/CR-6886 should include an expanded introductory section summarizing previous NRC studies of spent fuel shipping cask response to severe fire environments, including an explanation of the relationship between this report and NUREG/CR-6672 (SAND2000-0234).	There is no direct relationship between NUREG/CR-6672 and NUREG/CR-6886. NUREG/CR-6672 undertakes a detailed study of the risks associated with the transport of spent nuclear fuel by all possible modes, considering both mechanical loads and thermal loads imposed by conservatively defined bounding accident scenarios. Thermal loads were evaluated by postulating an extremely long duration (11 hours) fully engulfing pool fire at 1832°F (1000°C), which readily envelopes the "worst case" possibilities presented by any historical fire accident, including the Baltimore tunnel fire. The analyses in NUREG/CR-6672 use extremely conservative assumptions and highly simplified models of SNF packages for the thermal analyses, which tend to severely over-estimate the peak temperatures within the package, and do not consider the three-dimensional effects of a tunnel fire or any specific historic accident scenarios. The main effect of the modeling simplifications and conservatisms in

No.	Comment	Response
		NUREG/CR-6672 is to grossly over-estimate the peak predicted temperatures in an SNF package in the response to any fire scenario. Even with extremely conservative bounding assumptions, including assumptions related to accident frequency, severity and consequences, the analysis in NUREG/CR-6672 shows that the risks associated with the shipment of spent nuclear fuel by truck or rail are very small. The report further concludes that current regulations governing the transportation of spent nuclear fuel "adequately protect public health and safety."
11	The final version of NUREG/CR-6886 should include a more detailed discussion of the Nation[al] Transportation Safety Board (NTSB) investigation of the Baltimore Tunnel Fire, including the NTSB safety recommendations (R-04-15 and -16, issued January 5, 2005) and the NTSB decision not to issue an official report on the cause and history of the fire.	As discussed in Chapters 1, 2, 3, 4, 5 and 6 of NUREG/CR-6886, information from the NTSB was used in the process of determining a conservative representation of the Baltimore tunnel fire scenario, as well as consultations with experts at NIST and CNWRA. The NTSB performed a thorough investigation of this accident, but declined to issue a final report because the Board could not come to a decision on the cause of the accident. The cause of the accident is not relevant to the analyses presented in NUREG/CR-6886, which accepts as a given that the accident did indeed occur. Similarly, the NTSB safety recommendations R-04-15 and -16 are not relevant to the fire analysis. These recommendations concern the need for improved communications between CSX and the city of Baltimore, and improvements to the city's emergency preparedness plans.
12	The final version of NUREG/CR-6886 should include a detailed discussion of the 2001 analysis of the Baltimore Tunnel Fire prepared by Radioactive Waste Management Associates for the State of Nevada.	NUREG/CR-6886 is a case study of a historical event, not a peer review of other work related to general transportation accidents involving radioactive materials. The RWMA study is particularly problematic, since it is based on significantly different assumptions regarding the fire and the properties of the SNF packages, such that it is impossible to make meaningful comparisons between the two reports. The RWMA study was released less than 3 months after the accident, long before the NTSB, CNWRA, NIST, and NRC had finished investigating the event, and as a result the RWMA study is based on inaccurate and unsubstantiated assumptions about the nature, duration, and intensity of this fire scenario. The RWMA report overstates the intensity and duration of the fire (assuming a 5-day

No.	Comment	Response
		fire duration for the intense portion of the fire vs. the 3-hour duration confirmed by NTSB investigations.) The RWMA study inappropriately uses temperature predictions from the long-duration pool fires analyzed in NUREG/CR-6672 to estimate the tunnel fire environment. The RWMA report incorrectly models the behavior of the package and spent fuel, assuming an incorrect failure mechanism for fuel cladding (i.e., creep vs. pressure rupture), and neglects credible resistances in the release pathway (e.g., metal to metal contact and lid torque.) The RWMA report also overestimates the amount of Cesium that is available for release from the fuel rods. As a result, the RWMA report vastly overestimates the potential consequences of the Baltimore tunnel fire scenario when applied to an SNF package, and does not present a reliable analysis that could assist in determining the risks associated with transportation of spent nuclear fuel by rail.
13	The final version of NUREG/CR-6886 should include a detailed discussion of the 2002 analysis of the Baltimore Tunnel Fire prepared by the U.S. Department of Energy as part of the Final Environmental Impact Statement for Yucca Mountain (DOE/EIS-0250).	A direct comparison between the analyses in NUREG/CR-6886 and in DOE/EIS-0250 is not meaningful. The analysis in EIS-0250 does not evaluate the Baltimore tunnel fire specifically; instead it considers the maximum reasonable foreseeable accident, which is considered to envelope events such as the Baltimore tunnel fire scenario.
14	The final version of NUREG/CR-6886 should include side-by-side fire transient results and consequence analyses of the NAC LWT cask, with and without enclosure in an ISO container. (The discussion at page 7.17 implies that these analyses were performed, but they apparently were not reported.)	The NAC LWT was not analyzed without an ISO container in this study. This package was analyzed enclosed in an ISO container because that is the anticipated mode of transport when it is shipped by rail. The CoC for the NAC LWT requires that it be enclosed in either a personnel barrier (PB) or an ISO container. PBs commonly used for trucks are not shippable by rail, so for rail transport, an ISO would generally be required. Current DOE policy requires an ISO for truck packages shipped by rail, and every rail shipment of the LWT to date has been in an ISO container. The discussion on p. 7.17 is intended to show that the ISO container does not substantially shield the NAC LWT package from the fire, and peak component temperatures would be essentially the same, with or without an ISO container.

No.	Comment	Response
15	The final version of NUREG/CR-6886 should include an additional cask analysis, parallel to the approach described in Section 5, of a General Atomics GA-4 legal-weight truck cask, shipped on a rail car without enclosure in an ISO container.	This study evaluated the performance of three representative packages currently in service, based on resources that are postulated to be used. Including analyses for the GA-4 package in NUREG/CR-6886 would not be expected to substantially alter the results or conclusions obtained in this study. In addition, the thermal performance of the GA-4 package in an extra-regulatory fire has already been examined in NUREG-1768, *United States Nuclear Regulatory Commission Package Performance Study Test Protocols*. Additional analyses may be warranted for future studies, if the staff believes large scale use of a particular package is expected.
16	The final version of NUREG/CR-6886 should include an additional thermal analysis for each of the four casks, parallel to the approach described in Section 5, assuming that the cask is located 5 meters (16 feet) from the fire center.	As noted in the response to Comments 1, 2, and 3, the selected location of the SNF packages for this analysis is consistent with the physical attributes of the tunnel and the possible shipping configurations for an SNF package in the Baltimore tunnel fire scenario.
17	The final version of NUREG/CR-6886 should include an additional thermal analysis for each of the four casks, parallel to the approach described in Section 5, assuming that the cask is located within the hottest region of the fire.	See response to Comments 1, 2, 3, and 16.
18	The final version of NUREG/CR-6886 should include a re-examination of the potential for fuel cladding failure and release of radioactive materials, including fission products, at temperatures below the projected burst temperature of 1382°F (750°C) for Zircaloy cladding. (Additional attention should be given to the presence of older fuel with brittle and/or previously failed cladding.)	The limit of 1382°F (750°C) is a conservative lower bound on the temperature at which Zircaloy cladding might be expected to fail by burst rupture. There is no reason to suppose that this limit is not sufficient for fuel within the TN-68 cask when exposed to the Baltimore tunnel fire scenario, since this cask is licensed to carry only intact fuel assemblies. The HI-STAR 100 is licensed to carry failed fuel, but this analysis shows that this cask would not be expected to lose containment in the Baltimore tunnel fire scenario. This package design employs an inner canister (MPC) that is conservatively predicted to maintain its integrity throughout the entire fire transient. Radioactive materials, including fission

No.	Comment	Response
		products, would not be released from this package, even under conditions as severe as the Baltimore tunnel fire scenario. The NAC LWT is also licensed to carry failed fuel, but this package is quite small and can carry only a limited amount of spent nuclear material, its largest payload consisting of a single PWR assembly. Analysis of the consequences of postulating 100% failure of all rods in a single PWR assembly consisting of high burn-up, 3-yr-cooled fuel (see NUREG/CR-6672) shows that the potential release from this package remains below an A_2 quantity for this fire scenario, as discussed in Chapter 8.2.5. The available fission products from one PWR assembly of this type far exceeds that of any failed fuel the NAC LWT is licensed to carry. A payload that includes failed fuel does not adversely affect the potential consequences of the Baltimore tunnel fire scenario. Additional discussion of the potential consequences of the Baltimore tunnel fire scenario for the HI-STAR 100 and the NAC LWT when carrying failed fuel has been added to Chapter 8.
19	The final version of NUREG/CR-6886 should include a reexamination of the potential for fuel cladding failure and release of radioactive materials for higher burn-up fuels, specifically addressing the issues of radiation embrittlement, pellet degradation due to thermal cycling, and fission product buildup.	This analysis was performed assuming that all of the packages would be loaded with design basis fuel, based on the cask's licensing qualifications. The TN-68 and HI-STAR 100 packages are not licensed to carry high burn-up fuel. The NAC LWT is the only package considered in this study that is licensed to carry high burn-up fuel, in which case the total fuel load is limited to no more than 25 rods. As noted in the response to Comment 18, an analysis assuming 100% failure of all rods in a single high burn-up, 3-yr-cooled PWR assembly shows that the potential release from this package remains below an A_2 quantity for this scenario. The available fission products from one PWR assembly of this type far exceeds that of the maximum of 25 high burn-up fuel rods the NAC LWT is licensed to carry.

No.	Comment	Response
20	The final version of NUREG/CR-6886 should include a reexamination of the potential for release of radioactive materials for fuel assemblies with higher levels of CRUD activity (e.g., BWR assemblies with surface concentration up to150 $\mu Ci/cm^2$).	The current analysis (see Chapter 8) was performed assuming maximum CRUD activity of 300 $\mu Ci/cm^2$, and corresponding average activity of 150 $\mu Ci/cm^2$ for the TN-68. Given the conservative assumptions on the amount of CRUD that can detach from the rod surfaces and plate out, and the fact that 90% of the rods are cleaner than this assumed level of activity, this assumption is appropriately conservative for this analysis.
21	The final version of NUREG/CR-6886 should include a reexamination of the mechanisms for seal failure and release of radioactive materials, including seal failure long before maximum seal temperatures are reached, bolt failure, and pressure-induced blowout of failed seals.	Failure due to exceeding temperature limits is the only credible cause of seal failure in this accident scenario. The specified limits are inherently conservative, in that they are based on long-term service temperature limits, rather than transient limits. Temperatures are not high enough to consider bolt failure possible, and internal pressure increase is not sufficient by itself to compromise seals. As discussed in Chapter 8, the potential release of radioactive materials is not limited by the condition of the seals or by the time required for the seals to fail. The conclusion that there would be no release from the HI-STAR 100 is based on the welded inner canister remaining intact, not simply the integrity of the seals. For the TN-68 and the NAC LWT, the seals are assumed to fail, and the amount of the potential release is based primarily on the amount of CRUD material available for release from the package. It is not dependent on the time or mode of seal failure. The potential release is determined using a model developed by Sandia National Laboratory for analysis of CRUD contribution to shipping package containment requirements (SAND88-1358; see Ref. 26).
22	The final version of NUREG/CR-6886 should include a reexamination of the role of the HI-STAR 100 train carriage and cask restraints regarding heat shielding and heat conduction.	Heat shielding effects of these structures during the fire would act to decrease the heat load on the package during the fire; heat conduction after the fire would serve to hasten cool-down. Assumptions made in the analysis are conservative for both the fire and post-fire cool down.

No.	Comment	Response
23	The final version of NUREG/CR-6886 should include a discussion of the emergency response implications, and cask recovery implications, of the predicted damage to the neutron shielding for all three considered casks, and the loss of gamma shielding for the NAC LWT.	The loss of neutron shielding is expected in all 3 designs as a consequence of the regulatory fire (i.e., 30 minutes at 800°C). Existing regulations and procedures regarding emergency response should be sufficient for this scenario, as well. The NAC LWT does not lose its gamma shielding in this scenario. The lead melts during the fire, but is confined and held in place by the steel package body. Additional discussion has been added to Section 8.1 evaluating the consequences of lead melting and resolidification in this package. (See responses to Comments 5 through 9 above.)
24	The final version of NUREG/CR-6886 should include a reexamination of the uncertainties associated with the NIST FDS simulations of gas and wall temperatures 20-30 meters from the fire center. (These issues include the construction and benchmarking of the FDS code, selection of the conductivity value for the tunnel bricks, and potential inconsistencies with the materials analyses.)	Because of uncertainties and unknowns related to the fire scenario, the FDS simulation and the package analyses were performed using conservative assumptions. The results of the FDS simulations using realistic assumptions are in close agreement with the peak temperatures estimated from analyses of material recovered from the tunnel after the fire. (See the discussion in Chapter 3.) In addition, sensitivity studies were performed with FDS to determine the effect of varying parameters that could potentially affect peak predicted temperatures, including the thermal conductivity of the tunnel wall surfaces. The analysis predicting a fire duration of 7 hours is the result of specifying parameters that assume an unrealistically high rate of oxygen flow to the fire, in order to achieve complete combustion of the entire inventory of available fuel. The resulting fire conditions are an order of magnitude hotter than conditions predicted using realistic assumptions for the fire scenario. Variation in parameters due to uncertainties would generally result in a less severe fire transient. Additions to Chapters 2, 4, 5 and 6 expand the discussion of the conservatisms in the FDS analysis of the fire scenario and the modeling approach used in the analyses of the SNF packages.

No.	Comment	Response
25	The final version of NUREG/CR-6886 should include a comprehensive analysis of uncertainties in the following factors, and how these uncertainties might affect the results of the consequence assessment: fire size, location, and duration; gas and wall temperatures from the NIST FDS simulations; CNWRA metallurgical analyses; uncertainties in the package models; seal and cladding temperature limits; and heat transfer models for the neutron shield (including gap radiation in charred solid, and boiling heat transfer in liquid) and impact limiters.	Relevant discussions of all of these issues are included in the publicly posted version of the report, and have been expanded in Chapters 2, 5, 6, and 8 of the current Revision 1. Uncertainties related to all of these enumerated issues were considered and accounted for in a conservative manner in these analyses. Evaluation of less conservative variations within the range of uncertainties in these factors would result in shorter fire durations and lower fire temperatures, which would lower predicted package component temperatures.
26	The final version of NUREG/CR-6886 should include a discussion of any peer reviews conducted for this report, and any peer reviews conducted for two of the major supporting studies, NUREG/CR-6793 (NIST) and NUREG/CR-6799 (CNWRA).	NUREG/CR-6886 has not been subjected to external peer reviews. Instead, this document has undergone intense internal technical peer reviews by PNNL and NRC before publication, and was made available for public comment for a period of approximately 3 months. This permitted independent review by any and all interested parties. All public comments on this document are included in the final publication. An external peer review was not deemed necessary because of the very low risks associated with this scenario. This is due to the low frequency of the type of accident and the minimal consequences of postulated accident conditions. The observed frequency is once during 21 billion miles of train travel, which comprises the last 30 years of historical rail shipments. The potential consequences are estimated to be less than 0.3 of an A_2 quantity of release, and the analysis predicts large margins of temperature against cladding failure. For this study, a peer review would not be cost effective.

No.	Comment	Response
27	The possibility of fuel oil fire temperatures of 1650-2000°C for periods of time far in excess of the 30-minute test characteristic of Type B casks, make it impossible to consider that the circumstances know[n] about the Baltimore tunnel fire would be the worst circumstances that would be likely to apply in a fire situation affecting nuclear waste casks, during their transport.	The analyses in NUREG/CR-6886 predict the effects that a particular historical fire accident could be expected to have on three specific SNF transportation packages. This report does not attempt to define the worst possible fire accident. However, this is an extremely severe accident with a statistical frequency on the order of one such accident in 21 billion miles of train travel. This accident is bounded by the analyses in NUREG/CR-6672 and NUREG-0170 evaluating the risks associated with transportation of spent nuclear fuel.
28	The Advisory Committee on Nuclear Waste (ACNW) inquired during a public meeting on September 21, 2006, as to whether or not the figure of 21 billion rail miles traveled between 1975 and 2005, cited in the report, included DOE Naval Nuclear Propulsion Program waste shipments.	This mileage figure includes all commercial rail transportation for this period of time; however, it was not broken down into specific categories of rail transportation. DOE Naval Nuclear Propulsion Program waste shipments are commonly done on commercial railways and, as a result, would be included in this number.

NRC FORM 335
(9-2004)
NRCMD 3.7

U.S. NUCLEAR REGULATORY COMMISSION

BIBLIOGRAPHIC DATA SHEET

(See instructions on the reverse)

1. REPORT NUMBER
(Assigned by NRC, Add Vol., Supp., Rev., and Addendum Numbers, if any.)

NUREG/CR -6886, Rev. 2

2. TITLE AND SUBTITLE

Spent Fuel Transportation Package Response to the Baltimore Tunnel Fire Scenario

3. DATE REPORT PUBLISHED

MONTH	YEAR
February	2009

4. FIN OR GRANT NUMBER

J5575

5. AUTHOR(S)

H.E. Adkins, Jr. (PNNL)
J.M. Cuta (PNNL)
B.J Koeppel(PNNL)
A.D. Guzman (PNNL)
C.S. Bajwa (NRC)

6. TYPE OF REPORT

Final

7. PERIOD COVERED *(Inclusive Dates)*

8. PERFORMING ORGANIZATION - NAME AND ADDRESS *(If NRC, provide Division, Office or Region, U.S. Nuclear Regulatory Commission, and mailing address; if contractor, provide name and mailing address.)*

Pacific Northwest National Laboratory
902 Batelle Boulevard
Richland, WA 99352

9. SPONSORING ORGANIZATION - NAME AND ADDRESS *(If NRC, type "Same as above"; if contractor, provide NRC Division, Office or Region, U.S. Nuclear Regulatory Commission, and mailing address.)*

Division of Spent Fuel Storage and Transportation
Office of Nuclear Material Safety and Safeguards
U.S. Nuclear Regulatory Commission
Washington, D.C. 20555-0001

10. SUPPLEMENTARY NOTES

C. Bajwa, NRC Project Manager

11. ABSTRACT *(200 words or less)*

On July 18, 2001, a freight train carrying hazardous (non-nuclear) materials derailed and caught fire while passing through the Howard Street railroad tunnel in downtown Baltimore, Maryland. The United States Nuclear Regulatory Commission (USNRC), one of the agencies responsible for ensuring the safe transportation of radioactive materials in the United States, undertook an investigation of the train derailment and fire to determine the possible regulatory implications of this particular event for the transportation of spent nuclear fuel by railroad.

The USNRC assembled a team of experts from the National Transportation Safety Board, the National Institute of Standards and Technology, the Center for Nuclear Waste Regulatory Analyses, and the Pacific Northwest National Laboratory to determine the thermal conditions that existed in the Howard Street tunnel fire and analyze the potential effects of those conditions on various spent nuclear fuel (SNF) transportation package designs.

The staff's evaluation indicates that neither SNF particles nor fission products would be released from a package, carrying intact SNF, involved in a severe tunnel fire such as the Baltimore tunnel fire. A release of CRUD from the surface of fuel cladding, while a possibility for certain package designs, is highly unlikely, and would be within regulatory limits.

12. KEY WORDS/DESCRIPTORS *(List words or phrases that will assist researchers in locating the report.)*

Tunnel
Baltimore
Howard Street
Fire
Rail Car
Derailment
Spent Nuclear Fuel
Transportation Package

13. AVAILABILITY STATEMENT

unlimited

14. SECURITY CLASSIFICATION

(This Page)
unclassified

(This Report)
unclassified

15. NUMBER OF PAGES

16. PRICE

UNITED STATES
NUCLEAR REGULATORY COMMISSION
WASHINGTON, DC 20555-0001

OFFICIAL BUSINESS

WVMP SAR Reference 3-16

Defense Waste Processing Facility Wasteform and Canister Description, DP 1606, Rev. 2, R. G. Baxter, December 1988.

DP-1606
Rev 2
Distribution Category UC-721

DEFENSE WASTE PROCESSING FACILITY WASTEFORM AND CANISTER DESCRIPTION

RICHARD G. BAXTER

Approved by

Lucien M. Papouchado, Program Manager,
Waste Management Programs

Publication Date: December 1988

E. I. du Pont de Nemours & Co.
Savannah River Plant
Aiken, SC 29808

PREPARED FOR THE U. S. DEPARTMENT OF ENERGY UNDER CONTRACT DE-AC-09-76SR00001

mail Legacy 28

Acknowledgments

Many persons in the Savannah River Laboratory and Plant are responsible for the data in this report. In particular, the contributions of John R. Fowler and Richard E. Edwards for material and curie balances, and M. John Plodinec for glass chemistry and leachability, were important to the preparation of this document.

ABSTRACT

This document describes the reference wasteform and canister for the Defense Waste Processing Facility (DWPF) and updates DP-1606, Rev. 1, which was published in August 1983. The principal changes include revised feed and glass product compositions, an estimate of glass product characteristics as a function of time after the start of vitrification, and additional data on glass leaching performance. The feed and glass product composition data are identical to that described in the DWPF Basic Data Report, Revision 90/91 (see references).

The DWPF facility is located at the Savannah River Plant in Aiken, SC, and it is scheduled for construction completion during December 1989.

The wasteform is borosilicate glass containing approximately 28 wt % sludge oxides, with the balance consisting of glass-forming chemicals, primarily glass frit. Borosilicate glass was chosen because of its stability toward reaction with potential repository groundwaters, its relatively high ability to incorporate nuclides found in the sludge into the solid matrix, and its reasonably low melting temperature. The glass frit contains approximately 71% SiO_2, 12% B_2O_3, and 10% Na_2O.

Tests to quantify the stability of DWPF waste glass have been performed under a wide variety of conditions, including simulations of potential repository environments. Based on these tests, DWPF waste glass should easily meet repository criteria.

The canister is filled with about 3,700 lb of glass which occupies 85% of the free canister volume. The filled canister will generate approximately 690 watts when filled with oxides from 5-year-old sludge and precipitate from 15-year-old supernate. The radionuclide activity of the canister is about 233,000 curies, with an estimated radiation level of 5,600 rad/hour at the canister surface.

The canister is fabricated of standard 24 in. OD, schedule 20, type 304L stainless steel pipe with a dished bottom, domed head, and a combined lifting and welding flange on the head nozzle. The overall canister length is 9 ft. 10 in. (300 cm) with a wall thickness of 3/8 in. The canister length was selected to establish a practical cell height in the DWPF. The canister diameter was selected as an optimum size from glass quality considerations, a logical size for repository handling, and to ensure that a filled canister in either a single- or a double-containment shipping cask could be accommodated on a legal-weight truck. The overall dimensions and weight are compatible with repository requirements.

CONTENTS

LIST OF FIGURES

LIST OF TABLES

LIST OF TABLES, (contd)

DEFENSE WASTE PROCESSING FACILITY
WASTEFORM AND CANISTER DESCRIPTION

INTRODUCTION

This document describes the reference glass wasteform and canister for the Defense Waste Processing Facility (DWPF). The borosilicate glass wasteform and stainless steel canister are the reference package selected in December 1982, and they are the basis for the DWPF design and process.

HIGH LEVEL WASTEFORM CHARACTERISTICS

The wasteform for the DWPF is a borosilicate glass containing approximately 28% sludge oxides with the balance consisting of glass-forming chemicals, primarily glass frit. Borosilicate glass was chosen as a wasteform because of its stability toward attack by water, its relatively high ability to dissolve nuclides found in the sludge into the melt, its relatively low melting temperature, and because the process is based on well-developed technology.

Description of the waste glass characteristics is divided into three sections: composition, mechanical properties, and chemical stability. Sludge-precipitate processing is based on processing the 5-year-old or older sludge plus a 15-year-old or older supernate fraction. The sludge fraction contains the strontium and plutonium, and the supernate portion contains virtually all of the cesium. Mechanical properties of the waste glass are based on a typical frit, designated as Frit 131.* Other frits, such as Frits 165 and 200, have similar mechanical properties, based on experimental laboratory tests.

Data on the stability of waste glasses described in this report are from glasses simulating the DWPF product, which are based on Frit 165. Although the glasses produced in the DWPF will not be identical to glasses made from Frit 165, due to changes in the DWPF process after the development of Frit 165, the chemical stability is expected to be similar, based on experimental laboratory tests (see Glass Stability Programs under References).

COMPOSITION OF DWPF WASTE GLASS

Feed to the DWPF consists of two streams: settled, washed sludge and supernatant liquid. The sludge consists of hydroxides and hydrous oxides containing nearly all of the stable and radioactive fission products, and actinide elements, as well as elements added in the SRP separations processes. These are primarily iron, manganese, aluminum, and mercury. The sludge is treated with sodium hydroxide to dissolve hydrated aluminum oxides, washed with water to remove soluble salts to 2% on a dry basis, and then allowed to settle. The washed sludge is transferred as a 13% slurry to the DWPF slurry receipt adjustment tank (SRAT).

*Savannah River Laboratory frit designations.

The supernate solution containing dissolved salts is treated in the waste tanks with sodium tetraphenylborate to precipitate cesium, and with sodium titanate to absorb the trace amounts of strontium and plutonium compounds present in the supernate. These precipitates are transferred to the DWPF salt processing cell where the organic portion of the salts are decomposed to benzene and the inorganic portion is transferred to the slurry receipt adjustment tank.

Sludge Processing

A description of the chemical composition of sludge feed is shown in Tables 1A and 1B, the radionuclide content in Table 2, and the isotopic content in Table 3. The soluble solids (Table 1A) are principally $NaNO_3$ (41%), $NaNO_2$ (19%), NaOH (18%), and $NaAl(OH)_4$ (11%), which constitute about 89% of the soluble solids. Of the insolubles (Table 1B; zeolite composition is given in Table 18), $Fe(OH)_3$ (41%), $Al(OH)_3$ (16%), MnO_2 (7%), and $UO_2(OH)_2$ (7%) constitute approximately 70% of the insoluble solids. Activity of the sludge feed is 133 Ci/gal (Table 2) with a decay heat of 0.44 watt/gal for 5-year-old waste. Of this activity, 78% is due to Sr-90, Y-90, and Pm-147.

Precipitate Processing

A description of the chemical composition of the precipitate feed to the salt cell is shown in Table 4, the radionuclide content of feed from the precipitate process is shown in Table 5, and the isotopic content in Table 6. The principal compounds of the precipitate feed, on a water-free basis, are potassium tetraphenylborate (KTPB) (76%), $NaNO_3$ (6%), and NH4TBP (4%); these compounds constitute about 85% of the input stream. Activity of the feed from the precipitate process is 71.4 Ci/gal with a decay heat of 0.167 watt/gal for precipitate from 15-year-old supernate. Of this activity, about 99% is due to Cs-137 and its beta decay daughter Ba-137m.

The chemical composition of the feed from the salt cell to the SRAT is shown in Table 7, the radionuclide content in Table 8, and the isotopic content in Table 9. The principal components, on a water-free basis, are KCOOH (29%), H_3BO_3 (19%), and NaCOOH (13%). Activity of this feed to the SRAT is 76.5 Ci/gal with a decay heat of 0.178 watt/gal.

The chemical composition of combined sludge and precipitate waste glass is shown in Table 10, the radionuclide content is shown in Table 11, and the isotopic content in Table 12. Total activity is 63.1 Ci/lb with a decay heat of 0.187 watt/lb for 5-year-old sludge and precipitate from 15-year-old supernate. Thus, the 3,700 lb of glass in a DWPF canister contains about 233,000 Ci with a decay heat of 690 watts. The isotopes Y-90, Sr-90, Cs-137, Ba-137m, and Pm-147 contribute about 87% of the activity.

Chemical composition of the design basis frit, designated as Frit 200, is shown in Table 13A. Composition of the frit to be used during initial operations, Frit 202, is also shown. Frit 202 is approximately 77% SiO_2, 8% B_2O_3, and 7% Li_2O. The frit was developed after an extensive series of tests designed to produce a waste glass product with good leach resistance, high solubility for waste oxides, and a practical melting temperature. It is based on earlier efforts which resulted in the development of Frit 165. The performance of the DWPF glass is expected to be similar to that of Frit 165 glasses, based on experimental laboratory tests. Compositions of glasses expected to be produced by the DWPF are shown in Table 13B.

PHYSICAL PROPERTIES OF DWPF WASTE GLASS

Physical properties of DWPF waste glass have been measured and estimated by calculation. Most of the properties determined by experiment are based upon Frit 165 rather than the Frit 200; however, there are few significant differences. The principal differences between the two are that Frit 200 is higher in percent of SiO_2 and B_2O_3, but contains no ZrO_2. A chemical comparison between several of the frits evaluated is shown in Table 13A.

Physical properties of glass wasteforms are listed in Table 14. Of these values, the fractional thermal expansion, the density at 100°C, and the softening point were experimentally determined for Frit 165 glass. Other values are based on Frit 21 or other typical compositions.

Several other physical properties of SRP waste glasses have been estimated by calculation. Heat capacity, thermal conductivity, and density for three types of DWPF waste glass (composite, high iron, and high aluminum) have been calculated on the basis of glass containing approximately 28% sludge oxides and the balance glass Frit 131. Physical properties of waste glasses made in the range of frit compositions expected in the DWPF showed that these properties were invariant with changes in frit composition. Typical compositions of waste for these three types of glass are shown in Table 15.

Heat Capacity

Measured and calculated heat capacities of simulated waste glasses are listed in Table 16. C_{pt} is the true heat capacity at the indicated temperature. True specific heat as a function of temperature is also shown in Figure 1.

Density

Measured densities for simulated waste glass are listed in Table 17, and density as a function of temperature is shown in Figure 2 for the range of glasses expected in DWPF.

Thermal Conductivity

Calculated thermal conductivity of DWPF glass as a function of temperature is shown in Figure 3.

Electrical Resistivity

Measured electrical resistivity of the glass melt as a function of temperature is shown in Figure 4. At the operating melt temperature of 1,150°C, the resistivity is approximately 2.5 ohm-cm for composite glass.

Thermal Expansion

Waste glass measured thermal expansion as a function of temperature is shown in Figure 5 for composite glass, in Figure 6 for high-Al glass, and in Figure 7 for high-Fe glass.

Viscosity

Experimentally determined viscosities for the range of glasses expected in the DWPF are shown in Figure 8. At the nominal operating temperature of 1,150°C, the composite glass viscosity is about 30 poise.

CHEMICAL STABILITY OF DWPF WASTE GLASS

In accordance with the Nuclear Waste Policy Act of 1982, the canisters of waste glass produced in the DWPF will eventually go to a licensed federal repository for permanent disposal. Recent legislation indicates that the first repository will be in tuff at the Nevada Test Site. At the repository, the canister containing waste glass will be emplaced in the geology as part of a waste package. This package will contain the waste glass, the type 304L stainless steel canister, a metallic overpack to meet the containment requirement of 10 CFR 60, and possibly a packing material such as crushed rock or clay.

Reaction of waste glass with repository groundwater is the most likely mode of release of long-lived radioactive species to the environment. Borosilicate glass was chosen as the wasteform for the DWPF because of its stability when exposed to groundwater. Thus, Savannah River Laboratory (SRL) has focused on developing a quantitative understanding of the reaction between glass and groundwater over the range of conditions expected for liquid groundwater and DWPF glass interactions in candidate repository environments.

The expected range of conditions for each of three geologies is shown in the following table. The ranges have been derived from reference repository conditions for each of the geologies. The values are based on the assumption that the waste package containing DWPF glass in the repository will meet regulatory requirements, particularly the containment requirement imposed by the Nuclear Regulatory Commission in 10 CFR 60.

EXPECTED CONDITIONS FOR INTERACTIONS BETWEEN GROUNDWATER AND DWPF GLASS

PARAMETER	REPOSITORY CONDITION		
	SALT	BASALT	TUFF
Temperature	34 - 90°C	57 - 150°C	30 - 95°C
Pressure	2800 PSI	4700 PSI	Atmosperic
Groundwater	Brine	Silicate	Dilute Silicate
Eh	≈ 0 v	- 0.40 v	Oxidizing
pH	6	9.75	7.5
Flow	Static	Very Slow	Intermittent
Amount	Limited	Flooded	Limited

Studies on glass stability have been in progress at the Savannah River Laboratory for the past ten years. Early glass leaching characteristics of SRP simulated and actual waste glasses are summarized in report DP-1629 (see reference section). These early studies showed that DWPF glass reacted very slowly with groundwaters, and could immobilize the radionuclides in SRP waste. In this section, more recent results are summarized.

The program being carried out by SRL has two major components: mechanistic studies, and verification. SRL's mechanistic studies are directed toward developing a quantifiable model of long-term release from DWPF waste glass, while verification studies test the validity of the model and its predictions. Although these are separate functions, there is necessarily a large amount of interaction between the two components. For example, leaching models are used in the design of verification experiments to point out the appropriate parameters to measure. Conversely, verification

tests can indicate phenomena not considered in the modeling program, and thus are used to guide modeling efforts.

Glass - Groundwater Reaction Mechanisms

The SRL programs to identify and quantify the mechanisms of the reactions between waste glass and repository groundwaters include:

- Fundamental studies designed to quantify the effects of parameters such as glass composition, groundwater composition (including Eh, pH, and dissolved gases), or radiation on glass durability.

- Laboratory tests designed to quantify glass performance under conditions simulating actual potential repository environments.

The first item includes both theoretical and experimental efforts. The thermodynamic approach, first suggested by Paul and Newton, has been an important tool which has enabled SRL to compare the performance of a wide range of glasses and minerals based on their compositions. As Figure 9 shows, the performance of basalt from the Hanford reservation is virtually indistinguishable from that of the DWPF product.

SRL is also performing repository simulation tests in the laboratory, using both actual and simulated waste glasses. These tests are providing data which will be used to determine the stability of DWPF glass in a given repository. In these tests, waste glass and stainless steel samples (simulating a breached canister) are placed in a reaction vessel made from rock representative of one of the candidates for a repository - tuff, basalt, or salt (Figure 10). The reaction vessels used in these experiments are rock cups made from either tuff from outcrops at the Nevada Test Site, basalt from outcrops on the Hanford site, or salt from the WIPP site in New Mexico. Groundwater is then placed in these rock cups, and the cups are closed. For the tests in tuff, actual groundwater from a well (J-13) at the Nevada Test Site is used. In the case of basalt, a synthetic groundwater (GR-4), prepared in an oxygen-free environment, is used. For the salt tests, both inclusion and intrusion brines are used.

Although these laboratory tests are not all completed, they all indicate that the amount of radioactivity which will be free to travel with the groundwater will be a small fraction of the activity present in the waste glass. The results that follow are from the radioactive tests in tuff cups, in terms of concentrations.

In these tuff tests, solution concentrations of most elements were constant within experimental error after approximately 40 days, indicating that the rate of alteration of the glass had become very small. The final concentrations of species in solution were then used to provide estimates for the amount of material released by the waste glass. The concentrations were multiplied by an extremely conservative upper bound for the amount of groundwater which would be available for reaction (50 L), and then divided by the inventory of the individual species. This yielded the estimates of fractional release from these waste packages. The small fractions released are 500 - 1000 times less than the NRC requirement for the waste package as a whole. Similar numbers result from application of mass transfer methodology to the results of these tests. Thus, the tests indicate that DWPF glass should perform well in this environment.

RESULTS OF TUFF SIMULATED REPOSITORY TESTS

SPECIES	FINAL CONCENTRATION	ANNUAL FRACTIONAL RELEASE
Cs	0.9 μg/mL	6×10^{-8}
Sr	2.0	3×10^{-8}
Pu	0.03	1×10^{-8}

Verification Testing

The results and conclusions from SRL's mechanistic efforts are being verified in several ways:

- Extensive testing of waste glass in burial experiments in underground laboratories, to relate performance in the laboratory to the actual repository.
- Large-scale leaching experiments using thick slices from full-scale canisters of simulated waste glass, to relate the performance of laboratory-size samples to that of full-scale canisters of waste glass.
- Extensive testing of simulated and actual waste glasses prepared according to the DWPF process, to relate the performance of laboratory-prepared samples to that of glass made in the DWPF.

The most advanced of these verification programs is that in which samples of simulated waste glass have been buried in underground facilities. Extensive testing has been carried out in the Stripa mine in Sweden, where samples of several simulated waste glasses have been buried in granite for over a year. In this joint effort, scientists from SRL, KBS (the Swedish nuclear program), and the University of Florida have found only a slight interaction between glass and groundwater in the first month of testing, and virtually none thereafter. This agrees well with laboratory tests which also show that steady-state is reached rather quickly. The thermodynamic approach previously alluded to was also applied to these tests, with the results shown in Figure 11. The amount of material released in two years was approximately 50 times less than regulatory limits.

A more extensive set of burial tests has begun in the Waste Isolation Pilot Plant (WIPP) facility in New Mexico. In these tests, samples of simulated waste glasses from seven countries have been emplaced in salt approximately 2,000 feet underground. These samples are being subjected to brine attack under both expected and unexpected but possible conditions in a salt repository.

The relevance of the mechanistic studies have also been verified in other ways. For example, full-scale canisters of nonradioactive simulated waste glass, filled according to the DWPF process in the SRL Engineering Test Facility, have been sliced into sections 18 to 24 inches high. These

large slices were then immersed in large leach vessels of deionized water, and leached under conditions approximating the standard MCC-1 test. A companion set of experiments was performed with laboratory-size samples of the same glass to determine the appropriate relationship between laboratory and full-scale tests. When differences in surface preparation of the samples were removed from the data, there was excellent agreement between the two data sets.

SRL is also continuing to rigorously characterize and test glass samples made according to the DWPF process. The purpose of this effort is to establish that the results of tests of laboratory-prepared samples are relevant to the performance of DWPF glass. For example, samples of glass of the same composition were prepared in a 50 cc crucible, a 3 kg continuous electric melter, and in a 1,500 kg capacity continuous melter, with residence times ranging from 3 to 70 hours. As shown in Figure 12, the performance of the glass did not vary appreciably with the size of the melter. Thus, the performance of DWPF glass actually produced in the DWPF will be similar to that of glass made in the laboratory. Similar studies will determine the effects of other processing variables, such as melt temperature, on the performance of the DWPF product. Ultimately, a response surface model relating process variables to product performance will be generated.

DWPF CANISTER

Canister Grapple Assembly

The lifting grapple is specific for the DWPF canister and was developed by Remote Technology Corp. (REMOTEC) of Oak Ridge, TN (see references). The design is described in detail in the literature, therefore only the principles will be described here. Figure 13 is an assembly drawing..

Maximum size	Diameter =	600 mm
	Length =	1,000 mm
Capacity	6,820 kg, rated.	
Operation	Two-step release, failsafe. Transported by in-cell crane.	
Mechanism	All mechanical.	
Design life	60,000 cycles over 5 years without lubrication.	
Repair	Contact maintenance after high pressure wet decontamination.	
Failure recovery	Manual release activated by 4 kg maximum pull force.	
Materials	Stainless steel.	
Testing	Load test:	125% of rated load
	Cycle test:	500 cycles at rated load
	Misalignment:	Engage canister neck with 25 mm offset from grapple centerline
	Collision:	Strike object with crane traveling at 9 m/min.

Canister Dimensions

Canister dimensions and weight are shown in Figure 14 from drawing W832094 - Rev. 5, "DWPF Canister Assembly".

Principal dimensions and tolerances are:

Overall length	118.00 in. ± 0.06 in.
Outside diameter	24.00 in. ± 0.12 in.
Wall thickness	3/8 in. nominal pipe tolerance
Bow	0.12 in. max
Surface finish	125 rms
Inside volume	26.0 ft^3 nominal
Weight, empty	1100 lb
Weight, 85% full	4800 lb
Material	Type 304L stainless steel

Material of Construction

Type 304L stainless steel was chosen as the canister material for vitrified waste using the continuous melter process. This recommendation is based on long-term heating tests for up to 20,000 hours (2.3 yr) at temperatures that bracket those expected during interim storage. In these tests, the lifetime of canisters containing vitrified waste glass stored in air was predicted. The measured thickness of the reaction layer between the canister alloy and the canister alloy-environment, similar to that expected during interim storage, was extrapolated to estimate the time required for penetration of the 3/8-in thick canister.

Data from tests indicate that a 3/8-in. thick canister of type 304L stainless steel would not be penetrated for more than 8,000 years in a surface facility. By contrast, a 3/8-in. thick low carbon steel canister would be penetrated by oxidation in about 200 years of storage in a surface facility, and its strength would be reduced in a much shorter period.

Differences in canister lifetimes, predicted from these tests, are attributable to the differences in corrosion resistance of the candidate alloys. Both type 304L stainless steel and low carbon steel react similarly with vitrified waste, but type 304L stainless steel is much more resistant to both high temperature and atmospheric corrosion in a radiation field than is low carbon steel. The lifetime of canisters constructed from other compositions of austenitic stainless steels would be expected to be similar to that of type 304L.

Stainless steel has the additional advantage of forming a relatively thin oxide layer when heated by the molten glass. Tests made at Pacific Northwest Laboratory (PNL) indicate that an inert gas blanket would have to be used with a carbon steel canister to reduce the oxide scale formation to less than 22 lb per canister. Furthermore, the stainless steel surface is much easier to decontaminate by blasting with a frit-water slurry than is carbon steel.

The 3/8 in. nominal wall thickness of a 24-in. OD, schedule 20, stainless steel pipe is adequate for DWPF processing. A theoretical stress analysis was made on the reference canister just after it was filled with glass at the instantaneous pour rate of 3.8 lb/min. A maximum wall temperature of 427°C and a maximum bottom temperature of 649°C were assumed. The calculations show that the wall is sufficiently thick to permit the canister to be picked up immediately after it is filled, despite the residual shell hoop stress of 32,500 psi caused by the lower coefficient of thermal expansion of glass compared to that of stainless steel. Furthermore, the hoop stress quickly drops to about

5000 psi (at 500°C) due to the glass moving up into the canister void space as it gradually cools. Similarly, the thermal axial stresses were calculated to be 18,900 psi, and the simple static stresses due to weight were 477 psi shear and 177 psi axial. None of these stress levels indicates the need for a wall thickness greater than 3/8 in.

Canister Weight

The reference design canister is filled with approximately 165 gal of glass (22.1 ft^3) to a fill height of 91 in. This volume corresponds to a nominal weight of 3,700 lb for the current frit (Frit 200) and waste loading, and is about 85% of the available canister volume. The fill volume was chosen based upon operating experience where a 15% void is made available in the event of: low density foam partially filling the canister; "roping" of the glass stream causing voids in the frozen melt; and the possibility of spilling glass on the process room floor due to malfunction of load cells, level instrumentation, failure of pouring equipment, or operator error. After operating experience is gained, it may be possible to fill the canister to the top of the straight section of pipe at the intersection of the head with the cylinder. This volume is 25.3 ft^3 corresponding to a glass weight of 4,200 lb and a fill height of 104 in.

At the completion of pour, the centerline temperature at a point 37 in. from the canister base is about 750°C. At this temperature, the glass density can vary between 2.45 - 3.02 g/cm^3 corresponding to a glass fill weight ranging between 3,380 - 4,170 lb. The glass density variation is a function of the frit composition, waste loading, and waste composition.

Internal Pressurization Potential

Internal pressure within the canister is due to the accumulation of helium from alpha emissions of transuranic nuclides. A DWPF canister filled with waste glass produces about 0.32 cm^3 of helium per year at 40°C. The helium produced is assumed to diffuse through the glass into the void space above the solid glass surface. At the end of 1,000 years, the 103-liter void space pressure has increased by only 0.05 psi. This negligible pressure buildup is of no concern in waste package design. For the case of a canister filled to 25.3 ft^3 (733 L), the 23-liter void space pressure would increase by 0.2 psi.

Seal Weld

The reference process for sealing the canister is to resistance weld a 5-in. dia, 1/2-in. thick, type 304L stainless steel plug into the canister neck. A force of 75,000 lb, a current of 225,000 amps, and a voltage of approximately 10 volts is used to make the 1.5-sec weld. The technique was chosen after consideration of seven alternative processes including gas tungsten arc, gas metal arc, plasma arc, Thermit, electron beam, laser beam, and friction welding, because of the high weld quality and relatively simple equipment required. Weld tensile strength measurements were made on the upset resistance weld under varying conditions of oxidation to determine the need for machining the throat surface after the canister is filled with glass. An upset resistance weld with a 5-in. dia plug and a machine canister neck was leaktight to approximately 10^{-8} atm/cc/sec for a hydrostatic test pressure of 5,000 psi. If the canister neck is heated to 600°C, but not machined before it is welded, then the weld strength as measured by tensile and hydrostatic tests was reduced by about 20%. However, temperature measurements made on the canister neck during glass filling indicate that the maximum neck temperature does not exceed 300°C, so the canister seal weld is capable of withstanding at least 4,000 psi internal pressure while maintaining a leak tightness of 1×10^{-8} atm/cc/sec.

In the event that the canister is used in a repository with a flexible overpack and an open-ended sleeve, the canister could be subjected to relatively high lithostatic or hydrostatic pressures. The maximum pressure in a repository is expected to be less than 18 MPa (2,610 psi) which will buckle the 3/8-in. canister head above the glass melt surface. To prevent buckling, the head could have supporting ribs welded to the head interior or a thicker spherical head could be used. Present repository designs use rigid overpacks which are capable of withstanding repository pressures without collapsing.

Canister Decay Heat and Activity

Table 19 and Figure 15 describe the canister decay heat as a function of time for sludge-precipitate glass over a period of 5 to 1,000 years. The starting point is a sludge age of 5 years combined with precipitate from 15-year-old supernate. Figure 16 shows the canister activity for the same period. After a period of 300 years, the decay heat has decreased to about 7 watts and the activity to about 400 curies.

Fissionable Material Content

The fissionable material content of a sludge-precipitate glass canister is nominally 297 grams for sludge cooled 5 years, and for supernate cooled 15 years. Distribution of the thermal neutron fissionable nuclides is summarized below:

Fissionable Isotopes in One Canister

	g/lb of glass	g/can.[a]
U-233	4.43E-08	-
U-235	1.96E-02	73
Pu-239	5.61E-02	208
Pu-241	4.46E-03	16
		297

[a]Based on 3,700 lb of glass.

A nuclear criticality safety assessment was made for the DWPF glass melter and for storage of canisters in the interim storage building. The infinite neutron multiplication factor (k_∞) was calculated for two concentrations of Pu-239 and U-235 for the melter and the storage building.

Neutron Multiplication Factor (k_∞)
as a Function of Fissionable Isotopes
in Melter and Interim Storage Building

	Melter		Interim Storage Building	
	Conc 1	Conc 2	Conc 3	Conc 4
Pu-239[a]	1,120	560	280	140
U-235[a]	4,030	2,015	1,000	500
k_∞	0.110	0.063	0.012	0.008

[a] Grams of isotope in 3,650 lbs. of glass

Canister Gamma and Neutron Radiation

Canister radiation as a function of distance for glass containing 5-year-old sludge and precipitate from 15-year-old supernate is described in Table 20. The chemical composition of the glass waste is described in Table 21, the uranium and transuranic radionuclide content in Table 22, and a list of the major contributing isotopes to the gamma dose rate in Table 23.

Table 24 compares calculations of DWPF canister gamma radiation by four different codes and companies. The SRP calculation was made using the "ANISN" and "QAD" codes, the GA Technologies calculation was made using the "PATH" code, the Westinghouse calculation using the "SCAP" and ANISN-W codes, and Bechtel Inc., calculation using GRACE-II. ANISN is a one dimensional discrete ordinate code, the other three codes use point kernal integration techniques. All calculations were made using similar waste glass formulations.

Table 25 compares calculations of DWPF canister neutron radiation by three different methods. Although the calculations differ by a factor of less than 2, the contribution to the total radiation emitted from the canister is only 0.25 - 0.42 rem/hr.

Canister Surface Contamination

The criteria selected for canister surface contamination levels are identical to those specified for Department of Transportation cask shipping limits and are useful guides for canister decontamination by the frit-water slurry blasting technique. Canisters decontaminated to these levels are not expected to significantly contribute to air contamination within the Interim Storage Building. The canister surface contamination limits selected are:

Alpha	220 d/min/100 cm^2
Beta-Gamma	2200 d/min/100 cm^2

Labeling

Each canister will have a letter and four numbers located on the side wall and top head. The letter and numbers will be approximately 2 in. high and will be visible by television viewing. Each number will permit identification of the canister fabrication and processing history.

Canister Temperature

Table 26 describesthe temperature of a canister containing a sludge-precipitate wasteform at power levels of 425 to1000 watts, when in air at temperatures of 20°C and 38°C. Surface temperature of a 690-watt canister is estimated to be 58°C for an air temperature of 38°C. The centerline temperature is estimated to be 89°C for 38°C air temperature.

ESTIMATED PRODUCTION SCHEDULE

The power level and activity of canisters produced in the DWPF as a function of time is dependent on the mixing logistics of sludge, salt, and supernate in the waste tank farm.. In general, the intent is to remove waste from the oldest tanks first, since these tanks also contain the oldest waste. There are, however, practical constraints which limit the flexibility of transfer between areas, as well as between tanks, so that the present sludge inventory is segregated by processing area, somewhat segregated by type (HAW or LAW) and partially segregated by age.

The waste tank sludge and supernate blending schedule continues to be developed and refined. The preliminary schedule was described in "Characteristics of Spent Fuel, High-Level Waste, and Other Radioactive Wastes Which May Require Long-Term Isolation", DOE/RW-0184, December 1987. The data shown in Tables 27 and 28 of this report were developed from the 1988 Integrated Database and updates and the OCRWM December 1987 report. Since the Integrated Database information is developed each year, the schedule will become more accurate as hot startup is approached.

A description of the SRP waste inventory projected to the end of calendar year 1988 is shown in Table 27. At that time, the expected waste volume will be about 127,000 m^3 (33.4 million gallons), contains 778 million curies, and generates 2,300 kilowatts. Contributions of the principal fission product radionuclides are also shown. Of the total, Sr-90/Y-90 and Cs-137/Ba-137 contibute 70% of the total curies.

Table 28 describes the average radioactivity and thermal power per canister of waste glass as a function of time. The table covers the period from 1991 to 2022. Although the table reflects the best estimate of the schedule as of December 1988, it does not necessarily represent the actual processing schedule and tankage allocations; consequently, the data should be updated each year as the radioactive startup date approaches.

REFERENCES

DWPF References

R. G. Baxter, "Design and Construction of the Defense Waste Processing Facility Project at the Savannah River Plant," **Proceedings Waste Management '86, Vol 2,** Tucson, AZ (1986).

K. L. Walker, J. R. White, K. A. Farnstrom, and R. E. Eversole, "Canister Grapple for the Defense Waste Processing Facility." **Proceedings, 34th Conference on Remote Systems Technology** (1986).

Savannah River Plant, **Defense Waste Processing Facility, Basic Data Report,** DPSP-80-1033,E. I. du Pont de Nemours and Company, Savannah River Laboratory, Aiken, SC 29808 (April 1985).

M. D. Boersma, "Process Technology for Vitrification of Defense High-Level Waste at the Savannah River Plant." **ANS-Fuel Reprocessing and Waste Management,** Jackson Hole, WY (August 1984).

Computer Code References

CCC-254, ANISN-ORNL, A Multigroup One-Dimensional Discrete Ordinance Transport Code with Anisotropic Scattering. ORNL Radiation Shielding Information Center, Oak Ridge, TN (1983).

CCC-255, ANISN-W, A One Dimensional Discrete Ordinates Transport Computer Program, ORNL Radiation Shielding Information Center, Oak Ridge, TN (1971).

CCC-307, QAD-CG, A Combinatorial Geometry Version of QAD-PSA, A Point Kernal Code for Neutron and Gamma Ray Shielding Calculations, ORNL Radiation Shielding Information Center, Oak Ridge, TN (1979).

CCC-418, SCAP, Single Scatter, Albedo Scatter, and Point Kernel Analysis Program in Complex Geometry, ORNL Radiation Shielding Information Center, Oak Ridge, TN (1982).

Glass Stability Programs

M. J. Plodinec, G. G. Wicks, and N. E. Bibler, " An Assessment of Savannah River Borosilicate Glass in the Repository Environment," USDOE Report DP-1629, E. I. du Pont de Nemours and Co., Savannah River Laboratory, Aiken, SC 29808 (1982).

J. E. Mendel (ed), "Final Report of the Defense High-Level Waste Leaching Program," USDOE Report PNL-5157, Battelle-Pacific Northwest Laboratory, Richland, WA 99352 (1984).

M. J. Plodinec, "Characterization of Savannah River Plant Waste Glass," **Waste Management 85,** 441-5 (1985).

G. G. Wicks, "Nuclear Waste Glasses," **Treatise on Materials Science and Technology, Glass IV,** 57-118 (1985).

G. G. Wicks, "Savannah River Waste Glass Performance," USDOE Report DP-MS-86-35, E. I. du Pont de Nemours and Company, Savannah River Laboratory, Aiken, SC 29808 (1986).

N. E. Bibler, "Glass Performance in a Geologic Setting," USDOE Report DP-MS-86-119, E. I.

du Pont de Nemours and Company, Savannah River Laboratory, Aiken, SC 29808 (1986).

Glass Composition Development

P. D. Soper, D. D. Walker, M. J. Plodinec, G. J. Roberts, and L. F. Lightner, "Optimization of Glass Composition for the Vitrification of Nuclear Waste at the Savannah River Plant," **Bull. Am. Cer. Soc., 62,** 1013-8 (1983).

G. G. Wicks, W. D. Rankin and S. L. Gore, "International Waste Glass Study-Composition and Leachability Correlations," **Scientific Basis for Nuclear Waste Management, VIII,** 171-177 (1985).

M. J. Plodinec, "Vitrification Chemistry and Nuclear Waste," **J. Non-Cryst. Solids, 84,** 206-14 (1986).

C. M. Jantzen, "Systems Approach to Nuclear Waste Glass Development," **J. Non-Cryst. Solids, 84,** 215-25 (1986).

Modeling

R. M. Wallace and G. G. Wicks, "Leaching Chemistry of Defense Borosilicate Glass," **Scientific Basis for Nuclear Waste Management, VI,** 23-29 (1983).

M. J. Plodinec, C. M. Jantzen, and G. G. Wicks, "Thermodynamic Approach to Prediction of the Stability of Proposed Radwaste Glasses," **Advances in Ceramics - Nuclear Waste Management, 8,** 491-95 (1984).

C. M. Jantzen and M. J. Plodinec, "Thermodynamic Model of Natural, Medieval and Nuclear Waste Glass Durability," **J. Non-Cryst. Solids, 67,** 207-23 (1984).

M. J. Plodinec, C. M. Jantzen and G. G. Wicks, "Stability of Radioactive Waste Glasses Assessed from Hydration Thermodynamics," **Scientific Basis for Nuclear Waste Management, VII,** 755-62 (1985).

Long-Term Testing

J. K. Bates, D. J. Lam and M. J. Steindler, "Extended Leach Studies of Actinide-Doped SRL 131 Glass," **Scientific Basis for Nuclear Waste Management, VI,** 183-90 (1983).

G. G. Wicks, G. T. Chandler and R. M. Wallace, "Chemical Durability of SRP Waste Glass - Saturation Effects and Influence of SA/V", USDOE Report DP-MS-84-37, E. I. du Pont de Nemours and Company, Savannah River Laboratory, Aiken, SC 29808 (1984). Available from NTIS, PC A03/MF A01(GPO Dep.).

Waste Glass Saturation Effects and Influence of SA/V

G. G. Wicks, J. A. Stone, G. T. Chandler and S. Williams, **Long Term Behavior of Simulated Savannah River Plant Waste Glass,** USDOE Report DP-1728, E. I. du Pont de Nemours, and Company, Savannah River Laboratory, Aiken, SC 29808 (1986).

Groundwater Eh and pH Effects

C. M. Jantzen, "Effects of Eh (Oxidation Potential) on Borosilicate Waste Glass Durability," **Advances in Ceramics - Nuclear Waste Management, 8,** 385-393 (1984).

C. M. Jantzen, "Methods of Simulating Low Redox Potential (Eh) for a Basalt Repository," Scientific Basis for Nuclear Waste Management, VII, 613-621 (1984).

C. M. Jantzen and G. G. Wicks, "Control of Oxidation Potential for Basalt Repository Simulation Tests," Scientific Basis for Nuclear Waste Management, VIII, , 29-35 (1985).

C. M. Jantzen and N. E. Bibler, "The Role of Groundwater Oxidation Potential and Radiolysis on Waste Glass Performance in Crystalline Repository Environments," Scientific Basis for Nuclear Waste Management, IX, Materials Research Society, Pittsburgh, PA 219-229 (1986).

Effect of Pressure

G. G. Wicks, W. C. Mosley, P. G. Whitkop, and K. A. Saturday, "Durability of Simulated Waste Glass - Effects of Pressure and Formation of Surface Layers," J. Non-Cryst. Solids, 49, 413-28 (1982).

Radiation Effects

N. E. Bibler, "Effects of Alpha, Gamma, and Alpha-Recoil Radiation on Borosilicate Glass Containing Savannah River Plant Defense High-Level Nuclear Waste," Scientific Basis for Nuclear Waste Management, IV, Elsevier, New York, 681-87 (1982).

J. K. Bates, L. J. Jardine, K. F. Flynn, and M. J. Steindler, "The Application of Neutron Activation Analysis to the Determination of Leach Rates of Simulated Nuclear Waste Forms," USDOE Report ANL-81-34, Argonne National Laboratory, Argonne, IL (February 1982).

G. W. Arnold, C. J. M. Northrup, and N. E. Bibler, "Near-Surface Leaching Studies of Pb-Implanted Savannah River Waste Glass," Scientific Basis for Nuclear Waste Management, V, Elsevier, New York, 359-68 (1983).

N. E. Bibler, "Characterization of Borosilicate Glass Containing Savannah River Plant Radioactive Waste," Glastekn. Ber., 56K, 736-41 (1983).

J. E. Mendel (ed), "Final Report of the Defense High-Level Waste Leaching Mechanisms Program," USDOE Report PNL-5157, Battelle-Pacific Northwest Laboratory, Richland, WA 99352 (1984).

Devitrification

C. M. Jantzen, D. F. Bickford, D. G. Karraker and G. G. Wicks, "Time-Temperature-Transformation Kinetics in SRL Waste Glass," Advances in Ceramics - Nuclear Waste Management, 8, 30-38 (1984).

D. F. Bickford and C. M. Jantzen, "Devitrification Behavior of SRL Defense Waste Glass," Scientific Basis for Nuclear Waste Management, VII, Elsevier, New York, 557-66 (1984).

C. M. Jantzen and D. F. Bickford, "Leaching of Devitrified Glass Containing Simulated SRP Nuclear Waste," Scientific Basis for Nuclear Waste Management, VIII, Materials Research Society, Pittsburgh, PA, 135-46 (1985).

D. F. Bickford and C. M. Jantzen, "Devitrification of Defense Nuclear Waste Glasses: Role of Melt Insolubles," J. Non-Cryst. Solids, 84, 299-307 (1986).

Large-Scale Leach Tests

P. K. Smith, and C. A. Baxter, "Fracture During Cooling of Cast Borosilicate Glass Containing Nuclear Wastes," USDOE Report DP-1602, E. I. du Pont de Nemours & Co., Savannah River Laboratory, Aiken, SC (1981).

D. J. Pellarin and D. F. Bickford, **Large Scale Leach Test Facility: Development of Equipment and Methods, and comparison to MCC-1**, USDOE Report DPST-85-615, E. I. du Pont de Nemours and Company, Savannah River Laboratory, Aiken, SC 29808 (1985).

D. F. Bickford and D. J. Pellarin, "Large Scale Leach Testing of DWPF Canister Sections," **Scientific Basis for Nuclear Waste Management, X** (1987).

Interactions with Package Components

G. G. Wicks, B. M. Robnett and W. D. Rankin, "Chemical Durability of Glass Containing SRP Waste-Leachability Characteristics, Protective Layer Formation, and Repository Systems Interactions," **Scientific Basis for Nuclear Waste Management, V** 15-24 (1982).

D. B. Burns, B. H. Upton and G. G. Wicks, "Interactions of SRP Waste Glass with Potential Canisters and Overpack Metals," **J. Non-Cryst. Solids, 84,** 258-267 (1986).

In-Situ Tests

D. E. Clark, B. F. Zhu, L. L. Hench, G. G. Wicks and L. O. Werme, "An Evaluation of Six-Month Burial Data from Stripa," **Rivista della Staz. Sper. Vetro., 5,** 185-95 (1984).

D. E. Clark, B. F. Zhu, R. S. Robinson and G. G. Wicks, "Preliminary Report on a Glass Burial Experiment in Granite," **Advances in Ceramics - Nuclear Waste Management, 8,** 324-36 (1984).

A. Lodding, D. E. Clark, L. O. Werme, and G. G. Wicks, "SRL Glasses Leached in a Burial Environment: SIMS Study of Element Distributions," Proceeding of the 1984 International Symposium on Glass, in Beijing.

D. E. Clark, B. F. Zhu and G. G. Wicks, "Nuclear Waste Glass Leaching-Comparison of Laboratory and Field Tests," Proceeding of the 1984 International Symposium on Glass, in Beijing.

B. F. Zhu, D. E. Clark, L. L. Hench, G. G. Wicks and L. O. Werme, "One-Year Leaching of Three SRL Glasses in Granite," **Scientific Basis for Nuclear Waste Management, VIII,** 187-194 (1985).

G. G. Wicks, **WIPP/SRL In-Situ and Lab Testing Programs-Part I: MIIT Overview, Nonradioactive Waste Glass Studies,** USDOE Report DP-1706, E. I. du Pont de Nemours and Company, Savannah River Laboratory, Aiken SC 29808 (1986).

G. G. Wicks, M. E. Weinle, and M. A. Molecke, "WIPP/SRL In-Situ Tests-Part II: Pictorial History of MIIT and Final MIIT Matrices, Assemblies, and Sample Listings," USDOE Report DP-1733, E. I. du Pont de Nemours and Company, Savannah River Laboratory, Aiken, SC 29808 (1987).

B. F. Zhu, D. E. Clark, A. Lodding, and G. G. Wicks, "Two-Year Leaching Behavior of Three SRL Nuclear Waste Glasses in Granite." **Advances in Ceramics, 20** 1987.

A. Lodding, E. U. Engström, D. E. Clark, L. O. Werme and G. G. Wicks, "SIMS Analysis of Leached Layers Formed on SRL Glasses During Burial." **Advances in Ceramics, 20** 1987.

G. G. Wicks, M. E. Weinle, and M. A. Molecke, "WIPP/SRL In-Situ Tests - Part II: Pictorial History of MIIT and Final MIIT Matrices, Assemblies, and Sample Listings," USDOE Report DP-1733, E. I. du Pont de Nemours and Company, Savannah River Laboratory, Aiken, SC 29808 (1987).

Repository Simulation Tests

G. G. Wicks, N. E. Bibler, C. M. Jantzen and M. J. Plodinec, "Repository Simulation Tests." E. I. du Pont de Nemours and Company, Savannah River Laboratory, Aiken, SC 29808 (1984). Available from NTIS PC A02/MF A01 (GPO Dep.).

J. E. Mendel (ed.), "Final Report of the Defense High-Level Waste Leaching Mechanisms Program," USDOE Report PNL-5157, Battelle-Pacific Northwest Laboratory, Richland, WA 99352 (1984).

N. E. Bibler, G. G. Wicks and V. O. Oversby, "Leaching of SRP Nuclear Waste Glass in a Saturated Tuff Environment," **Scientific Basis for Nuclear Waste Management, VIII,** 247-56 (1985).

G. G. Wicks, "Nuclear Waste Vitrification - The Geology Connection," **J. Non-Cryst. Solids, 84,** 241-50 (1986).

N. E. Bibler, M. J. Plodinec, G. G. Wicks and C. M. Jantzen, "Glass Performance in a Geologic Setting." USDOE Report DP-MS-86-119, E. I. du Pont de Nemours and Company, Savannah River Laboratory, Aiken, SC 29808 (1986).

N. E. Bibler and C. M. Jantzen, "Materials Interactions Relating to Long-Term Geologic Disposal of Nuclear Waste Glass," **Scientific Basis for Nuclear Waste Management, X**(1987).

W. D. Rankin and G. G. Wicks, "Chemical Durability of SRP Waste Glass as a Function of Waste Loading." **J. Am. Cer. Soc., 66,** 417-420 (1983).

B. F. Zhu, D. E. Clark, L. L. Hench, and G. G. Wicks, "Leaching Behavior of Nuclear Waste Glass Heterogeneities." **J. Non-Cryst. Solids, 80,** 324-34 (1986).

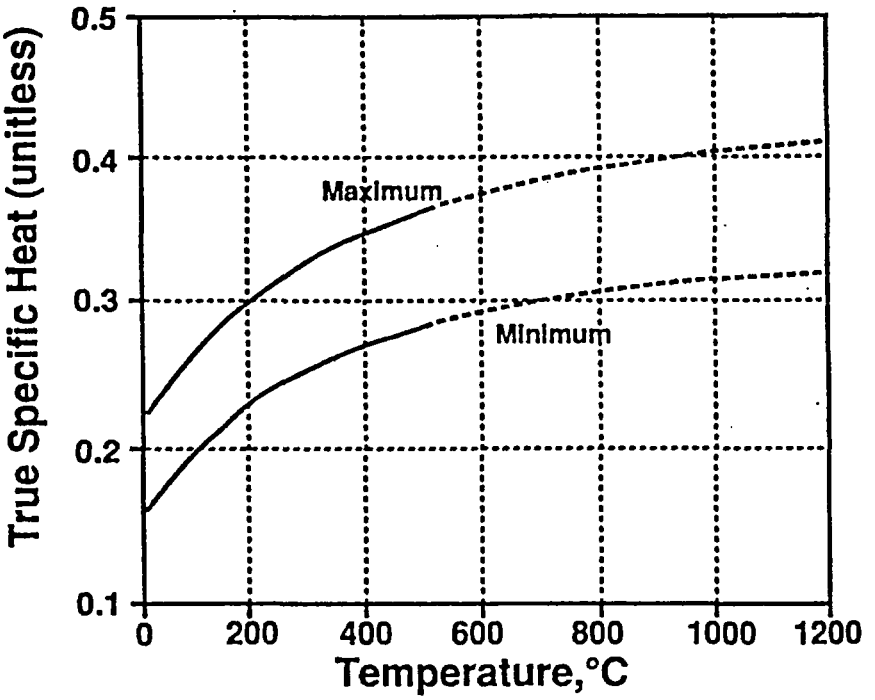

Figure 1. Calculated True Specific Heat of DWPF Glass

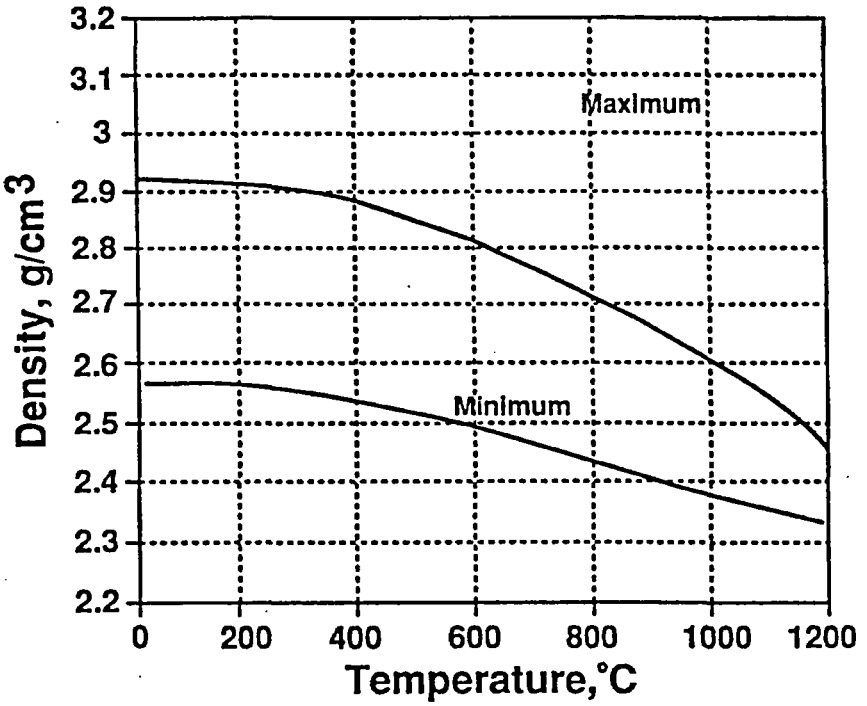

Figure 2. Calculated Density of DWPF Glass

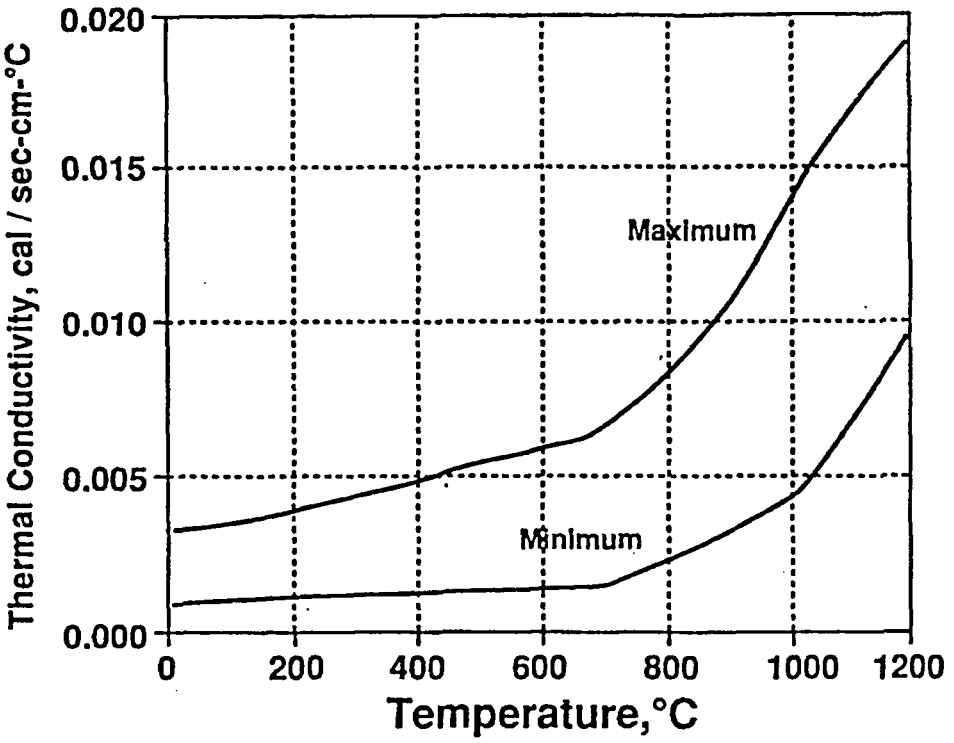

Figure 3. Calculated Thermal Conductivity of DWPF Glass

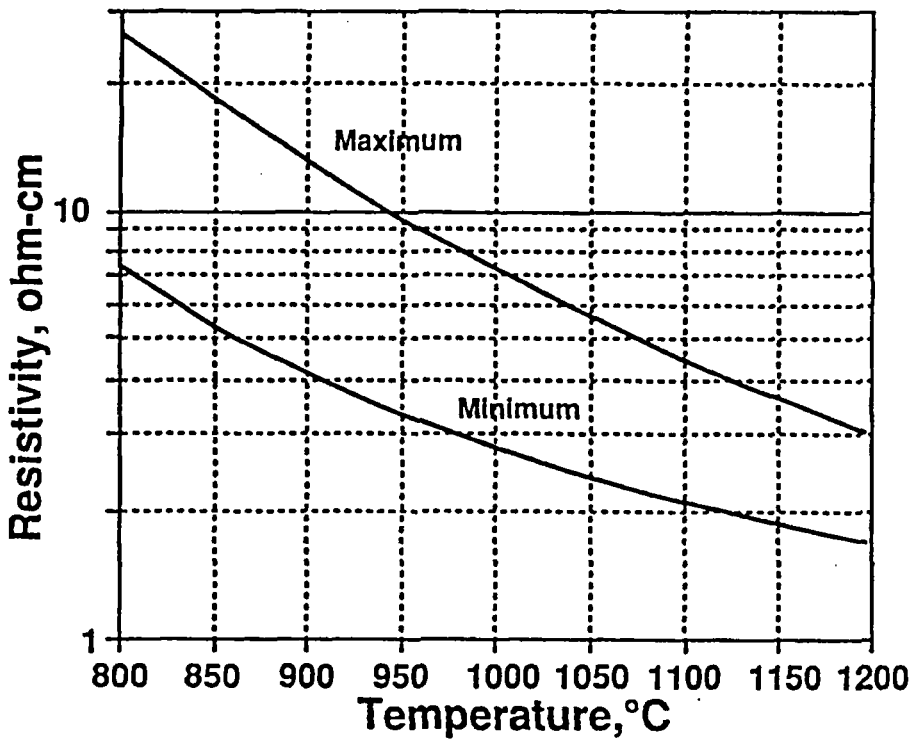

Figure 4. Experimental Resistivity of DWPF Glass

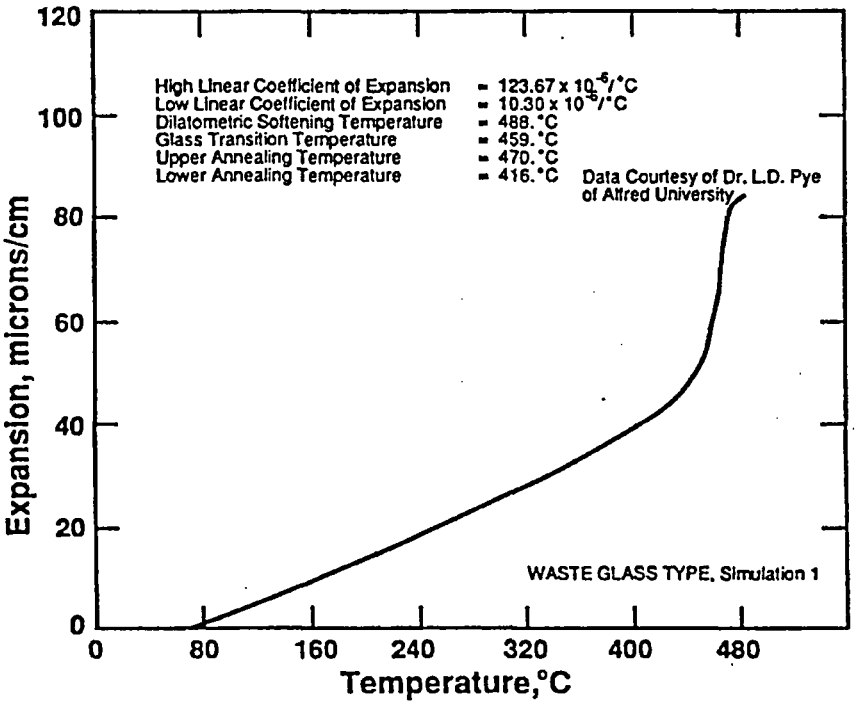

Figure 5. Experimental Thermal Expansion Data for Simulated Waste Glass, Simulation 1

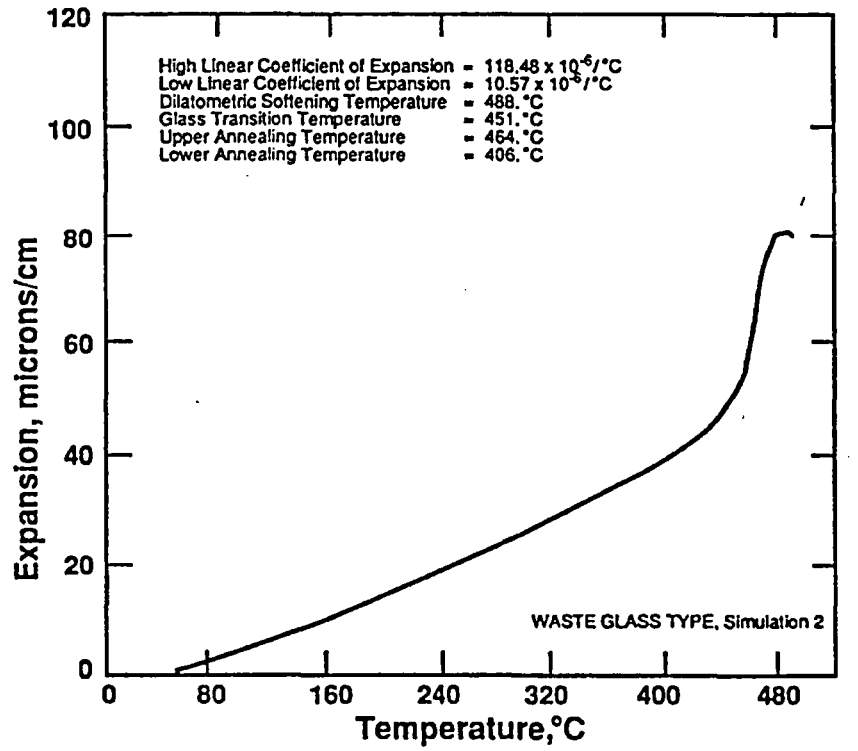

Figure 6. Experimental Thermal Expansion Data for Simulated Waste Glass, Simulation 2

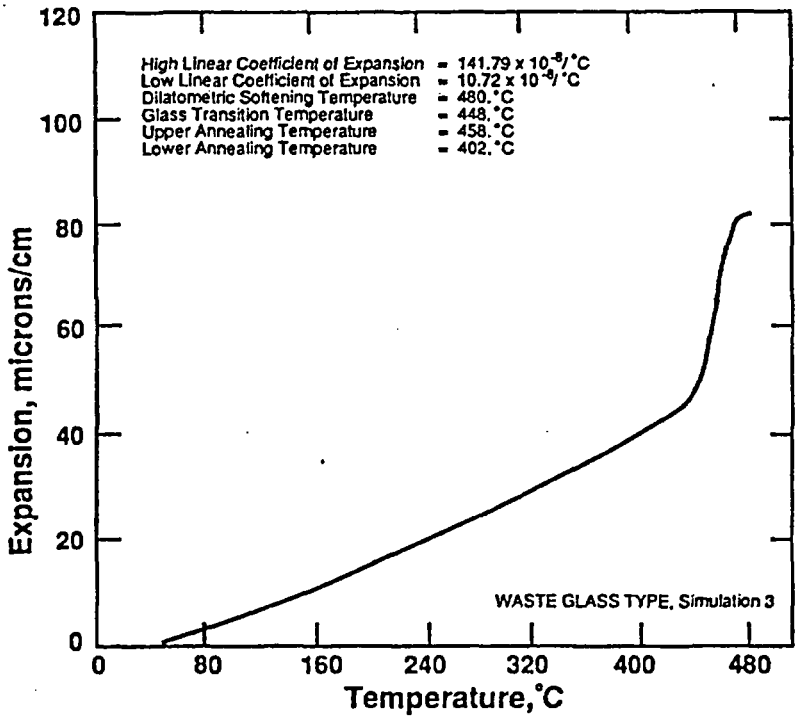

Figure 7. Experimental Thermal Expansion Data for Simulated Waste Glass, Simulation 3

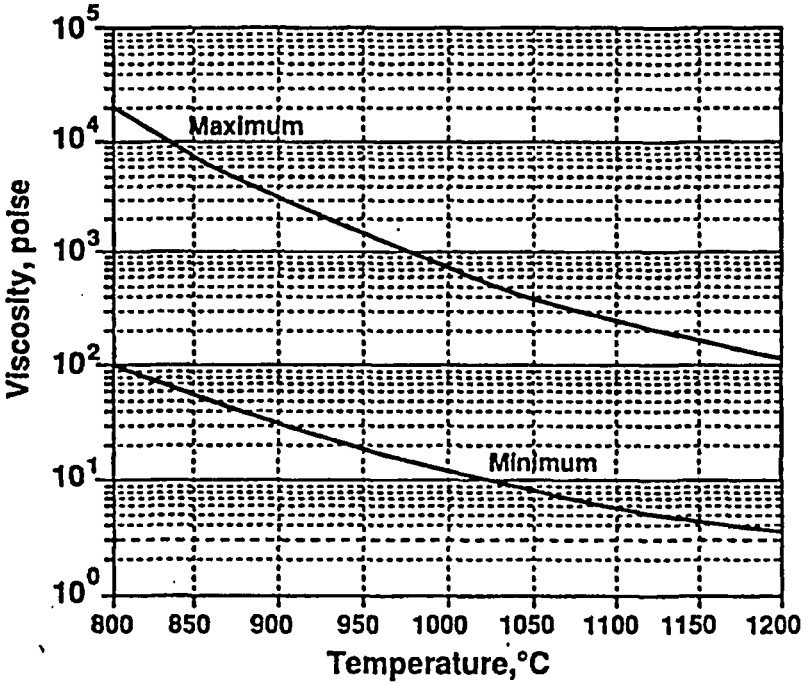

Figure 8. Experimental Viscosity of DWPF Glass

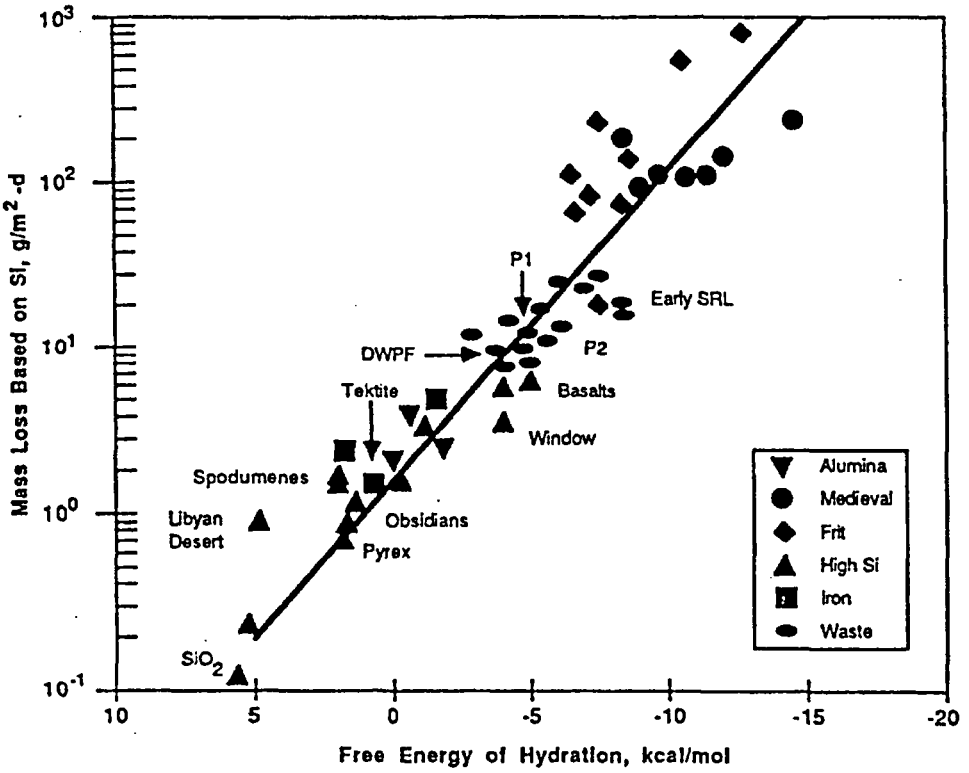

Figure 9. Durability of Glasses and Minerals in an MCC-1 Leach Test. Glasses were Exposed for 28 Days in 90°C Deionized Water.

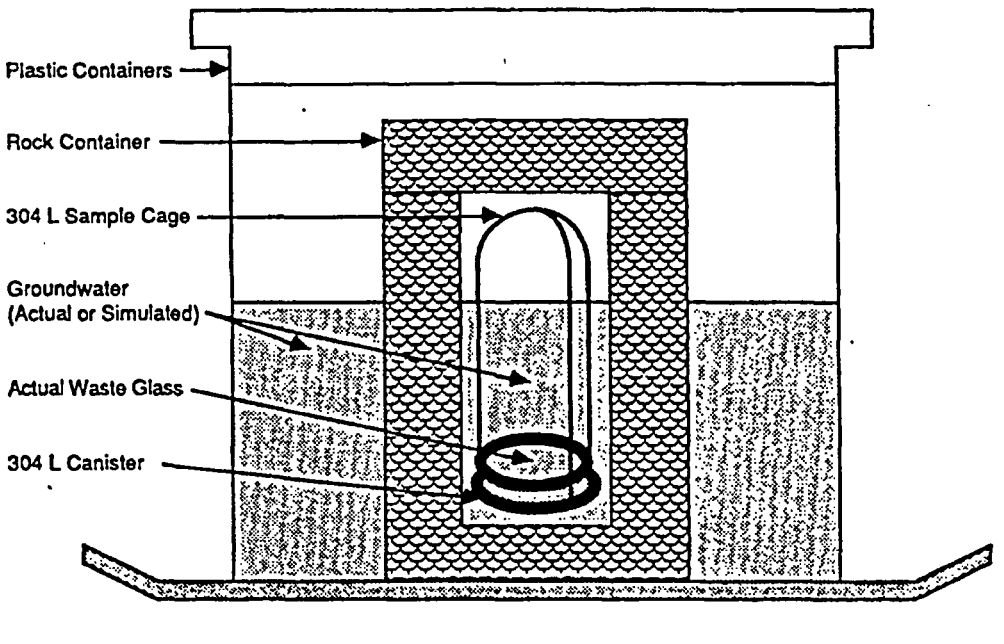

Figure 10. Repository Simulation Test Vessels

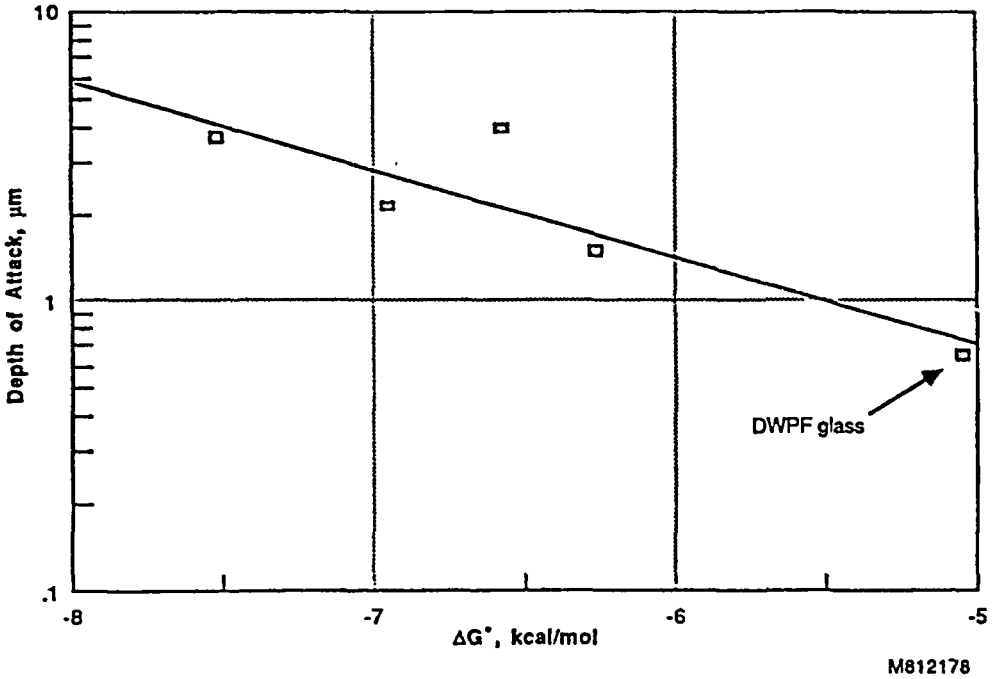

Figure 11. Results from 2-Year Burial Experiments

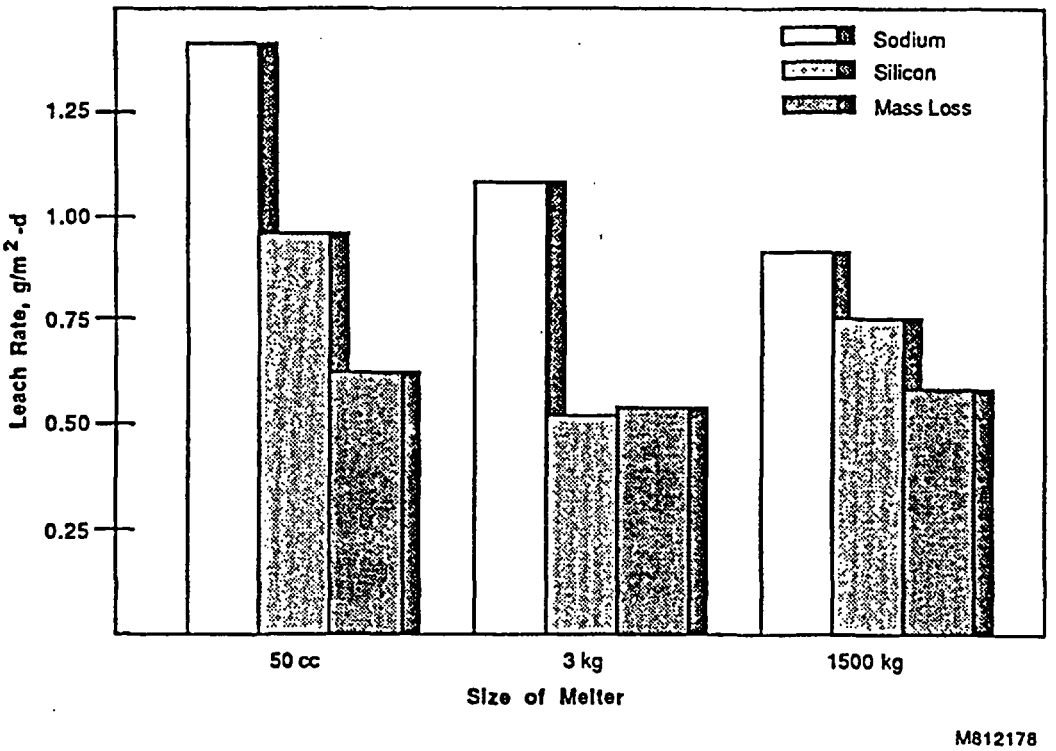

Figure 12. Effect of Melter Size on Glass Leaching

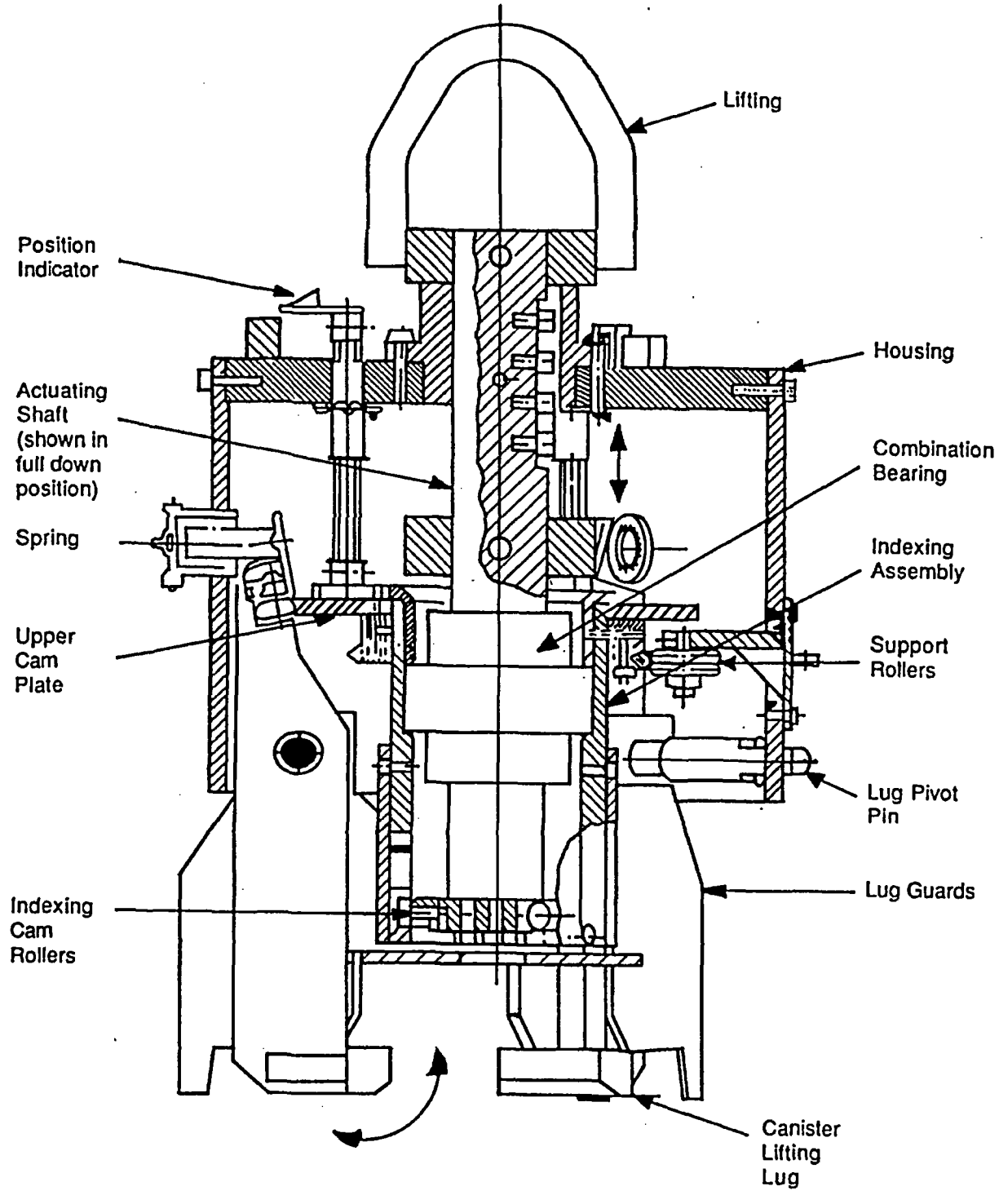

Figure 13. Canister Grapple

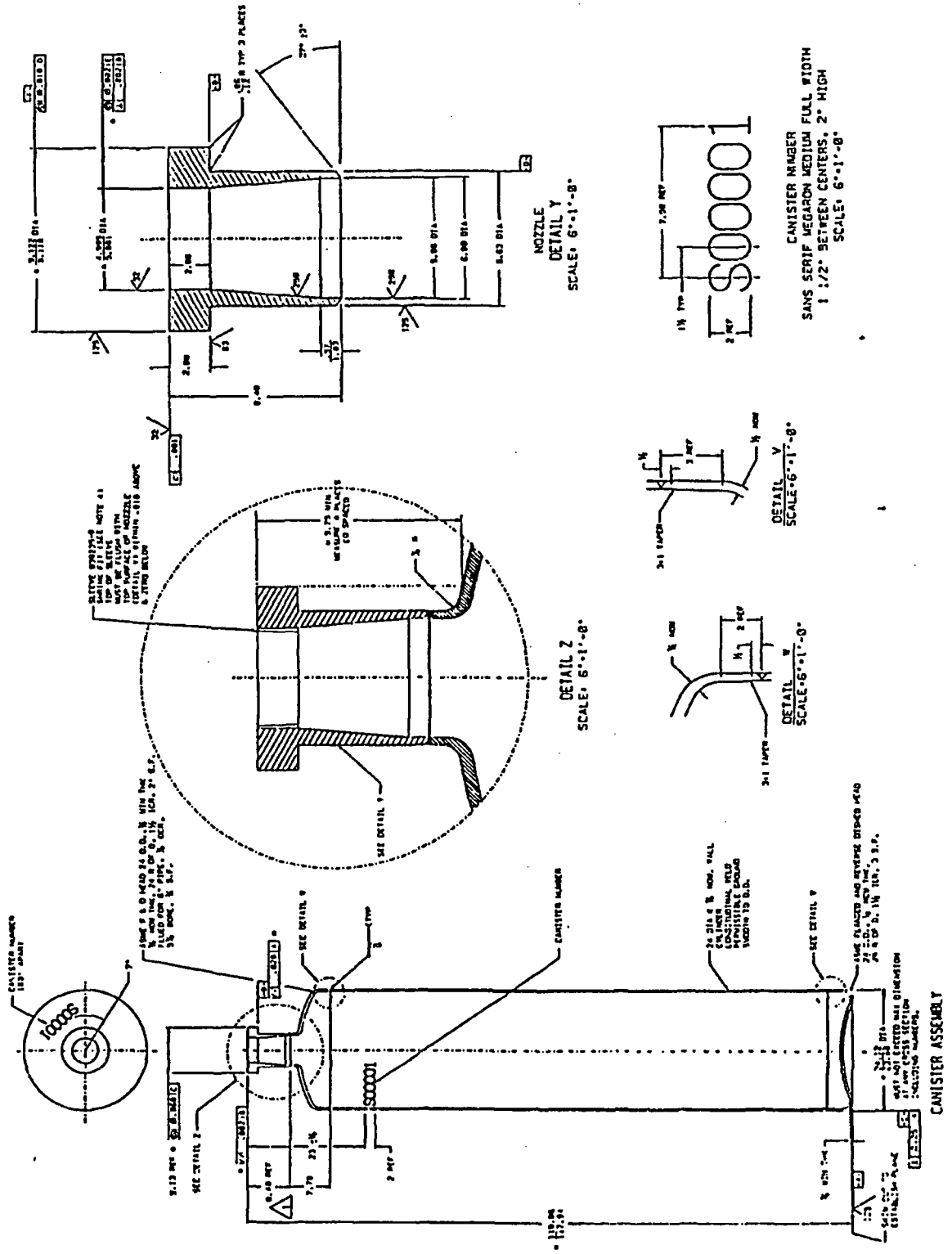

Figure 14. Canister Assembly

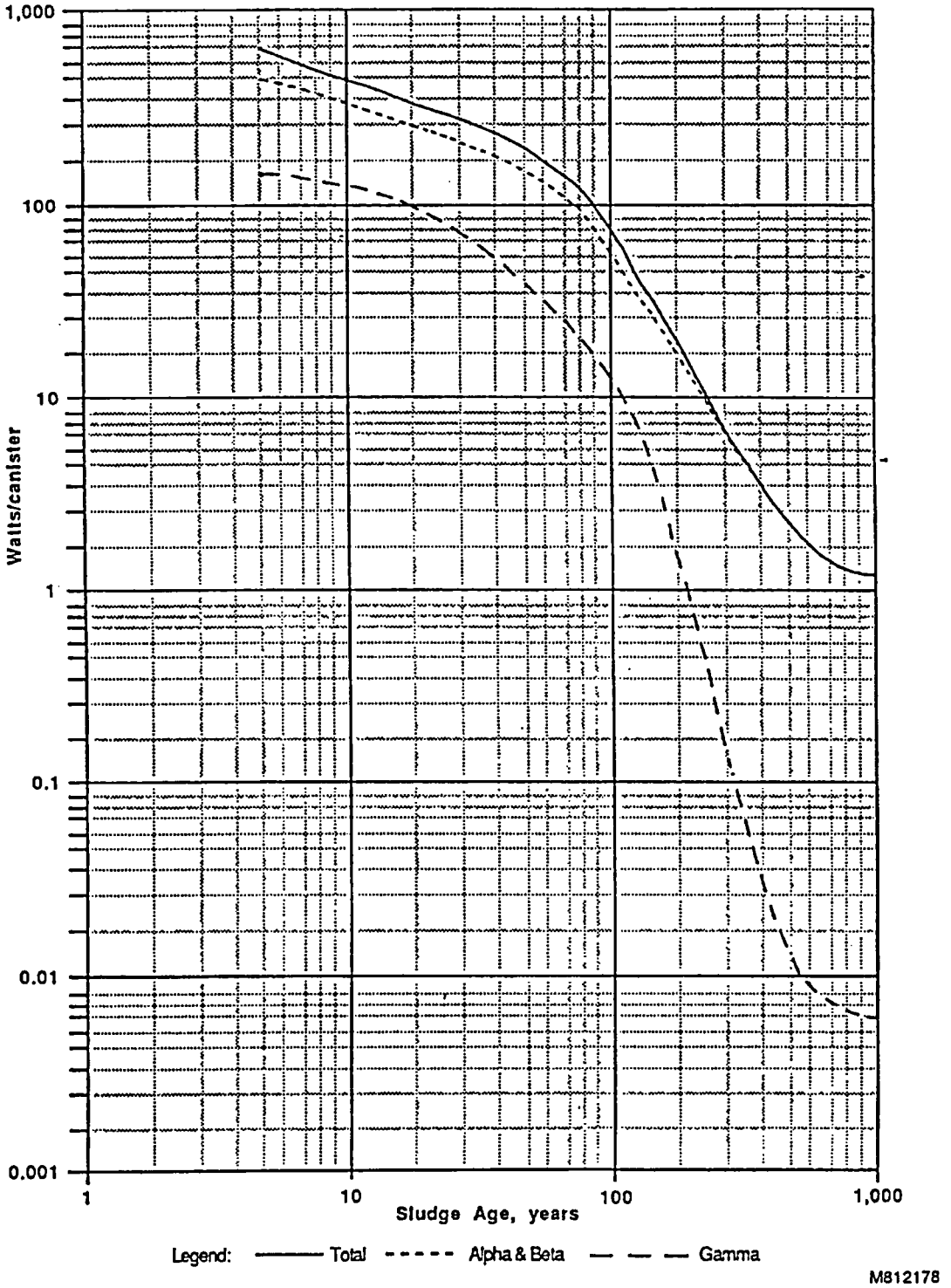

Figure 15. Sludge-Precipitate Canister Decay Heat

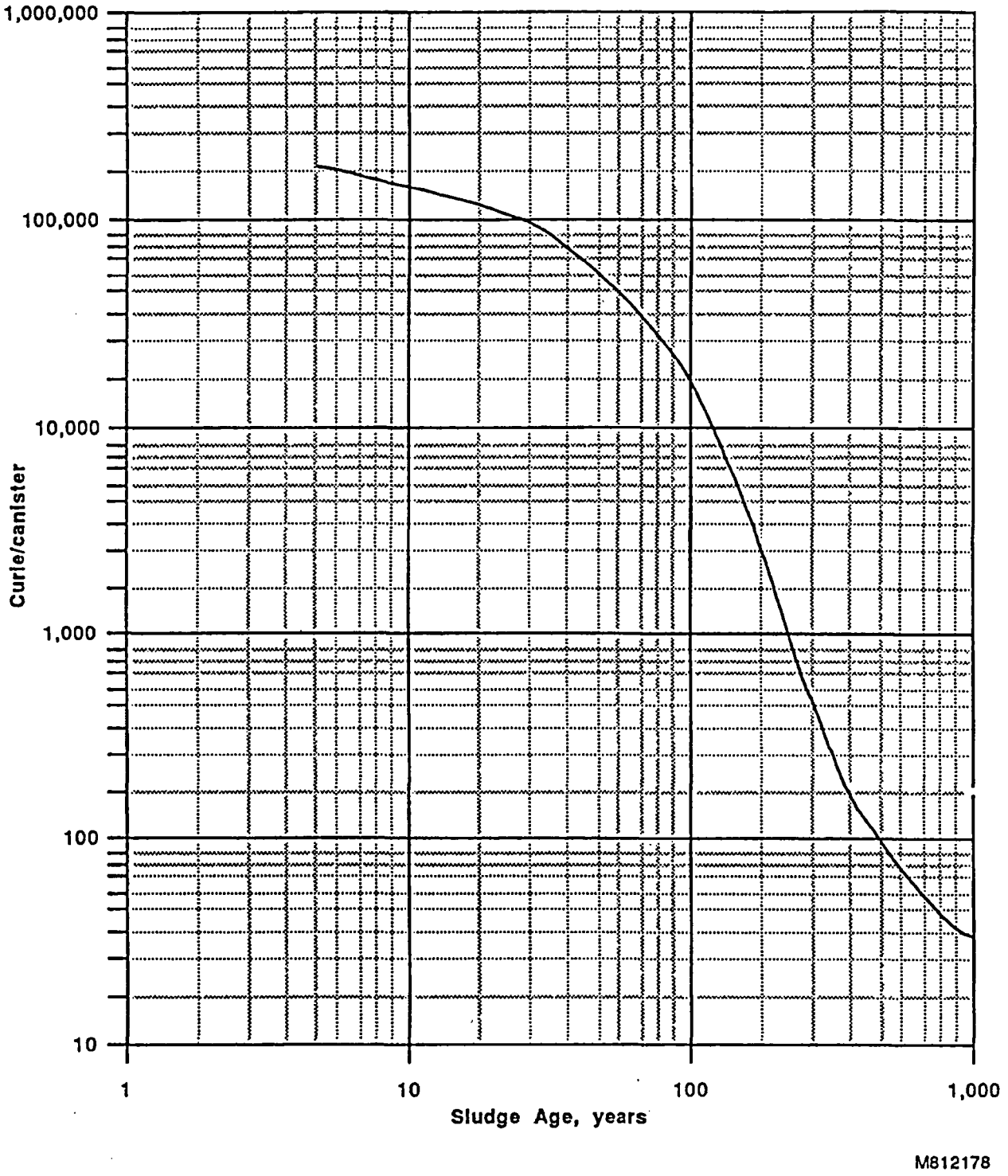

Figure 16. Sludge-Precipitate Canister Activity

Table 1A

Chemical Composition of Sludge Feed Soluble Solids (Dry Basis)

Component	wt%	Component	wt%
$Ba(NO_3)_2$	0.649E-02	Na_2SO_4	0.492E+01
$CaSO_4$	0.642E-03	NA_2SiO_3	0.116
$CsNO_3$	0.716E-02	NA_3PO_4	0.349
Group A[a]	0.390E-02	$NaAg(OH)_2$	0.191E-03
KNO_3	0.500	$NaAl(OH)_4$	0.107E+02
NH_4NO_3	0.199E-01	NaCl	0.307
Na[(HgO)(OH)]	0.829E-02	NaF	0.154
$Na_2C_2O_4$	0.267	NaI	0.372E-03
Na_2CO_3	0.432E+01	$NaNO_2$	0.194E+02
Na_2CrO_4	0.133	$NaNO_3$	0.406E+02
Na_2MoO_4	0.219E-01	NaOH	0.182E+02
Na_2RhO_4	0.552E-03	$UO_2(OH)_2$	0.302E-04
Na_2RuO_4	0.237E-02		

[a] Cd, Mo, Rb, Se, Tc, and Te.

Table 1B

Chemical Composition of Sludge Feed Insoluble Solids (Dry Basis)

Component	wt%	Component	wt%
AgOH	0.168	Na_2SO_4	0.132
$Al(OH)_3$	0.157E+02	Na_3PO_4	0.121E-01
$BaSO_4$	0.386	NaCl	0.110E+01
$Ca_3(PO_4)_2$	0.189	NaF	0.965E-01
CaC_2O_4	0.878	NaI	0.161E-01
$CaCO_3$	0.346E+01	$NaNO_3$	0.232E+01
CaF_2	0.151	NaOH	0.403E+01
$CaSO_4$	0.281	$Ni(OH)_2$	0.320E+01
Carbon	0.125	$PbCO_3$	0.114
$Co(OH)_3$	0.109E-01	$PbSO_4$	0.280
$Cr(OH)_3$	0.443	Pd(OH)2	0.622E-01
$CsNO_3$	0.124E-01	PuO_2	0.577E-01
$Cu(OH)_2$	0.159	RhO_2	0.262E-01
$Fe(OH)_3$	0.405E+02	RuO_2	0.134
Group A[a]	0.240	SiO_2	0.308E+01
Group B[b]	0.104E+01	$SrCO_3$	0.177
HgO	0.141E+01	ThO_2	0.567
KNO_3	0.536	$UO_2(OH)_2$	0.673E+01
$Mg(OH)_2$	0.400	$Y_2(CO_3)_3$	0.688E-01
MnO_2	0.691E+01	Zeolite	0.453E+01
		$Zn(OH)_2$	0.270

[a] Cd, Mo, Rb, Se, Tc, and Te.

[b] Ag, Am, Ce, Cm, Co, Cr, Eu, La, Nb, Nd, Np, Pm, Pr, Sb, Sm, Sn, Tb, Tl, and Zr.

Table 2

Radionuclide Content of Sludge Feed

Isotope	Ci/Gal	Isotope	Ci/Gal	Isotope	Ci/Gal
H-3	1.93E-05	Sb-126m	1.28E-04	Eu-154	5.48E-01
C-14	3.21E-08	Te-125m	2.56E-01	Eu-155	4.21E-01
Cr-51	8.24E-20	Te-127	1.12E-04	Eu-156	4.64E-35
Co-60	1.50E-01	Te-127m	1.14E-04	Tb-160	9.91E-10
Ni-59	2.08E-05	Te-129	2.84E-15	Tl-208	9.70E-07
Ni-63	2.58E-03	Te-129m	4.44E-15	U-232	1.17E-05
Se-79	1.58E-04	I-129	1.31E-08	U-233	1.38E-09
Rb-87	5.55E-10	Cs-134	1.41E-01	U-234	2.98E-05
Sr-89	3.72E-08	Cs-135	2.47E-06	U-235	1.37E-07
Sr-90	4.05E+01	Cs-136	4.26E-43	U-236	9.80E-07
Y-90	4.16E+01	Cs-137	1.34E+00	U-238	9.14E-06
Y-91	6.57E-07	Ba-136m	7.52E-42	Np-236	1.52E-11
Zr-93	9.90E-04	Ba-137m	1.28E+00	Np-237	7.74E-06
Zr-95	8.90E-06	Ba-140	8.95E-40	Pu-236	1.07E-04
Nb-94	8.39E-08	La-140	3.83E-40	Pu-237	7.81E-15
Nb-95	1.89E-05	Ce-141	3.18E-14	Pu-238	1.30E+00
Nb-95m	1.10E-07	Ce-142	8.45E-09	Pu-239	1.13E-02
Tc-99	2.78E-03	Ce-144	8.74E+00	Pu-240	7.59E-03
Ru-103	1.50E-11	Pr-143	1.06E-37	Pu-241	1.46E+00
Ru-106	2.00E+00	Pr-144	8.74E+00	Pu-242	1.07E-05
Rh-103m	1.46E-11	Pr-144m	1.04E-01	Am-241	9.47E-03
Rh-106	2.01E+00	Nd-144	4.27E-13	Am-242	1.26E-05
Pd-107	1.27E-05	Nd-147	1.12E-47	Am-242m	1.26E-05
Ag-110m	1.10E-04	Pm-147	2.14E+01	Am-243	5.06E-06
Cd-113	4.64E-17	Pm-148	6.16E-14	Cm-242	3.09E-05
Cd-115m	1.13E-12	Pm-148m	8.93E-13	Cm-243	4.88E-06
Sn-121m	2.54E-05	Sm-147	1.73E-09	Cm-244	9.40E-02
Sn-123	2.26E-04	Sm-148	5.02E-15	Cm-245	5.84E-09
Sn-126	1.29E-04	Sm-149	1.55E-15	Cm-246	4.66E-10
Sb-124	6.31E-11	Sm-151	2.16E-01	Cm-247	5.72E-16
Sb-125	7.34E-01	Eu-152	3.26E-03	Cm-248	5.98E-16
Sb-126	1.80E-05				

Total actvity	1.33E+02 Ci/Gal
Decay heat	
Total primary	4.21E-01 Watt/Gal
Total gammas	1.92E-02 Watt/Gal

Table 3

Partial Isotopic Content of Sludge Feed

Isotope	G/Gal	Isotope	G/Gal	Isotope	G/Gal
H-3	2.01E-09	Ru-104	7.21E-02	Te-125	2.86E-03
C-14	7.21E-09	Ru-106	5.98E-04	Te-125m	1.42E-05
Cr-51	8.92E-25	Rh-103	7.52E-02	Te-126	1.25E-04
Co-60	1.33E-04	Rh-103m	4.48E-19	Te-127	4.23E-11
Ni-59	2.57E-04	Rh-106	5.64E-10	Te-127m	1.21E-08
Ni-63	4.37E-05	Pd-104	9.85E-03	Te-128	3.41E-02
Se-77	3.66E-04	Pd-105	7.85E-02	Te-129	1.36E-22
Se-78	9.19E-04	Pd-106	5.06E-02	Te-129m	1.47E-19
Se-79	2.26E-03	Pd-107	2.46E-02	Te-130	1.23E-01
Se-80	5.40E-03	Pd-108	1.45E-02	I-127	1.99E-05
Se-82	1.09E-02	Pd-110	5.04E-03	I-129	7.40E-05
Rb-85	2.58E-03	Ag-109	5.13E-03	Cs-133	1.69E-02
Rb-87	6.34E-03	Ag-110m	2.32E-08	Cs-134	1.09E-04
Sr-88	2.02E-01	Cd-110	6.18E-04	Cs-135	2.14E-03
Sr-89	1.28E-12	Cd-111	2.91E-03	Cs-136	5.75E-48
Sr-90	2.97E-01	Cd-112	2.01E-03	Cs-137	1.54E-02
Y-89	1.37E-01	Cd-113	1.36E-04	Ba-134	2.89E-02
Y-90	7.65E-05	Cd-114	3.26E-03	Ba-136	3.06E-03
Y-91	2.68E-11	Cd-115m	4.42E-17	Ba-136m	2.77E-53
Zr-90	2.78E-02	Cd-116	1.51E-03	Ba-137	1.18E-01
Zr-91	2.21E-01	Sn-116	2.09E-04	Ba-137m	2.38E-09
Zr-92	2.27E-01	Sn-117	1.08E-03	Ba-138	1.05E+00
Zr-93	3.93E-01	Sn-118	1.16E-03	Ba-140	1.23E-44
Zr-94	2.51E-01	Sn-119	1.13E-03	La-139	3.80E-01
Zr-95	4.15E-10	Sn-120	1.17E-03	La-140	6.88E-46
Zr-96	2.52E-01	Sn-121m	4.72E-07	Ce-140	3.74E-01
Nb-94	4.48E-07	Sn-122	1.31E-03	Ce-141	1.12E-18
Nb-95	4.81E-10	Sn-123	2.75E-08	Ce-142	3.52E-01
Nb-95m	2.90E-13	Sn-124	1.96E-03	Ce-144	2.74E-03
Mo-95	2.52E-01	Sn-125	1.58E-61	Pr-141	3.51E-01
Mo-96	1.02E-03	Sn-126	4.54E-03	Pr-143	1.58E-42
Mo-97	2.40E-01	Sb-121	1.26E-03	Pr-144	1.16E-07
Mo-98	2.48E-01	Sb-123	1.59E-03	Pr-144m	5.76E-10
Mo-100	2.65E-01	Sb-124	3.60E-15	Nd-142	1.25E-03
Tc-99	1.64E-01	Sb-125	7.11E-04	Nd-143	4.19E-01
Ru-100	1.67E-03	Sb-126	2.15E-10	Nd-144	3.60E-01
Ru-101	1.94E-01	Sb-126m	1.63E-12	Nd-145	2.32E-01
Ru-102	1.43E-01	Te-122	2.69E-05	Nd-146	1.88E-01
Ru-103	4.65E-16	Te-124	1.25E-05	Nd-147	1.39E-52
Nd-148	1.09E-01	Eu-156	8.41E-40	Pu-238	7.57E-02
Nd-150	4.35E-02	Tb-159	1.81E-04	Pu-239	1.82E-01
Pm-147	2.31E-02	Tb-160	8.77E-14	Pu-240	3.34E-02
Pm-148	3.75E-19	Tl-206	1.99E-29	Pu-241	1.44E-02

Table 3 Contd

Partial Isotopic Content of Sludge Feed

Isotope	G/Gal	Isotope	G/Gal	Isotope	G/Gal
Pm-148m	4.18E-17	Tl-207	3.28E-19	Pu-242	2.73E-03
Sm-147	7.42E-02	Tl-208	3.29E-15	Am-241	2.76E-03
Sm-148	1.65E-02	Tl-209	9.63E-24	Am-242	1.55E-11
Sm-149	6.43E-03	U-232	5.42E-07	Am-242m	1.30E-06
Sm-150	9.13E-02	U-233	1.43E-07	Am-243	2.54E-05
Sm-151	8.19E-03	U-234	4.77E-03	Cm-242	9.32E-09
Sm-152	3.29E-02	U-235	6.33E-02	Cm-243	9.46E-08
Sm-154	5.85E-03	U-236	1.51E-02	Cm-244	1.16E-03
Eu-151	3.43E-04	U-238	2.72E+01	Cm-245	3.39E-08
Eu-152	1.84E-05	Np-236	1.16E-09	Cm-246	1.52E-09
Eu-153	1.81E-02	Np-237	1.10E-02	Cm-247	6.17E-12
Eu-154	2.03E-03	Pu-236	2.01E-07	Cm-248	1.41E-13
Eu-155	9.04E-04	Pu-237	6.47E-19		
	Total	3.60E+01 G/Gal			

Table 4

Chemical Composition of Precipitate Feed from In-Tank Processing to Salt Cell

Component	Water Free wt%
$Al(OH)_3$	0.47
CsTPB	0.79
$Fe(OH)_3$	0.49
$Hg(C_6H_5)_2$	0.88
KTPB	75.60
NH_4TPB	3.54
$Na_2C_2O_4$	0.97
Na_2CO_3	0.62
Na_2SO_4	0.71
$NaAl(OH)_4$	1.31
$NaNO_2$	1.48
$NaNO_3$	5.96
NAOH	2.40
NaTBP	0.66
$NaTi_2O_5H$	3.52
Others	0.60
Total	100.00

Table 5

Radionuclide Content of Precipitate Slurry Feed to the Salt Cell

Isotope	Ci/Gal	Isotope	Ci/Gal	Isotope	Ci/Gal
H-3	9.06E-05	Sb-124	8.88E-30	Tb-160	2.64E-27
C-14	1.98E-09	Sb-125	1.50E-02	Tl-208	2.67E-08
Co-60	3.28E-04	Sb-126	3.22E-05	U-232	1.67E-07
Ni-59	2.25E-07	Sb-126m	2.30E-04	U-233	2.45E-11
Ni-63	2.72E-05	Te-125m	2.15E-07	U-234	8.35E-07
Se-79	3.75E-07	Te-127	9.73E-20	U-235	1.48E-09
Rb-87	2.25E-10	Te-127m	9.94E-20	U-236	1.07E-08
Sr-89	7.92E-32	I-129	1.51E-10	U-238	9.91E-08
Sr-90	3.99E-01	Cs-134	1.66E-01	Np-236	1.96E-13
Y-90	4.12E-01	Cs-135	8.37E-05	Np-237	1.00E-07
Y-91	4.93E-28	Cs-137	3.60E+01	Pu-236	1.20E-07
Zr-93	4.08E-07	Ba-137m	3.44E+01	Pu-237	8.04E-41
Zr-95	6.26E-26	Ce-141	2.17E-50	Pu-238	1.53E-02
Nb-94	9.10E-10	Ce-142	3.63E-11	Pu-239	1.44E-04
Nb-95	1.32E-25	Ce-144	5.11E-06	Pu-240	9.71E-05
Nb-95m	7.74E-28	Pr-144	5.13E-06	Pu-241	1.16E-02
Tc-99	6.97E-05	Pr-144m	6.13E-08	Pu-242	1.37E-07
Ru-103	3.85E-41	Nd-144	1.85E-15	Am-241	2.40E-04
Ru-106	3.14E-05	Pm-147	6.56E-03	Am-242	1.55E-07
Rh-103m	3.75E-41	Pm-148	6.31E-43	Am-242m	1.56E-07
Rh-106	3.15E-05	Pm-148m	9.16E-42	Am-243	6.52E-08
Pd-107	1.38E-07	Sm-147	3.35E-11	Cm-242	1.28E-07
Ag-110m	3.18E-10	Sm-148	7.56E-17	Cm-243	4.94E-08
Cd-113	5.23E-20	Sm-149	2.32E-17	Cm-244	1.20E-03
Cd-115m	2.81E-40	Sm-151	3.02E-03	Cm-245	7.53E-11
Sn-121m	3.93E-05	Eu-152	1.07E-05	Cm-246	6.00E-12
Sn-123	1.21E-12	Eu-154	1.37E-03	Cm-247	7.38E-18
Sn-126	2.30E-04	Eu-155	5.54E-04	Cm-248	7.73E-18

Total activity	7.14E+01 Ci/Gal
Decay heat	
Total primary	4.33E-02 Watt/Gal
Total gammas	1.24E-01 Watt/Gal

Table 6

Partial Isotopic Content of Precipitate Slurry Feed to the Salt Cell

Isotope	G/Gal	Isotope	G/Gal	Isotope	G/Gal
H-3	9.43E-09	Ru-106	9.38E-09	Te-126	1.33E-09
C-14	4.44E-10	Rh-103	9.90E-04	Te-127	3.68E-26
Co-60	2.90E-07	Rh-103m	1.15E-48	Te-127m	1.05E-23
Ni-59	2.79E-06	Rh-106	8.85E-15	Te-128	3.63E-07
Ni-63	4.61E-07	Pd-104	1.07E-04	Te-129	1.74E-60
Se-77	8.63E-07	Pd-105	8.53E-04	Te-129m	1.88E-57
Se-78	2.18E-06	Pd-106	5.62E-04	Te-130	1.31E-06
Se-79	5.37E-06	Pd-107	2.68E-04	I-127	2.31E-07
Se-80	1.28E-05	Pd-108	1.58E-04	I-129	8.56E-07
Se-82	2.58E-05	Pd-110	5.50E-05	Cs-133	5.76E-01
Rb-85	1.04E-03	Ag-109	1.03E-02	Cs-134	1.28E-04
Rb-87	2.57E-03	Ag-110m	6.68E-14	Cs-135	7.26E-02
Sr-88	2.54E-03	Cd-110	6.93E-07	Cs-137	4.15E-01
Sr-89	2.72E-36	Cd-111	3.26E-06	Ba-134	3.82E-04
Sr-90	2.92E-03	Cd-112	2.25E-06	Ba-136	3.38E-05
Y-89	1.49E-03	Cd-113	1.54E-07	Ba-137	3.23E-03
Y-90	7.57E-07	Cd-114	3.67E-06	Ba-137m	6.39E-08
Y-91	2.01E-32	Cd-115m	1.10E-44	Ba-138	1.15E-02
Zr-90	2.85E-05	Cd-116	1.69E-06	Ce-140	1.61E-03
Zr-91	9.12E-05	Sn-116	3.74E-04	Ce-141	7.61E-55
Zr-92	9.36E-05	Sn-117	1.94E-03	Ce-142	1.51E-03
Zr-93	1.62E-04	Sn-118	2.08E-03	Ce-144	1.60E-09
Zr-94	1.04E-04	Sn-119	2.02E-03	Pr-141	1.51E-03
Zr-95	2.92E-30	Sn-120	2.10E-03	Pr-144	6.78E-14
Zr-96	1.08E-04	Sn-121m	7.32E-07	Pr-144m	3.38E-16
Nb-94	4.85E-09	Sn-122	2.34E-03	Nd-142	5.37E-06
Nb-95	3.36E-30	Sn-123	1.47E-16	Nd-143	1.80E-03
Nb-95m	2.04E-33	Sn-124	3.51E-03	Nd-144	1.56E-03
Mo-95	2.30E-03	Sn-126	8.10E-03	Nd-145	9.95E-04
Mo-96	9.33E-06	Sb-121	3.27E-04	Nd-146	8.10E-04
Mo-97	2.20E-03	Sb-123	4.13E-04	Nd-148	4.67E-04
Mo-98	2.26E-03	Sb-124	5.07E-34	Nd-150	1.87E-04
Mo-100	2.42E-03	Sb-125	1.45E-05	Pm-147	7.07E-06
Tc-99	4.11E-03	Sb-126	3.85E-10	Pm-148	3.84E-48
Ru-100	2.50E-05	Sb-126m	2.93E-12	Pm-148m	4.28E-46
Ru-101	1.93E-03	Te-122	2.87E-10	Sm-147	1.44E-03
Ru-102	2.13E-03	Te-124	1.34E-10	Sm-148	2.48E-04
Ru-103	1.19E-45	Te-125	4.04E-08	Sm-149	9.66E-05
Ru-104	1.07E-03	Te-125m	1.19E-11	Sm-150	1.37E-03
Sm-151	1.15E-04	U-232	7.78E-09	Pu-241	1.15E-04
Sm-152	4.93E-04	U-233	2.54E-09	Pu-242	3.49E-05
Sm-154	8.78E-05	U-234	1.34E-04	Am-241	6.98E-05
Eu-151	5.22E-06	U-235	6.86E-04	Am-242	1.91E-13
Eu-152	6.05E-08	U-236	1.65E-04	Am-242m	1.60E-08

Table 6 Contd

Partial Isotopic Content of Precipitate Slurry Feed to the Salt Cell

Isotope	G/Gal	Isotope	G/Gal	Isotope	G/Gal
Eu-153	1.01E-04	U-238	2.95E-01	Am-243	3.27E-07
Eu-154	5.07E-06	Np-236	1.49E-11	Cm-242	3.88E-11
Eu-155	1.19E-06	Np-237	1.43E-04	Cm-243	9.57E-10
Tb-159	7.76E-07	Pu-236	2.26E-10	Cm-244	1.48E-05
Tb-160	2.34E-31	Pu-237	6.66E-45	Cm-245	4.37E-10
Tl-206	8.54E-30	Pu-238	8.92E-04	Cm-246	1.95E-11
Tl-207	1.17E-20	Pu-239	2.32E-03	Cm-247	7.96E-14
Tl-208	9.08E-17	Pu-240	4.27E-04	Cm-248	1.82E-15
Tl-209	5.46E-25				
	Total	1.46E+00 G/Gal			

Table 7

Chemical Composition of Feed from Salt Cell

Component	Water Free wt%
$(BC_6H_5O)_3$	0.91
$(C_6H_5)_2$	5.03
$Al(OH)_3$	0.76
$C_6H_5B(OH)_2$	6.07
$C_6H_5HgCOOH$	1.31
C_6H_5OH	2.07
$CsCOOH$	0.50
$Cu(COOH)_2$	1.33
$Fe(OH)_3$	0.80
H_3BO_3	19.02
$HCOOH$	1.36
$KCOOH$	28.86
NH_4COOH	1.08
$Na_2C_2O_4$	1.58
Na_2SO_4	2.39
$NaAl(OH)_4$	2.14
$NaCOOH$	13.10
$NaNO_3$	5.02
$NaTi_2O_5H$	5.72
Others	0.95
Total	100.00

Table 8

Radionuclide Content of Feed from Salt Cell

Isotope	Ci/Gal	Isotope	Ci/Gal	Isotope	Ci/Gal
H-3	9.57E-05	Sb-124	9.51E-30	Tb-160	2.83E-27
C-14	7.45E-11	Sb-125	1.61E-02	Tl-208	2.86E-08
Co-60	3.51E-04	Sb-126	3.45E-05	U-232	1.79E-07
Ni-59	2.41E-07	Sb-126m	2.46E-04	U-233	2.62E-11
Ni-63	2.92E-05	Te-125m	2.31E-07	U-234	8.94E-07
Se-79	4.01E-07	Te-127	1.04E-19	U-235	1.59E-09
Rb-87	2.41E-10	Te-127m	1.06E-19	U-236	1.14E-08
Sr-89	8.48E-32	I-129	1.62E-10	U-238	1.06E-07
Sr-90	4.27E-01	Cs-134	1.78E-01	Np-236	2.10E-13
Y-90	4.42E-01	Cs-135	8.96E-05	Np-237	1.08E-07
Y-91	5.27E-28	Cs-137	3.85E+01	Pu-236	1.28E-07
Zr-93	4.37E-07	Ba-137m	3.69E+01	Pu-237	8.61E-41
Zr-95	6.70E-26	Cs-141	2.32E-50	Pu-238	1.63E-02
Nb-94	9.75E-10	Ce-142	3.89E-11	Pu-239	1.54E-04
Nb-95	1.41E-25	Ce-144	5.47E-06	Pu-240	1.04E-04
Nb-95m	8.28E-28	Pr-144	5.49E-06	Pu-241	1.24E-02
Tc-99	7.46E-05	Pr-144m	6.57E-08	Pu-242	1.47E-07
Ru-103	4.13E-41	Nd-144	1.98E-15	Am-241	2.57E-04
Ru-106	3.36E-05	Pm-147	7.03E-03	Am-242	1.66E-07
Rh-103m	4.01E-41	Pm-148	6.76E-43	Am-242m	1.67E-07
Rh-106	3.37E-05	Pm-148m	9.80E-42	Am-243	6.98E-08
Pd-107	1.47E-07	Sm-147	3.59E-11	Cm-242	1.37E-07
Ag-110m	3.40E-10	Sm148	8.10E-17	Cm-243	5.29E-08
Cd-113	5.60E-20	Sm-149	2.48E-17	Cm-244	1.29E-03
Cd-115m	3.01E-40	Sm-151	3.23E-03	Cm-245	8.06E-11
Sn-121m	4.21E-05	Eu-152	1.14E-05	Cm-246	6.42E-12
Sn-123	1.30E-12	Eu-154	1.47E-03	Cm-247	7.90E-18
Sn-126	2.46E-04	Eu-155	5.93E-04	Cm-248	8.28E-18

Total activity	7.65E+01 Ci/Gal
Decay heat	
Total primary	4.63E-02 Watt/Gal
Total gammas	1.32E-01 Watt/Gal

Table 9

Partial Isotopic Content of Feed from Salt Cell

Isotope	G/Gal	Isotope	G/Gal	Isotope	G/Gal
H-3	9.97E-09	Ru-106	1.00E-08	Te-126	1.43E-09
C-14	1.67E-11	Rh-103	1.06E-03	Te-127	3.94E-26
Co-60	3.10E-07	Rh-103m	1.23E-48	Te-127m	1.13E-23
Ni-59	2.99E-06	Rh-106	9.47E-15	Te-128	3.89E-07
Ni-63	4.94E-07	Pd-104	1.15E-04	Te-129	1.86E-60
Se-77	9.24E-07	Pd-105	9.14E-04	Te-129m	2.01E-57
Se-78	2.33E-06	Pd-106	6.02E-04	Te-130	1.41E-06
Se-79	5.75E-06	Pd-107	2.87E-04	I-127	2.47E-07
Se-80	1.37E-05	Pd-108	1.69E-04	I-129	9.16E-07
Se-82	2.77E-05	Pd-110	5.89E-05	Cs-133	6.16E-01
Rb-85	1.12E-03	Ag-109	1.11E-02	Cs-134	1.37E-04
Rb-87	2.75E-03	Ag-110m	7.16E-14	Cs-135	7.77E-02
Sr-88	2.73E-03	Cd-110	7.42E-07	Cs-137	4.45E-01
Sr-89	2.91E-36	Cd-111	3.49E-06	Ba-134	4.09E-04
Sr-90	3.13E-03	Cd-112	2.41E-06	Ba-136	3.62E-05
Y-89	1.59E-03	Cd-113	1.64E-07	Ba-137	3.46E-03
Y-90	8.11E-07	Cd-114	3.93E-06	Ba-137m	6.85E-08
Y-91	2.15E-32	Cd-115m	1.18E-44	Ba-138	1.23E-02
Zr-90	3.05E-05	Cd-116	1.81E-06	Ce-140	1.72E-03
Zr-91	9.76E-05	Sn-116	4.00E-04	Ce-141	8.15E-55
Zr-92	1.00E-04	Sn-117	2.07E-03	Ce-142	1.62E-03
Zr-93	1.74E-04	Sn-118	2.22E-03	Ce-144	1.71E-09
Zr-94	1.11E-04	Sn-119	2.16E-03	Pr-141	1.61E-03
Zr-95	3.12E-30	Sn-120	2.25E-03	Pr-144	7.26E-14
Zr-96	1.16E-04	Sn-121m	7.83E-07	Pr-144m	3.62E-16
Nb-94	5.20E-09	Sn-122	2.51E-03	Nd-142	5.75E-06
Nb-95	3.60E-30	Sn-123	1.58E-16	Nd-143	1.93E-03
Nb-95m	2.18E-33	Sn-124	3.75E-03	Nd-144	1.67E-03
Mo-95	2.46E-03	Sn-126	8.67E-03	Nd-145	1.07E-03
Mo-96	9.98E-06	Sb-121	3.50E-04	Nd-146	8.67E-04
Mo-97	2.35E-03	Sb-123	4.42E-04	Nd-148	5.00E-04
Mo-98	2.42E-03	Sb-124	5.43E-34	Nd-150	2.01E-04
Mo-100	2.59E-03	Sb-125	1.56E-05	Pm-147	7.57E-06
Tc-99	4.40E-03	Sb-126	4.12E-10	Pm-148	4.11E-48
Ru-100	2.68E-05	Sb-126m	3.13E-12	Pm-148m	4.59E-46
Ru-101	2.06E-03	Te-122	3.08E-10	Sm-147	1.54E-03
Ru-102	2.28E-03	Te-124	1.43E-10	Sm-148	2.65E-04
Ru-103	1.28E-45	Te-125	4.32E-08	Sm-149	1.03E-04
Ru-104	1.15E-03	Te-125m	1.28E-11	Sm-150	1.47E-03
Sm-151	1.23E-04	U-232	8.33E-09	Pu-241	1.23E-04
Sm-152	5.28E-04	U-233	2.72E-09	Pu-242	3.74E-05
Sm-154	9.40E-05	U-234	1.43E-04	Am-241	7.48E-05
Eu-151	5.59E-06	U-235	7.35E-04	Am-242	2.05E-13

Table 9 Contd

Partial Isotopic Content of Feed from Salt Cell

Isotope	G/Gal	Isotope	G/Gal	Isotope	G/Gal
Eu-152	6.48E-08	U-236	1.76E-04	Am-242m	1.71E-08
Eu-153	1.09E-04	U-238	3.16E-01	Am-243	3.50E-07
Eu-154	5.43E-06	Np-236	1.59E-11	Cm-242	4.15E-11
Eu-155	1.27E-06	Np-237	1.53E-04	Cm-243	1.02E-09
Tb-159	8.31E-07	Pu-236	2.42E-10	Cm-244	1.59E-05
Tb-160	2.50E-31	Pu-237	7.13E-45	Cm-245	4.68E-10
Tl-206	9.15E-30	Pu-238	9.55E-04	Cm-246	2.09E-11
Tl-207	1.25E-20	Pu-239	2.49E-03	Cm-247	8.52E-14
Tl-208	9.72E-17	Pu-240	4.57E-04	Cm-248	1.95E-15
Tl-209	5.85E-25				
	Total	1.56E+00 G/Gal			

Table 10

Chemical Composition of Sludge-Precipitate Glass

Component	Water Free wt%
Ag	0.05
Al_2O_3	3.96
B_2O_3	10.28
$BaSO_4$	0.14
$Ca_3(PO_4)_2$	0.07
CaO	0.85
$CaSO_4$	0.08
Cr_2O_3	0.12
Cs_2O	0.08
CuO	0.19
Fe_2O_3	7.04
FeO	3.12
K_2O	3.58
Li_2O	3.16
MgO	1.36
MnO	2.00
Na_2O	11.00
Na_2SO_4	0.36
NaCl	0.19
NaF	0.07
NiO	0.93
PbS	0.07
SiO_2	45.57
ThO_2	0.21
TiO_2	0.99
U_3O_8	2.20
Zeolite	1.67
ZnO	0.08
Others	0.58
Total	100.00

Table 11

Radionuclide Content of Sludge-Precipitate Glass

Isotope	Ci/Lb	Isotope	Ci/Lb	Isotope	Ci/Lb
Cr-51	2.51E-20	Te-125m	7.44E-02	Eu-155	1.28E-01
Co-60	4.58E-02	Te-127	3.24E-05	Eu-156	1.41E-35
Ni-59	6.46E-06	Te-127m	3.31E-05	Tb-160	3.02E-10
Ni-63	8.02E-04	Te-129	8.23E-16	Tl-208	3.04E-07
Se-79	4.58E-05	Te-129m	1.28E-15	U-232	3.61E-06
Rb-87	2.35E-10	Cs-134	9.09E-02	U-233	4.27E-10
Sr-89	1.15E-08	Cs-135	2.68E-05	U-234	9.24E-06
Sr-90	1.26E+01	Cs-136	2.11E-43	U-235	4.24E-08
Y-90	1.29E+01	Cs-137	1.17E+01	U-236	3.04E-07
Y-91	2.04E-07	Ba-136m	2.32E-42	U-238	2.83E-06
Zr-93	3.01E-04	Ba-137m	1.12E+01	Np-236	4.70E-12
Zr-95	2.71E-06	Ba-140	2.76E-40	Np-237	2.40E-06
Nb-94	2.60E-08	La-140	1.16E-40	Pu-236	3.29E-05
Nb-95	5.70E-06	Ce-141	9.68E-15	Pu-237	2.41E-15
Nb-95m	3.36E-08	Ce-142	2.59E-09	Pu-238	4.00E-01
Tc-99	8.30E-04	Ce-144	2.66E+00	Pu-239	3.48E-03
Ru-103	4.54E-12	Pr-143	3.23E-38	Pu-240	2.34E-03
Ru-106	6.07E-01	Pr-144	2.66E+00	Pu-241	4.50E-01
Rh-103m	4.41E-12	Pr-144m	3.20E-02	Pu-242	3.30E-06
Rh-106	6.09E-01	Nd-144	1.31E-13	Am-241	2.97E-03
Pd-107	3.97E-06	Nd-147	3.40E-48	Am-242	3.87E-06
Ag-110m	3.39E-05	Pm-147	6.52E+00	Am-242m	3.90E-06
Cd-113	1.35E-17	Pm-148	1.88E-14	Am-243	1.56E-06
Cd-115m	3.27E-13	Pm-148m	2.72E-13	Cm-242	9.42E-06
Sn-121m	2.13E-05	Sm-147	5.39E-10	Cm-243	1.50E-06
Sn-123	6.87E-05	Sm-148	1.56E-15	Cm-244	2.90E-02
Sn-126	1.19E-04	Sm-149	4.80E-16	Cm-245	1.81E-09
Sb-124	1.92E-11	Sm-151	6.68E-02	Cm-246	1.44E-10
Sb-125	2.29E-01	Eu-152	9.94E-04	Cm-247	1.78E-16
Sb-126	1.66E-05	Eu-154	1.67E-01	Cm-248	1.85E-16
Sb-126m	1.19E-04				

Total activity	6.31E+01 Ci/Lb
Decay heat	
Total primary	1.42E-01 Watts/Lb
Total gammas	4.45E-02 Watts/Lb

Table 12

Partial Isotopic Content of Sludge-Precipitate Glass

Isotope	G/Lb	Isotope	G/Lb	Isotope	G/Lb
Cr-51	2.72E-25	Rh-103	2.34E-02	Te-126	3.62E-05
Co-60	4.05E-05	Rh-103m	1.35E-19	Te-127	1.23E-11
Ni-59	7.99E-05	Rh-106	1.71E-10	Te-127m	3.50E-09
Ni-63	1.36E-05	Pb-104	3.09E-03	Te-128	9.86E-03
Se-77	1.06E-04	Pd-105	2.46E-02	Te-129	3.93E-23
Se-78	2.67E-04	Pd-106	1.58E-02	Te-129m	4.25E-20
Se-79	6.57E-04	Pd-107	7.71E-03	Te-130	3.57E-02
Se-80	1.57E-03	Pd-108	4.55E-03	Cs-133	1.84E-01
Se-82	3.17E-03	Pd-110	1.58E-03	Cs-134	7.02E-05
Rb-85	1.09E-03	Ag-109	5.13E-03	Cs-135	2.33E-02
Rb-87	2.68E-03	Ag-110m	7.14E-09	Cs-136	2.85E-48
Sr-88	6.25E-02	Cd-110	1.79E-04	Cs-137	1.35E-01
Sr-89	3.96E-13	Cd-111	8.42E-04	Ba-134	8.93E-03
Sr-90	9.20E-02	Cd-112	5.81E-04	Ba-136	9.47E-04
Y-89	4.25E-02	Cd-113	3.97E-05	Ba-136m	8.56E-54
Y-90	2.37E-05	Cd-114	9.46E-04	Ba-137	3.63E-02
Y-91	8.31E-12	Cd-115m	1.28E-17	Ba-137m	2.08E-08
Zr-90	8.47E-03	Cd-116	4.37E-04	Ba-138	3.23E-01
Zr-91	6.72E-02	Sn-116	1.93E-04	Ba-140	3.79E-45
Zr-92	6.90E-02	Sn-117	9.98E-04	La-139	1.16E-01
Zr-93	1.20E-01	Sn-118	1.07E-03	La-140	2.09E-46
Zr-94	7.66E-02	Sn-119	1.04E-03	Ce-140	1.15E-01
Zr-95	1.26E-10	Sn-120	1.08E-03	Ce-141	3.40E-19
Zr-96	7.69E-02	Sn-121m	3.97E-07	Ce-142	1.08E-01
Nb-94	1.39E-07	Sn-122	1.21E-03	Ce-144	8.33E-04
Nb-95	1.46E-10	Sn-123	8.36E-09	Pr-141	1.07E-01
Nb-95m	8.84E-14	Sn-124	1.82E-03	Pr-143	4.80E-43
Mo-95	7.37E-02	Sn-125	4.82E-62	Pr-144	3.52E-03
Mo-96	2.99E-04	Sn-126	4.17E-03	Pr-144m	1.76E-10
Mo-97	7.05E-02	Sb-121	4.96E-04	Nd-142	3.81E-04
Mo-98	7.24E-02	Sb-123	6.28E-04	Nd-143	1.28E-01
Mo-100	7.73E-02	Sb-124	1.10E-15	Nd-144	1.10E-01
Tc-99	4.89E-02	Sb-125	2.22E-04	Nd-145	7.08E-02
Ru-100	5.16E-04	Sb-126	1.98E-10	Nd-146	5.75E-02
Ru-101	5.95E-02	Sb-126m	1.51E-12	Nd-147	4.23E-53
Ru-102	4.40E-02	Te-122	7.82E-06	Nd-148	3.33E-02
Ru-103	1.40E-16	Te-124	3.64E-06	Nd-150	1.33E-02
Ru-104	2.22E-02	Te-125	8.30E-04	Pm-147	7.03E-03
Ru-106	1.81E-04	Te-125m	4.13E-06	Pm-148	1.14E-19
Pm-148m	1.27E-17	Tl-206	9.01E-30	Pu-239	5.61E-02
Sm-147	2.32E-02	Tl-207	1.04E-19	Pu-240	1.03E-02
Sm-148	5.10E-03	Tl-208	1.03E-15	Pu-241	4.46E-03
Sm-149	2.00E-03	Tl-209	3.12E-24	Pu-242	8.42E-04

Table 12 Contd

Partial Isotopic Content of Sludge-Precipitate Glass

Isotope	G/Lb	Isotope	G/Lb	Isotope	G/Lb
Sm-150	2.83E-02	U-232	1.68E-07	Am-241	8.64E-04
Sm-151	2.54E-03	U-233	4.43E-08	Am-242	4.79E-12
Sm-152	1.02E-02	U-234	1.48E-03	Am-242m	4.01E-07
Sm-154	1.80E-03	U-235	1.96E-02	Am-243	7.85E-06
Eu-151	1.06E-04	U-236	4.70E-03	Cm-242	2.84E-09
Eu-152	5.63E-06	U-238	8.43E+00	Cm-243	2.91E-08
Eu-153	5.56E-03	Np-236	3.56E-10	Cm-244	3.59E-04
Eu-154	6.20E-04	Np-237	3.40E-03	Cm-245	1.05E-08
Eu-155	2.76E-04	Pu-236	6.19E-08	Cm-246	4.69E-10
Eu-156	2.57E-40	Pu-237	2.00E-19	Cm-247	1.91E-12
Tb-159	5.53E-05	Pu-238	2.34E-02	Cm-248	4.36E-14
Tb-160	2.68E-14				
	Total	1.15E+01 G/Lb			

Table 13A

Chemical Composition of Glass Frits, wt%

Oxide	Frit Number					
	18	21	131	165	200[a]	202
SiO_2	52.5	52.5	57.9	68.0	70.5	77.0
Na_2O	22.5	18.5	17.7	13.0	10.4	6.0
TiO_2	10.0	10.0	1.0	-	-	-
B_2O_3	10.0	10.0	14.7	10.0	12.1	8.0
Li_2O	-	4.0	5.7	7.0	5.0	7.0
MgO	-	-	2.0	1.0	2.0	2.0
ZrO2	-	-	0.5	1.0	-	-
La_2O_3	-	-	0.5	-	-	-
CaO	5.0	5.0	-	-	-	-

[a] Design basis frit.

Table 13B

Projected DWPF Waste Glass Compositions, wt %

Major Glass Components	Constituent Sludge Type						
	Blend	Batch 1	Batch 2	Batch 3	Batch 4	HM	Purex
Al_2O_3	3.98	4.87	4.46	3.25	3.32	7.08	2.89
B_2O_3	8.01	7.69	7.70	7.69	8.11	6.94	10.21
$BaSO_4$	0.27	0.22	0.24	0.26	0.38	0.18	0.29
CaO	0.97	1.17	1.00	0.93	0.83	1.00	1.02
$CaSO_4$	0.077	0.12	0.11	0.10	0.0034	trace	0.12
Cr_2O_3	0.12	0.10	0.12	0.13	0.14	0.086	0.14
CuO	0.44	0.40	0.41	0.40	0.46	0.25	0.42
Fe_2O_3	6.95	8.39	7.11	7.48	7.59	4.95	8.54
FeO	3.11	3.72	3.15	3.31	3.36	2.19	3.78
Group A[a]	0.14	0.099	0.14	0.10	0.20	0.20	0.078
Group B[b]	0.36	0.22	0.44	0.25	0.60	0.89	0.084
K_2O	3.86	3.49	3.50	3.47	3.99	2.14	3.58
Li_2O	4.40	4.42	4.42	4.42	4.32	4.62	3.12
MgO	1.35	1.36	1.35	1.35	1.38	1.45	1.33
MnO	2.03	2.06	1.62	1.81	3.08	2.07	1.99
Na_2O	8.73	8.62	8.61	8.51	8.88	8.17	12.14
Na_2SO_4	0.10	0.10	0.12	0.096	0.13	0.14	0.12
NaCl	0.19	0.31	0.23	0.22	0.090	0.093	0.26
NiO	0.89	0.75	0.90	1.07	1.09	0.40	1.21
SiO_2	50.20	49.81	50.17	49.98	49.29	54.39	44.56
ThO_2	0.19	0.36	0.63	0.77	0.24	0.55	0.011
TiO_2	0.90	0.66	0.67	0.66	1.02	0.55	0.65
U_3O_8	2.14	0.53	2.30	3.16	0.79	1.01	2.89

[a] Tc, Se, Te, Rb, and Mo.

[b] Ag, Cd, Cr, Pd, Tl, La, Ce, Pr, Pm, Nd, Sm, Tb, Sn, Sb, Co, Zr, Nb, Eu, Np, Am, and Cm.

Table 14

Physical Properties of Glass Wasteforms

Property	Value
Thermal conductivity at 100°C	0.55 Btu/(hr)(ft) (°F)
Heat capacity at 100°C	0.22 cal/(g)(°C) also Btu/(lb)(°F)
Fractional thermal expansion[a]	1.2 x 10-5/°C
Young's modulus	9×10^6 psi
Tensile strength	9×10^3 psi
Compressive strength	1×10^5 psi
Poisson's ratio	0.2
Density at 100°C[a]	2.75 ± 0.05 g/cc
Softening point	488°C

[a] Experimentally determined for Frit 131 and Frit 165 glasses containing composite waste.

Table 15

Composition of Simulated Wastes

Component	Simulation 1[a]	Simulation 2[a]	Simulation 3[a]
Fe_2O_3	47.3	13.8	59.1
MnO_2	13.6	11.3	4.0
Zeolite[b]	10.2	10.2	9.7
Al_2O_3	9.5	49.3	1.4
NiO	5.8	2.0	10.1
SiO_2	4.1	4.5	2.9
CaO	3.5	0.9	4.0
Na_2O	3.1	5.0	5.9
Coal	2.3	2.3	2.1
Na_2SO_4	0.6	0.7	0.8
Glassformer/ waste ratio	70.2/29.8	71.3/27.7	70.2/29.8

[a] Simulation 1 is composite waste; simulation 2 is high aluminum waste; simulation 3 is high iron waste.

[b] Zeolite composition is given in Table 18.

Table 16

Heat Capacities of Simulated Waste Glasses

	Heat Capacity - c_{pt} (cal/(g)(°C)			
Temperature, °C	Calculated Simulation 1 (Composite)	Measured Simulation 1 (Composite)	Measured Simulation 2 (High Al)	Measured Simulation 3 (High Fe)
0		0.186		
50	-	0.20	0.19	0.20
100	0.237	0.21	0.21	0.21
200	0.271	0.23	0.23	0.23
300	0.296	0.27	0.25	0.25
400	0.314			
500	0.328			
600	0.338			
700	0.346			
800	0.353			
900	0.359			
950	0.361			
1000	0.363			
1025	0.364			
1050	0.365			
1075	0.366			
1100	0.367			
1125	0.368			
1150	0.369			
1175	0.369			
1200	0.370			
1250	0.372			
1300	0.373			

Table 17

Measured Density of SRP Simulated Waste Glasses

Glass	Density, g/cm3 at 25°C
Simulation 1 - composite	2.75
Simulation 2 - high Al	2.56
Simulation 3 - high Fe	2.92

Table 18

Zeolite Composition

Component	Wt %
SiO_2	48.0
H_2O	19.1
Al_2O_3	18.6
CaO	10.2
Na_2O	4.1

Table 19

Canister Decay Heat and Activity

Year	Design Basis Curies/Can	Waste Glass Watts/Can
5	233,000	690
10	171,000	517
20	129,000	406
30	101,000	324
40	80,000	262
50	63,000	211
60	50,000	171
70	39,000	139
80	31,000	115
90	25,000	94
100	20,000	78
200	2,200	17
300	400	7.2
400	160	4.1
500	96	2.7
600	70	2.0
700	57	1.6
800	49	1.4
900	45	1.2
1000	41	1.1

Table 20

Radiation from Canister of Sludge-Precipitate Glass

Distance, ft	Gamma, R/hr	Neutron, Mead hr	Total, rad hr
Surface	5570	420	5570
1	2190	97	2190
3	900	42	900
5	470	23	470
10	160	7.5	160
20	44	2.5	44
30	20	1.0	20
50	7	0.5	7
75	3	-	3
100	2	-	2

Table 21

Chemical Composition of Sludge-Precipitate Glass for Radiation Calculations[a]

Component	Wt %	Component	Wt %
Al_2O_3	3.96	MnO	2.00
B_2O_3	10.28	SiO_2	46.72
CaO	0.85	TiO_2	0.99
Fe_2O_3	7.04	U_3O_8	2.20
FeO	3.12	Na_2O	12.15
K_2O	3.58	NiO	0.93
Li_2O	3.16	Zeolite[b]	1.67
MgO	1.36		

[a] Compounds present at >0.8 wt %.
[b] Zeolite composition is given in Table 18.

Table 22

Source Terms for Sludge-Precipitate Glass for Radiation Calculations

Isotope	Ci/Lb	Neutron Yields, n/s/canister	
		a,n	SF
U-232	3.61E-06	6.811E-02	1.207E-03
U-233	4.27E-10	8.056E-02	2.104E-07
U-234	9.24E-06	1.743E+03	4.196E-02
U-235	4.24E-08	7.999	3.167E-02
U-236	3.04E-07	5.735E+01	1.321E-01
U-238	2.83E-06	5.339E+02	5.764E+02
Np-237	2.40E-06	4.528E+02	1.908E-03
Pu-236	3.29E-05	6.207E+03	9.927
Pu-233	4.00E-01	7.547E+07	2.732E+05
Pu-239	3.48E-03	6.565E+05	5.672
Pu-240	2.34E-03	4.415E+05	4.346E+04
Pu-241	4.50E-01	2.080E+03	0.0
Pu-242	3.30E-06	6.226E+02	6.834E+03
Am-241	2.97E-03	5.603E+05	4.156
Am-242	3.87E-06	0.0	0.0
Am-242m	3.90E-06	3.502	2.307E-01
Am-243	1.56E-06	2.943E+02	2.136E-02
Cm-242	9.42E-06	1.777E+03	2.563E+02
Cm-243	1.50E-06	2.830E+02	1.588E-08
Cm-244	2.90E-02	5.471E+06	1.450E+07
Cm-245	1.81E-09	3.415E-01	5.740E-09
Cm-246	1.44E-10	2.717E-02	1.400E+01
Cm-247	1.78E-16	3.358E-08	1.032E-12
Cm-248	1.85E-16	3.490E-08	5.075E-03

Table 23

Major Contributing Isotopes to Gamma Dose Rates

Isotope	R/hr at 10 ft	Percent of Dose
Cs/Ba-137	142.1	88.8
Eu-154	4.9	3.1
Co-60	3.1	2.0
Cs-134	3.1	1.9
Ce/Pr-144	2.6	1.6
Ru/Rh-106	2.3	1.4
Sb-125	1.8	1.1
Others	0.1	0.1
Total	160.0	100.0

Table 24

Gamma Radiation from Canister - Comparison of Calculations

Distance From Canister Surface, ft	SRP (ANISN/QAD-CG)[a] R/hr	GA (PATH)[a] R/hr	Westinghouse (SCAP/ANISN-W),[a] R/hr	Bechtel (GRACE-II),[a] R/hr
0	5,570	7,600	11,300	10,970
1	2,190	3,500	4,500	4,760
2	1,500	2,180		2,885
3	900	1,500	1,860	1,920
4	690	1,070		1,350
5	470			990
7	350	490		590
10	160	270		320
15	75	130		155
20	44			89
30	20	34		40
50	7	12		14
75	3	5		6
100	2	3		3

[a] Calculational code used.

Table 25

Neutron Radiation from Canister - Comparison of Calculations

Distance from Canister Surface, ft	SRP (ANISN),[a] mrem/hr	GA (DTF)[a] mrem/hr	Westinghouse (ORIGEN/SOURCES/ANISN/WEST),[a] mrem/hr
0	420	250	305
1	97		
3	42		
5	23		
10	7.5		
20	2.5		
30	1.0		
50	0.5		

[a] Calculational code used.

Table 26

Reference Canister Temperatures[a]

Watts	Surface Temp. °C	Centerline Temp. °C	Surrounding Air Temp. °C
425	34	50	20
510	54	71	38
1000	66	120	38

[a] Reference DWPF sludge-precipitate waste form: canister 24-in. OD by 118 in. high, 22 ft^3 of waste glass containing 28% sludge oxides, and air convection cooling.

Table 27

Projected Waste Inventory and Fission Product Radioactivity as of December 31, 1988

	Volume, (10^3) m^3	Activity (10^6) Ci	Power (10^3) W
Sludge	13.9	495.5	1546.1
Salt Cake	50.4	193.7	501.0
Liquid	62.1	88.8	245.3
Precipitate	0.2	1.3	3.3
Total	126.6	779.3	2295.7

NOTE: 1 m^3 = 264.2 gal.

Isotope	Curies
Sr-89	1,219,000
Sr-90	137,200,000
Y-90[a]	137,300,000
Y-91	2,633,000
Zr-95	4,805,000
Nb-95[a]	10,410,000
Ru-106	5,583,000
Rh-106[a]	5,583,000
Cs-137	141,500,000
Ba-137[a]	130,200,000
Ce-144	70,630,000
Pr-144[a]	70,640,000
Pm-147	60,220,000
Total	777,923,000

[a] Daughter isotopes.

Table 28

Estimated Production Schedule and Estimated Cumulative Average Radioactivity and Thermal Power per Canister of HLW Glass

End of Calendar Year	No. of Canisters Produced During Year	Cumulative No. of Canisters Produced	Cumulative Radioactivity Total, Ci(10^6)	Cumulative Radioactivity Per Canister, Ci	Cumulative Thermal Power Total, W(10^3)	Cumulative Thermal Power Per Canister, W
1991	0	0	--	--	--	--
92	102	102	--	--	--	--
93	410	512	32.9	64,260	87.3	171
94	410	922	52.9	57,380	142.7	155
95	410	1,332	70.0	52,550	190.9	143
96	410	1,742	81.7	46,900	223.5	128
97	410	2,152	91.0	42,290	249.1	116
98	410	2,562	100.5	39,230	275.0	107
99	376	2,938	110.3	37,540	302.1	103
2000	205	3,143	120.1	38,210	329.0	105
01	205	3,348	135.0	40,320	371.8	111
02	205	3,553	158.8	44,690	440.7	124
03	205	3,758	185.0	49,230	516.3	137
04	205	3,963	205.2	51,780	572.9	145
05	205	4,168	218.4	52,400	609.5	146
06	205	4,373	233.8	53,460	653.2	149
07	205	4,578	248.2	54,220	694.6	152
08	205	4,783	264.3	55,260	740.9	155
09	205	4,988	276.1	55,350	774.5	155
2010	205	5,193	283.9	54,670	798.0	154
11	161	5,354	296.4	55,360	835.5	156
12	30	5,384	306.4	56,910	864.9	161
13	31	5,415	313.1	57,820	884.3	163
14	30	5,445	317.5	58,310	896.4	165
15	31	5,476	370.5	58,530	904.4	165
16	30	5,506	323.0	58,660	910.8	165
17	31	5,537	326.0	58,880	918.7	166
18	30	5,567	329.4	59,170	929.2	167
19	31	5,598	336.0	60,020	949.6	170
2020	30	5,628	343.5	61,030	971.5	173
21	31	5,659	348.6	61,600	986.0	174
22	30	5,689	347.5	61,080	982.7	173

Calculated from estimates provided for 1988 Integrated Data Base. Year-by-year radioactivity and thermal power per canister do not necessarily represent actual processing schedules and tankage allocations. Radioactivity and thermal power shown are for fission products only. Radioactivity will be about 1% higher and thermal power about 6% higher when actinides are included.